CONVERGENCE BASIN ANALYSIS IN PERTURBED TRAJECTORY TARGETING PROBLEMS

by

Collin E. York

A Dissertation

Submitted to the Faculty of Purdue University

In Partial Fulfillment of the Requirements for the degree of

Doctor of Philosophy

School of Aeronautics and Astronautics

West Lafayette, Indiana

May 2023

THE PURDUE UNIVERSITY GRADUATE SCHOOL
STATEMENT OF COMMITTEE APPROVAL

Dr. Kathleen C. Howell, Chair

School of Aeronautics and Astronautics

Dr. Carolin Frueh

School of Aeronautics and Astronautics

Dr. Kenshiro Oguri

School of Aeronautics and Astronautics

Dr. Belinda Marchand

School of Aeronautics and Astronautics

Dr. Christopher D'Souza

NASA Johnson Space Center

Approved by:

Dr. Gregory A. Blaisdell

"This is how it should be done: lodge yourself on a stratum, experiment with the opportunities it offers, find an advantageous place on it, find potential movements of deterritorialization, possible lines of flight, experience them, produce flow conjunctions here and there, try out continuums of intensities segment by segment, have a small plot of new land at all times."[1]

- Gilles Deleuze and Félix Guattari

For my children, Neil and Wyatt, and my partner, Caroline —

[1]↑«Voilà donc ce qu'il faudrait faire: s'installer sur une strate, expérimenter les chances qu'elle nous offre, y chercher un lieu favorable, des mouvements de déterritorialisation éventuels, des lignes de fuite possibles, les éprouver, assurer ici et là des conjonctions de flux, essayer segment par segment des continuums d'intensités, avoir toujours un petit morceau d'une nouvelle terre.»[1]

ACKNOWLEDGMENTS

First, I must thank my wife, Caroline, for her endless love and support. When I had the crazy idea to change careers and, in the process, our lives, you immediately encouraged me to take the plunge. That encouragement never wavered as time passed, and it never faltered when I had to travel to Houston for months out of the year. I attribute my accomplishments to you just as much as myself.

Second, I would like to thank my children, Neil and Wyatt, whose laughs, smiles, and hugs have provided me with indescribable support.

I owe a significant debt of gratitude to my parents, Terry and Joy, who instilled in me the value of education from the very beginning. Thank you for encouraging me to explore my passions. Thank you for reading that first book on space to me over and over again. Thank you for always believing in me and teaching me to never stop believing in myself.

I would also like to thank my advisor, Professor Kathleen C. Howell. Thank you for welcoming me into your research group and for your mentorship over the past several years. Your technical insight and motivation to obtain a deeper understanding of the problem contributed significantly to my research and the way that I approach my work. Additionally, your understanding and support as I experienced challenges in my less traditional path through graduate school is greatly appreciated.

Of course, many thanks go to the members of the Multi-Body Dynamics Research Group. I appreciate your support and willingness to answer questions over the years. The friendship and exchange of ideas that you provided were invaluable to me.

In addition, I am grateful for the contributions of my committee members. I thank Dr. Christopher D'Souza for his exceptional mentorship both in the drafting of my dissertation as well as in my time spent at NASA's Johnson Space Center. I must also thank Dr. Belinda Marchand for providing guidance as I sought to formulate the critical questions that motivated my research. I would like to acknowledge Dr. Carolin Frueh and Dr. Kenshiro Oguri whose questions and feedback have inspired me to seek out new knowledge.

Thank you to Purdue University and the School of Aeronautics and Astronautics for their roles in the completion of my degree. I also greatly appreciate support provided by the NASA JSC 80NSSC18M0122 grant.

TABLE OF CONTENTS

LIST OF FIGURES

ABSTRACT

Increasingly, space flight missions are planned to traverse regions of space with complex dynamical environments influenced by multiple gravitational bodies. The nature of these systems produces motion and regions of sensitivity that are, at times, unintuitive, and the accumulation of trajectory dispersions from a variety of sources guarantees that spacecraft will deviate from their pre-planned trajectories in this complex environment, necessitating the use of a targeting process to generate a new feasible reference path. To ensure mission success and a robust path planning process, trajectory designers require insight into the interaction between the targeting process, the baseline trajectory, and the dynamical environment. In this investigation, the convergence behavior of these targeting processes is examined. This work summarizes a framework for characterizing and predicting the convergence behavior of perturbed targeting problems, consisting of a set of constraints, design variables, perturbation variables, and a reference solution within a dynamical system. First, this work identifies the typical features of a convergence basin and identifies a measure of worst-case performance. In the absence of an analytical method, efficient numerical discretization procedures are proposed based on the evaluation of partial derivatives at the reference solution to the perturbed targeting problem. A method is also proposed for approximating the tradespace of position and velocity perturbations that achieve reliable convergence toward the baseline solution. Additionally, evaluated scalar quantities are introduced to serve as predictors of the simulation-measured worst-case convergence behavior based on the local rate of growth in the constraints as well as the local relative change in the targeting-employed partial derivatives with respect to perturbations.

A variety of applications in different dynamical regions and force models are introduced to evaluate the improved discretization techniques and their correlation to the predictive metrics of convergence behavior. Segments of periodic orbits and transfer trajectories from past and planned missions are employed to evaluate the relative convergence performance across sets of candidate solutions. In the circular restricted three-body problem (CRTBP), perturbed targeting problems are formulated along a distant retrograde orbit and a near-rectilinear halo orbit (NRHO) in the Earth-Moon system. To investigate the persistence

of results from the CRTBP in an ephemeris force model, a targeting problem applied to an NRHO is analyzed in both force models. Next, an L_1-to-L_2 transit trajectory in the Sun-Earth system is studied to explore the effect of moving a maneuver downstream along a trajectory and altering the orientations of the gravitational bodies. Finally, a trans-lunar return trajectory is explored, and the convergence behavior is analyzed as the final maneuver time is varied.

1. INTRODUCTION

Space flight missions, such as those contributing to NASA's Artemis and Gateway programs, are increasingly leveraging dynamical structures in complex multi-body regimes. Additionally, there is a growing capability and desire to utilize on-board computing resources to conduct in-flight trajectory targeting. With mission success and crew safety at risk, trajectory designers and guidance, navigation, and control engineers require insight into the performance of these targeting algorithms as they produce new reference trajectories to accommodate the inevitable accumulation of dispersions that bring them off the pre-planned path. Strategies to measure and predict the robustness of a given combination of a reference trajectory and a targeting solution at the early stages of a mission design are crucial to mission success.

1.1 Motivation

One measure for assessing targeting robustness in spaceflight applications is the ability of a targeting scheme to determine a feasible trajectory in the presence of dynamical sensitivity. If the mission trajectory and targeter cannot accommodate sufficiently large dispersions, the result is unpredictable targeting behavior and, potentially, a failure to converge on an acceptable solution or, perhaps, any solution at all. When issues with convergence behavior emerge late in the mission design process, significant resources are wasted, and substantial rework must be completed. When convergence problems are identified during a mission, a compromise in mission objectives or a threat to crew safety may occur.

The objective of this effort is a characterization of the region around a reference solution for which a targeting strategy reliably converges upon a new feasible reference path. This region in perturbation space, denoted the *convergence basin*, is determined by an interaction between the dynamical properties of the reference, or baseline, path and the selection of the targeting scheme, including the constraints, design variables, and update formulation. Traditionally, sensitivity to perturbations is assessed through simulating the targeting process for a set of discrete points in the perturbation space and ensuring that the resulting simulations meet some convergence criteria. Yet, this discretized approach is computationally intensive,

requiring multiple numerically-integrated predictions and matrix inversion calculations. This investigation seeks to improve the analysis of convergence behavior by strategically employing discretized methods and introducing a basin metric produced from 1^{st}- and 2^{nd}-order state transition tensors evaluated solely on the reference path.

While the positive identification of a single reference solution with optimal convergence behavior from among a solution set is a desirable ultimate goal, such a comprehensive undertaking to guarantee optimality requires the full knowledge of nonlinearities in the region around the solution. Instead, the identification of unacceptable reference solutions with local information up to a given order serves to strategically reduce the solution space in the trajectory design process, allowing computational and human resources to focus further analysis on references that are likely acceptable.

1.2 Previous Contributions

Previous investigations have explored the characterization and improvement of convergence behavior for corrections schemes based on Newton-Raphson approaches [2]–[10]. In the field of applied mathematics, the convergence basin and its properties are investigated within the context of root-finding algorithms [2]. Local convergence analysis examines the radius of convergence around a particular local solution while semilocal convergence analysis is focused on determining convergence conditions of the iterative process for an initial guess [3]. Rall, Chen, Argyros and others develop strategies for determining the local convergence radii of a multidimensional Newton-Raphson corrections problems with the convergence at particular rates, e.g., quadratically or superlinearly; however, these approaches require analysis of derivatives continuously across the region of perturbation space[4], [6]–[9]. In the dynamical systems of interest to this investigation, this analysis is not possible, so the exact regions for which the Newton-Raphson process converges at a particular rate cannot be exactly determined. At the boundaries of these main basins, the convergence behavior becomes more complex. For polynomial root-finding algorithms in the complex plane, these boundaries between main basins form intricate fractal patterns [2], [10].

Because the nonlinearity of dynamical systems impacts the effectiveness of linear analysis techniques, other investigations focused on the development of measures of nonlinearity.[11]–[17] In estimation applications, measures of nonlinearity are employed to select between linear and nonlinear filter designs[11]–[13]. Junkins *et al.* define a nonlinearity index to quantify the change in the state transition matrix via a discretized sampling of trajectories [14], [15]. Park and Scheeres investigate nonlinear uncertainty propagation for spacecraft trajectories by deriving a local nonlinearity index to measure the deviation between a Taylor series solution constructed from state transition tensors of up to a given order and the true nonlinear system propagation for a sampled local neighborhood [16]. Jenson and Scheeres introduce a semianalytical tensor eigenpair measurement of nonlinearity to quantify the contribution of higher-order state transition tensors and determine directions of maximum nonlinearity [17].

The quantification of convergence behavior, directly and by proxy, is applied to the corrections in the flow of dynamical systems. Epitropakis and Vrahatis apply Newton's method, as well as alternative strategies, to the determination of regions of attraction for periodic orbits in nonlinear systems [2]. Oguri, Oshima, Campagnola, Gawlik, Marsden and other authors employ the Cauchy-Green tensor and measures of stretching in the state transition matrix to trajectory design problems [18], [19]. Harden and Spreen apply finite-time Lyapunov exponents (FTLEs) to node, or patch point, placement in a Two-Level Targeter (TLT) strategy within the CRTBP and ephemeris force models, respectively [20], [21]. Additionally, Spreen investigates the use of state transition tensors above 1^{st}-order in calculating FTLE values across arcs within a targeting problem [21], [22]. Then, FTLE values are also applied as weightings in the minimum norm update computation to improve the convergence behavior of the TLT [23]. By assuming that trajectory segments possessing a large magnitude of dynamical stretching correspond to a reduction in the validity of the linear corrections process, these investigations demonstrate improvements in the convergence behavior of the targeting algorithm. Muralidharan's investigation into robust station-keeping algorithms utilizes both the magnitude and direction of dynamical stretching through analysis of the Cauchy-Green tensor[24], [25]. The methodology in this investigation seeks to expand on

these results by measuring the convergence basin directly and correlating this measurement with the dynamical properties of the reference.

1.3 Current Work

The primary focus of this investigation is the development of a strategy for the prediction of convergence behavior amongst a set of possible reference solutions in the trajectory design process. From this overarching goal, the following specific objectives are put forth to build upon fundamental observations about convergence behavior, devise computationally-efficient characterizing parameters, and investigate applicability across a diverse and representative set of mission design problems:

1. *Develop both a theoretical and an associated empirical measurement technique to characterize the convergence basin for a given reference solution in a defined targeting problem.*

   To eventually predict the convergence behavior for a reference solution, the definition of an interesting and practical aspect of this behavior is necessarily required for subsequent prediction. The property to be measured is first defined theoretically and without consideration of the possibility of exact analytical measurement. Measurement techniques based on empirical sampling are devised with consideration for both accuracy and computational efficiency. The exploration of measurement approximations, including the treatment of simultaneous perturbations in both position and velocity, lends insight into potential benefits and the limitations of a predictive metric.

2. *Develop a scalar metric, evaluated on each reference solution, with the capability to predict significant trends in the convergence basin measurement across a set of reference solutions.*

   Analysis of the standard structure of a targeting problem motivates the derivation of a predictive metric from local behavior in the vicinity of the reference solution. The correlation of the basin measurements with this predictive metric are assessed and compared to Lyapunov exponent-based approaches. After demonstrating the applicability

of this approach for preliminary single-arc problems, the extension to problems with multiple arcs (e.g., multiple-shooting) and more complex constraint functions demonstrate its broader value and capacity for extension to more complex trajectory design problems.

3. *Verify the applicability of the predictive metric and compare its efficacy to alternative quantities through its application to a variety of design problems within various dynamical environments.*

   Many mission design problems lead to large design spaces, and the ability to triage the potential design alternatives with preliminary analysis tools is critical to focus on the most promising candidates. This investigation seeks to assess the ability of a predictive metric to identify unacceptable designs from a diverse set of applications, including the selection of candidate orbits within a periodic orbit family, correction maneuver placement along a previously-defined trajectory, and changes in the base epoch for a mission trajectory concept. Additionally, the ability to predict convergence behavior in different dynamical environments, i.e., the circular restricted three-body problem (CRTBP) as well as higher-fidelity models, is critical to demonstrating broad applicability.

The execution of this research plan yields powerful preliminary analysis tools for eliminating unacceptable solutions from a design space and focusing higher-fidelity perturbation analysis on more promising designs. In addition, the a priori determination of metrics that predict convergence behavior may improve the on-board planning of maneuvers.

2. DYNAMICAL MODELS

Dynamical models offer varying levels of fidelity and insight into the motion of a spacecraft within an environment dominated by the gravitational attraction of various bodies. In particular mission scenarios where the motion is predominantly influenced by two gravitational bodies moving in a nearly-circular orbit, e.g., the Earth-Moon vicinity, the simplifying assumptions of the CRTBP produce a dynamical model that yields insight via equilibrium solutions and an integral of the motion in a rotating reference frame. Structures and attributes of the underlying flow revealed through analysis of the CRTBP assist in determining qualitative behavior that may persist in higher-fidelity force models. In contrast, higher-fidelity $\mathcal{N}$-body models that use planetary ephemerides to model the precise locations of relevant gravitational bodies yield more accurate descriptions of the spacecraft motion at the expense of limited access to dynamical systems analysis techniques.

2.1 Gravitational $\mathcal{N}$-Body Problem

Newtonian mechanics details the development of a dynamical model for a system comprised of $\mathcal{N}$ bodies. An illustration of such a system appears in Figure 2.1 with unit vectors $\hat{\boldsymbol{X}}$, $\hat{\boldsymbol{Y}}$, and $\hat{\boldsymbol{Z}}$ representing an inertial reference frame I. Though, in reality, bodies do not possess perfectly-symmetric mass distributions, each body is assumed to be spherically symmetric. The movement of the body of interest P_i with mass $\tilde{m}_i$ relative to an inertially-fixed base point B under the influence of only gravitational forces is represented via the vector differential equation

$$\tilde{m}_i \frac{{}^{I}\mathrm{d}^2\tilde{\boldsymbol{r}}_{\boldsymbol{Bi}}}{\mathrm{d}\tilde{t}^2} = -\tilde{G}\sum_{\substack{j=1\\ j\neq i}}^{\mathcal{N}} \frac{\tilde{m}_i\tilde{m}_j}{\tilde{r}_{ji}^3}\tilde{\boldsymbol{r}}_{\boldsymbol{ji}} \tag{2.1}$$

where $\tilde{\boldsymbol{r}}_i$ is the position vector of P_i relative to an inertially-fixed base point, $\tilde{m}_j$ is the mass associated with each of the other primaries P_j, $\tilde{\boldsymbol{r}}_{\boldsymbol{ji}}$ is the position vector from P_j to P_i, $\tilde{G}$ is the universal gravitational constant in the appropriate dimensional units, and B denotes the barycenter of the system. Quantities marked above by a tilde ($\sim$) represent quantities with dimensional units, e.g., kilometers or seconds. Note that in Equation (2.1), the left superscript I denotes derivatives, i.e., rates of change, with respect to time as observed in

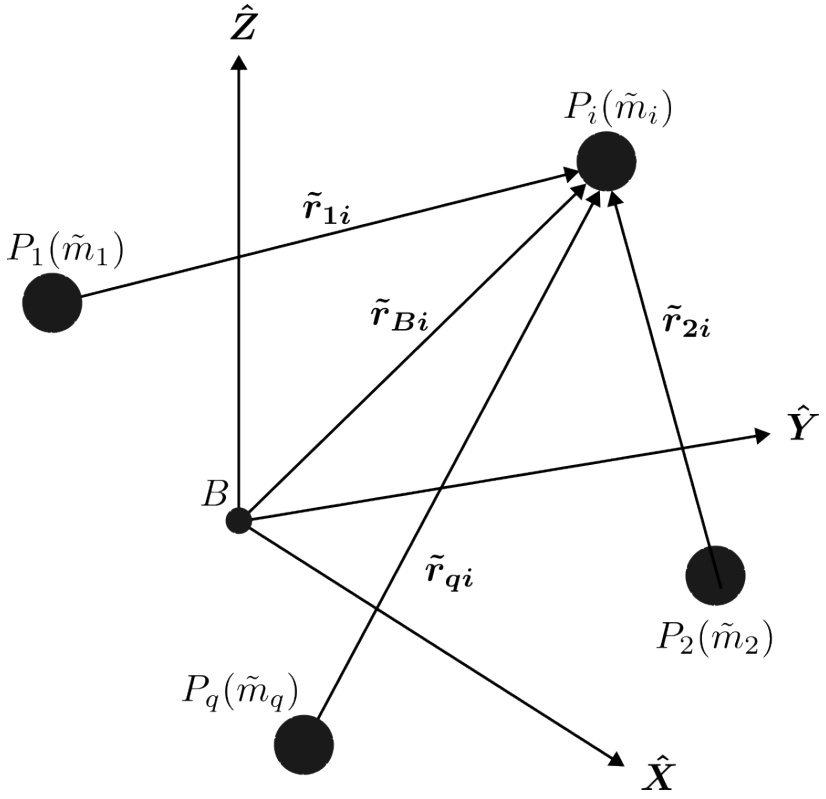

Figure 2.1. $\mathcal{N}$-Body Gravitational Model in the Inertial Frame

the inertial reference frame, and unbolded quantities denote vector magnitudes. Though this dynamical model for the $\mathcal{N}$-body problem incorporates an arbitrary number of bodies, the absence of a closed-form analytical solution and integrals of the motion limit its usefulness in understanding the fundamental dynamical properties of the system.

2.2 Circular Restricted Three-Body Problem

While the $\mathcal{N}$-body problem offers limited insight into the natural motion, a special case involving only three bodies is frequently used to identify qualitative flow properties through the search for equilibrium solutions and an integral of the motion. In systems with a small satellite and two major gravitational bodies, such as a spacecraft in star-planet or planet-moon systems, the CRTBP supplies a framework for investigating spacecraft motion and preliminary mission design before transitioning to a higher-fidelity model.

The three-body problem consists of three bodies P_1, P_2, and P_3 with masses $\tilde{m}_1$, $\tilde{m}_2$, and $\tilde{m}_3$, respectively. A vector differential equation for the motion of P_3 relative to an inertially fixed point as viewed by an inertial observer is described through Equation (2.1) such that

$$\tilde{m}_3 \frac{{}^{I}\mathrm{d}^2\tilde{\boldsymbol{r}}_{\boldsymbol{B3}}}{\mathrm{d}\tilde{t}^2} = -\tilde{G}\frac{\tilde{m}_3\tilde{m}_1}{\tilde{r}_{13}^3}\tilde{\boldsymbol{r}}_{\boldsymbol{13}} - \tilde{G}\frac{\tilde{m}_3\tilde{m}_2}{\tilde{r}_{23}^3}\tilde{\boldsymbol{r}}_{\boldsymbol{23}} \tag{2.2}$$

for the case when $\mathcal{N} = 3$. An illustration of the three-body problem appears in Figure 2.2. This formulation consists of 18 state variables (3 bodies each with 3 position states and 3

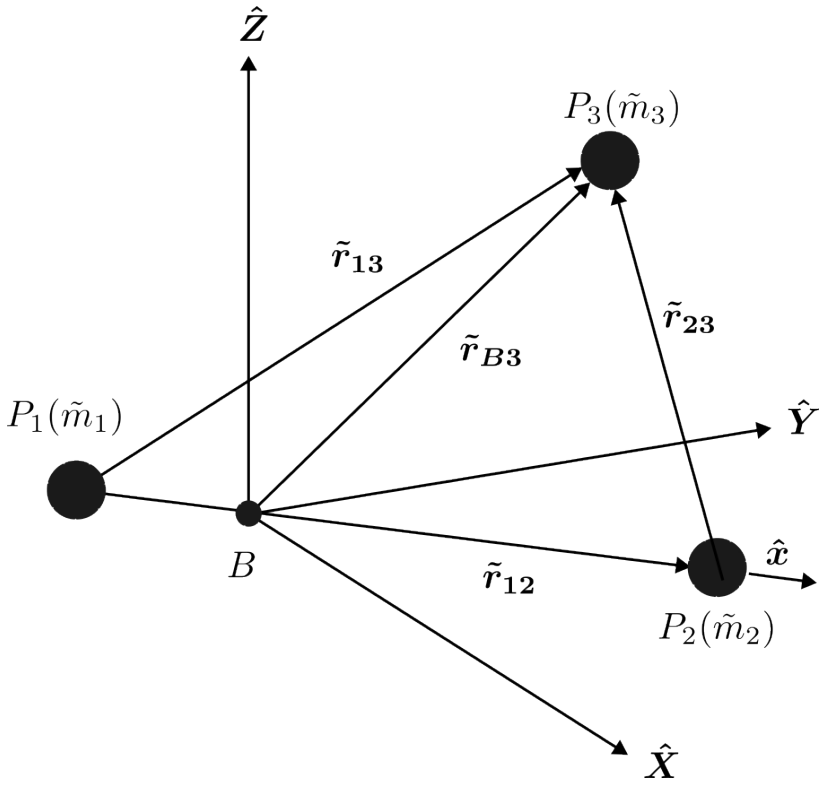

Figure 2.2. Three-Body Gravitational Model in the Inertial Frame

velocity states) and only 10 known integrals of motion [26]. Therefore, an analytical solution cannot be determined.

Simplifying assumptions are enforced to further explore the problem. The mass $\tilde{m}_3$ of body P_3 is assumed negligible in comparison to those of P_1 and P_2, and, therefore, P_3 does not influence the motions of P_1 and P_2. By convention, P_1 and P_2 are defined as the *primaries*, where P_1 is the larger body. This primary system satisfies the conditions for the two-body

problem. Consequently, its motion represented by a conic section, and the barycenter B lies along the vector $\tilde{\boldsymbol{r}}_{\mathbf{12}}$ that connects the two primaries, as illustrated in Figure 2.2. This motion is further assumed to be circular about the system barycenter, B, with mean notion $\tilde{N}$. A spacecraft in the vicinity of Earth and the Moon or the Sun and Earth, for example, is reflected by these assumptions.

2.2.1 Characteristic Quantities

Reformulating the CRTBP in terms of non-dimensional units yields benefits to both numerical and theoretical analysis of the problem. First, the difference in dimensional state variable magnitude, illustrated in the Earth-Moon system, where the Moon orbits relative to the Earth with approximate distance and velocity of 384,000 km and 1 km/s, respectively, produces challenges to the numerical computation of solutions. The process of scaling the state variables results in quantities that possess similar orders of magnitude, aiding in numerical analysis. Second, thoughtful non-dimensionalization allows generalization of the problem through a single parameter, μ. Both benefits arise from selecting constant characteristic quantities related to the two-body dimensional mean motion of the primaries, $\tilde{N}$, for example,

$$\tilde{N} = \sqrt{\frac{\tilde{G}(\tilde{m}_1 + \tilde{m}_2)}{\tilde{r}_{12}^3}} \tag{2.3}$$

as quantities to non-dimensionalize the system. The characteristic mass, m^*, is defined as the sum of the primary masses, i.e.,

$$m^* = \tilde{m}_1 + \tilde{m}_2 \tag{2.4}$$

The characteristic length l^* is defined as the distance between the two primaries,

$$l^* = \tilde{r}_{12} \tag{2.5}$$

and represents the semi-major axis of the simplified primary system. The characteristic time, t^*, is written

$$t^* = \sqrt{\frac{l^{*3}}{\tilde{G}m^*}} \tag{2.6}$$

such that the non-dimensional gravitational constant, G, is equal to unity and represents the reciprocal of the mean motion of the primary system. This identity for the gravitational constant is shown as

$$G = \tilde{G}\frac{m^* t^{*2}}{l^{*3}} = 1 \tag{2.7}$$

Following from the selection of characteristic quantities, the non-dimensional mean motion of primary system, N, is also equal to one, i.e.,

$$N = \tilde{N}t^* = \sqrt{\frac{\tilde{G}m^*}{l^{*3}}\frac{l^{*3}}{\tilde{G}m^*}} = 1 \tag{2.8}$$

Therefore, the circular orbit of the primary system possesses a period of $2\boldsymbol{\pi}$ in non-dimensional time.

The vector differential equation defining motion in the system is rewritten in a non-dimensional form using the characteristic quantities of the primary system and a mass parameter. Defining this non-dimensional mass parameter, μ, as the ratio of the mass of P_2 to the primary system mass, written

$$\mu = \frac{\tilde{m}_2}{m^*} \tag{2.9}$$

yields additional quantities relating characteristic quantities and system distances

$$1 - \mu = \frac{\tilde{m}_1}{m^*} \tag{2.10}$$

$$\frac{\tilde{r}_{B1}}{l^*} = \mu \tag{2.11}$$

$$\frac{\tilde{r}_{B2}}{l^*} = 1 - \mu \tag{2.12}$$

Furthermore, non-dimensionalization of the position vectors,

$$\boldsymbol{\rho} = \frac{\tilde{\boldsymbol{r}}_{\boldsymbol{B3}}}{l^*} \tag{2.13}$$

$$\boldsymbol{d} = \frac{\tilde{\boldsymbol{r}}_{\boldsymbol{13}}}{l^*} \tag{2.14}$$

$$\boldsymbol{r} = \frac{\tilde{\boldsymbol{r}}_{\boldsymbol{23}}}{l^*} \tag{2.15}$$

along with the introduction of a non-dimensional time variable, t,

$$t = \frac{\tilde{t}}{t^*} \tag{2.16}$$

allows for substitution into Equation (2.2), yielding a non-dimensional second order vector differential equation,

$$\frac{{}^I\mathrm{d}^2\boldsymbol{\rho}}{\mathrm{d}t^2} = -\frac{1-\mu}{d^3}\boldsymbol{d} - \frac{\mu}{r^3}\boldsymbol{r} \tag{2.17}$$

This formulation of the dynamical model accomplishes the goals of non-dimensionalization and generalization of the problem in terms of a single parameter.

2.2.2 Rotating Frame

Within the CRTBP, the Keplerian motion of the primary system is circular and confined to a plane. The non-inertial, rotating reference frame R, is defined with an origin at the barycenter B and a unit vector $\hat{\boldsymbol{x}}$ fixed on the line between P_1 and P_2, as illustrated in Figure 2.2. The unit vector $\hat{\boldsymbol{z}}$ is directed along the orbital angular momentum vector of the primary system and, therefore, perpendicular to the orbital plane of the primary bodies. Finally, unit vector $\hat{\boldsymbol{y}}$ completes the right-handed system and is defined as the cross product of the $\hat{\boldsymbol{z}}$ and $\hat{\boldsymbol{x}}$ unit vectors, i.e., $\hat{\boldsymbol{z}} \times \hat{\boldsymbol{x}}$. The reference frame rotates uniformly about the $\hat{\boldsymbol{z}}$ axis with a period of $2\boldsymbol{\pi}$.

Further analysis of the CRTBP is facilitated by the transition to the rotating reference frame R. The position vector from the barycenter to P_3, $\boldsymbol{\rho}$, is defined in the rotating frame as

$$\boldsymbol{\rho} = x\hat{\boldsymbol{x}} + y\hat{\boldsymbol{y}} + z\hat{\boldsymbol{z}} \tag{2.18}$$

and its projection in the $\hat{\boldsymbol{x}}$-$\hat{\boldsymbol{y}}$ plane is illustrated in Figure 2.3. The vector $\dot{\boldsymbol{\rho}}$ denotes the

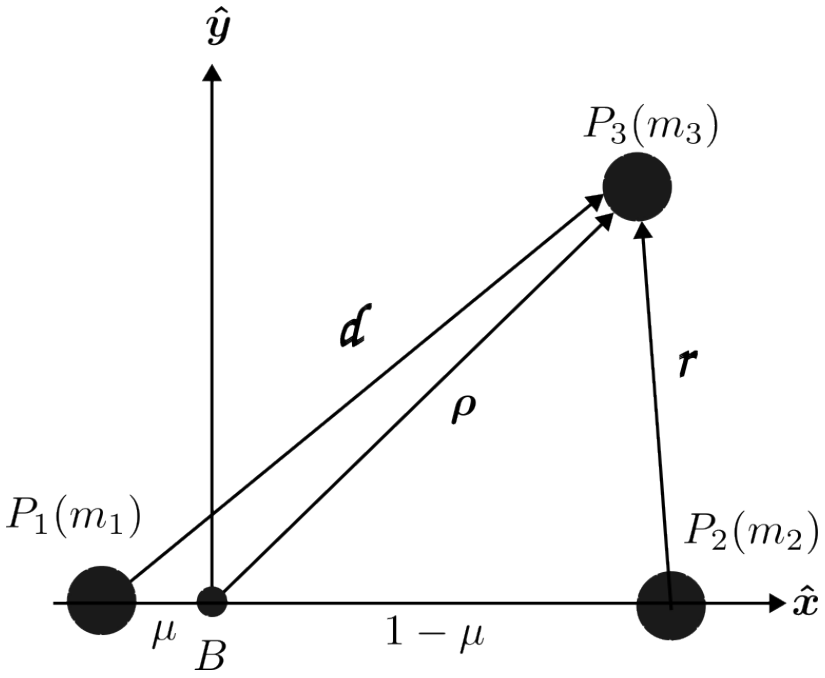

Figure 2.3. Circular Restricted Three-Body Problem Expressed in the Rotating Frame

non-dimensional time derivative with respect to an observer in the rotating frame,

$$\dot{\boldsymbol{\rho}} = \frac{{}^{R}\mathrm{d}\boldsymbol{\rho}}{\mathrm{d}t} = \dot{x}\hat{\boldsymbol{x}} + \dot{y}\hat{\boldsymbol{y}} + \dot{z}\hat{\boldsymbol{z}} \tag{2.19}$$

In this notation, a dot denotes the non-dimensional time derivative with respect to an observer in the rotating frame.

Due to the terms in the inertial formulation of the force model and the state representation in terms of a rotating frame, a kinematic expansion is required to relate the derivatives with respect to a rotating observer to those with respect to an inertial observer. The Basic

Kinematic Equation, also referred to as the Transport Equation, is employed to expand the left side of Equation (2.17), generating the expressions,

$$\frac{{}^{I}\mathrm{d}\boldsymbol{\rho}}{\mathrm{d}t} = \frac{{}^{R}\mathrm{d}\boldsymbol{\rho}}{\mathrm{d}t} + {}^{I}\boldsymbol{\omega}^{R} \times \boldsymbol{\rho} \tag{2.20}$$

$$\frac{{}^{I}\mathrm{d}^2\boldsymbol{\rho}}{\mathrm{d}t^2} = \frac{{}^{R}\mathrm{d}^2\boldsymbol{\rho}}{\mathrm{d}t^2} + 2{}^{I}\boldsymbol{\omega}^{R} \times \frac{{}^{R}\mathrm{d}\boldsymbol{\rho}}{\mathrm{d}t} + {}^{I}\boldsymbol{\omega}^{R} \times {}^{I}\boldsymbol{\omega}^{R} \times \boldsymbol{\rho} \tag{2.21}$$

for the first and second non-dimensional time derivatives relative to an inertial observer. Employing the definition ${}^{I}\boldsymbol{\omega}^{R} = N\hat{\boldsymbol{z}}$, where n is constant, Equation (2.21) yields

$$\frac{{}^{I}\mathrm{d}^2\boldsymbol{\rho}}{\mathrm{d}t^2} = (\ddot{x} - 2N\dot{y} - N^2x)\hat{\boldsymbol{x}} + (\ddot{y} + 2N\dot{x} - N^2y)\hat{\boldsymbol{y}} + \ddot{z}\hat{\boldsymbol{z}} \tag{2.22}$$

for the inertial acceleration of $\boldsymbol{\rho}$ as expressed in the rotating coordinate system. Since the right sides of Equations (2.17) and(2.21) must be equal, and recalling that $N = 1$, the expressions are rearranged to generate a second-order vector derivative in terms of the scalar components of the state variables $\boldsymbol{\rho}$ and $\dot{\boldsymbol{\rho}}$ as well as the parameter μ, i.e.,

$$\ddot{\boldsymbol{\rho}} = \begin{bmatrix} \ddot{x} \\ \ddot{y} \\ \ddot{z} \end{bmatrix} = \begin{bmatrix} 2\dot{y} + x - \frac{(1-\mu)(x+\mu)}{d^3} - \frac{\mu(x-1+\mu)}{r^3} \\ -2\dot{x} + y - \frac{(1-\mu)y}{d^3} - \frac{\mu y}{r^3} \\ -\frac{(1-\mu)z}{d^3} - \frac{\mu z}{r^3} \end{bmatrix} \tag{2.23}$$

where the nonlinear system is not a direct function of time. Thus, when converted to the rotating frame, the dynamical model reflects an autonomous system. Though a closed-form analytic solution is not available for the coupled and nonlinear differential equations, the system does permit a search for an integral of the motion and equilibrium solutions.

2.2.3 Integral of the Motion

In the CRTBP, one integral of the motion emerges from the formulation of the differential equations, i.e., the *Jacobi Constant*. This single constant of the motion assists in determining equilibrium solutions and bounded regions for motion of the infinitesimal third body. An alternative representation of the differential equations in terms of a "pseudo-potential"

function, $\mathcal{U}$, proves useful in determining a constant of the motion. This pseudo-potential function augments the gravitational potential energy with rotational energy that accommodates the rotation of the frame in the new formulation of the differential equations and is defined as

$$\mathcal{U} = \frac{1-\mu}{d} + \frac{\mu}{r} + \frac{x^2+y^2}{2} \tag{2.24}$$

Thus, an equivalent representation of the Equation (2.23), expressed in scalar form, appears as

$$\ddot{x} - 2\dot{y} = \frac{\partial \mathcal{U}}{\partial x} \tag{2.25}$$

$$\ddot{y} + 2\dot{x} = \frac{\partial \mathcal{U}}{\partial y} \tag{2.26}$$

$$\ddot{z} = \frac{\partial \mathcal{U}}{\partial z} \tag{2.27}$$

Operating on the differential equations in Equation (2.25)-(2.27) via a scalar dot product, or inner product, with the velocity relative to a rotating observer, i.e., $\dot{\boldsymbol{\rho}} \cdot \ddot{\boldsymbol{\rho}}$, results in

$$\dot{x}\ddot{x} + \dot{y}\ddot{y} + \dot{z}\ddot{z} = \frac{\partial \mathcal{U}}{\partial x}\dot{x} + \frac{\partial \mathcal{U}}{\partial y}\dot{y} + \frac{\partial \mathcal{U}}{\partial z}\dot{z} \tag{2.28}$$

where the terms containing $\dot{x}\dot{y}$ cancel. From the left side of Equation (2.28), integration with respect to non-dimensional time yields the expression

$$\int (\dot{x}\ddot{x} + \dot{y}\ddot{y} + \dot{z}\ddot{z})\,\mathrm{d}t = \frac{1}{2}(\dot{x}^2 + \dot{y}^2 + \dot{z}^2) + \text{const.} = \frac{\dot{\rho}^2}{2} + \text{const.} \tag{2.29}$$

Since the pseudo-potential is a function of only x, y, and z, the right side of Equation (2.28) represents the total derivative of U^* with respect to non-dimensional time, resulting in

$$\int \left(\frac{\partial \mathcal{U}}{\partial x}\dot{x} + \frac{\partial \mathcal{U}}{\partial y}\dot{y} + \frac{\partial \mathcal{U}}{\partial z}\dot{z} \right) \mathrm{d}t = \mathcal{U} + \text{const.} \tag{2.30}$$

Combining results from Equations (2.28)-(2.30) while consolidating the separate constants of integration produces an equation for a single constant, i.e.,

$$C = 2\mathcal{U} - \dot{\rho}^2 \tag{2.31}$$

where C is the constant of integration, and the unbolded $\dot{\rho}$ denotes the l_2-norm of the vector $\dot{\boldsymbol{\rho}}$. The constant C is the Jacobi Constant and provides the only known integral of motion for the CRTBP, representing an energy-like quantity for the CRTBP in the rotating frame.

2.2.4 Equilibrium Solutions

Additional insight into the dynamical environment is gained via computation of equilibrium solutions of the CRTBP. An equilibrium solution satisfies the governing differential equations when all derivatives with respect to a rotating observer are zero. Enforcing this condition on Equations (2.25)-(2.27) by setting the expressions on the left to zero provides a convenient representation, written as

$$\left.\frac{\partial \mathcal{U}}{\partial x}\right|_{\boldsymbol{\rho}_{eq}} = -\frac{(1-\mu)(x_{eq}+\mu)}{d_{eq}^3} - \frac{\mu(x_{eq}-1+\mu)}{r_{eq}^3} + x_{eq} = 0 \tag{2.32}$$

$$\left.\frac{\partial \mathcal{U}}{\partial y}\right|_{\boldsymbol{\rho}_{eq}} = -\frac{(1-\mu)y_{eq}}{d_{eq}^3} - \frac{\mu y_{eq}}{r_{eq}^3} + y_{eq} = 0 \tag{2.33}$$

$$\left.\frac{\partial \mathcal{U}}{\partial z}\right|_{\boldsymbol{\rho}_{eq}} = -\frac{(1-\mu)z_{eq}}{d_{eq}^3} - \frac{\mu z_{eq}}{r_{eq}^3} = 0 \tag{2.34}$$

where the subscript eq refers to equilibrium states. The conditions in Equation (2.34) are only satisfied when $z_{eq} = 0$; therefore, all equilibrium solutions exist in the primaries' orbital plane.

Noting that $y_{eq} = 0$ satisfies Equation (2.33), the equilibrium solutions on the $\hat{\boldsymbol{x}}$-axis are explored. Following this assumption, Equation (2.32) is rewritten in the form

$$-\frac{(1-\mu)(x_{eq}+\mu)}{|x_{eq}+\mu|^3} - \frac{\mu(x_{eq}-1+\mu)}{|x_{eq}-1+\mu|^3} + x_{eq} = 0 \tag{2.35}$$

which includes three regions for possible equilibrium solutions, $-\infty < x_{eq} < -\mu$, $-\mu < x_{eq} < 1-\mu$, and $1-\mu < x_{eq} < \infty$, resulting from singularities at the primary bodies. Since Equation (2.35) lacks an analytical solution, iterative numerical methods prove successful in approximating solutions in these three regions, labelled the collinear *libration points*, first discovered by Euler. These three points are denoted L_1, L_2, and L_3, in order of decreasing Jacobi Constant. First identified by Lagrange, two additional equilibrium solutions also exist, located off of the $\hat{\boldsymbol{x}}$-axis when $d_{eq} = r_{eq} = 1$. By substituting these values of unity into Equations (2.32) and (2.33), these libration points, i.e., L_4 and L_5, are determined at the vertices of equilateral triangles formed with additional vertices at P_1 and P_2. The L_4 point has an off-axis component $y_{eq} > 0$, and the L_5 point is its reflection across the $\hat{\boldsymbol{x}}$-axis. Figure 2.4 illustrates all five libration points, also commonly labelled *Lagrange points*, in the Earth-Moon system. The determination of Lagrange points for a given system serves as a

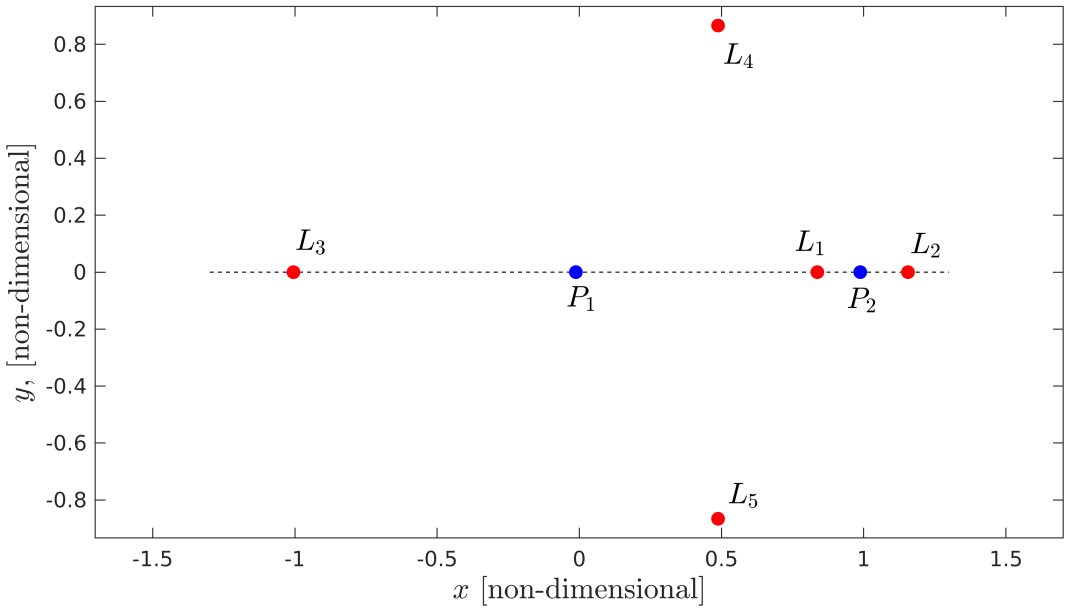

Figure 2.4. Lagrange Points in the Earth-Moon System to Scale

starting point for exploring the associated periodic motion n the system, as viewed in the rotating frame, and the bounded regions of space.

2.3 Higher-Fidelity $\mathcal{N}$-Body Ephemeris Model

Dynamical models that capture the epoch-dependency due to the forces of $\mathcal{N}$ gravitational bodies are required to construct higher-fidelity reference trajectories at later stages in the mission design process. To begin analysis of such a system, the equations of motion for a satellite P_i with mass m_i in an $\mathcal{N}$-body system with respect to an inertially-fixed base point, given in Equation (2.1), are manipulated to express the governing equations for the satellite's relative motion with respect to a central gravitation body P_q with mass m_q, i.e.,

$$\frac{{}^{I}\mathrm{d}^2\boldsymbol{r}_{qi}}{\mathrm{d}t^2} = -\frac{G(m_i+m_q)}{r_{qi}^3}\boldsymbol{r}_{qi} + G\sum_{\substack{j=1\\ j\neq q,i}}^{\mathcal{N}} m_j\left(\frac{\boldsymbol{r}_{ij}}{r_{ij}^3} - \frac{\boldsymbol{r}_{qj}}{r_{qj}^3}\right) \tag{2.36}$$

where $\boldsymbol{r}_{qi}$ represents the position vector from the central body to the body of interest. The assumption of spherically-symmetric bodies persists in this formulation, and the governing equations are formulated in terms of non-dimensional quantities according to the characteristic quantities of a selected analogous system in the CRTBP. The first term on the right side of Equation (2.36) represents the mutual gravitational attraction of the bodies P_q and P_i. For the specific case of the two-body problem where $\mathcal{N} = 2$, a closed-form solution exists and is represented geometrically via conic sections. The second term on the right side of Equation (2.36) represents the summation of perturbing accelerations on the bodies P_i and P_q due to additional gravitational bodies in the model. In this investigation, the mass m_i is assumed negligible compared to the masses of other bodies in the model. Numerical integration of Equation (2.36) facilities the computation of state histories for the body of interest, e.g., a spacecraft.

Existing software tools and data sets are useful for the numerical integration of the spacecraft motion. In this investigation, numerical integration within the $\mathcal{N}$-body ephemeris model is conducted with state variables expressed in the J2000 inertial reference frame using the Adaptive Trajectory Design (ATD) software tool developed at Purdue University[27].

NASA's Navigation and Ancillary Information Facility SPICE toolkit is incorporated for planetary ephemeris data [28]–[30]. The data set used for the state history of gravitational bodies is Development Ephemeris 430 (DE430), and data for the orientation of Earth is contained in Planetary Constants Kernel 10 (PCK 10)[29]. These data sets provide state and orientation information of gravitational bodies for the ranges of epoch time explored in this investigation.

3. DIFFERENTIAL CORRECTIONS

For the dynamical systems of interest, the equations of motion take the form of coupled, ordinary differential equations without a closed-form solution. Therefore, a reference spacecraft trajectory that satisfies a given set of constraints cannot be determined analytically. The search for a solution takes the form of a two-point boundary value problem, and iterative numerical methods provide a path to solve the problem. A class of numerical methods referred to as differential corrections, including collocation and discrete methods, are frequently employed to determine a reference solution [31], [32]. In particular, a differential corrections scheme based on the Newton-Raphson method is a common approach to solve these problems in astronautical applications due to its relative ease of implementation and convergence properties.

3.1 Newton-Raphson Differential Corrections Process

A multivariate formulation of the Newton-Raphson method, improved by Isaac Newton, Joseph Raphson, and Thomas Simpson and, perhaps, more appropriately named the Simpson Method [33]–[37], is employed to compute constrained solutions to a system of equations. The root-finding algorithm updates a set of n *design variables*, represented in vector form by $\boldsymbol{\mathcal{X}}$, to determine a solution under a set of m constraints, $\boldsymbol{\mathcal{F}}$, such that

$$\boldsymbol{\mathcal{F}}(\boldsymbol{\mathcal{X}}^*) = \mathbf{0} \tag{3.1}$$

where $\mathbf{0}$ is the zero vector of length m [21], [38], [39]. The asterisk $(*)$ denotes quantities associated with the reference, or baseline, solution in Equation (3.1). In general, an initial guess for the design variables will result in non-zero values for the components of the constraint vector, i.e.,

$$\boldsymbol{\mathcal{F}}(\boldsymbol{\mathcal{X}}) \neq \mathbf{0} \quad \text{(in general)} \tag{3.2}$$

An update to the design variables vector, $\delta\boldsymbol{\mathcal{X}}$, is sought to drive the design variables toward a solution, satisfying Equation (3.1). A Taylor series expansion of the constraint vector about the current design variable values leads to the following relation

$$\boldsymbol{\mathcal{F}}(\boldsymbol{\mathcal{X}} + \delta\boldsymbol{\mathcal{X}}) = \boldsymbol{\mathcal{F}}(\boldsymbol{\mathcal{X}}) + \frac{\partial \boldsymbol{\mathcal{F}}(\boldsymbol{\mathcal{X}})}{\partial \boldsymbol{\mathcal{X}}}\delta\boldsymbol{\mathcal{X}} + \text{Higher-Order Terms} \tag{3.3}$$

where $\frac{\partial \boldsymbol{\mathcal{F}}}{\partial \boldsymbol{\mathcal{X}}}$ denotes the *design Jacobian*. By truncating the series at 1$^{\text{st}}$-order and supposing the update will yield a solution, i.e., $\boldsymbol{\mathcal{X}} + \delta\boldsymbol{\mathcal{X}} = \boldsymbol{\mathcal{X}}^*$, Equation (3.3) is revised as

$$\underbrace{\boldsymbol{\mathcal{F}}(\boldsymbol{\mathcal{X}}^*)}_{\mathbf{0}} = \boldsymbol{\mathcal{F}}(\boldsymbol{\mathcal{X}}) + \frac{\partial \boldsymbol{\mathcal{F}}(\boldsymbol{\mathcal{X}})}{\partial \boldsymbol{\mathcal{X}}}\delta\boldsymbol{\mathcal{X}} \tag{3.4}$$

Under these assumptions, the design variable update $\delta\boldsymbol{\mathcal{X}}$ is defined as the solution to the equation

$$-\boldsymbol{\mathcal{F}}\Big|_{\boldsymbol{\mathcal{X}}} = \frac{\partial \boldsymbol{\mathcal{F}}}{\partial \boldsymbol{\mathcal{X}}}\Big|_{\boldsymbol{\mathcal{X}}} \delta\boldsymbol{\mathcal{X}} \tag{3.5}$$

where notation $(\cdot)\Big|_{\boldsymbol{\mathcal{X}}}$ implies evaluation with the current design variable values, $\boldsymbol{\mathcal{X}}$. The number of solutions to Equation (3.5) depends on the structure of the differential corrections problem.

In practice, the design variable-constraint relation, $\boldsymbol{\mathcal{F}}(\boldsymbol{\mathcal{X}})$, represents a nonlinear system of equations. Due to the 1$^{\text{st}}$-order approximation of the variational relationship employed in the Newton-Raphson process, these nonlinearities preclude the numerical determination of an exact solution, and, thus, iterative processes are employed until the constraint vector converges to a pre-determined tolerance. A *targeting problem* is defined as a particular formulation of governing equations, design variables, and constraints for which a reference solution is sought.

The method of computing the design variable update depends on the quantity of design variables and constraints. For a *fully-constrained* problem (i.e., $n = m$), the design variable update is straightforward to determine. Assuming the design Jacobian matrix $\frac{\partial \boldsymbol{\mathcal{F}}}{\partial \boldsymbol{\mathcal{X}}}$ is not

singular, a matrix inversion applied to Equation (3.5) leads to a design variable update computed as

$$\delta\boldsymbol{\mathcal{X}} = -\left.\frac{\partial\boldsymbol{\mathcal{F}}}{\partial\boldsymbol{\mathcal{X}}}\right|_{\boldsymbol{\mathcal{X}}}^{-1}\left.\boldsymbol{\mathcal{F}}\right|_{\boldsymbol{\mathcal{X}}} \tag{3.6}$$

Thus, a unique solution exists for the design variable update.

3.1.1 The Minimum-Norm Solution in Under-Constrained Problems

When the problem is *under-constrained* (i.e., $n > m$), an infinite number of solutions exist that satisfy Equation (3.5). The solution corresponding to the minimum change in the design variable vector magnitude, i.e., the *minimum-norm solution*, is sought for two major reasons. First, the large design variable updates may represent changes velocity or thrusting acceleration, potentially signaling increasing propellant cost. Additionally, large updates in the nonlinear system may push the design variables outside of the region of applicability of the 1st-order approximation provided by the design Jacobian. To determine the minimum-norm solution to Equation (3.5), a constrained optimization problem is formulated, i.e.,

$$\begin{aligned} &\text{minimize: } \delta\boldsymbol{\mathcal{X}}^T\delta\boldsymbol{\mathcal{X}} \\ &\text{subject to: } \left.\frac{\partial\boldsymbol{\mathcal{F}}}{\partial\boldsymbol{\mathcal{X}}}\right|_{\boldsymbol{\mathcal{X}}}\delta\boldsymbol{\mathcal{X}} + \left.\boldsymbol{\mathcal{F}}\right|_{\boldsymbol{\mathcal{X}}} = \mathbf{0} \end{aligned} \tag{3.7}$$

With the introduction of a vector of Lagrange multipliers, $\boldsymbol{\lambda}$, a cost functional, J, is mathematically described by

$$J = \delta\boldsymbol{\mathcal{X}}^T\delta\boldsymbol{\mathcal{X}} + \boldsymbol{\lambda}^T\left(\left.\frac{\partial\boldsymbol{\mathcal{F}}}{\partial\boldsymbol{\mathcal{X}}}\right|_{\boldsymbol{\mathcal{X}}}\delta\boldsymbol{\mathcal{X}} + \left.\boldsymbol{\mathcal{F}}\right|_{\boldsymbol{\mathcal{X}}}\right) \tag{3.8}$$

The minimum-cost solution arises from the condition that the partial derivatives of J with respect to $\delta\boldsymbol{\mathcal{X}}$ and $\boldsymbol{\lambda}$ are equal to zero, expressed

$$\left(\frac{\partial J}{\partial(\delta\boldsymbol{\mathcal{X}})}\right) = 2\delta\boldsymbol{\mathcal{X}} - \left.\frac{\partial\boldsymbol{\mathcal{F}}}{\partial\boldsymbol{\mathcal{X}}}\right|_{\boldsymbol{\mathcal{X}}}^{T}\boldsymbol{\lambda} = \mathbf{0} \tag{3.9}$$

$$\left(\frac{\partial J}{\partial\boldsymbol{\lambda}}\right) = \left.\frac{\partial\boldsymbol{\mathcal{F}}}{\partial\boldsymbol{\mathcal{X}}}\right|_{\boldsymbol{\mathcal{X}}}\delta\boldsymbol{\mathcal{X}} + \left.\boldsymbol{\mathcal{F}}\right|_{\boldsymbol{\mathcal{X}}} = \mathbf{0} \tag{3.10}$$

respectively. By algebraic manipulation, an expression for $\delta\boldsymbol{\mathcal{X}}$ is uncovered in terms of the Lagrange multipliers via Equation (3.9), i.e.,

$$\delta\boldsymbol{\mathcal{X}} = \frac{1}{2}\frac{\partial \boldsymbol{\mathcal{F}}}{\partial \boldsymbol{\mathcal{X}}}\bigg|_{\boldsymbol{\mathcal{X}}}^{T}\boldsymbol{\lambda} \tag{3.11}$$

and substituted into Equation (3.10) to develop an expression for $\boldsymbol{\lambda}$ in terms of known quantities, i.e.,

$$\boldsymbol{\lambda} = -2\left(\frac{\partial \boldsymbol{\mathcal{F}}}{\partial \boldsymbol{\mathcal{X}}}\bigg|_{\boldsymbol{\mathcal{X}}}\frac{\partial \boldsymbol{\mathcal{F}}}{\partial \boldsymbol{\mathcal{X}}}\bigg|_{\boldsymbol{\mathcal{X}}}^{T}\right)^{-1}\boldsymbol{\mathcal{F}}\big|_{\boldsymbol{\mathcal{X}}} \tag{3.12}$$

Substitution of Equation (3.12) into Equation (3.11) yields the minimum-norm solution for $\delta\boldsymbol{\mathcal{X}}$ that satisfies the constraining relation from Equation (3.5), i.e.,

$$\delta\boldsymbol{\mathcal{X}} = -\frac{\partial \boldsymbol{\mathcal{F}}}{\partial \boldsymbol{\mathcal{X}}}\bigg|_{\boldsymbol{\mathcal{X}}}^{T}\left(\frac{\partial \boldsymbol{\mathcal{F}}}{\partial \boldsymbol{\mathcal{X}}}\bigg|_{\boldsymbol{\mathcal{X}}}\frac{\partial \boldsymbol{\mathcal{F}}}{\partial \boldsymbol{\mathcal{X}}}\bigg|_{\boldsymbol{\mathcal{X}}}^{T}\right)^{-1}\boldsymbol{\mathcal{F}}\big|_{\boldsymbol{\mathcal{X}}} = -\frac{\partial \boldsymbol{\mathcal{F}}}{\partial \boldsymbol{\mathcal{X}}}\bigg|_{\boldsymbol{\mathcal{X}}}^{-P}\boldsymbol{\mathcal{F}}\big|_{\boldsymbol{\mathcal{X}}} \tag{3.13}$$

where the superscript $-P$ is shorthand notation for the Moore-Penrose pseudo-inverse. This result is used to compute design variable updates for implementations with more design variables than constraints.

3.1.2 The Least-Squares Solution in Over-Constrained Problems

For completeness, the computation of a design variable update when the problem is *over-constrained* (i.e., $n < m$) is examined. In general, no vector $\delta\boldsymbol{\mathcal{X}}$ solves the Equation (3.5) for over-constrained problems, so an optimization problem is formulated in search of the solution that minimizes the norm of the residual error, called the *least-squares solution*, i.e.,

$$\text{minimize: } \left(\frac{\partial \boldsymbol{\mathcal{F}}}{\partial \boldsymbol{\mathcal{X}}}\bigg|_{\boldsymbol{\mathcal{X}}}\delta\boldsymbol{\mathcal{X}} + \boldsymbol{\mathcal{F}}\big|_{\boldsymbol{\mathcal{X}}}\right)^{T}\left(\frac{\partial \boldsymbol{\mathcal{F}}}{\partial \boldsymbol{\mathcal{X}}}\bigg|_{\boldsymbol{\mathcal{X}}}\delta\boldsymbol{\mathcal{X}} + \boldsymbol{\mathcal{F}}\big|_{\boldsymbol{\mathcal{X}}}\right) \tag{3.14}$$

A cost functional, J_O, is introduced and expressed

$$J_O = \left(\frac{\partial \boldsymbol{\mathcal{F}}}{\partial \boldsymbol{\mathcal{X}}}\bigg|_{\boldsymbol{\mathcal{X}}}\delta\boldsymbol{\mathcal{X}} + \boldsymbol{\mathcal{F}}\big|_{\boldsymbol{\mathcal{X}}}\right)^{T}\left(\frac{\partial \boldsymbol{\mathcal{F}}}{\partial \boldsymbol{\mathcal{X}}}\bigg|_{\boldsymbol{\mathcal{X}}}\delta\boldsymbol{\mathcal{X}} + \boldsymbol{\mathcal{F}}\big|_{\boldsymbol{\mathcal{X}}}\right) \tag{3.15}$$

To find the critical point, partial derivative of J_O with respect to $\delta\boldsymbol{\mathcal{X}}$ set to zero and represented mathematically as

$$\left(\frac{\partial J_O}{\partial(\delta\boldsymbol{\mathcal{X}})}\right)^T = 2\frac{\partial\boldsymbol{\mathcal{F}}}{\partial\boldsymbol{\mathcal{X}}}\bigg|_{\boldsymbol{\mathcal{X}}}^T\frac{\partial\boldsymbol{\mathcal{F}}}{\partial\boldsymbol{\mathcal{X}}}\bigg|_{\boldsymbol{\mathcal{X}}}\delta\boldsymbol{\mathcal{X}} + 2\frac{\partial\boldsymbol{\mathcal{F}}}{\partial\boldsymbol{\mathcal{X}}}\bigg|_{\boldsymbol{\mathcal{X}}}^T\boldsymbol{\mathcal{F}}\big|_{\boldsymbol{\mathcal{X}}} = \mathbf{0} \tag{3.16}$$

By solving Equation (3.16) for $\delta\boldsymbol{\mathcal{X}}$, the least-squares solution for the design variable update is revealed as

$$\delta\boldsymbol{\mathcal{X}} = -\left(\frac{\partial\boldsymbol{\mathcal{F}}}{\partial\boldsymbol{\mathcal{X}}}\bigg|_{\boldsymbol{\mathcal{X}}}^T\frac{\partial\boldsymbol{\mathcal{F}}}{\partial\boldsymbol{\mathcal{X}}}\bigg|_{\boldsymbol{\mathcal{X}}}\right)^{-1}\frac{\partial\boldsymbol{\mathcal{F}}}{\partial\boldsymbol{\mathcal{X}}}\bigg|_{\boldsymbol{\mathcal{X}}}^T\boldsymbol{\mathcal{F}}\big|_{\boldsymbol{\mathcal{X}}} \tag{3.17}$$

assuming the matrix inversion is possible. Because there is not an *a priori* guarantee that the constraint vector magnitude is reducible to a chosen tolerance, the design variables and constraints should be selected to avoid the case of an over-constrained system.

3.2 Quadratic Convergence of Newton's Method

Under assumed conditions, a Newton-Raphson algorithm is expected to converge quadratically from a sufficiently-close initial guess to a local solution, $\boldsymbol{\mathcal{X}}^*$ [40], [41]. An outline of the proof demonstrates this property in the case of a fully-constrained targeting problem. A reformulation of Equation (3.6) to determine the $(k+1)^{\text{th}}$ iteration of the design variable vector yields

$$\boldsymbol{\mathcal{X}}^{k+1} = \boldsymbol{\mathcal{X}}^k - \frac{\partial\boldsymbol{\mathcal{F}}}{\partial\boldsymbol{\mathcal{X}}}\bigg|_{\boldsymbol{\mathcal{X}}^k}^{-1}\boldsymbol{\mathcal{F}}\big|_{\boldsymbol{\mathcal{X}}^k} \tag{3.18}$$

where the superscript denotes the iteration associated with the design variable values. Noting that $\boldsymbol{\mathcal{F}}\big|_{\boldsymbol{\mathcal{X}}^*} = \mathbf{0}$ is trivially added, the solution $\boldsymbol{\mathcal{X}}^*$ is subtracted from both sides of Equation (3.18) to evaluate the difference from the solution, i.e.,

$$\boldsymbol{\mathcal{X}}^{k+1} - \boldsymbol{\mathcal{X}}^* = \boldsymbol{\mathcal{X}}^k - \boldsymbol{\mathcal{X}}^* - \frac{\partial\boldsymbol{\mathcal{F}}}{\partial\boldsymbol{\mathcal{X}}}\bigg|_{\boldsymbol{\mathcal{X}}^k}^{-1}\left(\boldsymbol{\mathcal{F}}\big|_{\boldsymbol{\mathcal{X}}^k} - \boldsymbol{\mathcal{F}}\big|_{\boldsymbol{\mathcal{X}}^*}\right) \tag{3.19}$$

With the introduction of a scalar parameter $\eta \in [0,1]$, the Fundamental Theorem of Calculus implies

$$\boldsymbol{\mathcal{F}}\big|_{\boldsymbol{\mathcal{X}}^k} - \boldsymbol{\mathcal{F}}\big|_{\boldsymbol{\mathcal{X}}^*} = \int_0^1 \frac{\partial\boldsymbol{\mathcal{F}}}{\partial\boldsymbol{\mathcal{X}}}\bigg|_{\left(\boldsymbol{\mathcal{X}}^*+\eta(\boldsymbol{\mathcal{X}}^k-\boldsymbol{\mathcal{X}}^*)\right)}(\boldsymbol{\mathcal{X}}^k - \boldsymbol{\mathcal{X}}^*)\mathrm{d}\eta \tag{3.20}$$

The quantity $\frac{\partial \boldsymbol{\mathcal{F}}}{\partial \boldsymbol{\mathcal{X}}}\Big|_{\boldsymbol{\mathcal{X}}^*}\left(\boldsymbol{\mathcal{X}}^k - \boldsymbol{\mathcal{X}}^*\right)$ is added and subtracted inside the integral so that Equation (3.20) is equivalently expressed

$$\begin{aligned}\boldsymbol{\mathcal{F}}\Big|_{\boldsymbol{\mathcal{X}}^k} - \boldsymbol{\mathcal{F}}\Big|_{\boldsymbol{\mathcal{X}}^*} &= \int_0^1 \left(\frac{\partial \boldsymbol{\mathcal{F}}}{\partial \boldsymbol{\mathcal{X}}}\Big|_{\boldsymbol{\mathcal{X}}^*} + \frac{\partial \boldsymbol{\mathcal{F}}}{\partial \boldsymbol{\mathcal{X}}}\Big|_{\left(\boldsymbol{\mathcal{X}}^* + \eta(\boldsymbol{\mathcal{X}}^k - \boldsymbol{\mathcal{X}}^*)\right)} - \frac{\partial \boldsymbol{\mathcal{F}}}{\partial \boldsymbol{\mathcal{X}}}\Big|_{\boldsymbol{\mathcal{X}}^*}\right)(\boldsymbol{\mathcal{X}}^k - \boldsymbol{\mathcal{X}}^*)\mathrm{d}\eta \\ &= \int_0^1 \frac{\partial \boldsymbol{\mathcal{F}}}{\partial \boldsymbol{\mathcal{X}}}\Big|_{\boldsymbol{\mathcal{X}}^*}(\boldsymbol{\mathcal{X}}^k - \boldsymbol{\mathcal{X}}^*)\mathrm{d}\eta \\ &\quad \cdots + \int_0^1 \left(\frac{\partial \boldsymbol{\mathcal{F}}}{\partial \boldsymbol{\mathcal{X}}}\Big|_{\left(\boldsymbol{\mathcal{X}}^* + \eta(\boldsymbol{\mathcal{X}}^k - \boldsymbol{\mathcal{X}}^*)\right)} - \frac{\partial \boldsymbol{\mathcal{F}}}{\partial \boldsymbol{\mathcal{X}}}\Big|_{\boldsymbol{\mathcal{X}}^*}\right)(\boldsymbol{\mathcal{X}}^k - \boldsymbol{\mathcal{X}}^*)\mathrm{d}\eta\end{aligned} \tag{3.21}$$

Limiting the values of $\boldsymbol{\mathcal{X}}^k$ to the region about $\boldsymbol{\mathcal{X}}^*$ for which $\frac{\partial \boldsymbol{\mathcal{F}}}{\partial \boldsymbol{\mathcal{X}}}$ is locally K-Lipschitz, the Triangle Inequality of Integrals and the sub-multiplicative property of the l^2-norm allow the statement of an inequality from Equation (3.21), i.e.,

$$\begin{aligned}\left\|\boldsymbol{\mathcal{F}}\Big|_{\boldsymbol{\mathcal{X}}^k} - \boldsymbol{\mathcal{F}}\Big|_{\boldsymbol{\mathcal{X}}^*} - \frac{\partial \boldsymbol{\mathcal{F}}}{\partial \boldsymbol{\mathcal{X}}}\Big|_{\boldsymbol{\mathcal{X}}^*}(\boldsymbol{\mathcal{X}}^k - \boldsymbol{\mathcal{X}}^*)\right\| &\leq \int_0^1 \left\|\frac{\partial \boldsymbol{\mathcal{F}}}{\partial \boldsymbol{\mathcal{X}}}\Big|_{\left(\boldsymbol{\mathcal{X}}^* + \eta(\boldsymbol{\mathcal{X}}^k - \boldsymbol{\mathcal{X}}^*)\right)} - \frac{\partial \boldsymbol{\mathcal{F}}}{\partial \boldsymbol{\mathcal{X}}}\Big|_{\boldsymbol{\mathcal{X}}^*}\right\| \|\boldsymbol{\mathcal{X}}^k - \boldsymbol{\mathcal{X}}^*\|\mathrm{d}\eta \\ &\leq \int_0^1 K\|\boldsymbol{\mathcal{X}}^* + \eta(\boldsymbol{\mathcal{X}}^k - \boldsymbol{\mathcal{X}}^*) - \boldsymbol{\mathcal{X}}^*\| \, \|\boldsymbol{\mathcal{X}}^k - \boldsymbol{\mathcal{X}}^*\|\mathrm{d}\eta\end{aligned} \tag{3.22}$$

The resulting inequality in Equation (3.22) is simplified and expressed as

$$\left\|\boldsymbol{\mathcal{F}}\Big|_{\boldsymbol{\mathcal{X}}^k} - \boldsymbol{\mathcal{F}}\Big|_{\boldsymbol{\mathcal{X}}^*} - \frac{\partial \boldsymbol{\mathcal{F}}}{\partial \boldsymbol{\mathcal{X}}}\Big|_{\boldsymbol{\mathcal{X}}^*}(\boldsymbol{\mathcal{X}}^k - \boldsymbol{\mathcal{X}}^*)\right\| \leq \int_0^1 K\eta\|\boldsymbol{\mathcal{X}}^k - \boldsymbol{\mathcal{X}}^*\|^2\mathrm{d}\eta = \frac{K}{2}\|\boldsymbol{\mathcal{X}}^k - \boldsymbol{\mathcal{X}}^*\|^2 \tag{3.23}$$

Along the combined addition and subtraction of $\frac{\partial \boldsymbol{\mathcal{F}}}{\partial \boldsymbol{\mathcal{X}}}\Big|_{\boldsymbol{\mathcal{X}}^k}^{-1}\frac{\partial \boldsymbol{\mathcal{F}}}{\partial \boldsymbol{\mathcal{X}}}\Big|_{\boldsymbol{\mathcal{X}}^*}(\boldsymbol{\mathcal{X}}^k - \boldsymbol{\mathcal{X}}^*)$, taking the l_2-norm in Equation (3.19) allows the substitution of Equation (3.23), i.e.,

$$\begin{aligned}\|\boldsymbol{\mathcal{X}}^{k+1} - \boldsymbol{\mathcal{X}}^*\| &\leq \left\|I - \frac{\partial \boldsymbol{\mathcal{F}}}{\partial \boldsymbol{\mathcal{X}}}\Big|_{\boldsymbol{\mathcal{X}}^k}^{-1}\frac{\partial \boldsymbol{\mathcal{F}}}{\partial \boldsymbol{\mathcal{X}}}\Big|_{\boldsymbol{\mathcal{X}}^*}\right\|\|\boldsymbol{\mathcal{X}}^k - \boldsymbol{\mathcal{X}}^*\| \\ &\quad \cdots + \left\|\frac{\partial \boldsymbol{\mathcal{F}}}{\partial \boldsymbol{\mathcal{X}}}\Big|_{\boldsymbol{\mathcal{X}}^k}^{-1}\right\| \left\|\boldsymbol{\mathcal{F}}\Big|_{\boldsymbol{\mathcal{X}}^k} - \boldsymbol{\mathcal{F}}\Big|_{\boldsymbol{\mathcal{X}}^*} - \frac{\partial \boldsymbol{\mathcal{F}}}{\partial \boldsymbol{\mathcal{X}}}\Big|_{\boldsymbol{\mathcal{X}}^*}(\boldsymbol{\mathcal{X}}^k - \boldsymbol{\mathcal{X}}^*)\right\| \\ &\leq \left\|I - \frac{\partial \boldsymbol{\mathcal{F}}}{\partial \boldsymbol{\mathcal{X}}}\Big|_{\boldsymbol{\mathcal{X}}^k}^{-1}\frac{\partial \boldsymbol{\mathcal{F}}}{\partial \boldsymbol{\mathcal{X}}}\Big|_{\boldsymbol{\mathcal{X}}^*}\right\|\|\boldsymbol{\mathcal{X}}^k - \boldsymbol{\mathcal{X}}^*\| + \frac{K}{2}\left\|\frac{\partial \boldsymbol{\mathcal{F}}}{\partial \boldsymbol{\mathcal{X}}}\Big|_{\boldsymbol{\mathcal{X}}^k}^{-1}\right\|\|\boldsymbol{\mathcal{X}}^k - \boldsymbol{\mathcal{X}}^*\|^2\end{aligned} \tag{3.24}$$

The assumption that $\frac{\partial \boldsymbol{\mathcal{F}}}{\partial \boldsymbol{\mathcal{X}}}$ is locally K-Lipschitz yields the expression

$$\begin{aligned}\left\| I - \left.\frac{\partial \boldsymbol{\mathcal{F}}}{\partial \boldsymbol{\mathcal{X}}}\right|_{\boldsymbol{\mathcal{X}}^k}^{-1} \left.\frac{\partial \boldsymbol{\mathcal{F}}}{\partial \boldsymbol{\mathcal{X}}}\right|_{\boldsymbol{\mathcal{X}}^*} \right\| &= \left\| \left.\frac{\partial \boldsymbol{\mathcal{F}}}{\partial \boldsymbol{\mathcal{X}}}\right|_{\boldsymbol{\mathcal{X}}^k}^{-1} \left(\left.\frac{\partial \boldsymbol{\mathcal{F}}}{\partial \boldsymbol{\mathcal{X}}}\right|_{\boldsymbol{\mathcal{X}}^k} - \left.\frac{\partial \boldsymbol{\mathcal{F}}}{\partial \boldsymbol{\mathcal{X}}}\right|_{\boldsymbol{\mathcal{X}}^*} \right) \right\| \\ &\leq K \left\| \left.\frac{\partial \boldsymbol{\mathcal{F}}}{\partial \boldsymbol{\mathcal{X}}}\right|_{\boldsymbol{\mathcal{X}}^k}^{-1} \right\| \|\boldsymbol{\mathcal{X}}^k - \boldsymbol{\mathcal{X}}^*\|\end{aligned} \tag{3.25}$$

Substituting the result of Equation (3.25) into Equation (3.24) yields

$$\|\boldsymbol{\mathcal{X}}^{k+1} - \boldsymbol{\mathcal{X}}^*\| \leq \frac{3K}{2} \left\| \left.\frac{\partial \boldsymbol{\mathcal{F}}}{\partial \boldsymbol{\mathcal{X}}}\right|_{\boldsymbol{\mathcal{X}}^k}^{-1} \right\| \|\boldsymbol{\mathcal{X}}^k - \boldsymbol{\mathcal{X}}^*\|^2 \tag{3.26}$$

By further limiting the possible values of $\boldsymbol{\mathcal{X}}^k$ to the neighborhood about the solution $\boldsymbol{\mathcal{X}}^*$ where the condition $\left\| \left.\frac{\partial \boldsymbol{\mathcal{F}}}{\partial \boldsymbol{\mathcal{X}}}\right|_{\boldsymbol{\mathcal{X}}^k}^{-1} \right\| < \left\| \left.\frac{\partial \boldsymbol{\mathcal{F}}}{\partial \boldsymbol{\mathcal{X}}}\right|_{\boldsymbol{\mathcal{X}}^*}^{-1} \right\| < 2M$ is satisfied, the result of Equation (3.26) is rewritten as

$$\|\boldsymbol{\mathcal{X}}^{k+1} - \boldsymbol{\mathcal{X}}^*\| < 3KM \left\| \left.\frac{\partial \boldsymbol{\mathcal{F}}}{\partial \boldsymbol{\mathcal{X}}}\right|_{\boldsymbol{\mathcal{X}}^k}^{-1} \right\| \|\boldsymbol{\mathcal{X}}^k - \boldsymbol{\mathcal{X}}^*\|^2 \tag{3.27}$$

where K and M are scalars. When supposing $\|\boldsymbol{\mathcal{X}}^k - \boldsymbol{\mathcal{X}}^*\|$ is sufficiently small, e.g.,

$$\|\boldsymbol{\mathcal{X}}^k - \boldsymbol{\mathcal{X}}^*\| < \frac{1}{6KM} \implies \|\boldsymbol{\mathcal{X}}^{k+1} - \boldsymbol{\mathcal{X}}^*\| < \frac{1}{2} \|\boldsymbol{\mathcal{X}}^k - \boldsymbol{\mathcal{X}}^*\| \tag{3.28}$$

Equation (3.27) demonstrates that each subsequent update converges quadratically to the local solution. Importantly, no known analytic methods exist for verifying these assumptions or computing the associated constants within the dynamical systems and targeting problems of interest in this investigation. Therefore, this result only provides assurance that *some* region exists about the solution that demonstrates quadratic convergence.

3.3 Computation of Partial Derivatives

For targeting problems based on a Newton-Raphson corrections process, the computation of updates to the design variables is dependent on the partial derivatives of constraints with respect to these design variables, i.e., the design Jacobian $\frac{\partial \boldsymbol{\mathcal{F}}}{\partial \boldsymbol{\mathcal{X}}}$. In scenarios where the variational relationship or its time derivative is conducive to relatively-simple analytic expression, straightforward computation or numerical integration, respectively, is useful in evaluating

the design Jacobian. Alternatively, finite difference methods, a class of numerical methods, are useful in evaluating partial derivatives with cumbersome mathematical representations and time derivatives due to their ease of implementation. The selection of a particular method involves a trade-off between complexity in derivation and computation time.

3.3.1 The State Transition Matrix

In the analysis of nonlinear systems of differential equations, the numerical integration of the State Transition Matrix (STM) provides a 1$^{\text{st}}$-order approximation of relationship between the variation in the state at a final time, $\boldsymbol{x}(t;\boldsymbol{x_0},t_0)$, and the resulting variation in the state at an initial time, $\boldsymbol{x_0}$, along an integrated trajectory segment within a given dynamical system via a partial derivative, i.e., $\frac{\partial \boldsymbol{x}}{\partial \boldsymbol{x_0}}$. Beginning with a system governed by the ordinary differential equation, i.e.,

$$\frac{\mathrm{d}\boldsymbol{x}(t;\boldsymbol{x_0},t_0)}{\mathrm{d}t} = \boldsymbol{f}(\boldsymbol{x}(t;\boldsymbol{x_0},t_0),t) \tag{3.29}$$

the partial derivative of the governing equations with respect to the initial state is expressed

$$\frac{\partial}{\partial \boldsymbol{x_0}}\left(\frac{\mathrm{d}\boldsymbol{x}(t;\boldsymbol{x_0},t_0)}{\mathrm{d}t}\right) = \frac{\partial \boldsymbol{f}(\boldsymbol{x}(t;\boldsymbol{x_0},t_0),t)}{\partial \boldsymbol{x}(t;\boldsymbol{x_0},t_0)}\frac{\partial \boldsymbol{x}(t;\boldsymbol{x_0},t_0)}{\partial \boldsymbol{x_0}} = A(t)\frac{\partial \boldsymbol{x}(t;\boldsymbol{x_0},t_0)}{\partial \boldsymbol{x_0}} \tag{3.30}$$

where $A(t) = \frac{\partial \boldsymbol{f}}{\partial \boldsymbol{x}}$. Due to the independence of $\boldsymbol{x_0}$ and t, the order of differentiation is mutable, and Equation (3.30) is rewritten

$$\frac{\mathrm{d}}{\mathrm{d}t}\left(\frac{\partial \boldsymbol{x}(t;\boldsymbol{x_0},t_0)}{\partial \boldsymbol{x_0}}\right) = A(t)\frac{\partial \boldsymbol{x}(t;\boldsymbol{x_0},t_0)}{\partial \boldsymbol{x_0}} \tag{3.31}$$

The STM is defined as the matrix derivative $\Phi(t,t_0) = \frac{\partial \boldsymbol{x}}{\boldsymbol{x_0}}$, so Equation (3.31) is expressed in a more compact form by

$$\frac{\mathrm{d}\Phi(t,t_0)}{\mathrm{d}t} = A(t)\Phi(t,t_0) \tag{3.32}$$

revealing the differential equation that governs the STM as it evolves in time. The initial condition for integration of the STM is the identity matrix, i.e., $\Phi(t_0,t_0) = I$. Intuitively, a variation in state at the initial time is equal to itself. With this initial condition and

governing equations from Equation (3.32), numerical integration of the states and STM can be conducted simultaneously.

Though explicit state variable constraints are common in space flight trajectory targeting problems, quantities that are functions of state variables, e.g., altitude and flight path angle, at the end of a trajectory segment are frequently incorporated as constraints. A set of terminal constraints are represented by the vector $\boldsymbol{g}(\boldsymbol{x}(t;\boldsymbol{x_0}),t)$. The use of the chain rule for differentiation yields the expression

$$\begin{aligned}\frac{\partial \boldsymbol{g}(\boldsymbol{x}(t;\boldsymbol{x_0},t_0),t)}{\partial \boldsymbol{x_0}} &= \frac{\partial \boldsymbol{g}(\boldsymbol{x}(t;\boldsymbol{x_0},t_0),t)}{\partial \boldsymbol{x}(t;\boldsymbol{x_0},t_0)}\frac{\partial \boldsymbol{x}(t;\boldsymbol{x_0},t_0)}{\partial \boldsymbol{x_0}} \\ &= \frac{\partial \boldsymbol{g}(\boldsymbol{x}(t;\boldsymbol{x_0},t_0),t)}{\partial \boldsymbol{x}(t;\boldsymbol{x_0},t_0)}\Phi(t,t_0)\end{aligned} \tag{3.33}$$

The required partial derivatives are shown to be a function of the STM and the derivatives with respect to the state at the final time. Scenarios may arise that lead to impractical derivations of $\frac{\partial \boldsymbol{g}}{\partial \boldsymbol{x}}$ and $A(t)$ or numerical difficulties with the integration of the STM. In these situations, the computation of partial derivatives through finite differencing provides an alternative to analytic differentiation and numerical integration.

3.3.2 Partial Derivatives via Finite Difference

Finite difference methods are a class of numerical methods that approximate the derivative, or local slope, of a function at a desired point by evaluating the function at a number of discrete points in its vicinity. Though various strategies exist for selecting points for evaluation, e.g., forward and backward differencing, this investigation applies the method of central differencing for the numerical computation of derivatives. To illustrate the central differencing process, a scalar function $f(x)$, dependent on a scalar independent variable x, is introduced, and the slope is approximated by a secant line, i.e.,

$$\frac{\partial f(x)}{\partial x} = \frac{f(x+h) - f(x-h)}{2h} \tag{3.34}$$

where the evaluated points are perturbed by the small value h from the centrally-located point of interest. As the value of h approaches zero, the secant line collapses to the tangent

at the desired point, and the actual derivative is recovered. However, a value of zero for h in Equation (3.34) produces a singularity, so, in practice, the value of h is chosen to be sufficiently small without introducing numerical errors.

The central difference method extends to approximate partial derivatives in problems with multiple constraints and multiple independent variables. Given a targeting problem with the constraint vector $\boldsymbol{\mathcal{F}}(\boldsymbol{\mathcal{X}})$ as a function of the design variable vector $\boldsymbol{\mathcal{X}}$, the design Jacobian $\frac{\partial \boldsymbol{\mathcal{F}}}{\partial \boldsymbol{\mathcal{X}}}$ is constructed by conducting central differencing for each individual design variable $\mathcal{X}_i$. The standard basis vectors $\boldsymbol{e_i}$ are defined as vectors of length n, the length of $\boldsymbol{\mathcal{X}}$, with a value of one as the i^{th} component and zeros elsewhere. Similar to scalar expression Equation (3.34), the partial derivative of $\boldsymbol{\mathcal{F}}$ with respect to $\mathcal{X}_i$ is approximated through central differencing as a vector expressed by

$$\left.\frac{\partial \boldsymbol{\mathcal{F}}}{\partial \mathcal{X}_i}\right|_{\boldsymbol{\mathcal{X}}} = \frac{\boldsymbol{\mathcal{F}}(\boldsymbol{\mathcal{X}} + h\boldsymbol{e_i}) - \boldsymbol{\mathcal{F}}(\boldsymbol{\mathcal{X}} - h\boldsymbol{e_i})}{2h} \tag{3.35}$$

The design Jacobian matrix is constructed from these independent partial derivatives and expressed mathematically as

$$\left.\frac{\partial \boldsymbol{\mathcal{F}}}{\partial \boldsymbol{\mathcal{X}}}\right|_{\boldsymbol{\mathcal{X}}} = \begin{bmatrix} \left.\frac{\partial \boldsymbol{\mathcal{F}}}{\partial \mathcal{X}_1}\right|_{\boldsymbol{\mathcal{X}}} & \cdots & \left.\frac{\partial \boldsymbol{\mathcal{F}}}{\partial \mathcal{X}_n}\right|_{\boldsymbol{\mathcal{X}}} \end{bmatrix} \tag{3.36}$$

Because the central difference method only requires the capability to evaluate $\boldsymbol{\mathcal{F}}$ for different values of the design variables, the strategy is straightforward to implement when analytic differentiation and numerical integration processes are impractical.

3.4 Single-Shooting Differential Corrections

A single-shooting differential corrections strategy is commonly implemented to solve a two-point boundary value problem with constraints and design variables located at the initial and final times along a single propagated trajectory segment. To illustrate the mechanics of a single-shooting targeting problem, an example is constructed concerning a spacecraft that undergoes ballistic motion in the Earth-Moon system according to the governing equations

of the CRTBP, detailed in Equation (2.23). The spacecraft is constrained to have its actual position $\boldsymbol{\rho_1}$ match a desired position $\boldsymbol{\rho_{1,d}}$ at a fixed future time $t_1 = 4$ days, i.e.,

$$\boldsymbol{\mathcal{F}} = \boldsymbol{\rho_1} - \boldsymbol{\rho_{1,d}} = \mathbf{0} \tag{3.37}$$

To achieve the satisfaction of this constraint, the velocity $\dot{\boldsymbol{\rho}}_\mathbf{0}$ at the initial time t_0 is updated, simulating an impulsive maneuver by the spacecraft. The design variable vector is, therefore, expressed as

$$\boldsymbol{\mathcal{X}} = \dot{\boldsymbol{\rho}}_\mathbf{0} \tag{3.38}$$

The design Jacobian is computed via elements of the numerically-integrated STM and is expressed

$$\frac{\partial \boldsymbol{\mathcal{F}}}{\partial \boldsymbol{\mathcal{X}}} = \frac{\partial \boldsymbol{\rho_1}}{\partial \dot{\boldsymbol{\rho}}_\mathbf{0}} \tag{3.39}$$

This declaration of constraints and design variables completes the formulation for a fully-constrained targeting problem ($n = m$) with $n = 3$ and $m = 3$.

To compute a solution, the targeting problem requires values for the initial conditions and desired position. The initial state is expressed via dimensional position and velocity vectors as

$$\tilde{\boldsymbol{\rho}}_\mathbf{0} = \begin{bmatrix} 100,000 & 100,000 & 0 \end{bmatrix}^T \text{ km}, \quad \dot{\tilde{\boldsymbol{\rho}}}_\mathbf{0} = \begin{bmatrix} -0.85 & -1 & 0 \end{bmatrix}^T \text{ km/s} \tag{3.40}$$

The selected target position at the final time is expressed

$$\tilde{\boldsymbol{\rho}}_{\mathbf{1},d} = \begin{bmatrix} -100,000 & -50,000 & 0 \end{bmatrix}^T \text{ km} \tag{3.41}$$

Because the problem is fully-constrained, candidate values for the initial velocity $\dot{\boldsymbol{\rho}}_\mathbf{0}$ are computed iteratively according to Equation (3.6), seeking the unique local solution. The magnitude of the residual constraint error, $\|\boldsymbol{\mathcal{F}}\|$, at each iteration is shown in Figure 3.1a and decreases quadratically with each design variable update, a well-known property of Newton-Raphson corrections within the local vicinity of a solution [41]. The differential corrections process requires 5 iterations, concluding when the constraint error magnitude is

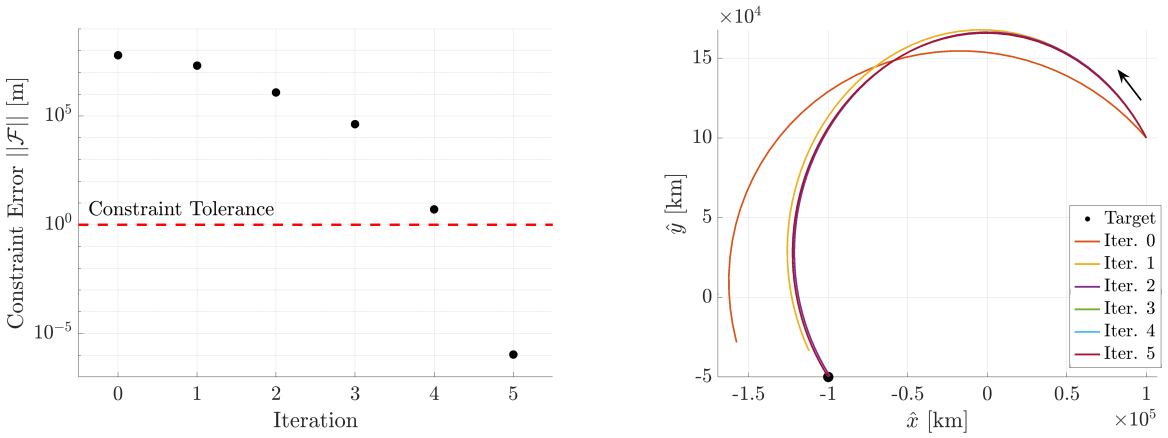

(a) Constraint Error Convergence

(b) Evolution of Trajectories at Each Iteration

Figure 3.1. Convergence Process in a Fully-Constrained, Single-Shooting Example

reduced to a value below the selected convergence tolerance of 1 m. As the design variables are updated, the resulting trajectories, plotted in Figure 3.1b, evolve with each iteration. The first and second targeting iterations produces relatively large changes as the terminal position approaches the target point. The subsequent iterations produce finer changes to refine the trajectory in the vicinity of the target. The convergence behavior demonstrated in Figures 3.1a and 3.1b represent typical characteristics of a targeting problem with a reasonable initial guess.

An under-constrained targeting problem is formulated by augmenting the design variables defined in Equation (3.38). Removing the implicit constraint on the time-of-flight, the value of the final time t_1 is appended to the design variable vector to produce a new targeting problem, i.e.,

$$\boldsymbol{\mathcal{X}} = \begin{bmatrix} \dot{\boldsymbol{\rho}}_{\mathbf{0}} \\ t_1 \end{bmatrix}, \quad \boldsymbol{\mathcal{F}} = \boldsymbol{\rho}_{\mathbf{1}} - \boldsymbol{\rho}_{\mathbf{1},d} = \mathbf{0} \tag{3.42}$$

and the problem satisfies the condition $n > m$ with $n = 4$ and $m = 3$. Maintaining the position constraint in Equation (3.37), the design Jacobian for the new targeting problem is expressed

$$\frac{\partial \boldsymbol{\mathcal{F}}}{\partial \boldsymbol{\mathcal{X}}} = \begin{bmatrix} \frac{\partial \boldsymbol{\rho}_{\mathbf{1}}}{\partial \dot{\boldsymbol{\rho}}_{\mathbf{0}}} & \frac{\mathrm{d}\boldsymbol{\rho}_{\mathbf{1}}}{\mathrm{d}t_1} \end{bmatrix} = \begin{bmatrix} \frac{\partial \boldsymbol{\rho}_{\mathbf{1}}}{\partial \dot{\boldsymbol{\rho}}_{\mathbf{0}}} & \dot{\boldsymbol{\rho}}_{\mathbf{1}} \end{bmatrix} \tag{3.43}$$

Because the targeting problem is under-constrained, an infinite number of solutions exist which satisfy the Newton-Raphson update relation in Equation (3.5), and the minimum-norm solution in Equation (3.17) is selected for the design variable update.

With the initial conditions given in Equation (3.40), the single-shooting differential corrections process is conducted to determine a solution to the targeting problem. At each iteration, the constraint error magnitudes and resulting trajectory arcs, shown in Figures 3.2a and 3.2b, respectively, exhibit trends similar to the fully-constrained scenario with quadratic convergence to a local solution. By augmenting the design variable vector to in-

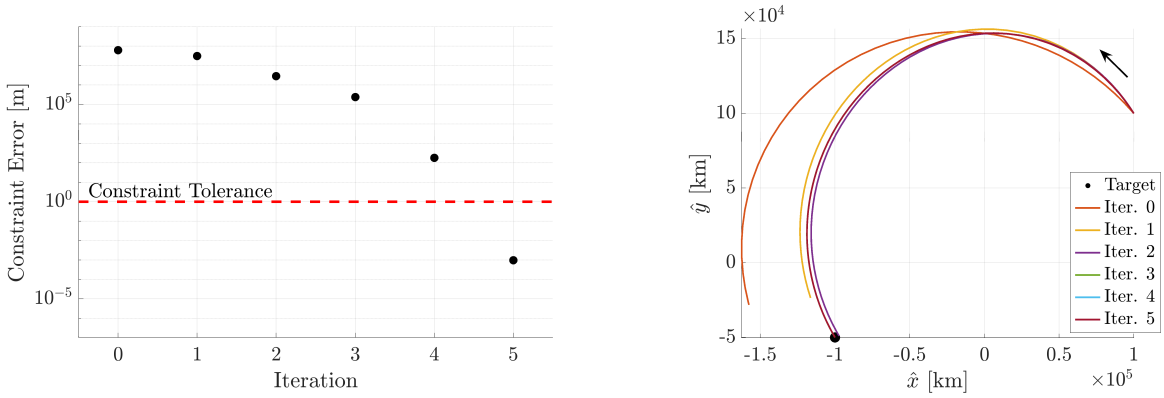

(a) Constraint Error Convergence

(b) Evolution of Trajectories at Each Iteration

Figure 3.2. Convergence Process in an Under-Constrained, Single-Shooting Example

clude the final time t_1, the converged solution is different than the particular local solution to the fully-constrained problem. In fact, the solution computed in the under-constrained targeting problem is not unique and exists as part of a local continuous family of solutions.

3.5 Constraint Manifolds and Continuation

A *constraint manifold* emerges from an under-constrained targeting problem and comprises a continuous set of solutions that evolve smoothly in the space comprised of the set of design variables, denoted *design space* or $\boldsymbol{\mathcal{X}}$-space, e.g., the components of $\dot{\boldsymbol{\rho}}_{\mathbf{0}}$. For all solutions $\boldsymbol{\mathcal{X}}^*$ on a constraint manifold, there exists a solution that satisfies

$$\boldsymbol{\mathcal{F}}(\boldsymbol{\mathcal{X}}^* + \boldsymbol{\varepsilon}) = \mathbf{0} \ , \quad 0 \leq \|\boldsymbol{\varepsilon}\| < \varepsilon_o \tag{3.44}$$

where ε_o is arbitrarily small and $\boldsymbol{\varepsilon}$ is a vector in $\boldsymbol{\mathcal{X}}$-space. The case where Equation (3.44) is only satisfied for $\boldsymbol{\varepsilon} = \mathbf{0}$ corresponds to the locally-unique point solution of a fully-constrained targeting problem.

The linear approximation provided by the design Jacobian $\frac{\partial \boldsymbol{\mathcal{F}}}{\partial \boldsymbol{\mathcal{X}}}$ gives insight into the form of the constraint manifold. Assuming $\frac{\partial \boldsymbol{\mathcal{F}}}{\partial \boldsymbol{\mathcal{X}}}$ evaluated at a particular solution $\boldsymbol{\mathcal{X}}^*$ possesses full rank with $n > m$, the null space of the matrix is defined as the vector space spanned by

$$\text{Null}\left(\left.\frac{\partial \boldsymbol{\mathcal{F}}}{\partial \boldsymbol{\mathcal{X}}}\right|_{\boldsymbol{\mathcal{X}}^*}\right) = \{\mathbf{0}, \boldsymbol{q_1}, \ldots, \boldsymbol{q_{n-m}}\} \text{ where } \left.\frac{\partial \boldsymbol{\mathcal{F}}}{\partial \boldsymbol{\mathcal{X}}}\right|_{\boldsymbol{\mathcal{X}}^*} \boldsymbol{q_i} = \mathbf{0} \tag{3.45}$$

The null vectors $\boldsymbol{q_i}$ associated with the linear system are locally tangent to the (often non-linear) constraint manifold at the particular solution $\boldsymbol{\mathcal{X}}^*$ [42], [43]. Within the linearized problem, the null vectors intuitively reflect directions of change in the design variables that will not result in changes in the (already-satisfied) constraint values. For a fully-constrained problem with a design Jacobian of full rank, the null space consists exclusively of the zero vector. In the particular scenario of $n - m = 1$, as in the under-constrained targeting problem defined by Equation (3.42), a continuation method that is guided by the single resulting null vector is useful in computing the 1-dimensional constraint manifold.

Various continuation methods exist to search for new solutions located on the same constraint manifold as a known particular solution. A 1-dimensional constraint manifold is represented by a single-parameter family of solutions to its associated targeting problem. Natural parameter continuation is commonly used to generate an initial guess for neighboring solutions in single-parameter family by perturbing some physical parameter in the system, e.g., position in the $\hat{\boldsymbol{x}}$ direction. While natural parameter continuation has an intuitive physical significance, the selection of a natural parameter is not always obvious, relying on previously-built intuition or trial-and-error. *Pseudo-arclength continuation* is another frequently-used strategy that leverages a fixed step in null vector of the design Jacobian evaluated at the current solution to generate an initial guess [42], [43]. Though lacking the same physical significance as a natural parameter, pseudo-arclength continuation is simple to implement and follows changes in slope of the constraint manifold with a sufficiently small step length.

The pseudo-arclength continuation method for a single-parameter family begins with an existing i^{th} particular solution, $\boldsymbol{\mathcal{X}}^{*(i)}$, to search for a new $(i+1)^{\text{th}}$ solution on the constraint manifold. The null vector of the design Jacobian evaluated at the existing solution, i.e., $\boldsymbol{q_1}^{(i)}$, defined in Equation (3.45), represents the tangent to the constraint manifold at that point. To ensure the new solution is displaced from the existing solution and, therefore, yields novel information about the manifold, an augmented constraint vector $\boldsymbol{\mathcal{G}}$ is formulated to enforce a step of length s, i.e, the pseudo-arclength, in the $\boldsymbol{q_1}^{(i)}$ direction relative to the existing solution, i.e.,

$$\boldsymbol{\mathcal{G}} = \begin{bmatrix} \boldsymbol{\mathcal{F}} \\ \left(\boldsymbol{\mathcal{X}} - \boldsymbol{\mathcal{X}}^{*(i)}\right)^T \boldsymbol{q_1}^{(i)} - s \end{bmatrix} \tag{3.46}$$

The introduction of this additional constraint produces a fully-constrained problem with a square augmented design Jacobian matrix expressed as

$$\frac{\partial \boldsymbol{\mathcal{G}}}{\partial \boldsymbol{\mathcal{X}}} = \begin{bmatrix} \frac{\partial \boldsymbol{\mathcal{F}}}{\partial \boldsymbol{\mathcal{X}}} \\ \boldsymbol{q_1}^{(i)^T} \end{bmatrix} \tag{3.47}$$

Because the multiplication of a null vector with negative one is also a null vector, the continuation process is possible in both the $\boldsymbol{q_1}^{(i)}$ and $-\boldsymbol{q_1}^{(i)}$ directions.

Returning to the under-constrained targeting problem outlined in Equation (3.42), pseudo-arclength continuation is useful to compute additional solutions along the constraint manifold. Discrete solutions on a portion of the constraint manifold are found by continuing in a non-physical, non-dimensional pseudo-arclength of $s = 0.01$. A sampling of trajectories on this portion of the constraint manifold are plotted in Figure 3.3a. The trajectory of the initial solution is colored red with subsequent results of the continuation process shifting from blue to yellow as distance along the manifold increases. Visually, it is evident that each solution begins from the same position $\boldsymbol{\rho_0}$ at the initial t_0 and terminates at the same target point $\boldsymbol{\rho_{1,d}}$. The slope in position of each solution at the initial point varies, confirming a variation in values for initial velocity, $\dot{\boldsymbol{\rho}}_{\mathbf{0}}$, a design variable across the solution family. To observe changes in the time-of-flight design variable t_1, the constraint manifold is plotted in $\boldsymbol{\mathcal{X}}$-space in Figure 3.3b, where the axes locating each solution are $\dot{x}_0$, $\dot{y}_0$, and t_1. The $\hat{\boldsymbol{z}}$ component

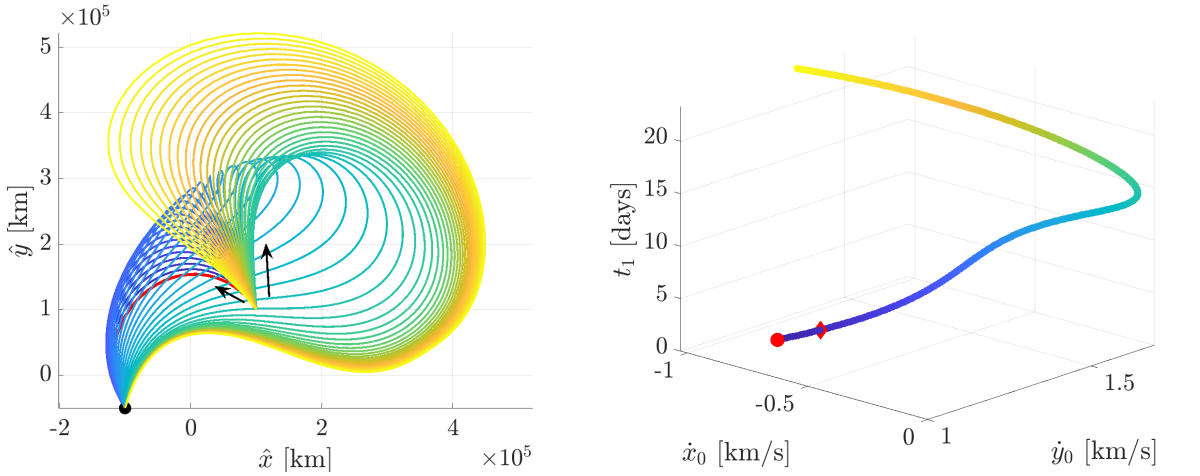

(a) Constraint Error Convergence (b) Evolution of Trajectories at Each Iteration

Figure 3.3. Constraint Manifold in an Under-Constrained, Single-Shooting Example

of initial velocity is always equal to zero for these planar trajectories and, therefore, is safely omitted. Though the representation of the constraint manifold appears continuous, Figure 3.3b is comprised of densely-packed discrete solutions, colored to reflect correspondence with the trajectories in Figure 3.3a. The continuation follows a single direction of the null vector, so the initial solution is located at one end of the manifold segment and represented by a red circle. Additionally, the solution computed from the fully-constrained example, defined by Equations (3.37) and (3.38), is represented by a red diamond. The fully-constrained point solution coincides with the under-constrained constraint manifold, illustrating its connection to the underlying under-constrained problem and the increase in dimension of the manifold as a design variable is added to the targeting problem formulation.

3.6 Multiple-Shooting Differential Corrections

In contrast to a single-shooting corrections process, *multiple-shooting* differential corrections involve the subdivision of a trajectory into multiple segments. Illustrated in an instructive analogy to the game of golf by Spreen [21], a multiple-shooting strategy provides significant advantages in many targeting scenarios. From a mission design perspective, this subdivision allows the convenient inclusion and concurrent targeting of maneuvers along the entire trajectory. Directly affecting the targeting process, the shortened propagation times

for each arc reduce the impact of compounding numerical error and help to mitigate the difficulties associated with complex dynamical regimes. Though a variety of multiple-shooting formulations exist, including two-level algorithms that divide corrections for position continuity and other constraints between an inner and outer loop, respectively [23], [44]–[48], the multiple-shooting method used in this investigation is inspired by the work of Grebow [38] and Pavlak [39] and produces updates to satisfy all of the constraints in parallel.

Additional notation is useful upon dividing the overall trajectory into smaller segments. Illustrated in Figure 3.4, the multiple-shooting problem is formulated in terms of k segments and $k+1$ nodes, enumerated $i = 0, \ldots, k$ by convention. The placement of nodes is commonly

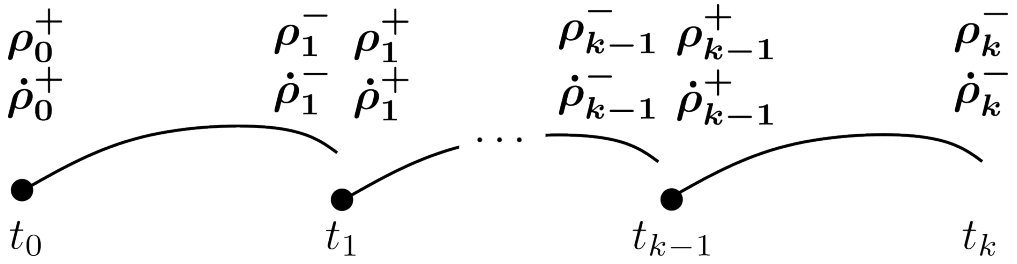

Figure 3.4. Schematic Representation of Multiple-Shooting Trajectory Segments

based on planned maneuvers or strategies that aim to improve the convergence behavior of the targeting problem [20], [22]. The numerical integration of each segment is defined in terms of an initial time t_i, a final time t_{i+1}, and an outgoing state, denoted with a plus $(+)$, that serves as the initial condition for the propagation. The integrated final state, or incoming state, at the end of the trajectory segment is denoted with a minus $(-)$. Naturally, a ballistic trajectory *qua* ballistic requires continuity between the incoming and outgoing state, and this state continuity constraint is mathematically expressed as

$$\boldsymbol{\mathcal{F}} = \begin{bmatrix} \boldsymbol{\rho}_i^- - \boldsymbol{\rho}_i^+ \\ \dot{\boldsymbol{\rho}}_i^- - \dot{\boldsymbol{\rho}}_i^+ \end{bmatrix} = \mathbf{0} \tag{3.48}$$

for each applicable node. To allow a maneuver modelled as an impulsive velocity change, the velocity component of the state continuity constraint is omitted. In this multiple-shooting

formulation, the time variables and the outgoing (+) state are assumed to be independent, and the incoming (−) states are functions of these independent variables, i.e.,

$$\begin{bmatrix} \boldsymbol{\rho}_{\boldsymbol{i}}^{-} \\ \dot{\boldsymbol{\rho}}_{\boldsymbol{i}}^{-} \end{bmatrix} = \boldsymbol{f}(\boldsymbol{\rho}_{\boldsymbol{i-1}}^{+}, \dot{\boldsymbol{\rho}}_{\boldsymbol{i-1}}^{+}, t_{i-1}, t_i) \tag{3.49}$$

Therefore, the times and outgoing state variables are frequently incorporated into the set of design variables for a multiple-shooting problem.

4. CONVERGENCE BASIN ANALYSIS

In flight, the true motion of a spacecraft inevitably deviates from its pre-planned reference trajectory due the differences between the modeled dynamics and the actual forces from the environment and the spacecraft itself, e.g., unmodeled gravitational forces and maneuver execution error. Additionally, knowledge of the true spacecraft motion is, in practice, unattainable and limited to discrete state estimations, themselves influenced by sources of navigation error. To incorporate these deviations from the pre-planned reference solution, the capability to attain new reference solutions during flight is critical to predict future motion and control the spacecraft to satisfy mission constraints.

4.1 Perturbed Targeting Problems

The pre-planned reference trajectory is assumed to be a solution to an associated targeting problem. In this investigation, the terms "reference" and "baseline" are used interchangeably to denote a known solution that is intended for the nominal trajectory. Deviations from this pre-planned reference solution are modeled as changes in a set of *perturbation variables*, represented in vector form by $\boldsymbol{\mathcal{Y}}$ with length p, that cause the spacecraft to move along a perturbed trajectory. As the solution to a targeting problem, the original reference solution satisfies the set of constraints $\boldsymbol{\mathcal{F}}$, i.e.,

$$\boldsymbol{\mathcal{F}}(\boldsymbol{\mathcal{X}}^*, \boldsymbol{\mathcal{Y}}^*) = \mathbf{0} \tag{4.1}$$

at particular values of the design variables and perturbation variables, $\boldsymbol{\mathcal{X}}^*$ and $\boldsymbol{\mathcal{Y}}^*$, respectively. The perturbation variables may be comprised of elements of the design variable vector $\boldsymbol{\mathcal{X}}$ and may incorporate additional variables in the problem. For example, an initial velocity may comprise the design variables in a problem while the perturbation variables may consist of the initial position, the initial velocity, or the entire initial state.

When a change in perturbation variables, $\delta\boldsymbol{\mathcal{Y}}$, is applied to the original reference solution, the resulting perturbed trajectory, in general, does not satisfy the constraints. To compute

a new solution, a Newton-Raphson corrections process is applied to a *perturbed targeting problem* to update the design variables via the solution to

$$\boldsymbol{\mathcal{F}}|_{(\boldsymbol{\mathcal{X}},\boldsymbol{\mathcal{Y}})} = -\left.\frac{\partial \boldsymbol{\mathcal{F}}}{\partial \boldsymbol{\mathcal{X}}}\right|_{(\boldsymbol{\mathcal{X}},\boldsymbol{\mathcal{Y}})} \delta\boldsymbol{\mathcal{X}} \tag{4.2}$$

rewritten from Equation (3.5). The design variable update $\delta\boldsymbol{\mathcal{X}}$ at each iteration is computed with the design Jacobian and constraint vector evaluated at the evolving values of $\boldsymbol{\mathcal{X}}$ and $\boldsymbol{\mathcal{Y}}$ via matrix inversion or the minimum-norm solution. If a variable, such as the spacecraft position at a given time, is incorporated in the set of perturbation variables, $\boldsymbol{\mathcal{Y}}$, but not in the set of design variables, $\boldsymbol{\mathcal{X}}$, it remains unchanged in the corrections process. The computation of a new solution that is the same as the reference solution is only possible if all perturbation variables are also design variables; otherwise, the perturbations persist in the new solution.

The concept of the constraint manifold for a targeting problem solution, defined by Equation (3.44), is extended to account for the introduction of perturbation variables. In a perturbed targeting problem, a constraint manifold is comprised of a continuous set of solutions that evolve smoothly in the space defined by the union of the design and perturbation spaces, $\boldsymbol{\mathcal{X}}$-space and $\boldsymbol{\mathcal{Y}}$-space, respectively. For all solutions $(\boldsymbol{\mathcal{X}}^*, \boldsymbol{\mathcal{Y}}^*)$ on a constraint manifold, there exists a solution on that manifold that satisfies

$$\boldsymbol{\mathcal{F}}(\boldsymbol{\mathcal{X}}^* + \boldsymbol{\varepsilon}_{\boldsymbol{\mathcal{X}}}, \boldsymbol{\mathcal{Y}}^* + \boldsymbol{\varepsilon}_{\boldsymbol{\mathcal{Y}}}) = \mathbf{0} \ , \quad 0 \leq \|\boldsymbol{\varepsilon}_{\boldsymbol{\mathcal{X}}}\| < \varepsilon_{o,\mathcal{X}} \ , \quad 0 \leq \|\boldsymbol{\varepsilon}_{\boldsymbol{\mathcal{Y}}}\| < \varepsilon_{o,\mathcal{Y}} \tag{4.3}$$

where $\varepsilon_{o,\mathcal{X}}$ and $\varepsilon_{o,\mathcal{Y}}$ are arbitrarily small and $\boldsymbol{\varepsilon}_{\boldsymbol{\mathcal{X}}}$ and $\boldsymbol{\varepsilon}_{\boldsymbol{\mathcal{Y}}}$ are in the $\boldsymbol{\mathcal{X}}$- and $\boldsymbol{\mathcal{Y}}$-spaces, respectively. Two solutions are located on the same constraint manifold if they are connected by continuous solutions on the manifold. Notably, continuation may be required in both $\boldsymbol{\mathcal{X}}$ and $\boldsymbol{\mathcal{Y}}$ to connect the new solution to the reference solution.

The *convergence basin*, or *basin of attraction*, for a given reference solution in a perturbed targeting problem is defined as the region in perturbation space, or $\boldsymbol{\mathcal{Y}}$-space, for which each associated new solution is linked to the reference solution by continuation along a constraint manifold. For cases where more than one constraint manifold exists globally, each

constraint manifold possesses its own local main convergence basin, typically bounded by chaotic behavior. Therefore, assurance that perturbations remain within the main basin implies that the perturbed targeting problem reliably converges to a related solution and avoids unpredictable convergence behavior.

4.1.1 Example: Polynomial Root-Finding

A polynomial root-finding problem is introduced to visualize the properties of any convergence basin in perturbation space. A scalar constraint function, $f(z)$, is a function of a complex number z, i.e.,

$$f(z) = z^3 - 2z - 4 = 0 \tag{4.4}$$

with roots at $z^* = -1+\mathrm{i},\ -1-\mathrm{i},\ 2$. In this scenario, the design variables and the perturbation variables are both defined as the real and imaginary components of $z = x + \mathrm{i}y$, meaning the perturbation space is represented as the complex plane. The resulting perturbed targeting problem is expressed as

$$\boldsymbol{\mathcal{F}} = (x+\mathrm{i}y)^3 - 2(x+\mathrm{i}y) - 4 = 0, \quad \boldsymbol{\mathcal{X}} = \begin{bmatrix} x & y \end{bmatrix}^T, \quad \boldsymbol{\mathcal{Y}} = \begin{bmatrix} x & y \end{bmatrix}^T \tag{4.5}$$

This relatively simple 3$^{\text{rd}}$-order polynomial exposes the major characteristics and the complexity of convergence basins in general.

Newton-Raphson corrections schemes are applied to each point in a dense sampling of the perturbation space, and two useful visualizations of the convergence basins are produced. In Figure 4.1a, the perturbation space (complex plane) is colored according to the converged root of the corrections process. The perturbation space is roughly split into thirds, corresponding to the three complex roots of the polynomial, with large main basins are separated by a fractal boundary layer with chaotic behavior. In Figure 4.1b, the complex plane is colored according to the number of iterations required to attain a solution to within the selected tolerance value. This method is frequently used to visually represent the convergence basin [2], [49], [50]. The number of iterations required to produce a solution as the initial guess is perturbed outward from a local solution increases monotonically as long as the initial

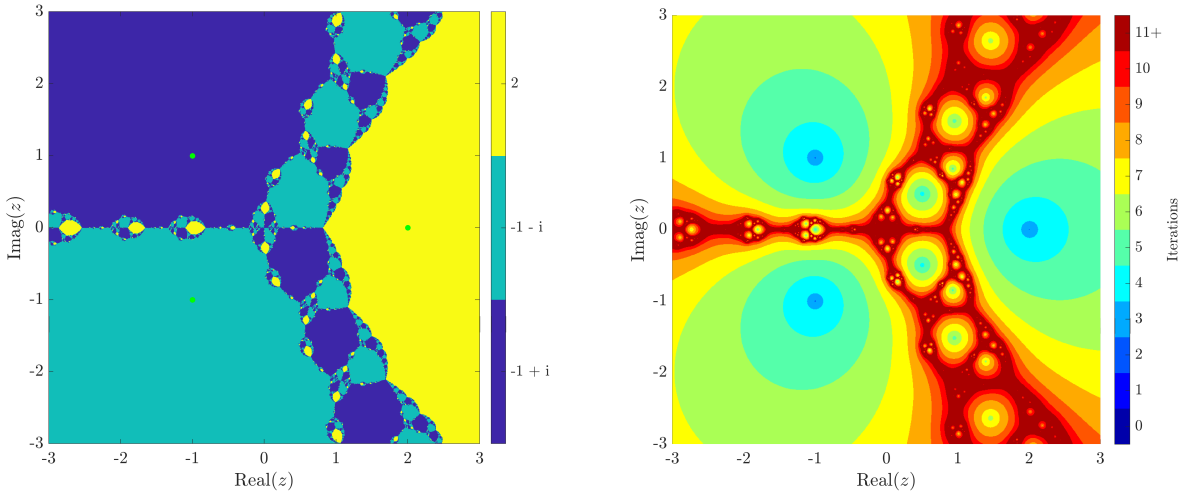

(a) Solved Root in Complex Plane

(b) Iterations in Complex Plane

Figure 4.1. Convergence Behavior for a 3rd-Order Polynomial Example

perturbation resides within the main basin. This structure for a monotonic main basin in the local vicinity of a solution and boundary regions of chaotic convergence behavior forms the foundation of this investigation.

4.1.2 Example: Equilibrium Points in the CRTBP

As the model for the constraint function is updated to more complex nonlinear equations, the inherent structure of the convergence basin in perturbation space persists; however, the patterns are less intuitive than those in the polynomial model. To investigate this behavior, the equilibrium locations in the Earth-Moon CRTBP are determined via Newton-Raphson targeting. Since the equilibrium points exist in the $\hat{\boldsymbol{x}}$-$\hat{\boldsymbol{y}}$ plane, the equations of motion from Equation (2.23) are used to constrain the planar accelerations, $\ddot{x}$ and $\ddot{y}$, to equal 0. The x and y position components are selected as both design variables and perturbation variables for this perturbed targeting scenario. The velocities are set to 0 by the definition of an equilibrium point. The perturbed targeting problem is expressed as

$$\boldsymbol{\mathcal{F}} = \begin{bmatrix} x - \frac{(1-\mu)(x+\mu)}{d^3} - \frac{\mu(x-1+\mu)}{r^3} \\ y - \frac{(1-\mu)y}{d^3} - \frac{\mu y}{r^3} \end{bmatrix} = \mathbf{0} \ , \ \boldsymbol{\mathcal{X}} = \begin{bmatrix} x \\ y \end{bmatrix} \ , \ \boldsymbol{\mathcal{Y}} = \begin{bmatrix} x \\ y \end{bmatrix} \tag{4.6}$$

and is fully-constrained, leading to unique point solutions. A similar analysis of a system with primary bodies of equal mass in the CRTBP is conducted by Zotos [50].

For initial points in a dense sampling of the primary orbital plane, the resulting convergence basins are again examined through plotting the roots, i.e., the converged solutions, and the required number of iterations in Figures 4.2a and 4.2b, respectively. In Figure 4.2a, each

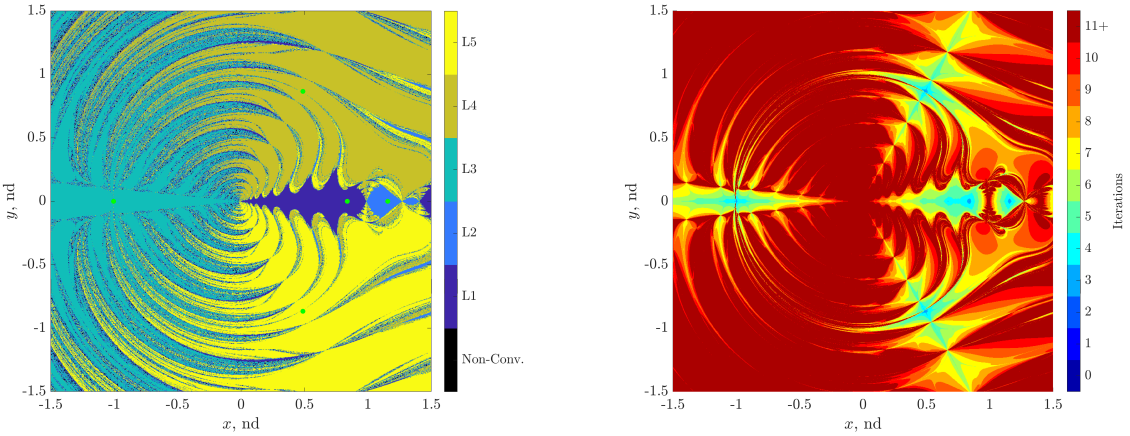

(a) Solved Root in the Plane

(b) Iterations in the Plane

Figure 4.2. Convergence Behavior for Equilibrium Points in the CRTBP

equilibrium solution is marked as a green dot, and the initial guesses across the plane are colored with a dot according the converged Lagrange point. A local vicinity for each solution is visible for which the perturbations return to the solution. However, the global geometry of these basins is less easily articulated than for the geometry of the 3$^{\text{rd}}$-order polynomial example, and the chaotic boundaries do not align with any obvious intuition about the problem. In Figure 4.2b, a local main basin — no matter the size — for which the required number of iterations increases monotonically is visible for each equilibrium point. The characteristic structure of locally-organized main basins within a chaotic boundary region persists in the equations governing this dynamical system. A—presumably unintended—artistic representation of the global convergence behavior of a highly-complex, nonlinear perturbed targeting problem is illustrated by Jackson Pollock's appropriately-titled *Convergence* (1952) [51], shown in Figure 4.3, where the viewer may imagine small islands of monotonic convergence behavior amidst a tumultuous, chaotic sea.

Figure 4.3. Convergence (1952) by Jackson Pollock, Copyright by Pollock-Krasner Foundation / Artists Rights Society (ARS) [51]

4.2 Convergence Basin Width

In space flight applications, the convergence behavior of interest corresponds to that of the main basin associated with the reference solution. Perturbations that carry the spacecraft into a region of chaotic convergence behavior present significant risks to crew safety and mission success. Therefore, the robust design of a trajectory and targeting scheme should ensure that any expected perturbations remain within the main basin. A parameter or metric to characterize the main basin is sought that successfully quantifies this robustness.

A schematic of the main basin for a reference solution is illustrated in Figure 4.4 as a means to construct an appropriate characterization measure. The reference solution is represented by the black point; the colored contours emanating from this point reflect theoretical continuous regions for which the perturbed targeting problem converges within various iteration limits, k_{max}. As the contours shift from green to yellow, more iterations are required to converge from a perturbed trajectory to a feasible solution in the vicinity of the reference. The red area reflects the chaotic region bounding the main basin where the convergence behavior is unpredictable. The *basin width*, $\|\delta\boldsymbol{\mathcal{Y}}_{(k_{max})}\|$, is defined as the radius of the largest hyper-sphere such that all enclosed points converge within $k_{\max}$ iterations. The construction of the defining hyper-sphere in the plane, i.e., a circle, is illustrated in Figure 4.4 for

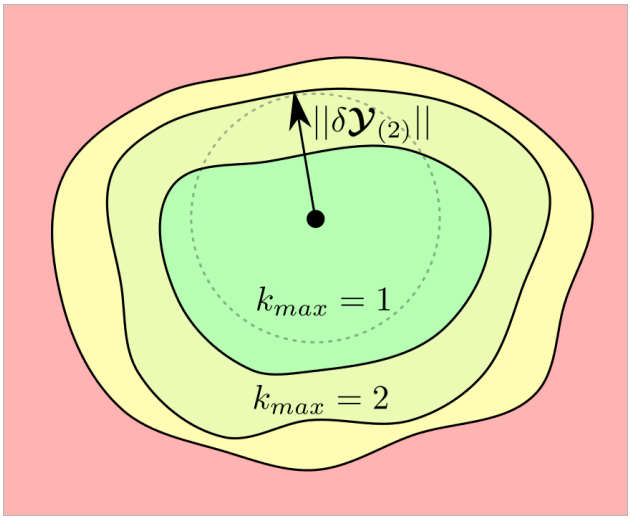

Figure 4.4. Theoretical Basin Width

$k_{max} = 2$. As long as k_{max} is selected to be sufficiently small, the basin width defines a key feature of the main basin. Ideally, the theoretical basin width is determined by continuously traversing the perturbation space.

The theoretical basin width is only truly known if an analytical solution exists to describe the perturbation space. Since the convergence basins cannot be determined analytically in the problems of interest, numerical methods are required to approximate the measurement. Illustrated in Figure 4.5a, a naïve discretization of the perturbation space is the closest method to approximating a continuous interrogation of the space, assuming the spacing between points is sufficiently refined. Another similar approach is the discretization along a series shells defined by hyper-spheres with increasing radii, illustrated in Figure 4.5b. These discretization methods do not directly utilize information about the perturbed targeting problem, and, due to their brute-force nature, these approaches are computationally expensive and impractical, requiring a full targeting simulation at each discretized point in the p-dimensional perturbation space.

4.3 First-Order Basin Analysis

The costly-nature of the naïve discretization strategies motivates the identification of a more discriminating discretization technique that focuses analysis in directions that are likely

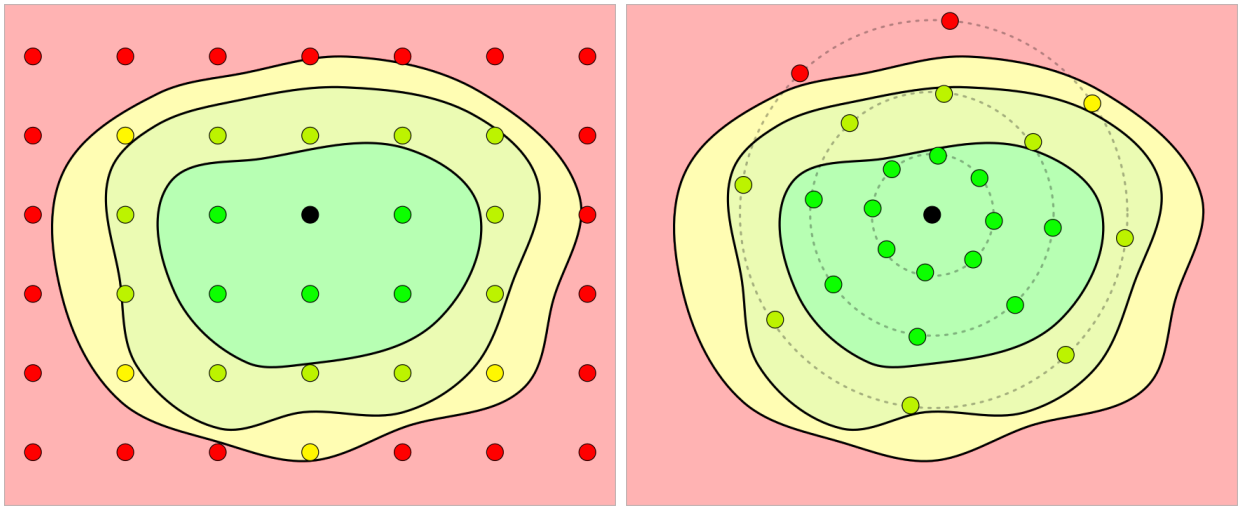

(a) Regular Grid (b) Expanding Shells

Figure 4.5. "Naïve" Perturbation Space Discretization Schemes

correlated with the theoretical basin width measurement. An intuitive heuristic method to limit the number of targeting simulations necessary to approximate the basin width is a search in the direction in perturbation space that produces the largest change in the constraint vector. Information gathered from the 1st-order derivatives assists in this process. The *perturbation Jacobian* $\frac{\partial \mathcal{F}}{\partial \mathcal{Y}}$ represents the change in the constraints with respect to changes in the perturbation variables, and its singular value decomposition (SVD) provides information about the local maximum rate of change.

4.3.1 Singular Value Decomposition

The SVD, first discovered independently by Eugenio Beltrami (1835-1899) and Camille Jordan (1838-1921) with later substantial theoretical contributions by James Joseph Sylvester (1814-1897), Erhard Schmidt (1876-1959), and Hermann Weyl (1885-1955) [52], provides an informative factorization of a real m-by-n matrix. Originally developed for the investigation of bilinear systems of equations [53], the SVD allows the factorization of the matrix $A \in \mathbb{R}^{m \times n}$ expressed as

$$A = U \Sigma V^T \tag{4.7}$$

with $U \in \mathbb{R}^{m\times m}$, $\Sigma \in \mathbb{R}^{m\times n}$, and $V \in \mathbb{R}^{n\times n}$. Further examination of these matrices yields valuable insight.

This decomposition is meaningfully understood in terms of *singular vectors* and *singular values*. The diagonal matrix Σ is comprised of the singular values σ_i for $i = 1, \ldots, k$ where $k = \min\{m, n\}$. The singular values are computed as the square roots of the k leading eigenvalues of A^TA and AA^T. The singular values of A are shown to be non-negative by first asserting that AA^T and A^TA are positive semi-definite matrices with non-negative eigenvalues. This property is demonstrated for A^TA by observing

$$\begin{aligned} \boldsymbol{x}^T(A^TA)\boldsymbol{x} &= \boldsymbol{x}^TA^TA\boldsymbol{x} \\ &= (A\boldsymbol{x})^T(A\boldsymbol{x}) \\ &= \|A\boldsymbol{x}\|^2 \\ &\geq 0 \end{aligned} \tag{4.8}$$

and is similarly shown for AA^T. By convention, the positive square roots are selected, and the singular values are arranged in descending order such that $\sigma_1 \geq \sigma_2 \geq \cdots \geq \sigma_k$. The columns of the unitary matrices U and V are comprised of the left and right singular vectors, $\boldsymbol{u_i}$ and $\boldsymbol{v_i}$, computed as the eigenvectors of AA^T and A^TA, respectively, and are arranged in correspondence to the appropriate singular value, σ_i. The singular values and singular vectors satisfy a relationship expressed as

$$\sigma_i\boldsymbol{u_i} = A\boldsymbol{v_i} \tag{4.9}$$

and the SVD is rewritten as

$$A = U\Sigma V^T = \begin{bmatrix} \boldsymbol{u_1} & \ldots & \boldsymbol{u_m} \end{bmatrix} \begin{bmatrix} \sigma_1 & & 0 \\ & \ddots & \\ 0 & & \sigma_k \end{bmatrix} \begin{bmatrix} \boldsymbol{v_1} & \ldots & \boldsymbol{v_n} \end{bmatrix}^T \tag{4.10}$$

where the additional rows or columns of zeros are omitted from $m \times n$ matrix Σ for simplicity. Further, the maximum, or *dominant*, singular value of A is equivalent to its l_2-norm, i.e.,

$\sigma_1 = \|A\|$. The largest possible scaling between the magnitudes of $\boldsymbol{x}$ and $A\boldsymbol{x}$ is achieved when $\boldsymbol{x}$ is parallel to the dominant right singular vector, $\boldsymbol{v_1}$. Information revealed by the SVD is, therefore, useful in determining the direction of a perturbation that will yield the largest change in the constraint vector magnitude.

4.3.2 Principal Direction Analysis

The relationship between changes in the perturbation variables and their resulting changes in the constraints gives insight into the structure of the convergence basin, permitting a more focused discretization technique. By applying the SVD, the perturbation Jacobian $\frac{\partial \boldsymbol{\mathcal{F}}}{\partial \boldsymbol{\mathcal{Y}}}$ evaluated at the reference solution is expressed

$$\left.\frac{\partial \boldsymbol{\mathcal{F}}}{\partial \boldsymbol{\mathcal{Y}}}\right|_{(\boldsymbol{\mathcal{X}}^*, \boldsymbol{\mathcal{Y}}^*)} = U\Sigma V^T = \begin{bmatrix} \boldsymbol{u_1} & \dots & \boldsymbol{u_m} \end{bmatrix} \begin{bmatrix} \sigma_1 & & 0 \\ & \ddots & \\ 0 & & \sigma_k \end{bmatrix} \begin{bmatrix} \boldsymbol{v_1} & \dots & \boldsymbol{v_p} \end{bmatrix}^T \tag{4.11}$$

which is a particular expression of the general decomposition in Equation (4.10). The right singular vectors $\boldsymbol{v_i}$ comprise an orthonormal basis and are denoted the *principal directions* in perturbation space ($\boldsymbol{\mathcal{Y}}$-space). Based on the 1st-order approximation of the perturbation Jacobian, perturbations applied in these principal directions produce changes in the constraints, scaled by the singular values σ_i, in the corresponding constraint space ($\boldsymbol{\mathcal{F}}$-space) directions along the left singular vector $\boldsymbol{u_i}$. Because the actual function that maps changes in the perturbation variables to changes in the constraints is, generally, nonlinear, the applicability of this approximation degrades as the magnitude of the perturbation increases. The principal directions provide insight into the local structure of the convergence basin where linear corrections processes are useful and predictable.

Intuitively, the principal direction associated with the dominant singular value is likely to correspond to the theoretical basin width, because perturbations in this dominant principal direction produce the largest increase in $\|\boldsymbol{\mathcal{F}}(\boldsymbol{\mathcal{X}}, \boldsymbol{\mathcal{Y}})\|$. Therefore, the perturbation space is discretized by steps along the $\pm\boldsymbol{v_1}$ directions, as illustrated on the schematic convergence basin in Figure 4.6. Employing the same discretization method along the remaining prin-

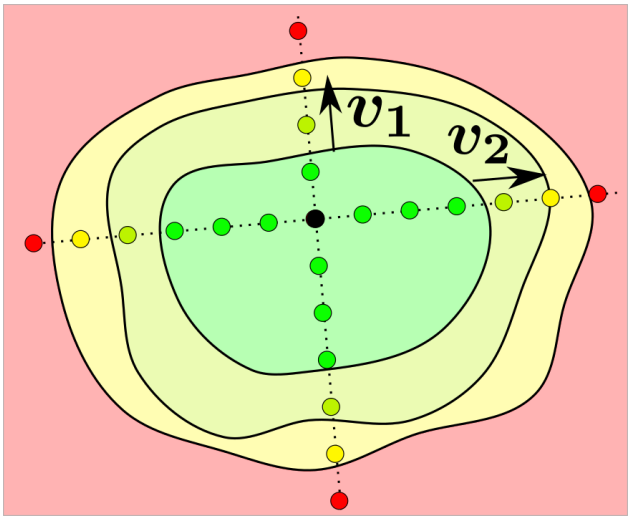

Figure 4.6. Principal Direction Analysis

cipal directions provides additional value for a variety of reasons. In scenarios without a clearly-dominant singular value, e.g., $\sigma_1 \approx \sigma_2$, the constraint vector magnitude may increase uniformly in multiple orthogonal directions, and a search in these additional principal directions is useful to determine the limiting behavior. Also, discretization in the remaining principal directions helps to determine if nonlinearity affects the local main convergence basin in unpredictable ways. In this way, the principal direction analysis is intended to provide a reasonable approximation for the worst-case convergence behavior.

In this investigation, the implementation of *principal direction analysis* (PDA) is designed to measure the approximate basin width to within a chosen tolerance. The process is initialized with a sufficiently small step along $\boldsymbol{v_1}$, and a new solution is found via the Newton-Raphson corrections process. If number of iterations required to compute a solution is less than or equal to the iteration limit, the lower bound for the basin width measurement is set to the present perturbation magnitude, and the process is repeated for a perturbation magnitude scaled by 1.1, chosen to allow growth but avoid large changes in behavior. When a targeting problem requires a number of iterations greater than the limit to reach convergence, the upper bound for the basin width measurement is set to the present perturbation magnitude, and a bisection process is initiated to refine the lower and upper bounds. The bisection process is concluded when a relative error less than 0.1% is achieved. The analysis

is repeated for the positive and negative directions associated with each principal direction, i.e, $\pm\boldsymbol{v_i}$, and the convergence basin width is approximated as the minimum value across all directions. For the regular grid or expanding shell discretization methods, the number of targeting simulations required increases exponentially with the number of perturbation variables p. In contrast, the number of simulations required for PDA increases linearly with p, providing an efficient strategy for approximating the convergence basin width.

4.4 Finite Time Lyapunov Exponent-Based Metrics

The identification of a single, evaluated metric to characterize the local convergence behavior at a reference solution is sought. In contrast to computationally-intensive discretization methods that characterize convergence behavior directly through the full simulation of numerous targeting problems, previous investigators infer convergence properties in the neighborhood of a baseline solution via the computation of dynamical properties evaluated at the baseline solution itself. Particularly, quantities derived from the Cauchy-Green tensor are employed to characterize the amount of dynamical stretching in state perturbations over time [20]–[25].

The left and right Cauchy-Green tensors (CGTs) are expressed in terms of the STM as $\Phi\Phi^T$ and $\Phi^T\Phi$, respectively, where the connection to the SVD of Φ is apparent. The eigenvalues of the CGTs, corresponding to the singular values of the STM, represent stretching or contracting magnitudes of variations along principal axes of a fixed-volume hyper-ellipsoid in phase space. The principal axes at the initial and final times are computed as the respective eigenvectors of the right and left CGTs, equivalent to the right and left singular vectors of the STM. In connection to the SVD, the largest stretching magnitude computed from the CGT is equal to the largest singular value, or l_2-norm, of the STM. The *local Lyapunov exponent* (LLE) measures the maximum rate of exponential growth in an infinitesimal variation at the initial time over an infinite time horizon, i.e.,

$$\text{LLE} = \lim_{T\to\infty} \frac{1}{T} \ln(\|\Phi(t_0 + T, t_0)\|) \tag{4.12}$$

where T is the horizon time. One definition of deterministic chaos in a dynamical system is the possession of a positive LLE [54]. Knowledge of the flow characteristics over an infinite time horizon is impractical—notably, impossible—and may be undesirable when studying the effects of perturbations over a fixed time-of-flight. Therefore, a finite-time formulation, denoted the *finite-time Lyapunov exponent* (FTLE), is introduced and expressed as

$$\text{FTLE} = \frac{1}{T} \ln(\|\Phi(t_0 + T, t_0)\|) \tag{4.13}$$

to quantify the rate of stretching in state variations over a finite horizon time. Incorporating insight from investigations by Spreen that omit division by the horizon time [21], analogous quantities are introduced to quantify the largest magnitudes of stretching in the design Jacobian and perturbation Jacobian matrices, i.e.,

$$\lambda_{\boldsymbol{\mathcal{X}}} = \ln\left(\left\|\left.\frac{\partial \boldsymbol{\mathcal{F}}}{\partial \boldsymbol{\mathcal{X}}}\right|_{(\boldsymbol{\mathcal{X}}^*, \boldsymbol{\mathcal{Y}}^*)}\right\|\right) \tag{4.14}$$

$$\lambda_{\boldsymbol{\mathcal{Y}}} = \ln\left(\left\|\left.\frac{\partial \boldsymbol{\mathcal{F}}}{\partial \boldsymbol{\mathcal{Y}}}\right|_{(\boldsymbol{\mathcal{X}}^*, \boldsymbol{\mathcal{Y}}^*)}\right\|\right) \tag{4.15}$$

Because both Jacobian matrices play a role in the perturbed targeting problem, these FTLE-inspired quantities serve as candidate metrics to investigate for correlations with measured convergence basin width values. Intuition dictates that larger values of $\lambda_{\boldsymbol{\mathcal{X}}}$ or $\lambda_{\boldsymbol{\mathcal{Y}}}$, reflecting larger growth in the magnitude of constraint vector, are likely to correlate with a smaller region associated with the main convergence basin.

4.5 Perturbation Variable Tradespace

Combined perturbations in position and velocity are frequently of interest to trajectory designers in space flight applications. A single basin width measurement along an associated vector comprised of these dimensionally-dissimilar quantities in perturbation space lacks an intuitive physical interpretation and is of limited use. A trajectory designer may seek to compute the magnitude of a perturbation in position that may be accommodated in combination with a given magnitude of a velocity perturbation. Therefore, the broader tradespace

that describes convergence behavior for combinations of perturbation magnitudes in position and velocity has significant value. Ideally, an analytical or sufficiently-dense numerical representation of the convergence basin would provide this tradespace, defining the boundary of an iteration contour, comparable to a Pareto frontier, that balances the magnitudes of individual position and velocity perturbations for each iteration limit. Unfortunately, this tradespace suffers from the same lack of an analytical representation as the individual position and velocity sub-problems, and a full numerical representation is impractical for rapid analysis. The simple application of PDA to a problem with dissimilar perturbation variables does not provide significant insight, because the principal directions correspond to fixed directions and relative proportions of position and velocity perturbations that represent single points in the tradespace. A new strategy is required to approximate the relationship between allowable perturbations in dissimilar variables.

Analysis of the tradespace for a state perturbation applied at a particular time is begun by decomposing the perturbation variable set, $\boldsymbol{\mathcal{Y}}$, into the subsets $\boldsymbol{\mathcal{Y}}_1$ and $\boldsymbol{\mathcal{Y}}_2$, representing the position and velocity components, respectively. The perturbation Jacobian $\frac{\partial \boldsymbol{\mathcal{F}}}{\partial \boldsymbol{\mathcal{Y}}}$ is decomposed into a block matrix form, i.e.,

$$\frac{\partial \boldsymbol{\mathcal{F}}}{\partial \boldsymbol{\mathcal{Y}}} = \begin{bmatrix} \frac{\partial \boldsymbol{\mathcal{F}}}{\partial \boldsymbol{\mathcal{Y}}_1} & \frac{\partial \boldsymbol{\mathcal{F}}}{\partial \boldsymbol{\mathcal{Y}}_2} \end{bmatrix} \tag{4.16}$$

where, for example, $\boldsymbol{\mathcal{Y}}_1 = \boldsymbol{\rho_0}$ and $\boldsymbol{\mathcal{Y}}_2 = \dot{\boldsymbol{\rho}}_\mathbf{0}$ for a perturbation at some initial time t_0. The block components of Equation (4.16) are expressed in their SVD form as

$$\left.\frac{\partial \boldsymbol{\mathcal{F}}}{\partial \boldsymbol{\mathcal{Y}}_i}\right|_{(\boldsymbol{\mathcal{X}}^*, \boldsymbol{\mathcal{Y}}^*)} = U_i \Sigma_i V_i^T = \begin{bmatrix} \boldsymbol{u_{i,1}} & \dots & \boldsymbol{u_{i,m}} \end{bmatrix} \begin{bmatrix} \sigma_{i,1} & & 0 \\ & \ddots & \\ 0 & & \sigma_{i,k_i} \end{bmatrix} \begin{bmatrix} \boldsymbol{v_{i,1}} & \dots & \boldsymbol{v_{i,p_i}} \end{bmatrix}^T \tag{4.17}$$

where p_i is the length of $\boldsymbol{\mathcal{Y}}_i$ and $k_i = \min\{m, p_i\}$. By convention, the singular values and singular vectors are arranged in descending order of singular value. These block components represent the perturbation Jacobian matrices of the independent position and velocity sub-problems, and the vector $\boldsymbol{v_{i,1}}$ is the dominant singular vector in each sub-problem.

Based on empirical analysis, a heuristic model is introduced to approximate the convergence tradespace in position and velocity perturbations. The dominating features of the

iteration contours that define the tradespace are approximated by interrogating the plane formed by the independent principal directions $\boldsymbol{v_{1,1}}$ and $\boldsymbol{v_{2,1}}$, denoted as the *principal plane*. This approximation reduces the discretization from the full six-dimensional space (i.e., spatial position and velocity) to the discretization of points along the parameterized vector $\boldsymbol{\eta}(s)$, i.e.,

$$\boldsymbol{\eta}(s) = \begin{bmatrix} s\boldsymbol{v}_{1,1} \\ (1-s)\boldsymbol{v}_{2,1} \end{bmatrix}, \qquad s \in [0,1] \tag{4.18}$$

as schematically illustrated in Figure 4.7a. A line search and bisection method similar to

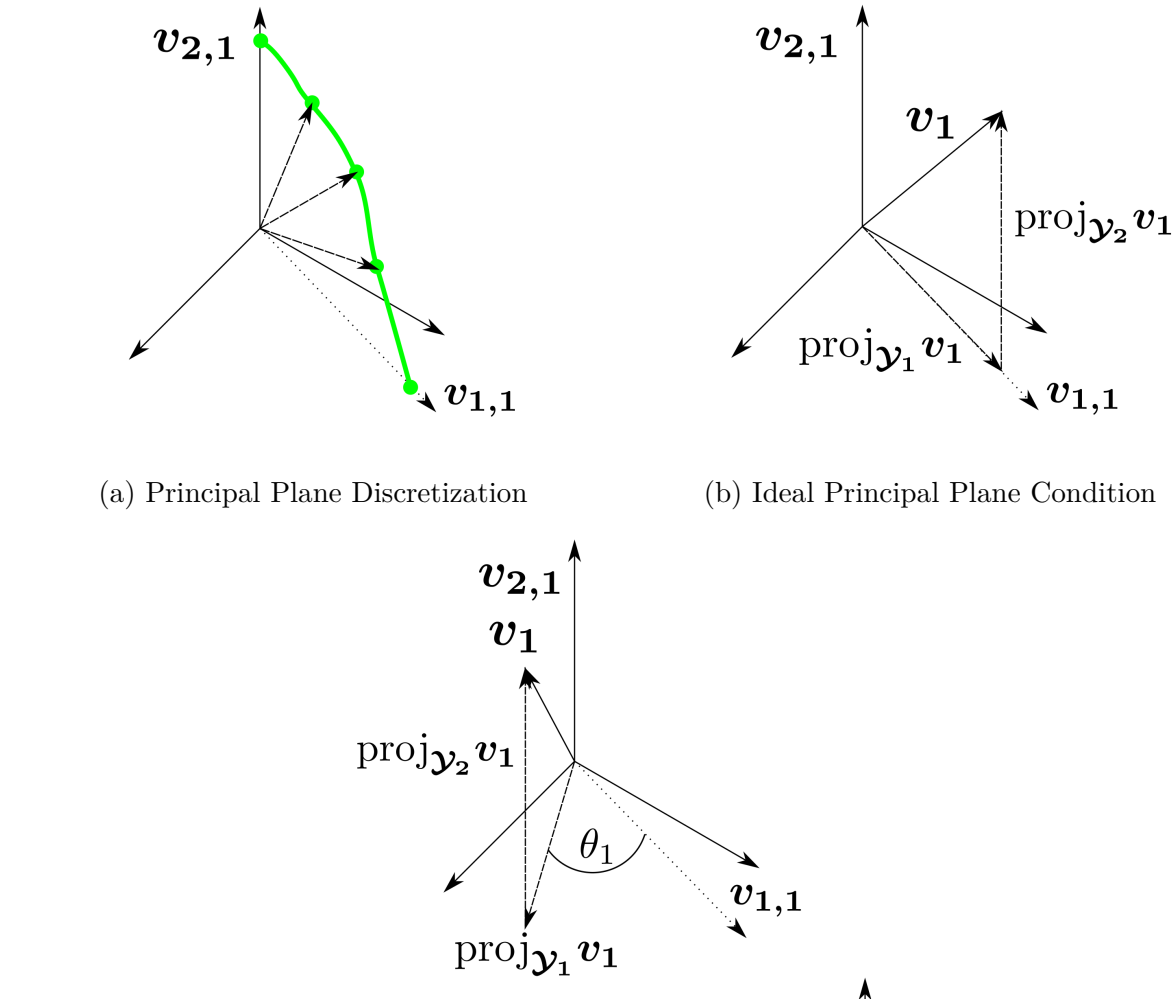

(a) Principal Plane Discretization

(b) Ideal Principal Plane Condition

(c) Principal Plane Projection Angle

Figure 4.7. Principal Plane Tradespace Analysis

that employed in PDA is conducted for each value of the parameter s to explore characterize

convergence behavior in the plane. Approximation of the true tradespace with the measured convergence behavior in the principal plane is supported if the dominant combined and independent principal directions, i.e., $\boldsymbol{v_1}$, $\boldsymbol{v_{1,1}}$, and $\boldsymbol{v_{2,1}}$, lie in a plane.

The principal plane heuristic model assumes the critical features of the tradespace lie in a single plane. With the assumption that the dominant singular vector, $\boldsymbol{v_1}$, corresponds to the critical behavior of the physically-unintuitive combined position and velocity perturbation space, the principal plane model implies the vector $\boldsymbol{v}_1$ is a linear combination of the orthogonal vectors $\boldsymbol{v}_{1,1}$ and $\boldsymbol{v}_{2,1}$, i.e.,

$$\beta \boldsymbol{v_1} = \alpha_1 \begin{bmatrix} \boldsymbol{v_{1,1}} \\ \boldsymbol{0} \end{bmatrix} + \alpha_2 \begin{bmatrix} \boldsymbol{0} \\ \boldsymbol{v_{2,1}} \end{bmatrix} \tag{4.19}$$

A three-dimensional schematic of the three vectors constructing the principal plane is illustrated in Figure 4.7b with $\boldsymbol{\mathcal{Y}}_1$-space in a plane and $\boldsymbol{\mathcal{Y}}_2$-space as the orthogonal vector. In general, the co-planar of the assumption of the principal plane heuristic is not satisfied and, even in the linear system derived from the perturbation Jacobian, these vectors may not lie in a plane, as illustrated in Figure 4.7c. The angles θ_i for each subspace, are defined to measure this deviation, i.e.,

$$\theta_i = \angle \left(\text{proj}_{\boldsymbol{\mathcal{Y}}_i} \boldsymbol{v}_1, \boldsymbol{v}_{i,1} \right) \tag{4.20}$$

where $\angle(\cdot, \cdot)$ is the angle between two vectors and $\text{proj}_{\boldsymbol{\mathcal{Y}}_i}(\cdot)$ is the projection of a vector onto $\boldsymbol{\mathcal{Y}}_i$-space. However, convergence behavior in the principal plane is likely to offer valuable insight into the tradespace when the co-planar assumption is satisfied or very-nearly satisfied, i.e., $\theta_i \approx 0$. At the very least, convergence behavior that is unacceptable in the principal plane is guaranteed to be equally or more unacceptable in a fuller discretization strategy.

The conditions under which the three dominant vectors are co-planar, i.e., $\theta_i = 0$, are determined by assuming $\boldsymbol{v_1}$ is a linear combination of $\boldsymbol{v_{1,1}}$ and $\boldsymbol{v_{2,1}}$. By the properties of the SVD, $\boldsymbol{v_1}$ is an eigenvector of $\frac{\partial \boldsymbol{\mathcal{F}}}{\partial \boldsymbol{\mathcal{Y}}}^T \frac{\partial \boldsymbol{\mathcal{F}}}{\partial \boldsymbol{\mathcal{Y}}}$ with eigenvalue σ_1, implying

$$\sigma_1^2 \begin{bmatrix} \alpha \boldsymbol{v_{1,1}} \\ \boldsymbol{v_{2,1}} \end{bmatrix} = \frac{\partial \boldsymbol{\mathcal{F}}}{\partial \boldsymbol{\mathcal{Y}}}^T \frac{\partial \boldsymbol{\mathcal{F}}}{\partial \boldsymbol{\mathcal{Y}}} \begin{bmatrix} \alpha \boldsymbol{v_{1,1}} \\ \boldsymbol{v_{2,1}} \end{bmatrix} \tag{4.21}$$

where terms are colored red and blue to assist in readability and highlight their association with $\boldsymbol{\mathcal{Y}}_1$ and $\boldsymbol{\mathcal{Y}}_2$, respectively. The expansion of the right side of the equation reveals the necessary conditions such that these dominating principal directions lie in a principal plane, i.e.,

$$\begin{aligned}
\frac{\partial \boldsymbol{\mathcal{F}}}{\partial \boldsymbol{\mathcal{Y}}}^T \frac{\partial \boldsymbol{\mathcal{F}}}{\partial \boldsymbol{\mathcal{Y}}} \begin{bmatrix} \alpha \boldsymbol{v_{1,1}} \\ \boldsymbol{v_{2,1}} \end{bmatrix} &= \begin{bmatrix} \frac{\partial \boldsymbol{\mathcal{F}}}{\partial \boldsymbol{\mathcal{Y}}_1} & \frac{\partial \boldsymbol{\mathcal{F}}}{\partial \boldsymbol{\mathcal{Y}}_2} \end{bmatrix}^T \begin{bmatrix} \frac{\partial \boldsymbol{\mathcal{F}}}{\partial \boldsymbol{\mathcal{Y}}_1} & \frac{\partial \boldsymbol{\mathcal{F}}}{\partial \boldsymbol{\mathcal{Y}}_2} \end{bmatrix} \begin{bmatrix} \alpha \boldsymbol{v_{1,1}} \\ \boldsymbol{v_{2,1}} \end{bmatrix} \\
&= \begin{bmatrix} U_1 \Sigma_1 V_1^T & U_2 \Sigma_2 V_2^T \end{bmatrix}^T \begin{bmatrix} U_1 \Sigma_1 V_1^T & U_2 \Sigma_2 V_2^T \end{bmatrix} \begin{bmatrix} \alpha \boldsymbol{v_{1,1}} \\ \boldsymbol{v_{2,1}} \end{bmatrix} \\
&= \begin{bmatrix} V_1 \Sigma_1^T U_1^T U_1 \Sigma_1 V_1^T & V_1 \Sigma_1^T U_1^T U_2 \Sigma_2 V_2^T \\ V_2 \Sigma_2^T U_2^T U_1 \Sigma_1 V_1^T & V_2 \Sigma_2^T U_2^T U_2 \Sigma_2 V_2^T \end{bmatrix} \begin{bmatrix} \alpha \boldsymbol{v_{1,1}} \\ \boldsymbol{v_{2,1}} \end{bmatrix} \\
&= \begin{bmatrix} V_1 \Sigma_1^T \Sigma_1 V_1^T & V_1 \Sigma_1^T U_1^T U_2 \Sigma_2 V_2^T \\ V_2 \Sigma_2^T U_2^T U_1 \Sigma_1 V_1^T & V_2 \Sigma_2^T \Sigma_2 V_2^T \end{bmatrix} \begin{bmatrix} \alpha \boldsymbol{v_{1,1}} \\ \boldsymbol{v_{2,1}} \end{bmatrix} \\
&= \begin{bmatrix} \alpha V_1 \Sigma_1^T \Sigma_1 V_1^T \boldsymbol{v_{1,1}} + V_1 \Sigma_1^T U_1^T U_2 \Sigma_2 V_2^T \boldsymbol{v_{2,1}} \\ \alpha V_2 \Sigma_2^T U_2^T U_1 \Sigma_1 V_1^T \boldsymbol{v_{1,1}} + V_2 \Sigma_2^T \Sigma_2 V_2^T \boldsymbol{v_{2,1}} \end{bmatrix}
\end{aligned} \tag{4.22}$$

By substituting Equation (4.22) into the left side of Equation (4.21), the top row is expressed as

$$\begin{aligned}
\sigma_1^2 \alpha \boldsymbol{v_{1,1}} &= \alpha V_1 \Sigma_1^T \Sigma_1 V_1^T \boldsymbol{v_{1,1}} + V_1 \Sigma_1^T U_1^T U_2 \Sigma_2 V_2^T \boldsymbol{v_{2,1}} \\
&= (\alpha \sigma_{1,1}^2 + \sigma_{1,1} \sigma_{2,1} \boldsymbol{u_{1,1}}^T \boldsymbol{u_{2,1}}) \boldsymbol{v_{1,1}} \\
&\quad \cdots + \sigma_{2,1} (\sigma_{1,2} \boldsymbol{u_{1,2}}^T \boldsymbol{u_{2,1}} \boldsymbol{v_{1,2}} + \cdots + \sigma_{1,k_1} \boldsymbol{u_{1,k_1}}^T \boldsymbol{u_{2,1}} \boldsymbol{v_{1,k_1}})
\end{aligned} \tag{4.23}$$

where the right side contains components in all $\boldsymbol{v_{1,j}}$ directions. The left side of Equation (4.23) is directed along the vector $\boldsymbol{v_{1,1}}$, but the right side contains components in all $\boldsymbol{v_{1,j}}$ directions. A possible contradiction is evident, because the principal directions $\boldsymbol{v_{1,j}}$ form an orthonormal basis. Therefore, this condition is only true if the constraint principal directions $\boldsymbol{u_{1,1}}$ and $\boldsymbol{u_{2,1}}$ are parallel, or $\boldsymbol{u_{1,1}}^T \boldsymbol{u_{2,1}} = 1$. Additionally, note that these conditions are approximately met if the singular values are dominant, i.e., $\sigma_{1,1}, \sigma_{2,1} \gg \sigma_{1,j}, \sigma_{2,j}$ for $j \neq 1$. The same conditions are implied via an analysis of the bottom row of Equation (4.22).

Two conditions emerge in assessing the assumption that the dominant principal directions share a plane. The angle between the constraint principal directions $\boldsymbol{u_{1,1}}$ and $\boldsymbol{u_{2,1}}$ and the relative magnitudes of the singular values suggest criteria expressed as follows

$$\angle(\boldsymbol{u_{1,1}}, \boldsymbol{u_{2,1}}) \approx 0 \tag{4.24}$$

$$\frac{\sigma_{i,1}}{\sigma_{i,2}} \gg 1 \tag{4.25}$$

that are expected to correlate with $\theta_i \approx 0$. If these conditions are met, the co-planar assumption is reasonable, supporting the use of the principal plane heuristic model to approximate the tradespace. If evidence suggests that the co-planar assumption on the dominant principal directions is not reasonable for a given perturbed targeting problem, the principal plane heuristic model may still provide insight; however, convergence performance may be lower than that measured on the plane.

4.6 Second-Order Basin Analysis

While analysis of the Jacobians in the perturbed targeting problem give some insight into the local structure of the convergence basin for a reference solution, these 1^{st}-order analysis techniques yield theoretically-limited information. Though intuition suggests that large changes in the constraints for relatively small perturbations, implied by large singular values, are likely to result in convergence difficulties, the evidence supporting this idea is not contained in the linear model itself. In fact, if the actual system closely follows the local linear model, a linear differential corrections process has little difficulty computing suitable updates and achieving convergence even for highly-sensitive problems with large degrees of stretching. Difficulties with linear differential corrections strategies arise from the nonlinearity or curvature in the problem that degrade the applicability of the linear model. In principle, a nonlinear targeting problem with a very high degree of linear stretching (i.e., high singular values) but very low curvature should be a better candidate for linear differential corrections than a nonlinear targeting problem with a very low degree of linear stretching (i.e., small singular values) but relatively significant curvature. Therefore, a methodology is introduced

to incorporate 2^{nd}-order effects as a predictor of convergence behavior in perturbed targeting problems.

Various methods exist for computing a measure of nonlinearity in a nonlinear system. Junkins and Singla propose a method for expressing the nonlinearity of a system as the difference between the linear approximations of a nonlinear system at a mean state and a worst-case empirically-sampled state [14], [55]. Park and Scheeres employ sampling to evaluate the worst-case relative contributions of higher-order state transition tensors for uncertainty progagation in complex dynamical regimes [13], [16]. A strategy proposed by Hahn and Edgar employs the linear controllability and observability Grammians evaluated at both the reference state and empirically-sampled points, seeking to link a nonlinearity measure to a particular stable, control-affine system [56]. Avoiding a costly sampling process, Jenson and Scheeres evaluate the local relative contribution of nonlinear terms associated with the local dynamics tensors and state transition tensors of k^{th}-order where each of the k dimensions is length-n through the use of tensor eigenpairs [17]. This investigation seeks to propose a measure of nonlinearity that both avoids empirical sampling by evaluating quantites on the reference solution and relates to a particular perturbed targeting problem instead of the general dynamical flow of the state. The proposed strategy to measure 2^{nd}-order nonlinearity is motivated by a desire to quantify the local rate of change in the design Jacobian with respect to changes in the perturbation variables at the reference solution.

4.6.1 Convergence Basin Metric

The derivation of a 2^{nd}-order metric begins with an observation regarding the typical approach for evaluating the design Jacobian in differential corrections processes. As suggested in the variational equation defining the Newton-Raphson design variable update, expressed in Equation (3.5), the partial derivatives are evaluated along each iteration of the perturbed trajectory rather than the baseline solution. In other words, the design Jacobian $\frac{\partial \boldsymbol{\mathcal{F}}}{\partial \boldsymbol{\mathcal{X}}}$ is evaluated at the current values of the design and perturbation variables $(\boldsymbol{\mathcal{X}}, \boldsymbol{\mathcal{Y}})$ in contrast

to the values of the baseline solution $(\boldsymbol{\mathcal{X}}^*, \boldsymbol{\mathcal{Y}}^*)$. With terms evaluated at both $(\boldsymbol{\mathcal{X}}, \boldsymbol{\mathcal{Y}})$ and $(\boldsymbol{\mathcal{X}}^*, \boldsymbol{\mathcal{Y}}^*)$, a matrix quantity,

$$\Psi = \left.\frac{\partial \boldsymbol{\mathcal{F}}}{\partial \boldsymbol{\mathcal{X}}}\right|^{-1}_{(\boldsymbol{\mathcal{X}}^*, \boldsymbol{\mathcal{Y}}^*)} \left.\frac{\partial \boldsymbol{\mathcal{F}}}{\partial \boldsymbol{\mathcal{X}}}\right|_{(\boldsymbol{\mathcal{X}}, \boldsymbol{\mathcal{Y}})} \tag{4.26}$$

and an associated scalar value,

$$\psi = \max\{\sigma_{\max}(\Psi), \sigma_{\min}(\Psi)^{-1}\} \tag{4.27}$$

are defined where $\sigma_{\max}$ and $\sigma_{\min}$ denote the maximum and minimum singular values, respectively. For scenarios with under-constrained targeting problems where the inverse of the rank-k matrix does not exist, the pseudo-inverse is used instead, and the k^{th}-smallest singular value is substituted for the minimum. These quantities are employed to develop a measure of similarity between the design Jacobian matrices evaluated at the two points. Assuming continuity of the derivatives in the neighborhood of the solution, the matrix Ψ approaches the identity matrix as the perturbed trajectory is brought arbitrarily close to the baseline solution, i.e.,

$$\lim_{(\boldsymbol{\mathcal{X}}, \boldsymbol{\mathcal{Y}}) \to (\boldsymbol{\mathcal{X}}^*, \boldsymbol{\mathcal{Y}}^*)} \Psi = I, \qquad \lim_{(\boldsymbol{\mathcal{X}}, \boldsymbol{\mathcal{Y}}) \to (\boldsymbol{\mathcal{X}}^*, \boldsymbol{\mathcal{Y}}^*)} \psi = 1 \tag{4.28}$$

As the value of ψ increases from 1, a larger difference exists between the linear models associated with the design Jacobian matrices evaluated at the baseline solution and the perturbed trajectory, reflecting the effect of nonlinear terms in the problem.

A sample scenario is introduced to visualize the correlation between the features in the contour map of number of required iterations and the scalar ψ across the perturbation space for a perturbed targeting problem. In this scenario, the reference solution is generated from a segment along a planar Lyapunov orbit about the Earth-Moon L_2 point in the CRTBP. The targeting problem is formulated to constrain the position at the final time to its reference value on the periodic orbit, and the design variables consist of the planar velocity components at the initial time. For simplicity, the perturbation variables are defined as the set of design

variables, allowing the map of the perturbation space to function as a visualization of the design variable space as well. In mathematical notation, the sample perturbed targeting problem is formulated as

$$\boldsymbol{\mathcal{F}} = \boldsymbol{\rho}^{-}(t_f) - \boldsymbol{\rho_d} \ , \ \boldsymbol{\mathcal{X}} = \dot{\boldsymbol{\rho}}^{+}(t_0) \ , \ \boldsymbol{\mathcal{Y}} = \dot{\boldsymbol{\rho}}^{+}(t_0) \tag{4.29}$$

From the full targeting simulations in a discretized grid across the perturbation space, the iterations required for convergence and the quantity ψ, evaluated at each initial point, are plotted in Figures 4.8a and 4.8b, respectively. In these plots, the reference solution is rep-

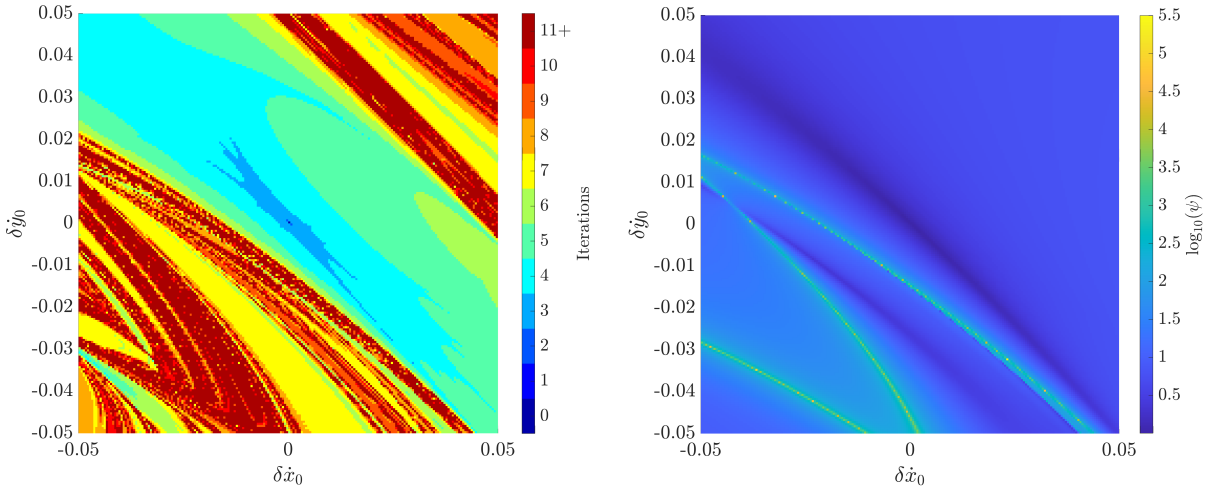

(a) Iterations in Perturbation Space

(b) ψ in Perturbation Space

Figure 4.8. Sample Correlation Between ψ and Convergence Basin Features

resented by the origin. A trough in ψ, passing through the reference solution, is visible in Figure 4.8b that aligns with the region of rapid convergence in Figure 4.8a. In the lower-left corner, structural ridges defined by elevated values of ψ correspond to the transition into chaotic convergence behavior. In the upper-right, the transition to chaos is not clearly represented in the map of ψ; however, these structures in the iteration plots appear to relate to the iterative nature of a Newton-Raphson corrections process. A small sampling of perturbations that originate across the upper-right boundary cross the lower-left boundary on subsequent iterations. From this example, *boundaries* associated with the changing design Jacobian matrix and *pseudo-boundaries* associated with the iterative update process are visible as key

features of convergence basins in perturbed targeting problems. The quantity ψ, related to the relative similarity of the design Jacobian matrices at the reference solution and across the perturbation space, appears to correlate with some visible boundaries in the convergence basin. Though ψ is useful in characterizing the convergence basin, the computation of the quantity still requires the evaluation of the design Jacobian at numerous discrete points in the perturbation space.

In pursuit of a metric that is evaluated solely on the reference solution, quantification of the local change in ψ near the reference solution is useful in characterizing the local relative nonlinearity in the problem. Through a Taylor series expansion about the reference solution, the design Jacobian along the perturbed trajectory is approximated as

$$\left.\frac{\partial \boldsymbol{\mathcal{F}}}{\partial \boldsymbol{\mathcal{X}}}\right|_{(\boldsymbol{\mathcal{X}},\boldsymbol{\mathcal{Y}})} \approx \left.\frac{\partial \boldsymbol{\mathcal{F}}}{\partial \boldsymbol{\mathcal{X}}}\right|_{(\boldsymbol{\mathcal{X}}^*,\boldsymbol{\mathcal{Y}}^*)} + \left.\frac{\partial^2 \boldsymbol{\mathcal{F}}}{\partial \boldsymbol{\mathcal{X}}\partial \boldsymbol{\mathcal{Y}}}\right|_{(\boldsymbol{\mathcal{X}}^*,\boldsymbol{\mathcal{Y}}^*)} (\delta\boldsymbol{\mathcal{Y}} \otimes I) \tag{4.30}$$

where $\otimes$ is the Kronecker product. In this formulation, the 2^{nd}-order partial derivative term is reformatted, or flattened, from a $m \times n \times p$ tensor into a $m \times (np)$ matrix, i.e.,

$$\frac{\partial^2 \boldsymbol{\mathcal{F}}}{\partial \boldsymbol{\mathcal{X}}\partial \boldsymbol{\mathcal{Y}}} = \begin{bmatrix} \frac{\partial^2 \boldsymbol{\mathcal{F}}}{\partial \boldsymbol{\mathcal{X}}\partial \mathcal{Y}_1} & \frac{\partial^2 \boldsymbol{\mathcal{F}}}{\partial \boldsymbol{\mathcal{X}}\partial \mathcal{Y}_2} & \cdots & \frac{\partial^2 \boldsymbol{\mathcal{F}}}{\partial \boldsymbol{\mathcal{X}}\partial \mathcal{Y}_p} \end{bmatrix} \tag{4.31}$$

where p is the number of perturbation variables in $\boldsymbol{\mathcal{Y}}$ [57], [58]. Substituting the expansion of the design Jacobian into Equation (4.26) yields a local approximation of the similarity matrix Ψ, i.e.,

$$\Psi \approx \left.\frac{\partial \boldsymbol{\mathcal{F}}}{\partial \boldsymbol{\mathcal{X}}}\right|^{-1}_{(\boldsymbol{\mathcal{X}}^*,\boldsymbol{\mathcal{Y}}^*)} \left(\left.\frac{\partial \boldsymbol{\mathcal{F}}}{\partial \boldsymbol{\mathcal{X}}}\right|_{(\boldsymbol{\mathcal{X}}^*,\boldsymbol{\mathcal{Y}}^*)} + \left.\frac{\partial^2 \boldsymbol{\mathcal{F}}}{\partial \boldsymbol{\mathcal{X}}\partial \boldsymbol{\mathcal{Y}}}\right|_{(\boldsymbol{\mathcal{X}}^*,\boldsymbol{\mathcal{Y}}^*)} (\delta\boldsymbol{\mathcal{Y}} \otimes I) \right) \tag{4.32}$$

Distribution of the inverse term allows the simplification of Equation (4.32), i.e.,

$$\Psi \approx I + \left.\frac{\partial \boldsymbol{\mathcal{F}}}{\partial \boldsymbol{\mathcal{X}}}\right|^{-1}_{(\boldsymbol{\mathcal{X}}^*,\boldsymbol{\mathcal{Y}}^*)} \left.\frac{\partial^2 \boldsymbol{\mathcal{F}}}{\partial \boldsymbol{\mathcal{X}}\partial \boldsymbol{\mathcal{Y}}}\right|_{(\boldsymbol{\mathcal{X}}^*,\boldsymbol{\mathcal{Y}}^*)} (\delta\boldsymbol{\mathcal{Y}} \otimes I) \tag{4.33}$$

Thus, the deviation of this quantity from identity, denoted the *normalized change in the Jacobian*, reduces to

$$\Delta\Psi = \left.\frac{\partial \boldsymbol{\mathcal{F}}}{\partial \boldsymbol{\mathcal{X}}}\right|^{-1}_{(\boldsymbol{\mathcal{X}}^*,\boldsymbol{\mathcal{Y}}^*)} \left.\frac{\partial^2 \boldsymbol{\mathcal{F}}}{\partial \boldsymbol{\mathcal{X}}\partial \boldsymbol{\mathcal{Y}}}\right|_{(\boldsymbol{\mathcal{X}}^*,\boldsymbol{\mathcal{Y}}^*)} (\delta\boldsymbol{\mathcal{Y}} \otimes I) \tag{4.34}$$

and is a function of the partial derivatives evaluated at the reference solution $(\boldsymbol{\mathcal{X}}^*, \boldsymbol{\mathcal{Y}}^*)$ and the perturbation $\delta\boldsymbol{\mathcal{Y}}$. Intuitively, if a small normalized change in the Jacobian is desired for a large perturbation magnitude, the contribution from the expression $\left.\frac{\partial \boldsymbol{\mathcal{F}}}{\partial \boldsymbol{\mathcal{X}}}\right|^{-1}_{(\boldsymbol{\mathcal{X}}^*,\boldsymbol{\mathcal{Y}}^*)} \left.\frac{\partial^2 \boldsymbol{\mathcal{F}}}{\partial \boldsymbol{\mathcal{X}}\partial \boldsymbol{\mathcal{Y}}}\right|_{(\boldsymbol{\mathcal{X}}^*,\boldsymbol{\mathcal{Y}}^*)}$, denoted the *normalized rate of change in the design Jacobian*, should be as small as possible. Therefore, the *basin metric*, denoted γ, is then defined as

$$\gamma = \left\| \left.\frac{\partial \boldsymbol{\mathcal{F}}}{\partial \boldsymbol{\mathcal{X}}}\right|^{-P}_{(\boldsymbol{\mathcal{X}}^*,\boldsymbol{\mathcal{Y}}^*)} \left.\frac{\partial^2 \boldsymbol{\mathcal{F}}}{\partial \boldsymbol{\mathcal{X}}\partial \boldsymbol{\mathcal{Y}}}\right|_{(\boldsymbol{\mathcal{X}}^*,\boldsymbol{\mathcal{Y}}^*)} \right\|^{-1} \tag{4.35}$$

written in a general form with the pseudo-inverse. Representing a more gradual relative change in the design Jacobian across the perturbation space, larger basin metric values are expected to correlate with the larger measured values of basin width. Values of γ are straightforward to compute via the l_2-norm of the flattened $n \times (np)$ matrix; however, this approach corresponds to a singular vector of length np instead of the perturbation vector of length p, prohibiting a physical interpretation of the associated singular vector. Therefore, higher-order tensor analysis methods are useful in extracting additional information about the normalized change in the Jacobian in perturbation space.

4.6.2 Higher-Order Singular Values and Singular Vectors

A variety of methods exist to extend the SVD from matrices to tensors of higher order. Though none of the existing higher-order analogs preserve all of the properties of the matrix SVD, many methods select critical properties of interest, e.g., lower-rank tensor approximation or decomposition into a core tensor and multiple matrices [52], [59]–[61]. A theory of singular values and singular vectors for higher-order tensors proposed by Lim provides a particularly useful framework for the analysis of the normalized change in the Jacobian in perturbation space [61]. This extended theory of singular values and singular vectors yields

an improved method for computing the basin metric γ as well as a direction in perturbation space associated with the largest normalized change in the Jacobian.

The definition of higher-order singular values and singular vectors begins with an examination of the Rayleigh quotient, $\frac{\boldsymbol{x}^T A \boldsymbol{x}}{\|\boldsymbol{x}\|^2}$, for a symmetric matrix, A. The eigenvalues and eigenvectors of A are the critical values and critical points, respectively, of a constrained optimization problem expressed as

$$L(\boldsymbol{x}, \lambda) = \boldsymbol{x}^T A \boldsymbol{x} - \lambda(\|\boldsymbol{x}\|^2 - 1) \tag{4.36}$$

where $\|\cdot\|$ represents the l_2-norm and λ is a Lagrange multiplier. In an analogous manner, the singular values and singular vectors of an—in general—non-symmetric matrix $A \in \mathbb{R}^{m \times n}$ are the critical values and critical points of the constrained optimization problem expressed

$$L(\boldsymbol{x}, \boldsymbol{y}, \sigma) = \boldsymbol{x}^T A \boldsymbol{y} - \sigma(\|\boldsymbol{x}\|\|\boldsymbol{y}\| - 1) \tag{4.37}$$

It is worth reinforcing that, unlike the assumptions for Equation (4.36), A can be any real matrix of size $m \times n$. The critical values and points, i.e., solutions for which $\nabla L(\boldsymbol{x_c}, \boldsymbol{y_c}, \sigma_c) = 0$, satisfy the expressions

$$\sigma_c \boldsymbol{x_c} = A \boldsymbol{y_c} \ , \ \frac{\boldsymbol{x_c}}{\|\boldsymbol{x_c}\|} = \boldsymbol{u} \ , \ \frac{\boldsymbol{y_c}}{\|\boldsymbol{y_c}\|} = \boldsymbol{v} \tag{4.38}$$

which is equivalent to the relationship between singular values and singular vectors of a matrix in Equation (4.9). With this definition, the important property Lim seeks to preserve in a higher-order extension is that the singular values and singular vectors reflect the critical points for the scaling magnitude and directions of the higher-order tensor [61].

Though the definition of singular values and singular vectors is generalized to tensors of an arbitrarily large degree under l_k-norms with arbitrary integer values of k [61], the particular extension of the SVD to a tensor of 3$^{\text{rd}}$-order (i.e., $A \in \mathbb{R}^{m \times n \times p}$) under the l_2-norm provides benefits to the analysis of a perturbed targeting problem. The 3$^{\text{rd}}$-order tensor A is comprised of elements a_{j_1, j_2, j_3} where $j_1 = 1, \ldots, m$, $j_2 = 1, \ldots, n$, and $j_3 = 1, \ldots, p$. To

reflect "multiplication on 3 sides" [61], a multilinear functional $A(\boldsymbol{x_1}, \boldsymbol{x_2}, \boldsymbol{x_3})$ is defined and expressed mathematically as

$$A(\boldsymbol{x_1}, \boldsymbol{x_2}, \boldsymbol{x_3}) = \sum_{j_1=1}^{m} \sum_{j_2=1}^{n} \sum_{j_3=1}^{p} a_{j_1,j_2,j_3} x_{j_1}^{(1)} x_{j_2}^{(2)} x_{j_3}^{(3)} \tag{4.39}$$

where the superscript (k) represents multiplication of the vector across the k^{th}-dimension. The singular values and singular vectors are defined as the critical values and points associated with the quotient $\frac{A(\boldsymbol{x_1},\boldsymbol{x_2},\boldsymbol{x_3})}{\|\boldsymbol{x_1}\|\|\boldsymbol{x_2}\|\|\boldsymbol{x_3}\|}$ and are the solution to a constrained optimization problem formulated as

$$L(\boldsymbol{x_1}, \boldsymbol{x_2}, \boldsymbol{x_3}, \sigma) = A(\boldsymbol{x_1}, \boldsymbol{x_2}, \boldsymbol{x_3}) - \sigma(\|\boldsymbol{x_1}\|\|\boldsymbol{x_2}\|\|\boldsymbol{x_3}\| - 1) \tag{4.40}$$

The critical values and points of this optimization problem satisfy the expressions

$$\begin{aligned} A(I_m, \boldsymbol{x_2}, \boldsymbol{x_3}) &= \sigma \boldsymbol{x_1} \\ A(\boldsymbol{x_1}, I_n, \boldsymbol{x_3}) &= \sigma \boldsymbol{x_2} \\ A(\boldsymbol{x_1}, \boldsymbol{x_2}, I_p) &= \sigma \boldsymbol{x_3} \end{aligned} \tag{4.41}$$

$$\|\boldsymbol{x_1}\| = \|\boldsymbol{x_2}\| = \|\boldsymbol{x_3}\| = 1 \tag{4.42}$$

which are analogous to the conditions in Equations (4.9) and (4.38). The solution for $\boldsymbol{x_i}$ is denoted the *mode-i singular vector*. Consistent with the matrix definition, the l_2-norm of A is then equal to the largest singular value, i.e.,

$$\|A\| = \sigma_{\max}(A) \tag{4.43}$$

This theory of singular values and singular vectors is directly applicable to the problem of determining the local maximum normalized change in the Jacobian in perturbation space for a particular solution to a perturbed targeting problem.

With a higher-order definition of singular values, the basin metric, expressed in Equation (4.35), is reformulated in terms of its *tensor basin metric* analog, i.e.,

$$\gamma' = \sigma_{\max}\left(\left.\frac{\partial \boldsymbol{\mathcal{F}}}{\partial \boldsymbol{\mathcal{X}}}\right|^{-P}_{(\boldsymbol{\mathcal{X}}^*,\boldsymbol{\mathcal{Y}}^*)} \left.\frac{\partial^2 \boldsymbol{\mathcal{F}}}{\partial \boldsymbol{\mathcal{X}}\partial \boldsymbol{\mathcal{Y}}}\right|_{(\boldsymbol{\mathcal{X}}^*,\boldsymbol{\mathcal{Y}}^*)}\right)^{-1} \tag{4.44}$$

where the argument is reformatted as a 3rd-order tensor in $(n \times n \times p)$-form. This quantity is interpreted as maximum norm of the normalized change in Jacobian, i.e., $\|\Delta\Psi\|$, that is achievable by a perturbation $\delta\boldsymbol{\mathcal{Y}}$ of unit length. The mode-3 singular vector associated with the largest singular value, $\boldsymbol{v'}$, represents the direction of this perturbation. In this investigation, the tensor basin metric γ' and the mode-3 singular vector $\boldsymbol{v'}$ are computed via the `fmincon` function in MATLAB as the solution to the constrained optimization problem expressed in "flattened" form as

$$\begin{aligned} \text{maximize: } & \left\| \left.\frac{\partial \boldsymbol{\mathcal{F}}}{\partial \boldsymbol{\mathcal{X}}}\right|^{-P}_{(\boldsymbol{\mathcal{X}}^*,\boldsymbol{\mathcal{Y}}^*)} \left.\frac{\partial^2 \boldsymbol{\mathcal{F}}}{\partial \boldsymbol{\mathcal{X}}\partial \boldsymbol{\mathcal{Y}}}\right|_{(\boldsymbol{\mathcal{X}}^*,\boldsymbol{\mathcal{Y}}^*)} (\boldsymbol{v'} \otimes I_n) \right\| \\ \text{subject to: } & \|\boldsymbol{v'}\| - 1 = 0 \end{aligned} \tag{4.45}$$

which is equivalent to the formulation in Equation (4.40). The information provided by the mode-3 singular vector $\boldsymbol{v'}$ makes it useful as an additional 2nd-order principal direction to augment the 1st-order PDA method for approximating the convergence basin width.

4.6.3 Computing Second-Order Partial Derivatives

As with the computation of 1st-order partial derivatives, both analytical and numerical methods exist for computing the 2nd-order partial derivatives in a perturbed targeting problem. When analytical expressions for these quantities or their time derivatives are readily available, the direct computation or numerical integration of these derivatives is an expedient strategy. However, when the expressions are impractical to derive or induce numerical difficulties, central differencing facilitates a straightforward computation strategy at the expense of additional function calls and numerical trajectory propagations.

Where analytic 2nd-order derivatives of the equations of motion exist and are convenient to derive, such as in the CRTBP, the higher-order state transition tensors are numerically integrated in time along the reference trajectory. To derive the relationship between the 2nd-order state transition tensor and its time-derivative, notation is borrowed in part from Majji, Junkins, and Turner as well as Park and Scheeres [16], [57]. For a dynamical system defined as in Equation (3.29), the time-derivative of the STM is rewritten from Equation (3.32) in an element-wise form, i.e.,

$$\frac{\mathrm{d}\Phi_{i,a}}{\mathrm{d}t} = \sum_{\alpha=1}^{n} \frac{\partial \boldsymbol{f}_i}{\partial \boldsymbol{x}_\alpha} \Phi_{\alpha,a} \tag{4.46}$$

where the subscripts denote the indices in ascending modal direction. For example, $\Phi_{2,1}$ dictates the element in the 2nd place for mode-1 (i.e., the 2nd row) and the 1st place for mode-2 (i.e., the 1st column). The 2nd-order state transition tensor is then governed by the ordinary differential equation given by

$$\frac{\mathrm{d}\Phi_{i,ab}}{\mathrm{d}t} = \sum_{\alpha=1}^{n} \left(\frac{\partial \boldsymbol{f}_i}{\partial \boldsymbol{x}_\alpha} \Phi_{\alpha,ab} + \sum_{\beta=1}^{n} \frac{\partial^2 \boldsymbol{f}_i}{\partial \boldsymbol{x}_\alpha \partial \boldsymbol{x}_\beta} \Phi_{\alpha,a} \Phi_{\beta,b} \right) \tag{4.47}$$

and is numerically integrated with the initial condition $\Phi_{i,ab}(t_0) = 0$. Note that the state and STM are required to integrate this differential equation, so the state and state transition tensor histories are integrated together along the trajectory.

Central differencing is an alternative method to compute higher-order partial derivatives to characterize a perturbed targeting problem. The direct central differencing of the 1st-order partial derivative is one strategy for computing the 2nd-order derivative, i.e.,

$$\left. \frac{\partial^2 \boldsymbol{\mathcal{F}}}{\partial \mathcal{X}_i \partial \mathcal{Y}_j} \right|_{(\boldsymbol{\mathcal{X}}, \boldsymbol{\mathcal{Y}})} = \frac{\frac{\partial \boldsymbol{\mathcal{F}}}{\partial \mathcal{X}_i}(\boldsymbol{\mathcal{X}}, \boldsymbol{\mathcal{Y}} + h\boldsymbol{e_j}) - \frac{\partial \boldsymbol{\mathcal{F}}}{\partial \mathcal{X}_i}(\boldsymbol{\mathcal{X}}, \boldsymbol{\mathcal{Y}} - h\boldsymbol{e_j})}{2h} \tag{4.48}$$

where h is a small step size and $\boldsymbol{e_j}$ is a vector with one in the j^{th}-place and zeros elsewhere. Alternatively, the 2^{nd}-order partial derivatives are computed directly from function evaluations via

$$\left.\frac{\partial^2 \boldsymbol{\mathcal{F}}}{\partial \mathcal{X}_i \partial \mathcal{Y}_j}\right|_{(\boldsymbol{\mathcal{X}},\boldsymbol{\mathcal{Y}})} = \frac{\begin{array}{c}\boldsymbol{\mathcal{F}}(\boldsymbol{\mathcal{X}} + h\boldsymbol{e_i}, \boldsymbol{\mathcal{Y}} + h\boldsymbol{e_i}) - \boldsymbol{\mathcal{F}}(\boldsymbol{\mathcal{X}} - h\boldsymbol{e_i}, \boldsymbol{\mathcal{Y}} + h\boldsymbol{e_i}) \\ - \boldsymbol{\mathcal{F}}(\boldsymbol{\mathcal{X}} + h\boldsymbol{e_i}, \boldsymbol{\mathcal{Y}} - h\boldsymbol{e_i}) + \boldsymbol{\mathcal{F}}(\boldsymbol{\mathcal{X}} - h\boldsymbol{e_i}, \boldsymbol{\mathcal{Y}} - h\boldsymbol{e_i})\end{array}}{4h^2} \tag{4.49}$$

While the central differencing methods are straightforward to implement, computation with very small values of h is subject to sources of numerical error associated with catastrophic cancellation and loss of significance [21]. Therefore, care is required to ensure the computed partial derivatives yield meaningful information about the system.

4.7 Effects of Constraint Scaling

Frequently, scale factors are applied to improve the numerical conditioning of the constraints in a targeting problem. The use of non-dimensional state variable quantities in a set of constraints are one common application of this practice. The scaling of the constraint vector is also potentially advantageous with the introduction of dimensional quantities or quantities derived from the states, e.g., flight path angle relative to a primary body measured in degrees, that may produce a mismatch in the order of magnitudes of constraint values and partial derivatives. Therefore, an understanding of the effects of constraint scaling on the computed design variable update and the characterization strategies is of interest.

In the Newton-Raphson update process outlined in Equations (3.6) and (3.17), the computation of the design variable update is unaffected by scaling of the constraints. To demonstrate this property, a scaled constraint vector is introduced as

$$\bar{\boldsymbol{\mathcal{F}}} = S_{\boldsymbol{\mathcal{F}}} \boldsymbol{\mathcal{F}} \tag{4.50}$$

where $S_{\boldsymbol{\mathcal{F}}}$ is a square $m \times m$ matrix with positive entries on the main diagonal and zeros elsewhere. The partial derivatives with respect to the design variables $\boldsymbol{\mathcal{X}}$ and the perturbation variables $\boldsymbol{\mathcal{Y}}$ are given by

$$\frac{\partial \bar{\boldsymbol{\mathcal{F}}}}{\partial \boldsymbol{\mathcal{X}}} = S_{\boldsymbol{\mathcal{F}}} \frac{\partial \boldsymbol{\mathcal{F}}}{\partial \boldsymbol{\mathcal{X}}} \tag{4.51}$$

$$\frac{\partial \bar{\boldsymbol{\mathcal{F}}}}{\partial \boldsymbol{\mathcal{Y}}} = S_{\boldsymbol{\mathcal{F}}} \frac{\partial \boldsymbol{\mathcal{F}}}{\partial \boldsymbol{\mathcal{Y}}} \tag{4.52}$$

and a similar procedure produces scaled partial derivatives of higher order. From Equation (3.6), the design variable update $\delta\boldsymbol{\mathcal{X}}$ in a fully-constrained corrections problem is computed via

$$\begin{aligned}
\delta\bar{\boldsymbol{\mathcal{X}}} &= \left.\frac{\partial \bar{\boldsymbol{\mathcal{F}}}}{\partial \boldsymbol{\mathcal{X}}}\right|^{-1}_{(\boldsymbol{\mathcal{X}},\boldsymbol{\mathcal{Y}})} \left.\bar{\boldsymbol{\mathcal{F}}}\right|_{(\boldsymbol{\mathcal{X}},\boldsymbol{\mathcal{Y}})} \\
&= \left(S_{\boldsymbol{\mathcal{F}}} \left.\frac{\partial \boldsymbol{\mathcal{F}}}{\partial \boldsymbol{\mathcal{X}}}\right|_{(\boldsymbol{\mathcal{X}},\boldsymbol{\mathcal{Y}})} \right)^{-1} \left. S_{\boldsymbol{\mathcal{F}}} \boldsymbol{\mathcal{F}} \right|_{(\boldsymbol{\mathcal{X}},\boldsymbol{\mathcal{Y}})} \\
&= \left.\frac{\partial \boldsymbol{\mathcal{F}}}{\partial \boldsymbol{\mathcal{X}}}\right|^{-1}_{(\boldsymbol{\mathcal{X}},\boldsymbol{\mathcal{Y}})} S^{-1}_{\boldsymbol{\mathcal{F}}} \left. S_{\boldsymbol{\mathcal{F}}} \boldsymbol{\mathcal{F}} \right|_{(\boldsymbol{\mathcal{X}},\boldsymbol{\mathcal{Y}})} \\
&= \left.\frac{\partial \boldsymbol{\mathcal{F}}}{\partial \boldsymbol{\mathcal{X}}}\right|^{-1}_{(\boldsymbol{\mathcal{X}},\boldsymbol{\mathcal{Y}})} \left. \boldsymbol{\mathcal{F}} \right|_{(\boldsymbol{\mathcal{X}},\boldsymbol{\mathcal{Y}})} \\
&= \delta\boldsymbol{\mathcal{X}}
\end{aligned} \tag{4.53}$$

Similarly, the design variable update is demonstrated to be independent of constraint scaling in an under-constrained problem by observing

$$\begin{aligned}
\delta\bar{\boldsymbol{\mathcal{X}}} &= \left.\frac{\partial \bar{\boldsymbol{\mathcal{F}}}}{\partial \boldsymbol{\mathcal{X}}}\right|^{T}_{(\boldsymbol{\mathcal{X}},\boldsymbol{\mathcal{Y}})} \left(\left.\frac{\partial \bar{\boldsymbol{\mathcal{F}}}}{\partial \boldsymbol{\mathcal{X}}}\right|_{(\boldsymbol{\mathcal{X}},\boldsymbol{\mathcal{Y}})} \left.\frac{\partial \bar{\boldsymbol{\mathcal{F}}}}{\partial \boldsymbol{\mathcal{X}}}\right|^{T}_{(\boldsymbol{\mathcal{X}},\boldsymbol{\mathcal{Y}})} \right) \left.\bar{\boldsymbol{\mathcal{F}}}\right|_{(\boldsymbol{\mathcal{X}},\boldsymbol{\mathcal{Y}})} \\
&= \left.\frac{\partial \boldsymbol{\mathcal{F}}}{\partial \boldsymbol{\mathcal{X}}}\right|^{T}_{(\boldsymbol{\mathcal{X}},\boldsymbol{\mathcal{Y}})} S^{T}_{\boldsymbol{\mathcal{F}}} \left(S_{\boldsymbol{\mathcal{F}}} \left.\frac{\partial \boldsymbol{\mathcal{F}}}{\partial \boldsymbol{\mathcal{X}}}\right|_{(\boldsymbol{\mathcal{X}},\boldsymbol{\mathcal{Y}})} \left.\frac{\partial \boldsymbol{\mathcal{F}}}{\partial \boldsymbol{\mathcal{X}}}\right|^{T}_{(\boldsymbol{\mathcal{X}},\boldsymbol{\mathcal{Y}})} S^{T}_{\boldsymbol{\mathcal{F}}} \right)^{-1} \left. S_{\boldsymbol{\mathcal{F}}} \boldsymbol{\mathcal{F}} \right|_{(\boldsymbol{\mathcal{X}},\boldsymbol{\mathcal{Y}})} \\
&= \left.\frac{\partial \boldsymbol{\mathcal{F}}}{\partial \boldsymbol{\mathcal{X}}}\right|^{T}_{(\boldsymbol{\mathcal{X}},\boldsymbol{\mathcal{Y}})} S^{T}_{\boldsymbol{\mathcal{F}}} S^{-T}_{\boldsymbol{\mathcal{F}}} \left(\left.\frac{\partial \boldsymbol{\mathcal{F}}}{\partial \boldsymbol{\mathcal{X}}}\right|_{(\boldsymbol{\mathcal{X}},\boldsymbol{\mathcal{Y}})} \left.\frac{\partial \boldsymbol{\mathcal{F}}}{\partial \boldsymbol{\mathcal{X}}}\right|^{T}_{(\boldsymbol{\mathcal{X}},\boldsymbol{\mathcal{Y}})} \right)^{-1} S^{-1}_{F} \left. S_{\boldsymbol{\mathcal{F}}} \boldsymbol{\mathcal{F}} \right|_{(\boldsymbol{\mathcal{X}},\boldsymbol{\mathcal{Y}})} \\
&= \left.\frac{\partial \boldsymbol{\mathcal{F}}}{\partial \boldsymbol{\mathcal{X}}}\right|^{T}_{(\boldsymbol{\mathcal{X}},\boldsymbol{\mathcal{Y}})} \left(\left.\frac{\partial \boldsymbol{\mathcal{F}}}{\partial \boldsymbol{\mathcal{X}}}\right|_{(\boldsymbol{\mathcal{X}},\boldsymbol{\mathcal{Y}})} \left.\frac{\partial \boldsymbol{\mathcal{F}}}{\partial \boldsymbol{\mathcal{X}}}\right|^{T}_{(\boldsymbol{\mathcal{X}},\boldsymbol{\mathcal{Y}})} \right)^{-1} \left. \boldsymbol{\mathcal{F}} \right|_{(\boldsymbol{\mathcal{X}},\boldsymbol{\mathcal{Y}})} \\
&= \delta\boldsymbol{\mathcal{X}}
\end{aligned} \tag{4.54}$$

Neglecting numerical issues arising from a poorly-conditioned problem, the design variable update is unaffected by the constraint scaling. Therefore, the form of the convergence basin remains unchanged; however, the number of iterations required to converge from each perturbed point to a solution increases or decreases depending on the new relative magnitude of the convergence tolerance.

Though the form of the convergence basin remains unchanged in $\boldsymbol{\mathcal{Y}}$-space, the right singular vectors of $\frac{\partial \boldsymbol{\mathcal{F}}}{\partial \boldsymbol{\mathcal{Y}}}\Big|_{(\boldsymbol{\mathcal{X}}^*, \boldsymbol{\mathcal{Y}}^*)}$ employed in the PDA strategy and their associated singular values change when the constraints are scaled. Though the right singular vectors remain orthogonal as a property of the SVD, the vectors are collectively rotated in the perturbation space as the constraint scale factors evolve. To illustrate this evolution in the singular values and singular vectors, the sample targeting problem along an L_2 Lyapunov orbit in the Earth-Moon system, formulated in Equation (4.29), is re-examined with the constraint scaling matrix $S_{\boldsymbol{\mathcal{F}}}$, expressed

$$S_{\boldsymbol{\mathcal{F}}}(\xi) = \begin{bmatrix} 1 & 0 \\ 0 & \xi \end{bmatrix} \tag{4.55}$$

as a function of the parameter ξ. For the scaled perturbation Jacobian matrix, $\frac{\partial \bar{\boldsymbol{\mathcal{F}}}}{\partial \boldsymbol{\mathcal{Y}}}\Big|_{(\boldsymbol{\mathcal{X}}^*, \boldsymbol{\mathcal{Y}}^*)}$, the angular change in the dominant right singular vector $\boldsymbol{v_1}$ is plotted in Figure 4.9a for ξ ranging from 10^{-5} to 10^5. In this targeting scenario, the principal directions rotate by approximately

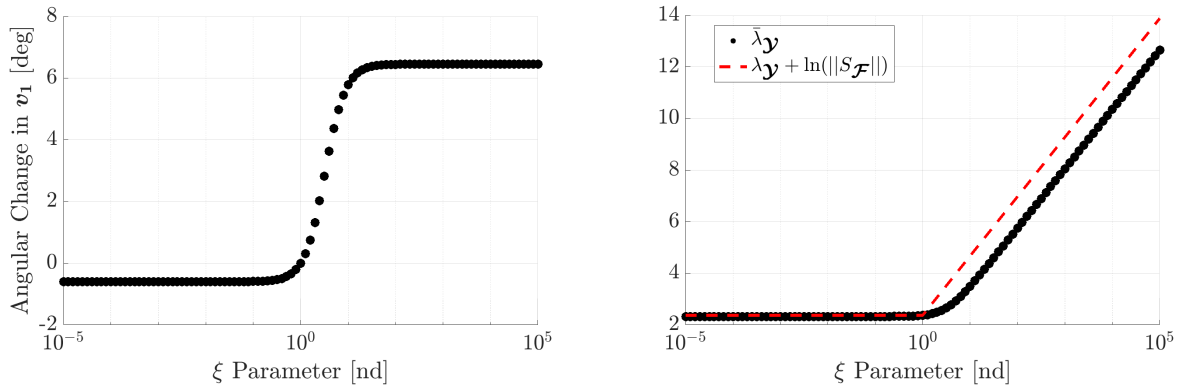

(a) Dominant Right Singular Vector

(b) FTLE-Based Quantity

Figure 4.9. Example Impact of Constraint Scaling on Perturbation Jacobian-Derived Quantities

7 deg as the scaling parameter ξ is varied. While a small angular deviation is unlikely to significantly alter the PDA-measured basin width in the monotonic portion of the main basin, other systems and targeting problems may lead to larger angular deviations. Similarly, the FLTE-based quantity $\bar{\lambda}_{\boldsymbol{\mathcal{Y}}}$, a function of the maximum singular value of $\frac{\partial \bar{\boldsymbol{\mathcal{F}}}}{\partial \bar{\boldsymbol{\mathcal{Y}}}}\Big|_{(\boldsymbol{\mathcal{X}}^*, \boldsymbol{\mathcal{Y}}^*)}$ as shown in Equation (4.15), is computed for the range of values for the ξ parameter and plotted in Figure 4.9b. Though the FLTE-based quantity in the scaled problem cannot be directly computed from the value in the unscaled problem, an inequality bounds the value of $\bar{\lambda}_{\boldsymbol{\mathcal{Y}}}$, i.e.,

$$\begin{aligned} \bar{\lambda}_{\boldsymbol{\mathcal{Y}}} &= \ln\left(\left\|\frac{\partial \bar{\boldsymbol{\mathcal{F}}}}{\partial \bar{\boldsymbol{\mathcal{Y}}}}\Big|_{(\boldsymbol{\mathcal{X}}^*, \boldsymbol{\mathcal{Y}}^*)}\right\|\right) \\ &= \ln\left(\left\|S_{\boldsymbol{\mathcal{F}}}\frac{\partial \boldsymbol{\mathcal{F}}}{\partial \boldsymbol{\mathcal{Y}}}\Big|_{(\boldsymbol{\mathcal{X}}^*, \boldsymbol{\mathcal{Y}}^*)}\right\|\right) \\ &\leq \ln\left(\|S_{\boldsymbol{\mathcal{F}}}\|\left\|\frac{\partial \boldsymbol{\mathcal{F}}}{\partial \boldsymbol{\mathcal{Y}}}\Big|_{(\boldsymbol{\mathcal{X}}^*, \boldsymbol{\mathcal{Y}}^*)}\right\|\right) \end{aligned} \tag{4.56}$$

Plotted in Figure 4.9b, this inequality provides an upper bound for $\bar{\lambda}_{\boldsymbol{\mathcal{Y}}}$, expressed as

$$\bar{\lambda}_{\boldsymbol{\mathcal{Y}}} \leq \lambda_{\boldsymbol{\mathcal{Y}}} + \ln\left(\|S_{\boldsymbol{\mathcal{F}}}\|\right) \tag{4.57}$$

From the figures, it is clear that the values of $\bar{\lambda}_{\boldsymbol{\mathcal{Y}}}$ and the orientation of the principal directions is dependent on ξ and, therefore, the relative scaling of the constraint functions. Additionally, the "correct" scaling parameter is not necessarily obvious *a priori* for an arbitrary perturbed targeting problem.

The basin metrics and higher-order singular vectors associated with the normalized rate of change in the design Jacobian are invariant under a scaling operation on the constraint values. The matrix norm-approximated γ and the higher-order singular value γ', defined in Equations (4.35) and (4.44), respectively, have analogous basin metrics $\bar{\gamma}$ and $\bar{\gamma}'$ in the scaled problem defined by the parameter ξ in Equation (4.55). The normalized rate of change in

the design Jacobian is invariant to the scaling of the constraints, assuming the scaling the matrix is diagonal with positive entries, i.e.,

$$\begin{aligned}\left.\frac{\partial \bar{\boldsymbol{\mathcal{F}}}}{\partial \boldsymbol{\mathcal{X}}}\right|^{-P}_{(\boldsymbol{\mathcal{X}}^*,\boldsymbol{\mathcal{Y}}^*)} \left.\frac{\partial^2 \bar{\boldsymbol{\mathcal{F}}}}{\partial \boldsymbol{\mathcal{X}}\partial \boldsymbol{\mathcal{Y}}}\right|_{(\boldsymbol{\mathcal{X}}^*,\boldsymbol{\mathcal{Y}}^*)} &= \left.\frac{\partial \boldsymbol{\mathcal{F}}}{\partial \boldsymbol{\mathcal{X}}}\right|^{-P}_{(\boldsymbol{\mathcal{X}}^*,\boldsymbol{\mathcal{Y}}^*)} S_F^{-1} S_{\boldsymbol{\mathcal{F}}} \left.\frac{\partial^2 \boldsymbol{\mathcal{F}}}{\partial \boldsymbol{\mathcal{X}}\partial \boldsymbol{\mathcal{Y}}}\right|_{(\boldsymbol{\mathcal{X}}^*,\boldsymbol{\mathcal{Y}}^*)} \\ &= \left.\frac{\partial \boldsymbol{\mathcal{F}}}{\partial \boldsymbol{\mathcal{X}}}\right|^{-P}_{(\boldsymbol{\mathcal{X}}^*,\boldsymbol{\mathcal{Y}}^*)} \left.\frac{\partial^2 \boldsymbol{\mathcal{F}}}{\partial \boldsymbol{\mathcal{X}}\partial \boldsymbol{\mathcal{Y}}}\right|_{(\boldsymbol{\mathcal{X}}^*,\boldsymbol{\mathcal{Y}}^*)}\end{aligned} \tag{4.58}$$

so the basin metric value and the mode-3 singular direction $\boldsymbol{v}'$, defined in Equation (4.45), are theoretically unchanged. The change in magnitude of $\bar{\gamma}'$ and the angular deviation of $\boldsymbol{v}'$ in the plane are depicted in Figures 4.10a and 4.10b for a values of ξ ranging from 10^{-5} to 10^{5}. The values of the basin metric have an error on the order of 10^{-12} or less, and the mode-3

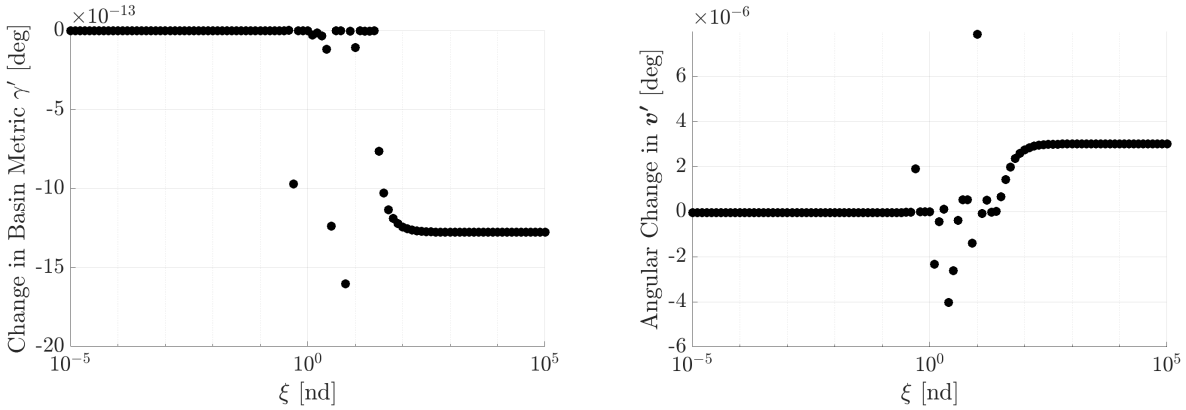

(a) Basin Metric

(b) Mode-3 Singular Vector $\boldsymbol{v}'$

Figure 4.10. Example Impact of Constraint Scaling on Normalized Change in Design Jacobian-Derived Quantities

singular vector changes orientation by angular deviations on the order of 10^{-6} deg. Because these values are computed via a constrained optimization problem, the tolerances in the optimizer as well as other numerical errors result in these very small deviations, sometimes observed as noise, from their theoretically-constant nature. An advantage to these quantities derived from the normalized change in the design Jacobian is that unique values characterize each perturbed targeting problem, irrespective of constraint scaling.

5. APPLICATION TO AN EARTH-MOON DISTANT RETROGRADE ORBIT

A set of perturbed targeting problems related to a distant retrograde orbit (DRO) in the Earth-Moon system is introduced to evaluate the validity of the proposed strategies, i.e, the 1st-order FTLE-inspired metrics, the 2nd-order basin metric, PDA, and the principal plane approximation, in characterizing the influence of state perturbations on convergence behavior. The selected DRO underlying the following scenarios is a particular member of a family of planar periodic orbits in the Earth-Moon CRTBP, and the limitation of its motion to the $\hat{\boldsymbol{x}}$-$\hat{\boldsymbol{y}}$ plane permits an intuitive representation of planar position and velocity perturbation subspaces in two-dimensional figures as a means to visualize the convergence behavior. As a periodic solution in the CRTBP, the selected DRO has an orbital period of $T \approx 13.2$ days and lunar distance of 70,000 km at the $\hat{\boldsymbol{x}}$-crossing with a $-\hat{\boldsymbol{y}}$-directed velocity in the rotating frame as viewed by a rotating observer. This particular periodic orbit is notable for analysis, because it provides a representation in the CRTBP of the destination orbit for the Orion spacecraft in the Artemis I mission [62]–[64]. The convergence behavior of perturbed targeting problems involving single- and two-maneuver scenarios on the DRO is studied to evaluate the various characterization strategies introduced in this investigation.

5.1 Single-Maneuver Targeting

Modeling the targeting of an initial station-keeping maneuver for a spacecraft arriving on various points along the DRO, a single-maneuver targeting scenario is formulated that implements a velocity change at the initial time to target the position of the 70,000 km lunar distance at an $\hat{\boldsymbol{x}}$-crossing downstream. The maneuver time, t_0, is measured relative to the propagation from a $\hat{\boldsymbol{x}}$-crossing of the reference motion at $t_{ref} = 0$, and the time of the targeted crossing, t_1, reflects two periods of the orbit beyond the reference time, i.e., $t_1 = 2T$. The reference motion associated with a maneuver time of $t_0 \approx 0.54T$ is illustrated in Figure 5.1a. A scenario with a total time-of-flight corresponding to less than one period of the DRO is illustrated in Figure 5.1b with a maneuver time of $t_0 \approx 1.54T$, exactly one

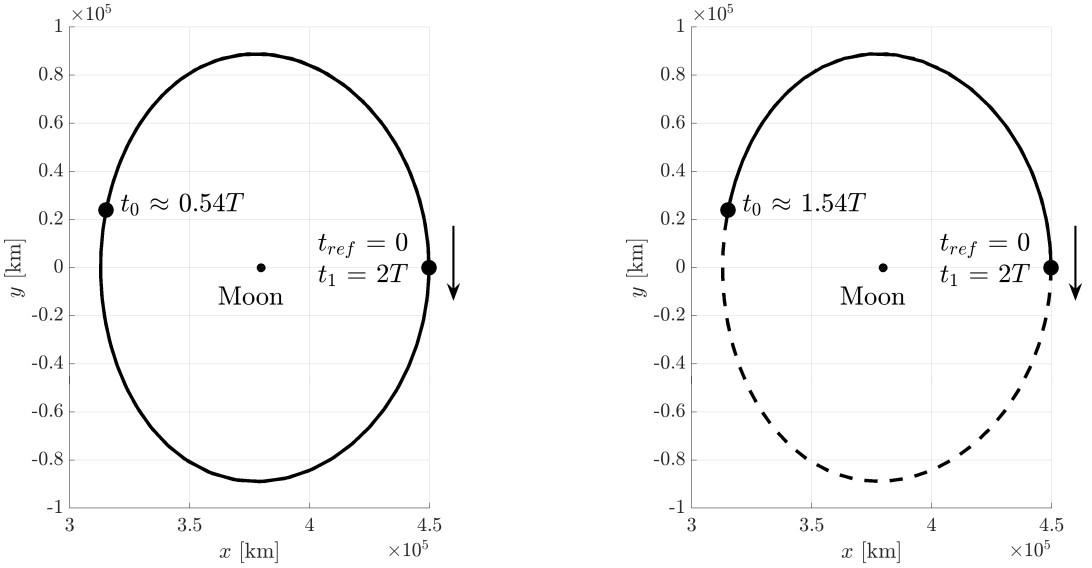

(a) Maneuver at $t_0 \approx 0.54T$

(b) Maneuver at $t_0 \approx 1.54T$

Figure 5.1. 70,000 km DRO Trajectory and Single-Maneuver Reference Locations

period less than in Figure 5.1a. The dashed line in the figure reflects the untraveled segment of the reference DRO, and the arrow represents the flow direction of the periodic orbit.

The perturbed targeting problem is formulated such that the planar velocity components at the initial time, t_0, serve as design variables to target the desired final position vector, $\boldsymbol{\rho_d}$, at the final time t_1 under the influence of perturbations in initial position and velocity. Mathematically, these constraints, design variables, and perturbation variables are expressed as

$$\boldsymbol{\mathcal{F}} = \boldsymbol{\rho}(t_1)^- - \boldsymbol{\rho_d} \ , \ \boldsymbol{\mathcal{X}} = \dot{\boldsymbol{\rho}}(t_0)^+ \ , \ \boldsymbol{\mathcal{Y}} = \begin{bmatrix} \boldsymbol{\mathcal{Y}}_1 \\ \boldsymbol{\mathcal{Y}}_2 \end{bmatrix} = \begin{bmatrix} \boldsymbol{\rho}(t_0)^+ \\ \dot{\boldsymbol{\rho}}(t_0)^+ \end{bmatrix} \tag{5.1}$$

where the target position is expressed most clearly in its dimensional form, i.e.,

$$\tilde{\boldsymbol{\rho}}_{\boldsymbol{d}} = \begin{bmatrix} 70,000 + \tilde{r}_{B2} & 0 & 0 \end{bmatrix}^T \text{ km} \tag{5.2}$$

where $\tilde{r}_{B2}$ is the dimensional distance from the system barycenter to the Moon. To characterize the convergence behavior across a range of possible mission designs, the maneuver

time, t_0, associated with the arrival point along the orbit, is varied from t_{ref} to 6 hours prior to t_1.

Because the full set of perturbation variables is comprised of dimensionally-dissimilar position and velocity components, the perturbation subspaces, $\boldsymbol{\mathcal{Y}}_1$ and $\boldsymbol{\mathcal{Y}}_2$, corresponding to planar initial position and velocity, respectively, are first individually analyzed. The execution of a "naïve" discretization scheme, e.g., regular grid or expanding shells, requires a non-trivial amount of computation time, especially when repeated over numerous values of t_0; therefore, the PDA discretization scheme that exploits information from the derivatives at the reference solution yields approximate results for a preliminary analysis of candidate maneuver times. The largest perturbation magnitude for which the targeting problem converges within 3 iterations is measured along each principal direction in the $\boldsymbol{\mathcal{Y}}_1$ and $\boldsymbol{\mathcal{Y}}_2$ subspaces, and the results are depicted in Figure 5.2a and 5.2b, respectively. Each vector $\boldsymbol{v_{i,j}}$ represents the left

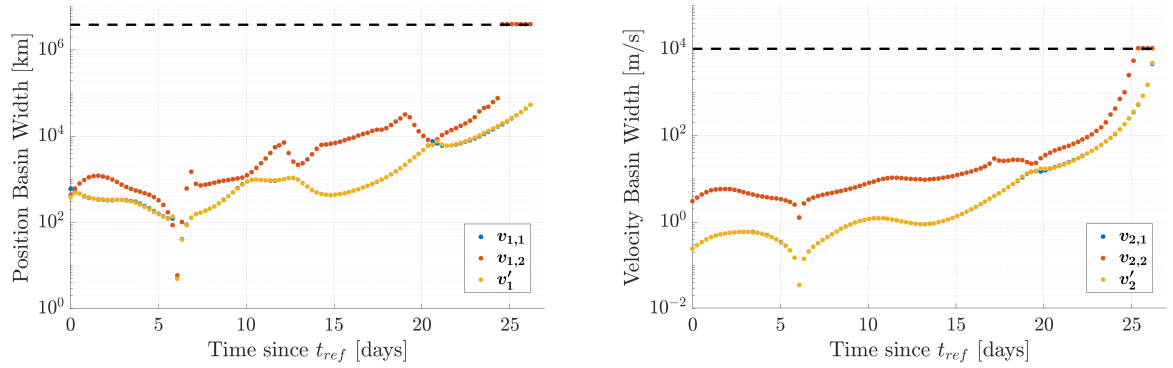

(a) Position Perturbation Subspace

(b) Velocity Perturbation Subspace

Figure 5.2. Individual Principal Direction Measurements for the Single-Maneuver DRO Scenario with a 3-Iteration Limit

(or mode-2) singular vector of $\frac{\partial \boldsymbol{\mathcal{F}}}{\partial \boldsymbol{\mathcal{Y}}_i}\Big|_{(\boldsymbol{\mathcal{X}}^*,\boldsymbol{\mathcal{Y}}^*)}$ associated with the singular value $\sigma_{i,j}$ and signifies principal directions of growth from the 1st-order derivative as defined in Equation (4.17). For example, the dominant right singular vector in the velocity perturbation subspace is expressed as $\boldsymbol{v_{2,1}}$. Defined in Equation (4.45), each vector $\boldsymbol{v_i'}$ is the dominant mode-3 singular vector associated with the tensor $\frac{\partial \boldsymbol{\mathcal{F}}}{\partial \boldsymbol{\mathcal{Y}}_i}\Big|^{-1}_{(\boldsymbol{\mathcal{X}}^*,\boldsymbol{\mathcal{Y}}^*)} \frac{\partial^2 \boldsymbol{\mathcal{F}}}{\partial \boldsymbol{\mathcal{X}} \partial \boldsymbol{\mathcal{Y}}_i}\Big|_{(\boldsymbol{\mathcal{X}}^*,\boldsymbol{\mathcal{Y}}^*)}$ and reflects the direction with the largest normalized rate of change in the design Jacobian.

In Figure 5.2a, the position basin measurements express the largest physical perturbations in position in each vector direction for which the targeting problem converges within 3 iterations. The trends are seen more clearly by comparing the resulting measurements in each direction to the overall minimum value that defines the basin width measurement. Figures 5.3a, 5.3b, and 5.3c show the measurements along the vectors $\boldsymbol{v_{1,1}}$, $\boldsymbol{v_{1,2}}$, and $\boldsymbol{v_1'}$, respectively, compared to the overall minimum value in black. Discretization along the

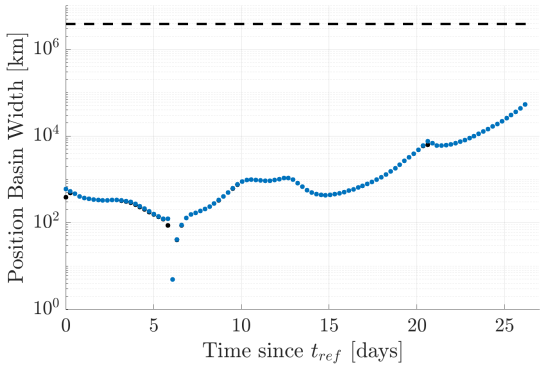

(a) Measurements Along $\boldsymbol{v_{1,1}}$

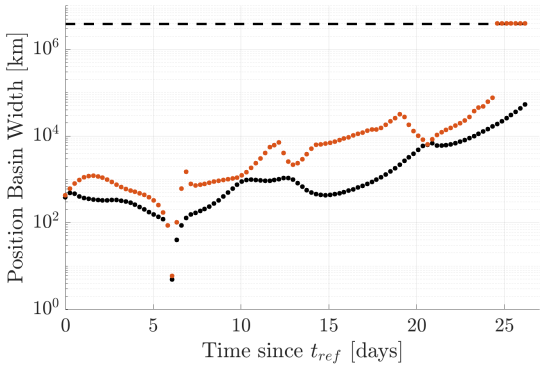

(b) Measurements Along $\boldsymbol{v_{1,2}}$

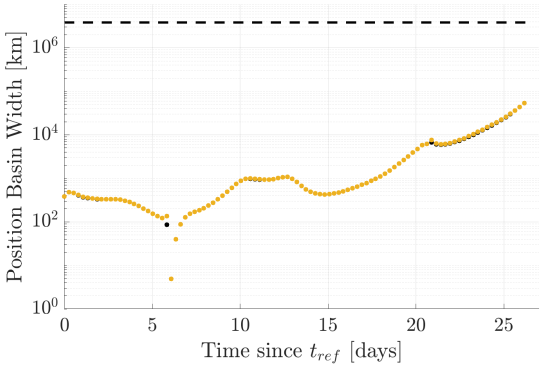

(c) Measurements Along $\boldsymbol{v_1'}$

Figure 5.3. Individual Principal Direction Measurements for the Single-Maneuver DRO Scenario Compared to Minimum

dominant right singular vector, $\boldsymbol{v_{1,1}}$, and the vector $\boldsymbol{v_1'}$ yield nearly identical results, visually represented by the overlapping nature of the blue and yellow points in the figure. This finding signals that the perturbation directions in position-space that generate the largest growth in the constraint vector as well as the largest normalized change in the design Jacobian are approximately aligned. In this scenario, therefore, the additional computational complexity

of computing $\boldsymbol{v}_1'$ is not necessary to approximate the convergence basin width; however, the additional computation of the 2$^{\text{nd}}$-order information is useful in supporting the validity of the 1$^{\text{st}}$-order results. Depicted by the higher values associated with the orange points, a larger allowable perturbation is observed in the $\boldsymbol{v}_{\mathbf{1,2}}$-direction, correlating with a smaller singular value and less expected growth in the constraint vector. As the maneuver time approaches 25 days, the measurements along the $\boldsymbol{v}_{\mathbf{1,2}}$ vector exceed the analysis limit of 10 non-dimensional units, represented by the dashed line.

In Figure 5.2b, a similar analysis of perturbations in $\boldsymbol{\mathcal{Y}}_2$-space, i.e., the velocity components at time t_0, reveals similar findings. The basin width measurements along the vectors $\boldsymbol{v}_{\mathbf{2,1}}$ and $\boldsymbol{v}_{\mathbf{2}}'$ are visually indistinguishable, suggesting that the directions corresponding to the largest growth in the constraint vector as well as the largest growth in the normalized change in the design Jacobian are nearly aligned. For a limit of 3 iterations in the corrections process, the PDA-approximated basin width for each maneuver time is given by the minimum measured value in Figures 5.2a and 5.2b across all of the principal directions.

By repeating this PDA process for various differential corrections iteration limits, a characterization of the local main convergence basins is produced for range of possible of maneuver times. The basin width measurements for perturbations in the initial position across the set of possible maneuver times are colored in Figure 5.4a for limits of 3 through 8 iterations. For all of the analyzed iteration limits, a consistent trend is observed in the basin width measurement as the maneuver time is varied. The local minima and maxima, reflecting times for which the convergence basin is largest or smallest relative to the nearby maneuver times, occur at roughly the same values of t_0 for each iteration limit. A sharp decrease in the convergence basin width, or basin contraction, is evident at a maneuver time of $t_0 \approx 6.08$ days ≈ 1.4 non-dimensional time units, highlighting a duration in time for which the targeting problem is particularly sensitive to perturbations in position. Notably, the convergence behavior does not display obvious signs of periodicity despite the periodic nature of the underlying motion in the reference solution.

For comparison, the evaluated basin metrics that incorporate information from 2$^{\text{nd}}$-order derivatives in the perturbed targeting problem are shown in Figure 5.4b. Obtained as the result of the constrained optimization problem in Equation (4.45), the quantity γ_1', defined

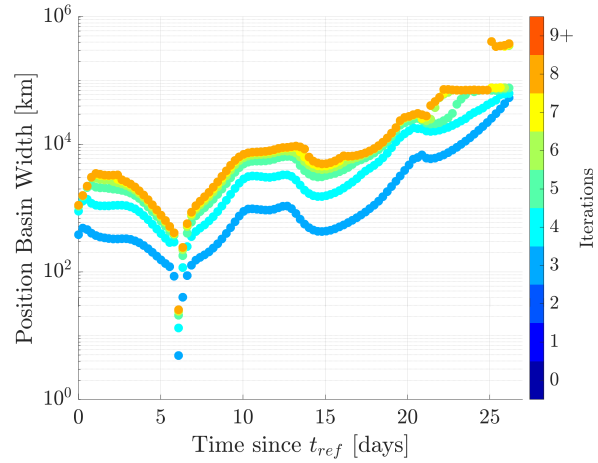

(a) Position Basin Width via PDA

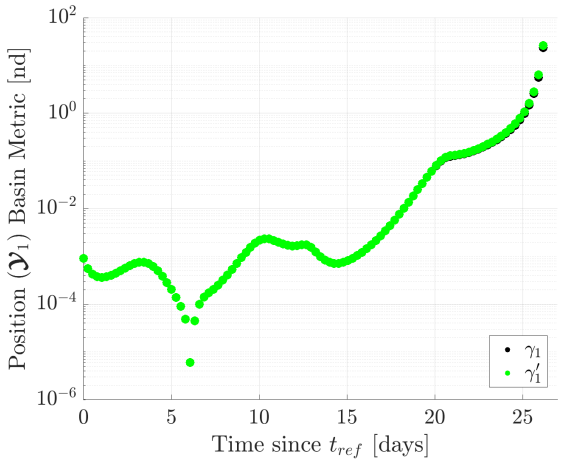

(b) Position Basin Metric

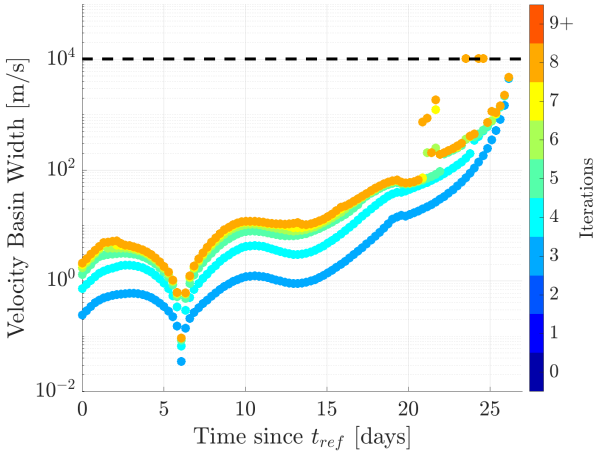

(c) Velocity Basin Width via PDA

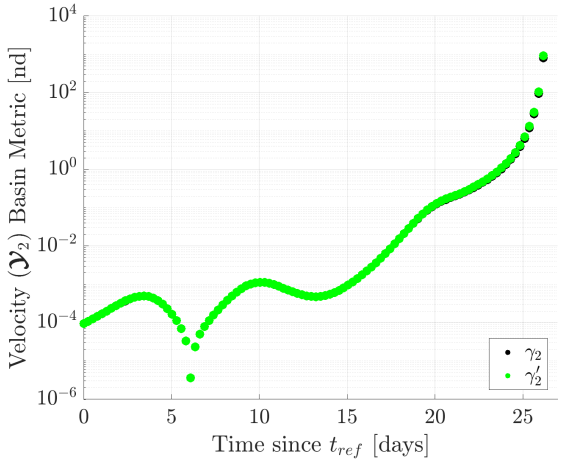

(d) Velocity Basin Metric

Figure 5.4. Single-Maneuver DRO Scenario PDA Basin Width Measurements and Evaluated Basin Metrics

in Equation (4.44), is the higher-order singular value associated with $\boldsymbol{v}_1'$ and the largest normalized change in the design Jacobian due to position perturbations. Defined in terms of the matrix l_2-norm in Equation (4.35), the quantity γ_1 approximates the quantity γ_1' without the need for an iteratively-solved optimization problem. The values of γ_1 and γ_1' overlap in Figure 5.4b, signifying that the additional computational complexity in solving the optimization problem is not necessary in this particular scenario. In contrast to the PDA-measured basin width values in Figure 5.4a, the evaluated basin metrics in Figure 5.4b do not require any simulation of the targeting problem itself but instead rely solely on the

partial derivatives evaluated at the reference solution. Comparing Figures 5.4a and 5.4b, the same trends in convergence behavior appear in the measured basin width values and the evaluated basin metrics. Most importantly, the severe basin contraction at $t_0 \approx 6.08$ days is predicted in the evaluated quantities.

The convergence behavior for this single-maneuver targeting problem under perturbations in the initial velocity is characterized in terms of the PDA-measured basin width and evaluated basin metric values in Figures 5.4c and 5.4d. In Figure 5.4c, the trend in convergence behavior as the maneuver time is changed is generally consistent across the range of iteration limits. However, a departure from the underlying trend appears with limits of 6 or more iterations for $t_0 > 21$ days, visually depicted by the irregular, scattered nature of the measurements. This scattered departure from the trend indicates that the local main convergence basin is not be well-defined for limits of 6 or more iterations, and perturbation space has already transitioned into the chaotic region between monotonic basins. This finding highlights the importance of choosing sufficiently-low iteration limits to ensure the PDA strategy is accessing the main basin around the reference solution. Where the iteration limit is appropriate for the characterizing the main basin, the evaluated basin metrics, γ_2 and γ_2', plotted in Figure 5.4d, are useful predictors of the measured behavior. The expansion and contraction of the convergence basin as the maneuver time is varied correlates directly with the evaluated 2^{nd}-order basin metric values, which themselves provide similar information.

While the basin metrics derived from the normalized change in the design Jacobian necessitate the computation of 2^{nd}-order partial derivatives, the FTLE-inspired quantities defined in Equation (4.14) and (4.15) only require 1^{st}-order derivative information. The FTLE-inspired quantities associated with the design Jacobian, position perturbation Jacobian, and velocity perturbation Jacobian, expressed as $\lambda_{\boldsymbol{\mathcal{X}}}$, $\lambda_{\boldsymbol{\mathcal{Y}}_1}$, and $\lambda_{\boldsymbol{\mathcal{Y}}_2}$, respectively, are relevant. However, the formulation of this perturbed targeting problem in Equation (5.1) results in the equivalence of $\lambda_{\boldsymbol{\mathcal{X}}}$ and $\lambda_{\boldsymbol{\mathcal{Y}}_2}$, so the values of $\lambda_{\boldsymbol{\mathcal{Y}}_1}$ and $\lambda_{\boldsymbol{\mathcal{Y}}_2}$ for the range of maneuver times is shown in Figure 5.5. The values are multiplied by a constant of -1, because the FTLE-inspired quantities are expected to vary inversely with the size of the convergence basin. Put simply, greater growth in the constraint vector is posited to yield smaller main convergence basins. Though some features correlate with the structure, including some minima and max-

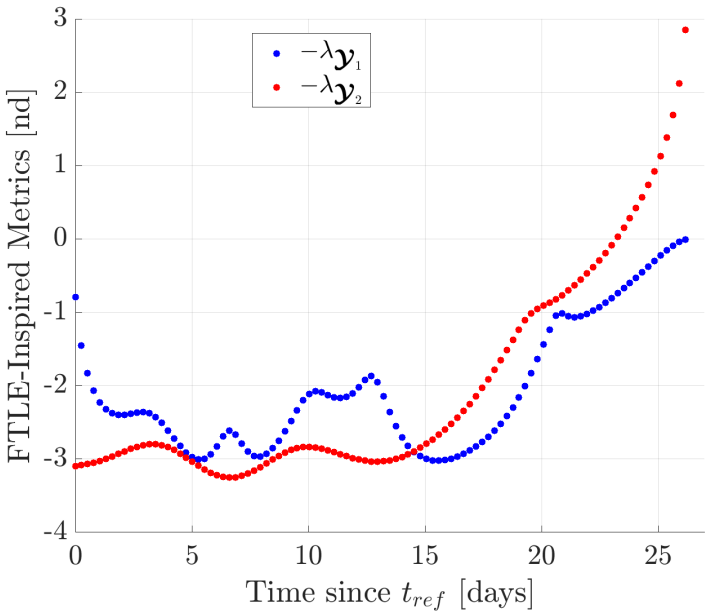

Figure 5.5. FTLE-Inspired Quantities in the Single-Maneuver DRO Scenario

ima, of the measured basin widths in Figures 5.4a and 5.4c, the significant feature of the basin contraction at $t_0 \approx 6.08$ days is not captured by the FTLE-inspired quantities. These results confirm the possible effectiveness of FTLE-inspired quantities in indirectly predicting convergence behavior in previous investigations while demonstrating the potential limitations of these strategies that only employ 1$^{\text{st}}$-order derivative information.

The information gained about the convergence behavior in the individual position and velocity perturbation subspaces from discretization through PDA or the evaluated metrics provides practical guidance for identifying poorly-performing maneuver times and down-selecting from the set of design alternatives. However, by their nature, the strategies for the investigation of the perturbed targeting problem used to this point do not reflect the combined impact of perturbations in position and velocity on the convergence behavior. Therefore, the investigation shifts to incorporate full state perturbations in a position-velocity tradespace analysis.

Scenarios with two different values of the maneuver time t_0 are examined to investigate the principal plane discretization technique as a viable, more computationally-efficient alternative to a brute-force discretization scheme in determining the position-velocity tradespace.

The maneuver times are selected to produce conditions that represent both the satisfaction and violation of the in-plane conditions, described by Equations (4.20), (4.24), (4.25), that support the heuristic use of the principal plane as a determiner of features critical to the tradespace. Figure 5.6a includes a plot of the angle between the dominating right singular vectors, denoted the constraint principal directions, in $\boldsymbol{\mathcal{Y}}_1$ and $\boldsymbol{\mathcal{Y}}_2$, i.e., $\angle(\boldsymbol{u_{1,1}}, \boldsymbol{u_{2,1}})$, which is equal to zero in the ideal case of the principal plane, as t_0 evolves along the two periods of the reference DRO. Figure 5.6b displays the ratios between the two largest singular values

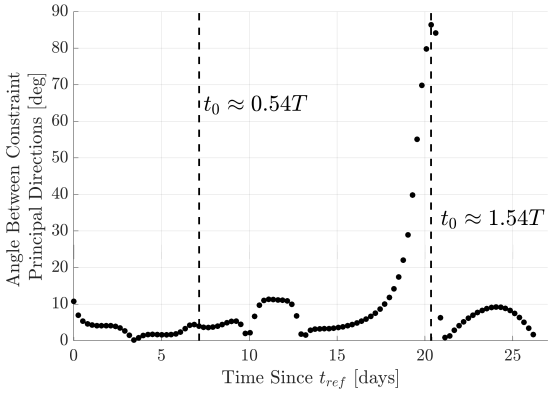

(a) Angle Between Constraint Principal Directions

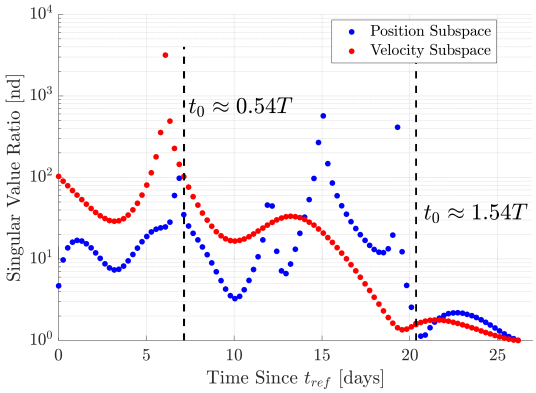

(b) Singular Value Ratio

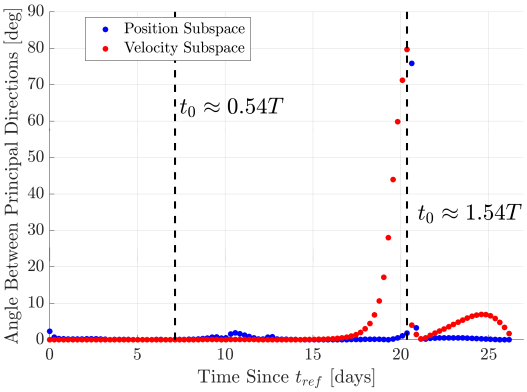

(c) Principal Direction Projection Angles

Figure 5.6. Principal Plane Conditions for Single-Maneuver DRO Targeting

in the $\boldsymbol{\mathcal{Y}}_1$ and $\boldsymbol{\mathcal{Y}}_2$ perturbation subspaces, i.e., $\frac{\sigma_{i,1}}{\sigma_{i,2}}$, which is ideally much greater than unity, as the maneuver time is similarly varied. Examining the case where $t_0 \approx 0.54T$, the angle between the dominating constraint principal directions is small, and the ratios of the singular values suggest that clearly-dominating principal directions exist. Together, these conditions

imply that the dominant principal directions at $t_0 \approx 0.54T$ in $\boldsymbol{\mathcal{Y}}$, $\boldsymbol{\mathcal{Y}}_1$, and $\boldsymbol{\mathcal{Y}}_2$ very-nearly lie in a principal plane. As predicted, the three directions $\boldsymbol{v_1}$, $\boldsymbol{v_{1,1}}$, and $\boldsymbol{v_{2,1}}$ are approximately co-planar, illustrated by the nearly-zero values of θ_1 and θ_2 from Equation (4.20) in Figure 5.6c. Alternatively, if the maneuver time is displaced downstream by exactly one period of the DRO to $t_0 \approx 1.54T$, the angle $\angle(\boldsymbol{u_{1,1}}, \boldsymbol{u_{2,1}})$ is nearly 90 deg, and the ratio of the singular values is close to one, indicating the lack of clearly-dominating principal directions in the $\boldsymbol{\mathcal{Y}}_1$ and $\boldsymbol{\mathcal{Y}}_2$ subspaces. These conditions violate the principal plane assumptions and, consequently, do not produce co-planar $\boldsymbol{v_1}$, $\boldsymbol{v_{1,1}}$, and $\boldsymbol{v_{2,1}}$ vectors, as indicated by the large angular deviations in Figure 5.6c. Therefore, the scenario where $t_0 \approx 0.54T$ represents conditions that support the use of the principal plane approximation, and the scenario where $t_0 \approx 1.54T$ suggests that the principal plane approximation may not fully represent the tradespace. These two scenarios are selected for more detailed analysis of the tradespace under both favorable and unfavorable conditions.

5.1.1 Favorable Principal Plane Conditions ($t_0 \approx 0.54T$)

While PDA provides an efficient characterization of the convergence behavior induced by independent position and velocity perturbations as the design parameter t_0 is varied, the interrogation of the targeting problem at a single value of $t_0 \approx 0.54T$ permits a demonstration of the correlation between the theoretical basin widths and the PDA-measured approximate basin width values. Illustrated in Figure 5.7a, the planar position perturbation subspace is discretized, and the number of iterations required to converge to a solution is recorded as the color associated with the point of the initial perturbation. The principal directions of the perturbation Jacobian $\frac{\partial \boldsymbol{\mathcal{F}}}{\partial \boldsymbol{\mathcal{Y}}_1}$, $\boldsymbol{v_{1,1}}$ and $\boldsymbol{v_{1,2}}$, are plotted in white and labelled according to their singular value. In the position perturbation subspace, the local main basin develops monotonically outward from the origin, and the direction along which the number of required iterations increases the most rapidly corresponds to the principal direction with the dominant singular value $\sigma_{1,1} = 16.36$. In the orthogonal principal direction, the singular value $\sigma_{1,2}$ has a significantly smaller value of 0.47, signifying that the constraint vector magnitude locally experiences less growth for a perturbation of the same size. Figure 5.7a confirms the

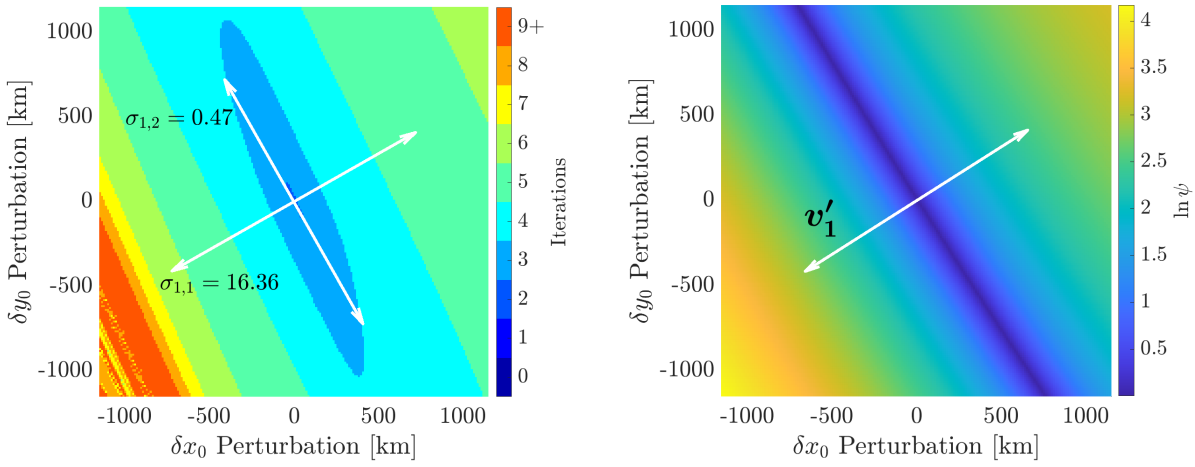

(a) Iterations to Converge

(b) Evaluated Scalar ψ

Figure 5.7. The Position Perturbation Space $\boldsymbol{\mathcal{Y}}_1$ for Single-Maneuver DRO Targeting ($t_0 \approx 0.54T$)

expected behavior as the number of required update iterations increases more gradually in this direction. For comparison, the natural log of the scalar ψ, defined in Equation (4.27), is evaluated for each initial perturbation in $\boldsymbol{\mathcal{Y}}_1$ and plotted in Figure 5.7b. The quantity ψ serves as a scalar metric for the change in the design Jacobian when evaluated at the reference solution and at each perturbed initial condition. The mode-3 singular vector $\boldsymbol{v_1'}$, plotted in white, is directed toward the steepest gradient in ψ, and the boundary in the lower left corner of Figure 5.7a where the iteration count rapidly transitions to red and chaotic behavior corresponds to the rapid change in ψ in Figure 5.7b. Additionally, regions where ψ is small correspond to regions of rapid convergence to a solution. The connection of the 2^{nd}-order metrics γ_1 and γ_1' to the local largest rate of change in ψ and the vector $\boldsymbol{v_1'}$ helps explain their effectiveness as a relative measure of convergence basin width.

Similar behavior is observed in the velocity perturbation subspace in Figure 5.8a where the local structure of the convergence basin is captured by the principal directions and their singular values. In Figure 5.8b, the evaluated measure of change in the Jacobian at each perturbed point, ψ, increases rapidly in the direction associated with the vector $\boldsymbol{v_2'}$, corresponding to the largest local normalized change in the design Jacobian at the reference solution. The vectors $\boldsymbol{v_{2,1}}$ and $\boldsymbol{v_2'}$, representing growth in the constraint vector and change

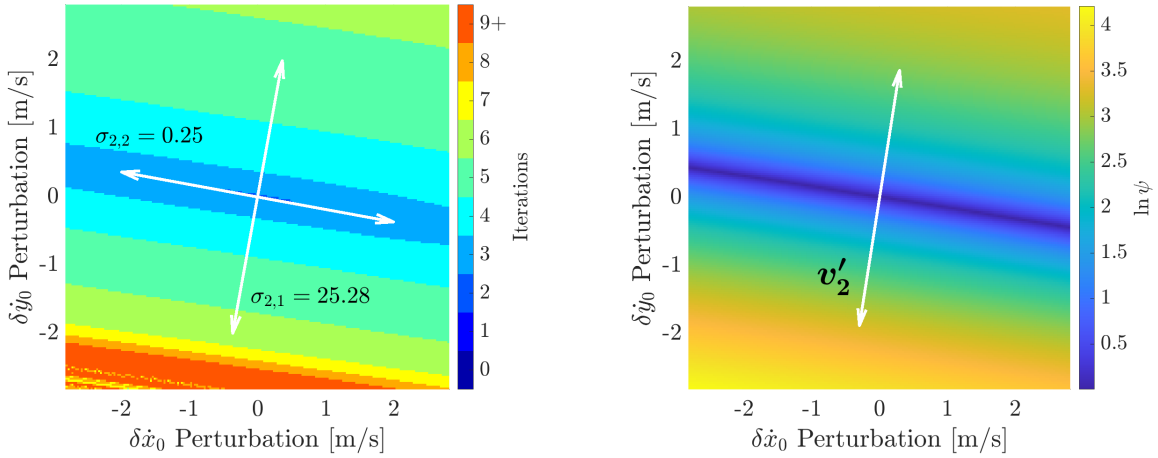

(a) Iterations to Converge

(b) Evaluated Scalar ψ

Figure 5.8. The Velocity Perturbation Space $\mathcal{Y}_2$ for Single-Maneuver DRO Targeting ($t_0 \approx 0.54T$)

in the design Jacobian, respectively, both point toward the nearest boundary of the main basin.

The characterizations of the tradespace of allowable position and velocity perturbations via the principal plane approximation and a full discretization across expanding shells are compared under favorable conditions for the principal plane assumption. In this planar analysis, the expanding shell discretization is conducted by selecting discrete points on circles, reflecting this analysis of planar perturbations, of increasing radius in the position and velocity perturbation subspaces. A targeting problem is simulated for each possible pair of perturbed initial conditions from the position and velocity subspaces. To illustrate the critical features of the tradespace, each point in Figure 5.9a corresponds to the maximum number of iterations required to converge to a solution for over all points of a given pair of position and velocity perturbation magnitudes, i.e., a pair of two particular circles in the planar position and velocity subspaces. For example, state perturbations within a circle in position space with a radius of 200 km and within a circle in velocity space with a radius of 1 m/s always convergence in 5 or fewer iterations. In the scenario, the contours that define iteration limits in the tradespace have a nearly-linear form. Similar to the depictions of the independent perturbation subspaces in Figures 5.7a and 5.12a, the gradient begins to

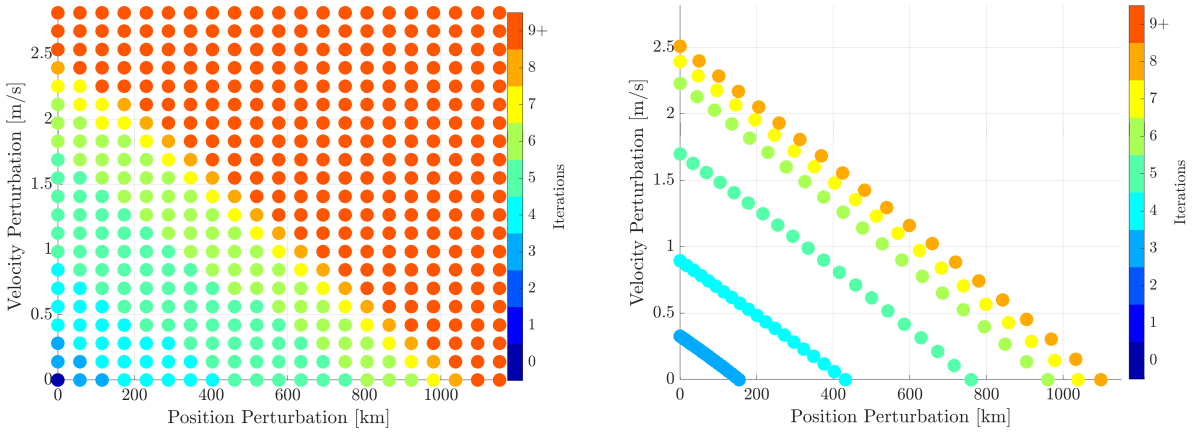

(a) Expanding Shell Discretization

(b) Principal Plane Approximation

Figure 5.9. Position-Velocity Tradespace for Single-Maneuver DRO Targeting ($t_0 \approx 0.54T$)

increase for limits of greater than 6 iterations as the main basin transitions toward chaotic behavior. The results of a principal plane analysis are depicted in Figure 5.9b where each point represents the largest magnitude along the parameterized principal plane search vector $\boldsymbol{\eta}(s)$, defined in Equation (4.18), for which all targeting simulations converge within a given iteration limit. The principal plane is constructed from the vectors $\boldsymbol{v_{1,1}}$ and $\boldsymbol{v_{2,1}}$, arising from the 1$^{\text{st}}$-order perturbation Jacobian, because higher-order singular vector analysis yields approximately-equivalent information in this case, as observed in Figures 5.2a and 5.2b. As predicted from the satisfaction of the co-planar conditions, the limited discretization along the vectors $\boldsymbol{\eta}(s)$ in the principal plane accurately approximates the locations of the iteration contours produced in the broader expanding shell analysis. Arising from a more focused strategy, this prediction comes with a substantially lower computational cost.

By employing the scalar quantity ψ from Equation (4.27), a purely-evaluated strategy lends insight into the form of the position-velocity tradespace without the need for any iterative targeting simulations. Shown in Figure 5.10, the maximum value of ψ, measuring the difference between the design Jacobian at the perturbed point, $\frac{\partial \boldsymbol{\mathcal{F}}}{\partial \boldsymbol{\mathcal{X}}}\Big|_{(\boldsymbol{\mathcal{X}},\boldsymbol{\mathcal{Y}})}$ and the design Jacobian at the reference solution, $\frac{\partial \boldsymbol{\mathcal{F}}}{\partial \boldsymbol{\mathcal{X}}}\Big|_{(\boldsymbol{\mathcal{X}}^*,\boldsymbol{\mathcal{Y}}^*)}$, is plotted for each combination of position and velocity perturbation magnitudes in the full expanding-shell discretization and visualized with interpolated shading to illustrate the behavior. The diagonal contours of constant color

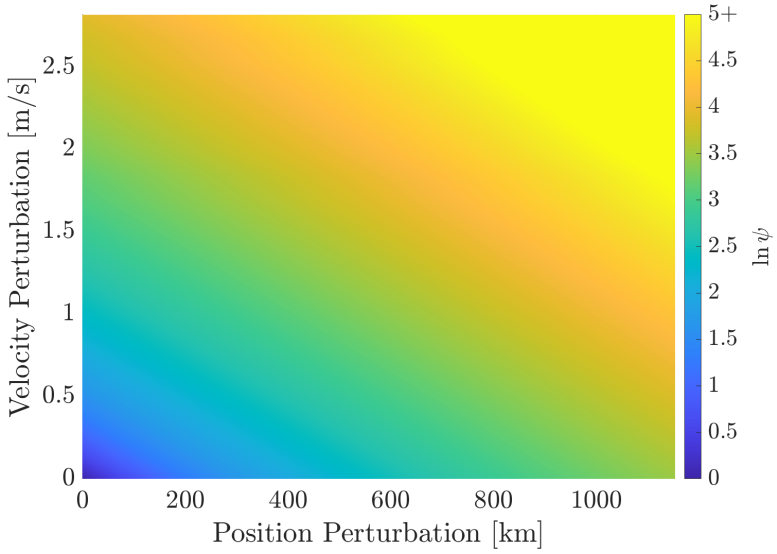

Figure 5.10. Evaluated Scalar ψ in the Position-Velocity Tradespace for Single-Maneuver DRO Targeting ($t_0 \approx 0.54T$)

match the tradespace representations depicted in Figures 5.9a and 5.9b. Though the form of the simulated tradespace is apparent in the plot of this evaluated quantity, the upper bound for the color scale, reaching saturation at $\ln \psi = 5$, is manually selected to highlight this similarity, limiting its use in determining the exact locations of the constant-iteration contours and the chaotic boundary region. However, the correlation between the tradespace and the values of ψ at each point demonstrate the connection between the form of the main basin and the normalized change in the design Jacobian.

5.1.2 Unfavorable Principal Plane Conditions ($t_0 \approx 1.54T$)

The second targeting scenario chosen for analysis is associated with a maneuver time of $t_0 \approx 1.54T$, reflecting unfavorable conditions for the co-planar assumption in the principal plane heuristic. In Figures 5.6a, 5.6b, and 5.6c, the high angular difference between the dominant constraint principal directions and the low singular value ratio of the independent subspaces reflect the measured deviation of the principal directions from a single principal plane. First, the individual position and velocity perturbation subspaces are characterized to show how the basin structure relates to the principal directions and singular values.

Illustrated in Figure 5.11a, the principal directions $\boldsymbol{v_{1,1}}$ and $\boldsymbol{v_{1,2}}$ in the position subspace possess singular values of 3.45 and 2.13, respectively, predicting a more uniform growth in the constraint vector and development of the convergence basin in all directions near the origin. As shown in Figure 5.11a, this behavior is confirmed from the simulation of discretized

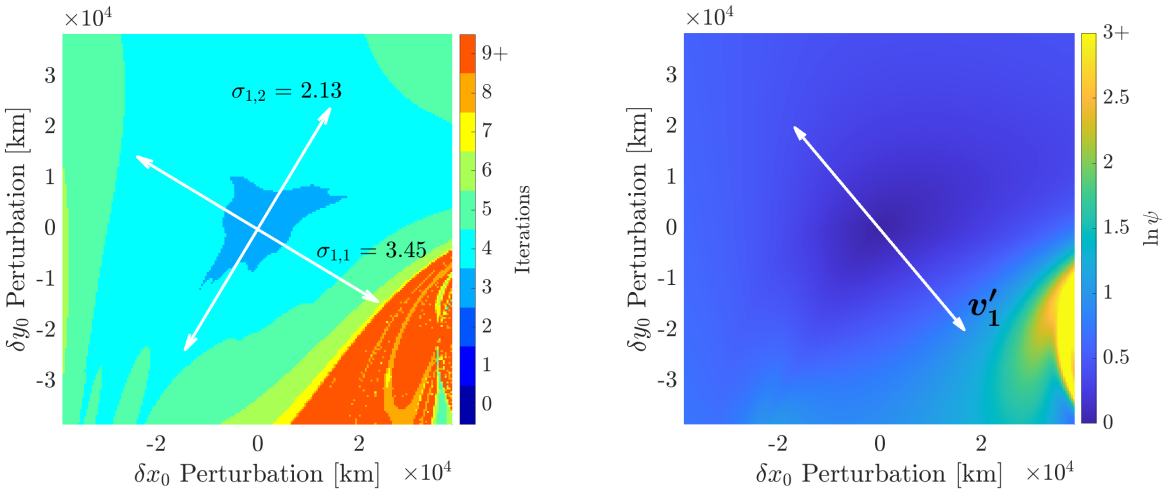

(a) Iterations to Converge

(b) Evaluated Scalar ψ

Figure 5.11. The Position Perturbation Space $\mathcal{Y}_1$ for Single-Maneuver DRO Targeting ($t_0 \approx 1.54T$)

points in the planar perturbation space. At each perturbed initial condition, the scalar ψ is evaluated to measure the change in the design Jacobian from the reference, and the results are plotted in Figure 5.11b. The vector $\boldsymbol{v_1'}$ appears to point in the direction of the most rapid change in ψ near the reference solution, located at the origin, and the boundary of the main basin seen in Figure 5.11a corresponds to elevated values of ψ. However, the vector $\boldsymbol{v_1'}$, a function of the 1st- and 2nd-order derivatives in the problem, does not point directly at the bounding structure for high iteration counts. This behavior is not unexpected due to the very large magnitude of the perturbations compared to the Earth-Moon system and the influence of higher-order terms away from the neighborhood of the reference solution.

With singular values of 2.38 and 1.51 for the matrix $\frac{\partial \mathcal{F}}{\partial \mathcal{Y}_2}\Big|_{(\mathcal{X}^*,\mathcal{Y}^*)}$, the velocity perturbation subspace, plotted in Figure 5.12a, exhibits similar uniformity of development for small iteration counts. With this more uniform development of the basin, the principal directions are not visually distinguished for this maneuver time as easily as the scenario with a maneuver

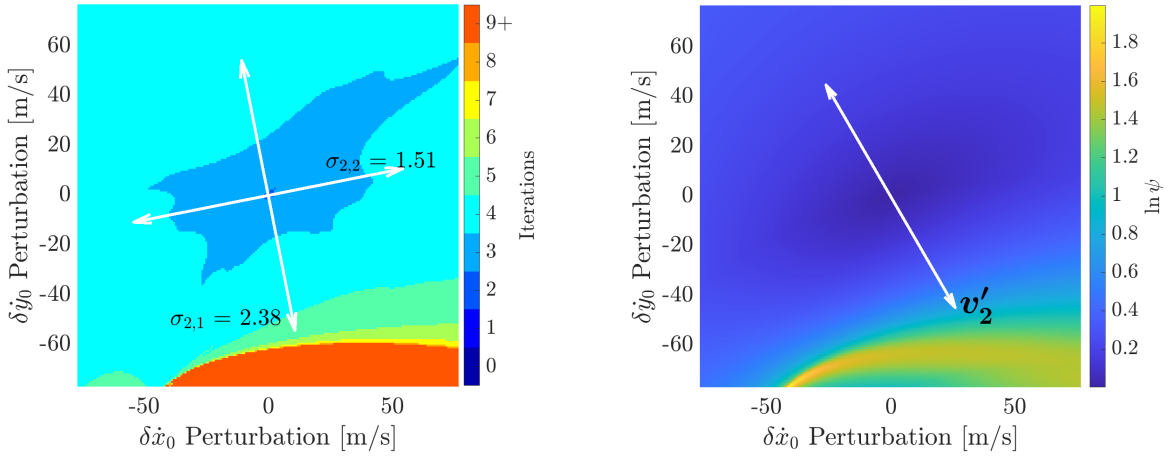

(a) Iterations to Converge

(b) Evaluated Scalar ψ

Figure 5.12. The Velocity Perturbation Space $\boldsymbol{\mathcal{Y}}_2$ for Single-Maneuver DRO Targeting ($t_0 \approx 1.54T$)

at $t_0 \approx 0.54T$, shown in Figure 5.8a. However, the ambiguity does not, in fact, significantly impact the error in the PDA-measured basin width for sufficiently-small iteration limits, because this uniformity implies that any measurement direction that is a linear combination of the principal directions with similar singular value magnitudes yields a similar growth rate in the constraints. In Figure 5.12b, the vector $\boldsymbol{v_2'}$, indicating the direction with the largest normalized change in the design Jacobian due to velocity perturbations, is directed toward the bounding structure of the main basin, and the structure itself appears to correspond to elevated values of ψ in the $\boldsymbol{\mathcal{Y}}_2$ perturbation space.

Due to its nonconformity with the principal plane assumptions, the maneuver time of $t_0 \approx 1.54T$ offers an opportunity to examine deviations between the position-velocity tradespace in principal plane and the fuller expanding shell discretization. The points in Figure 5.13a are colored according to the maximum number of iterations required to converge on a solution for each pair of position and velocity perturbation magnitudes. Similar to the previous scenario, the required iteration count steeply increases in the tradespace for limits of 6 iterations and above. This behavior is reflected in the results of the principal plane approximation, computed by simulating targeting problems in plane constructed from $\boldsymbol{v_{1,1}}$ and $\boldsymbol{v_{2,1}}$ and displayed in Figure 5.13b where the iteration contours become densely-

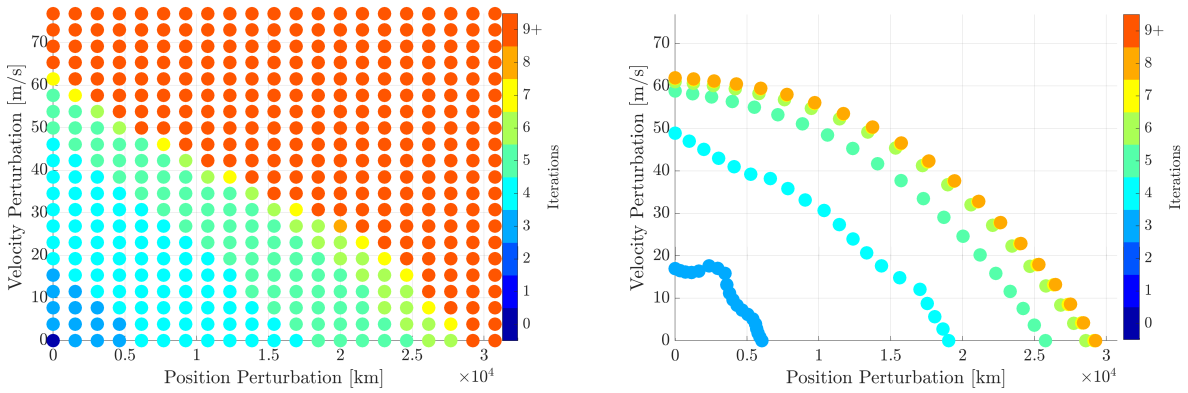

(a) Expanding Shell Discretization

(b) Principal Plane Approximation

Figure 5.13. Position-Velocity Tradespace for Single-Maneuver DRO Targeting ($t_0 \approx 1.54T$)

packed. In this scenario, the principal plane approximation slightly over-predicts the allowable perturbation magnitudes in the tradespace, suggesting that the actual critical features of the tradespace exist outside of the principal plane. This result is not surprising due to its violation of the principal plane assumptions. However, the tradespace represented in the principal plane yields a reasonable approximation for a preliminary analysis of the perturbed targeting problem and chosen maneuver time for a significantly-reduced number of targeting simulations.

As an alternative to the principal plane approximation, the evaluated quantity ψ is computed across the full position and velocity perturbation space to produce insight into the position-velocity tradespace. Depicted in Figure 5.14, the maximum value of ψ for pairs of position and velocity perturbation magnitudes in the 4-dimensional (planar position and velocity) expanding-shell discretization reflect the evolution of the design Jacobian, i.e., the partial derivatives used in the differential corrections process, in the perturbation space. The boundary of the dark blue region, signifying a relative similarity between the Jacobian matrices at the perturbed point and reference solution, correlates with boundary of the boundary of the main basin depicted in Figure 5.13a. Though intervention is required to select the upper limit for the coloration of the space, the form of the evolution of ψ and the critical features of the tradespace are consistent. This result indicates that the form of the

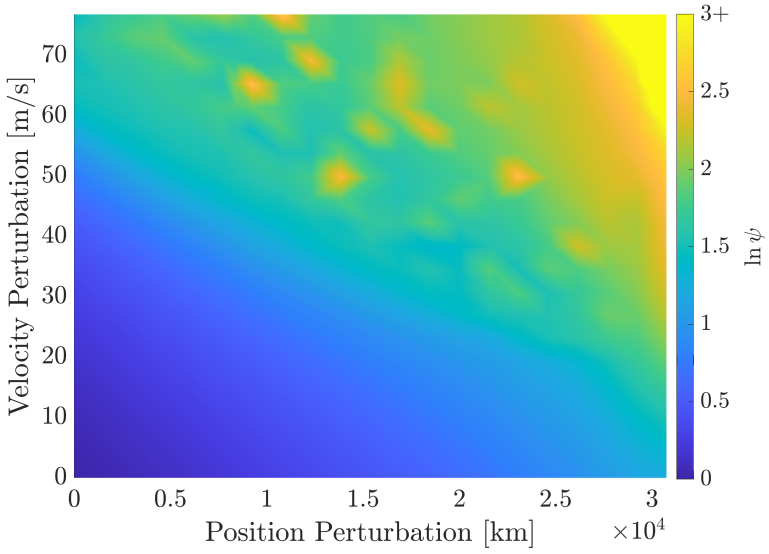

Figure 5.14. Evaluated Scalar ψ in the Position-Velocity Tradespace for Single-Maneuver DRO Targeting ($t_0 \approx 1.54T$)

convergence basin is related to the normalized change in the design Jacobian as perturbations are applied to the reference solution.

5.2 Two-Maneuver Targeting

A related targeting problem with two maneuvers is formulated to assess the convergence behavior characterization strategies from this investigation in a scenario that uses a multiple-shooting differential corrections strategy. Employing motion in the vicinity of the same underlying DRO, the first maneuver is executed at a fixed time of $t_0 = 0$ and located at the defining 70,000 km $\hat{\boldsymbol{x}}$-axis crossing, previously at t_{ref}, in the reference solution. A second maneuver is executed at time t_1 downstream, which is treated as parameter for studying possible design alternatives. Chosen to highlight connections to the single-maneuver scenario, reference trajectories are illustrated for $t_1 \approx 0.54T$ and $t_1 \approx 1.54T$ in Figures 5.15a and 5.15b, respectively. These impulsive maneuvers target the full reference state at $t_2 = 2T$, and the constraints are formulated to allow the position at t_1 to vary while being continuous across the incoming (superscript $-$) and outgoing (superscript $+$) states. State perturbations are

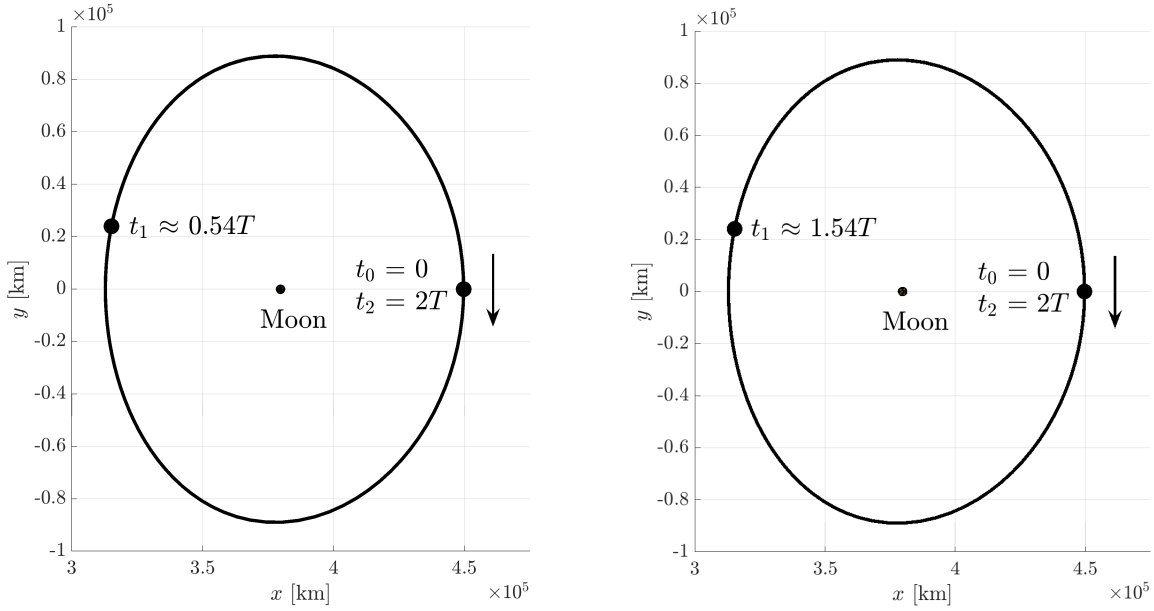

(a) Maneuver at $t_1 \approx 0.54T$ (b) Maneuver at $t_1 \approx 1.54T$

Figure 5.15. 70,000 km DRO Trajectory and Two-Maneuver Reference Locations

introduced at the first maneuver time, t_0, and the resulting perturbed targeting problem is formulated as

$$\boldsymbol{\mathcal{F}} = \begin{bmatrix} \boldsymbol{\rho}(t_1)^- - \boldsymbol{\rho}(t_1)^+ \\ \boldsymbol{\rho}(t_2)^- - \boldsymbol{\rho_d} \\ \dot{\boldsymbol{\rho}}(t_2)^- - \dot{\boldsymbol{\rho}}_{\boldsymbol{d}} \end{bmatrix} , \boldsymbol{\mathcal{X}} = \begin{bmatrix} \dot{\boldsymbol{\rho}}(t_0)^+ \\ \boldsymbol{\rho}(t_1)^+ \\ \dot{\boldsymbol{\rho}}(t_1)^+ \end{bmatrix} , \boldsymbol{\mathcal{Y}} = \begin{bmatrix} \boldsymbol{\mathcal{Y}}_1 \\ \boldsymbol{\mathcal{Y}}_2 \end{bmatrix} = \begin{bmatrix} \boldsymbol{\rho}(t_0) \\ \dot{\boldsymbol{\rho}}(t_0) \end{bmatrix} \tag{5.3}$$

where $\boldsymbol{\rho_d}$ and $\dot{\boldsymbol{\rho}}_{\boldsymbol{d}}$ denote the desired final position and velocity vectors on the reference orbit. To ground the analysis in a concrete scenario, this targeting problem is intended to reflect a possible method for station-keeping on the reference DRO after the execution of the single-maneuver arrival problem discussed above. To characterize the convergence behavior across a range of possible mission designs, the time of the second maneuver, t_1, is varied from 6 hours after t_0 to 6 hours before t_2, covering nearly two periods of the reference DRO.

The PDA strategy is implemented to study the impact of independent perturbations in initial position and velocity on the convergence behavior as t_1 is varied in this multiple-shooting problem. The principal directions consist of the set of j right singular vectors of

$\frac{\partial \mathcal{F}}{\partial \mathcal{Y}_i}\Big|_{(\mathcal{X}^*,\mathcal{Y}^*)}$ and the mode-3 singular vectors of $\frac{\partial \mathcal{F}}{\partial \mathcal{X}}\Big|^{-1}_{(\mathcal{X}^*,\mathcal{Y}^*)} \frac{\partial^2 \mathcal{F}}{\partial \mathcal{X} \partial \mathcal{Y}_i}\Big|_{(\mathcal{X}^*,\mathcal{Y}^*)}$, denoted $\boldsymbol{v}_{i,j}$ and $\boldsymbol{v}'_i$, respectively. The largest magnitude of position perturbation to result in convergence within 3 iterations is plotted in Figure 5.16a for each principal direction over the range of possible times for t_1. The dashed lines represent a chosen upper limit of 10 non-dimensional units that

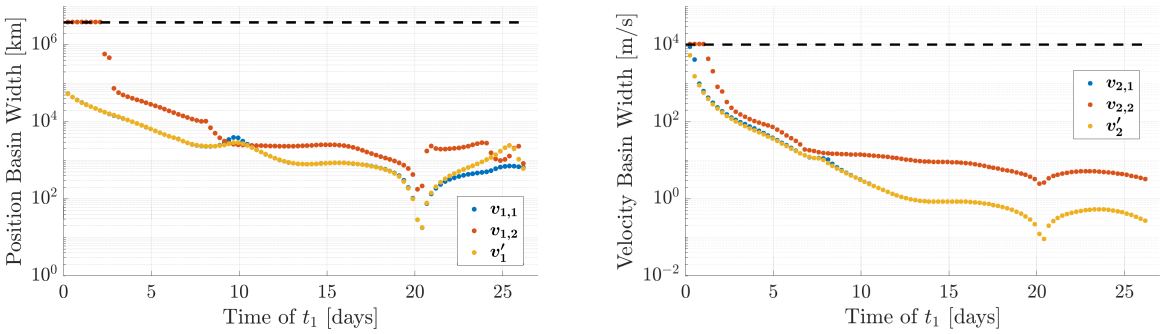

(a) Position Perturbation Subspace

(b) Velocity Perturbation Subspace

Figure 5.16. Individual Principal Direction Measurements for the Two-Maneuver DRO Scenario with a 3-Iteration Limit

prevent the computation of preposterously large measurements. Similarly, the basin width values measured via PDA in the velocity subspace is shown in Figure 5.16b. In the position subspace, discretization and simulation along the dominant right singular vector, $\boldsymbol{v}_{\mathbf{1,1}}$, and the direction of the largest normalized rate of change in the design Jacobian, $\boldsymbol{v}'_{\mathbf{1}}$, yield similar results for the basin width approximations across the majority of maneuver times, and the vector $\boldsymbol{v}_{\mathbf{1,2}}$ with a smaller singular value permits larger perturbation magnitudes. However, deviations from this trend are evident in two regions. First, discretization in all 3 directions produce similar basin width measurements when t_1 is approximately 10 days downstream from the initial time. Additionally, when the time of the maneuver at t_1 is over 21 days after the initial perturbation, the basin width measurements across the principal directions result from discretization along $\boldsymbol{v}_{\mathbf{1,1}}$. In the velocity subspace, the basin width approximation is dominated by measurements in the $\boldsymbol{v}_{\mathbf{2,1}}$ and $\boldsymbol{v}'_{\mathbf{2}}$ directions that visually overlap in Figure 5.16b. These results reinforce the potential limitations of the heuristic that motivates PDA as an approximation for the basin width and the benefits of discretizing in all principal directions as a mitigation strategy.

A more complete description of the convergence behavior is attained by varying the targeting iteration limit from 3 to 8 and selecting the minimum basin width value for each principal direction. The PDA-measured basin width in the $\mathcal{Y}_1$ subspace, associated with planar position perturbations at t_0, is plotted in Figure 5.17a for each update iteration limit. The evaluated basin metrics γ_1 and γ_1', defined in Equations (4.35) and (4.44), respectively,

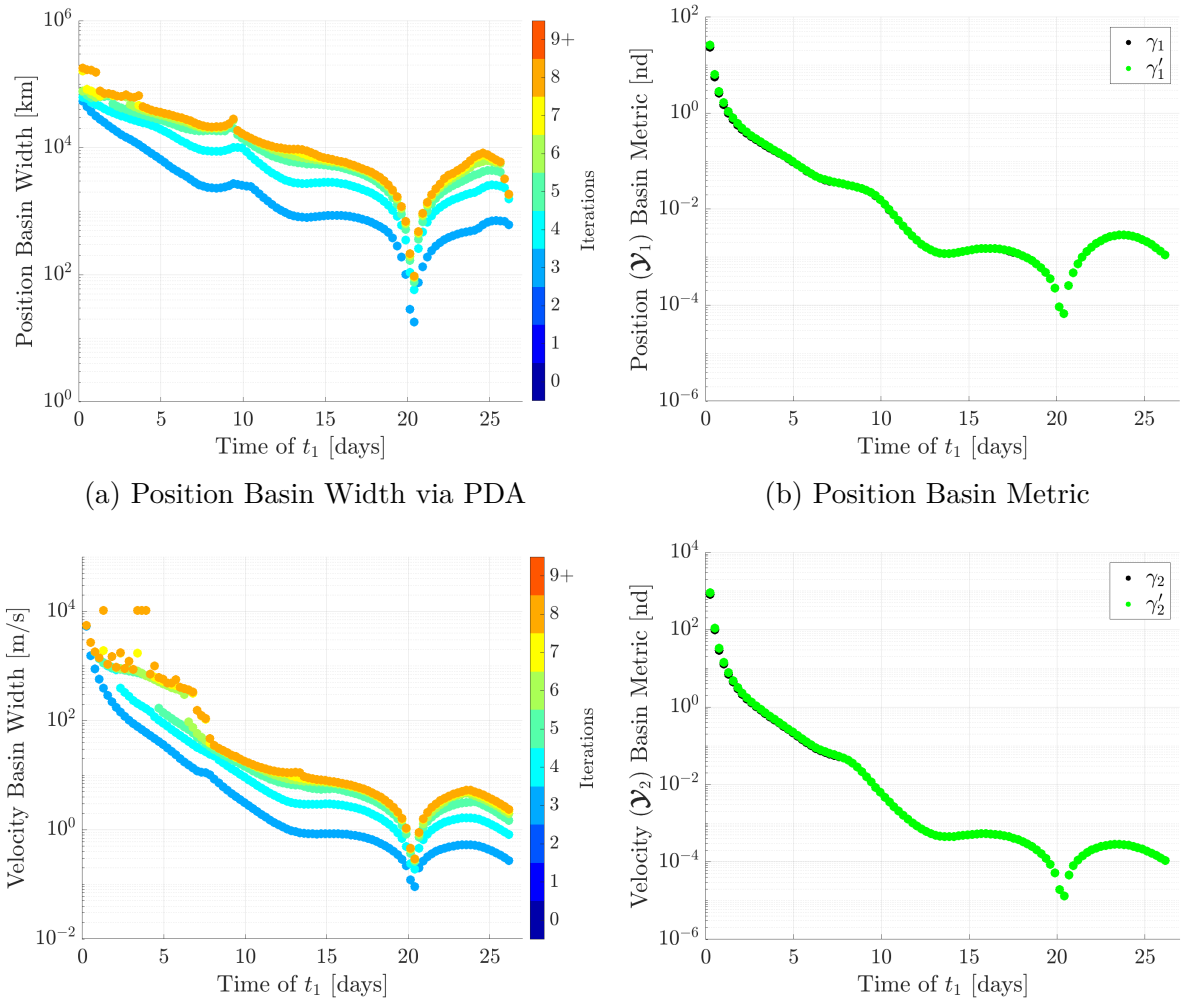

(a) Position Basin Width via PDA

(b) Position Basin Metric

(c) Velocity Basin Width via PDA

(d) Velocity Basin Metric

Figure 5.17. Two-Maneuver DRO Scenario PDA Basin Width Measurements and Evaluated Basin Metrics

for each candidate maneuver time t_1 are plotted in Figure 5.17b. Upon visual inspection, strong correlation exists between the trends of the basin width measurements and the basin metric values at the reference solutions as the parameter t_1 evolves. Importantly, the abrupt

basin contraction at $t_1 \approx 20.2$ days is predicted by the basin metric values and confirmed in the PDA-measured basin widths. The basin widths and metric values for the Y_2 velocity subspace are plotted in Figures 5.17c and 5.17d, respectively. Again, the forms of the basin width contours and the basin metric values share key features, and the contraction in the basin width is predicted by the values of γ_2 and γ_2'. In this targeting scenario, the values of γ_i, produced by the matrix norm, and the values of γ_i', higher-order singular values resulting from the optimization problem in Equation (4.45), are approximately equivalent and provide similar insights into the problem.

An alternative characterization of the convergence behavior according to the FTLE-inspired, evaluated quantities from Equations (4.15) and (4.14) does not possess as strong of a predictive capability. The FTLE-inspired quantities from the independent perturbation Jacobian matrices and the design Jacobian matrix are shown in Figure 5.18. None of these

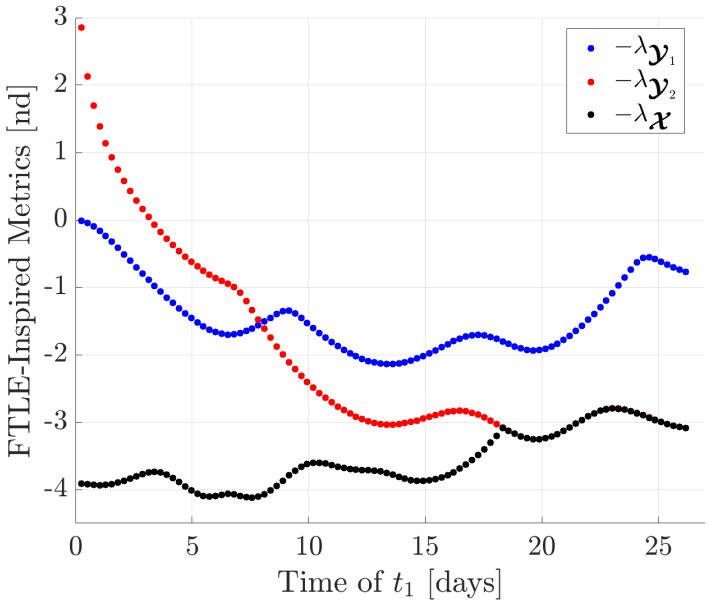

Figure 5.18. FTLE-Inspired Quantities in the Two-Maneuver DRO Scenario

metrics fully predict the behavior observed in Figures 5.17a and 5.17c, and, in particular, none of the FTLE-inspired metrics predict the rapid decrease in basin width at $t_1 \approx 20.2$ days, suggesting that the increased cost of computing 2^{nd}-order derivatives for the basin metrics is warranted.

Analogous to the single-maneuver targeting problem, the principal plane conditions detailed in Equations (4.24), (4.25), and (4.20) are examined to select one favorable and one unfavorable time for the maneuver at t_1 for detailed analysis of the position-velocity tradespace. Analysis of the linear models suggests the principal plane heuristic approximation is likely to correlate with the theoretical tradespace when there is a small angle between the dominant constraint-space principal directions, i.e., $\angle(\boldsymbol{u_{1,1}}, \boldsymbol{u_{2,1}}) \approx 0$, and a large ratio of singular values in the independent subspaces, i.e., $\frac{\sigma_{i,1}}{\sigma_{i,2}} \gg 1$. The values of the constraint-space angle and the singular value ratio are plotted in Figures 5.19a and 5.19b, respectively. As predicted, the

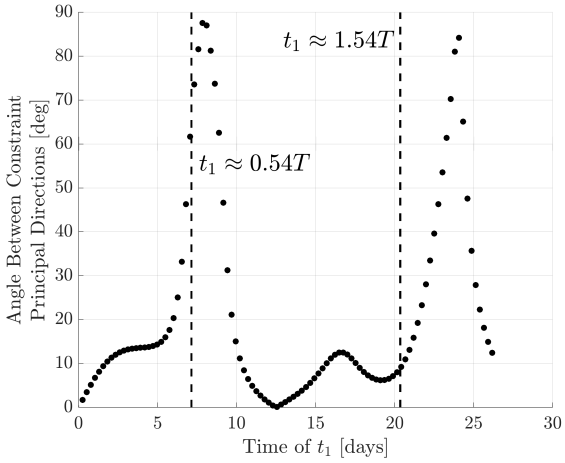

(a) Angle Between Constraint Principal Directions

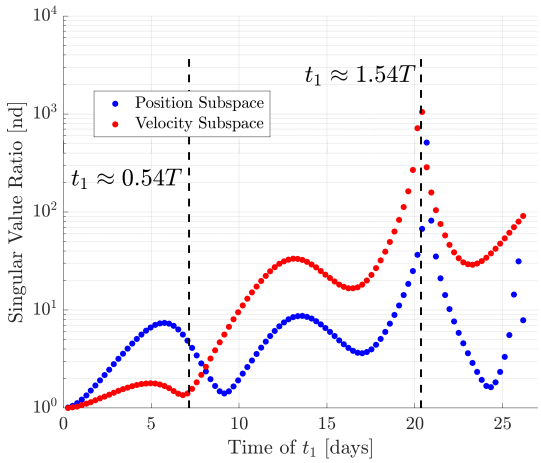

(b) Singular Value Ratio

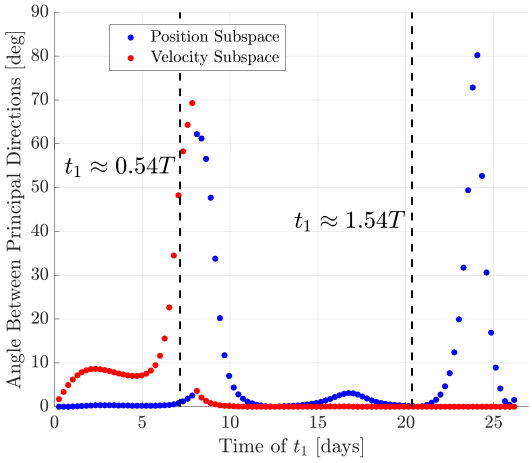

(c) Principal Direction Projection Angles

Figure 5.19. Principal Plane Conditions for Two-Maneuver DRO Targeting

satisfaction of these conditions correlates with nearly co-planar principal directions $\boldsymbol{v_1}$, $\boldsymbol{v_{1,1}}$ and $\boldsymbol{v_{2,1}}$, which is confirmed by the plots of the angular deviation θ_i from Equation (4.20) depicted in Figure 5.19c. From inspection of these results, the maneuver time of $t_1 \approx 1.54T$ is favorable for an approximation of the tradespace via analysis of the principal plane due to its nearly co-planar principal directions and dominant singular values of the perturbation Jacobian matrices $\frac{\partial \mathcal{F}}{\partial \mathcal{Y}_1}\Big|_{(\mathcal{X}^*,\mathcal{Y}^*)}$ and $\frac{\partial \mathcal{F}}{\partial \mathcal{Y}_2}\Big|_{(\mathcal{X}^*,\mathcal{Y}^*)}$. Alternatively, the maneuver time of $t_1 \approx 0.54T$ is unfavorable for the application of the principal plane heuristic due to its large out-of-plane angles and singular values of similar magnitude. Interestingly, this observation is the reverse of the single-maneuver targeting analysis, highlighting the importance of incorporating both the trajectory and the targeting problem formulation in convergence basin analysis.

5.2.1 Favorable Principal Plane Conditions ($t_1 \approx 1.54T$)

An exploration of the two-maneuver scenario with $t_1 \approx 1.54T$ is begun by first assessing the alignment of the principal directions in the independent position and velocity perturbation subspaces with form of the local main convergence basin. Given perturbations at the time of the first maneuver, t_0, the number of iterations required to achieve convergence is plotted across $\mathcal{Y}_1$, or the position subspace, in Figure 5.20a. The principal direction vectors

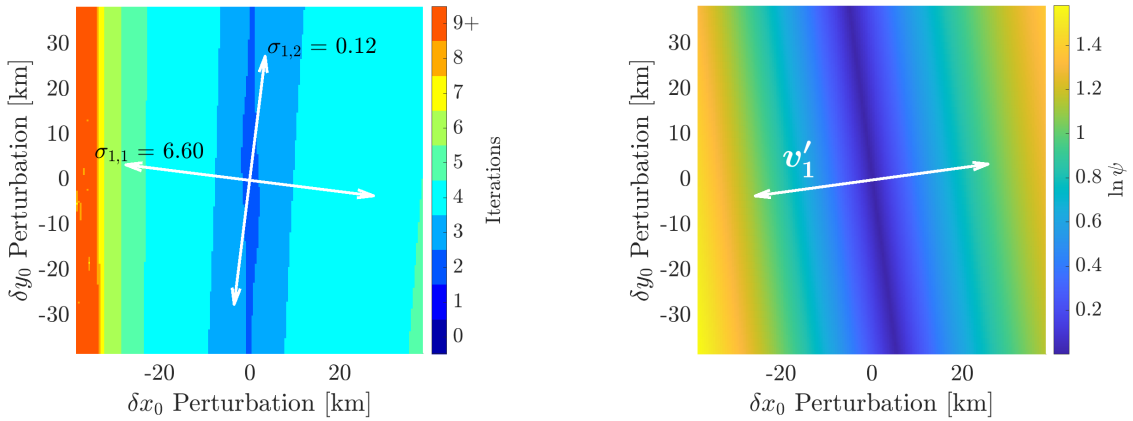

(a) Iterations to Converge

(b) Evaluated Scalar ψ

Figure 5.20. The Position Perturbation Space $\mathcal{Y}_1$ for Two-Maneuver DRO Targeting ($t_1 \approx 1.54T$)

$\boldsymbol{v_{1,1}}$ and $\boldsymbol{v_{1,2}}$ are plotted in white and labelled according to the associated singular values of $\frac{\partial \boldsymbol{\mathcal{F}}}{\partial \boldsymbol{\mathcal{Y}}_1}\Big|_{(\boldsymbol{\mathcal{X}}^*, \boldsymbol{\mathcal{Y}}^*)}$. In the plane, a dominant direction with the most rapid change in required iterations clearly exists and is closely aligned with the dominant singular vector $\boldsymbol{v_{1,1}}$. Figure 5.20b depicts the values of ψ, a measure of the similarity of the design Jacobian matrix $\frac{\partial \boldsymbol{\mathcal{F}}}{\partial \boldsymbol{\mathcal{X}}}\Big|_{(\boldsymbol{\mathcal{X}}, \boldsymbol{\mathcal{Y}})}$ at each perturbed point to the matrix at the reference solution, and the vector $\boldsymbol{v_1'}$ that reflects the direction with the largest local normalized change in the design Jacobian matrix. In this perturbed targeting scenario, the values of ψ are relatively-low compared to the values of previously-examined scenarios and develop with some symmetry in the perturbation space. In contrast, the increase in iterations and the edge of the main basin observed in Figure 5.20a does not exhibit the same symmetry. The misalignment between these results suggests that the difficulty in the corrections process observed in the initial position perturbation subspace is not primarily driven by change in the design Jacobian across that space but, instead, by another mechanism. Because the partial derivatives in the problem are computed with the dependency assumptions for multiple-shooting problems from Equation (3.49), all interactions between perturbations in the position at the time t_0 and the state variables at the times t_1 and t_2 as the trajectory is updated beyond the first iteration are not captured in this method, revealing a limitation in its descriptive capability.

The convergence behavior in the initial velocity perturbation space, $\boldsymbol{\mathcal{Y}}_2$, is described by both the local growth in the constraints and the normalized change in the design Jacobian matrix. The number of iterations required to converge to a new solution is plotted across the $\boldsymbol{\mathcal{Y}}_2$ space with the principal directions $\boldsymbol{v_{2,1}}$ and $\boldsymbol{v_{2,2}}$ in Figure 5.21a, and the corresponding depiction of the values of ψ in the space are plotted in Figure 5.21b with the vector $\boldsymbol{v_2'}$. In Figure 5.21a, the dominant singular value of $\frac{\partial \boldsymbol{\mathcal{F}}}{\partial \boldsymbol{\mathcal{Y}}_2}\Big|_{\boldsymbol{\mathcal{X}}^*, \boldsymbol{\mathcal{Y}}^*)}$ is three orders of magnitude larger than smaller singular value, and the form of the convergence basin follows the structure of the right singular vectors. Additionally, the direction with the largest local normalized change in the design Jacobian matrix, indicated by the mode-3 singular vector $\boldsymbol{v_2'}$, is closely aligned with the dominant singular vector $\boldsymbol{v_{2,1}}$ and the steepest gradient in the iteration count. In contrast to the results in the $\boldsymbol{\mathcal{Y}}_1$ space, convergence in the $\boldsymbol{\mathcal{Y}}_2$ space appears to be largely driven by the predicted local growth in the constraints and the normalized change in the design Jacobian.

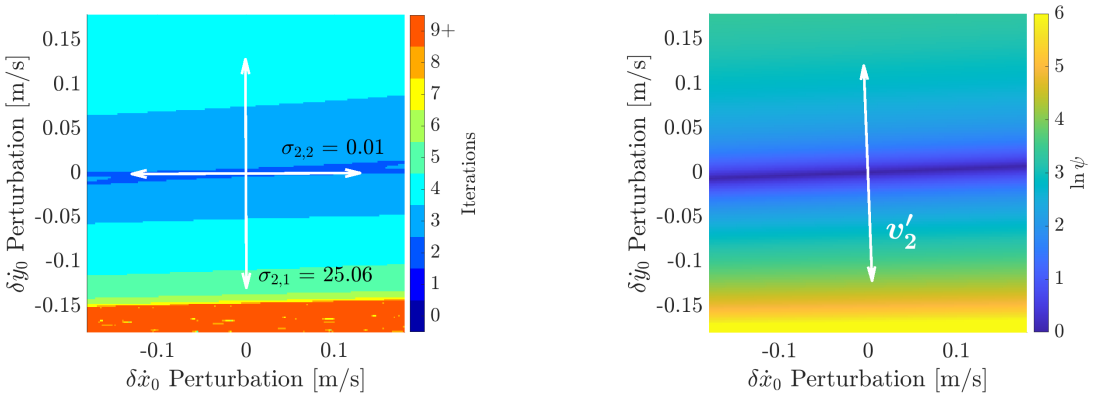

(a) Iterations to Converge (b) Evaluated Scalar ψ

Figure 5.21. The Velocity Perturbation Space $\mathcal{Y}_2$ for Two-Maneuver DRO Targeting ($t_1 \approx 1.54T$)

To characterize the tradespace of position and velocity perturbations, the principal plane approximation is compared to a discretization across a series of expanding shells in the full perturbation space. Because the scenario with a maneuver time of $t_1 \approx 1.54T$ satisfies the assumption of nearly co-planar directions $\boldsymbol{v_{1,1}}$, $\boldsymbol{v_{2,1}}$, and $\boldsymbol{v_1}$, the critical features of the tradespace are expected to appear in an interrogation of the principal plane, constructed via $\boldsymbol{v_{1,1}}$ and $\boldsymbol{v_{2,1}}$. The tradespace characterized by the maximum number of iterations required to converge to a solution for each pair of position and velocity perturbation magnitudes is plotted in Figure 5.22a. The results of the principal plane analysis is illustrated in Figure

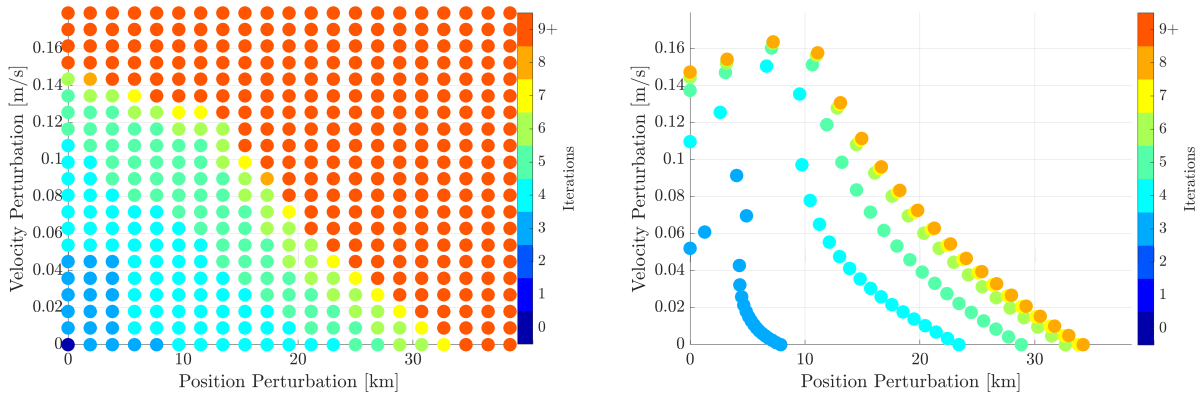

(a) Expanding Shell Discretization (b) Principal Plane Approximation

Figure 5.22. Position-Velocity Tradespace for Two-Maneuver DRO Targeting ($t_0 \approx 1.54T$)

5.22b where each point represents the largest magnitude along the vector $\boldsymbol{\eta}(s)$, defined in Equation (4.18), in the principal plane for which all targeting simulations converge within a given iteration limit, indicated according to the color of the point. As predicted from analysis of the co-planar conditions, limiting the discretization of the perturbation space to the parameterized vectors $\boldsymbol{\eta}(s)$ in the principal plane provides an accurate approximation for the iteration Pareto frontiers in the broader analysis via an expanding shell discretization while requiring fewer simulations.

The form of the position-velocity tradespace is compared to the trends in ψ across the full state perturbation space, plotted in Figure 5.23. Each pair of position and velocity perturba-

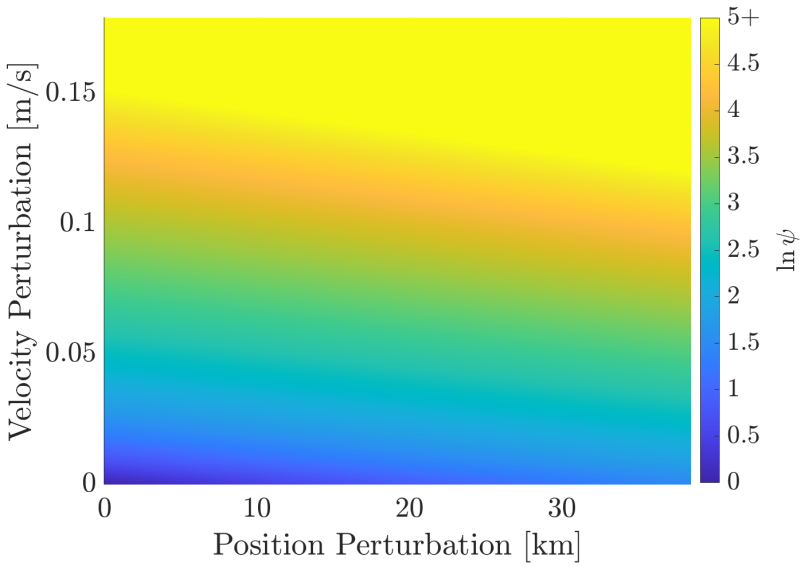

Figure 5.23. Evaluated Scalar ψ in the Position-Velocity Tradespace for Two-Maneuver DRO Targeting ($t_0 \approx 1.54T$)

tion magnitudes is colored according to the maximum evaluated magnitude of ψ, measuring the largest normalized change in the design Jacobian across the perturbation space. Though the upper bound of the color gradient is intentionally selected to make any similarity in form apparent, the underlying values are unchanged by this choice. The independent analysis of velocity perturbations in Figure 5.21a suggests that values of ψ correlate with the form of the basin for perturbations with relatively significant velocity perturbations and relatively small perturbations in position, roughly corresponding to transition from orange to yellow

in Figure 5.23. Analysis of the independent position perturbation space did not demonstrate a clear correlation with ψ, consequently, the form of the tradespace is not predicted by the values of ψ where position perturbations have the largest contribution.

5.2.2 Unfavorable Principal Plane Conditions ($t_1 \approx 0.54T$)

For the two-maneuver DRO targeting scenario where the second impulsive event is executed at $t_1 \approx 0.54T$, the singular values of the independent perturbation Jacobian matrices are closer in magnitude, suggesting a more uniform development of the convergence basin and a more challenging characterization process. The $\boldsymbol{\mathcal{Y}}_1$ perturbation space, defined as perturbations in position at the time of the first maneuver t_0, is shown in Figure 5.24a with each point colored according to the number of targeting iterations required to achieve convergence. The right singular vectors of $\frac{\partial \boldsymbol{\mathcal{F}}}{\partial \boldsymbol{\mathcal{Y}}_1}\Big|_{(\boldsymbol{\mathcal{X}}^*, \boldsymbol{\mathcal{Y}}^*)}$ are drawn on the figure with their cor-

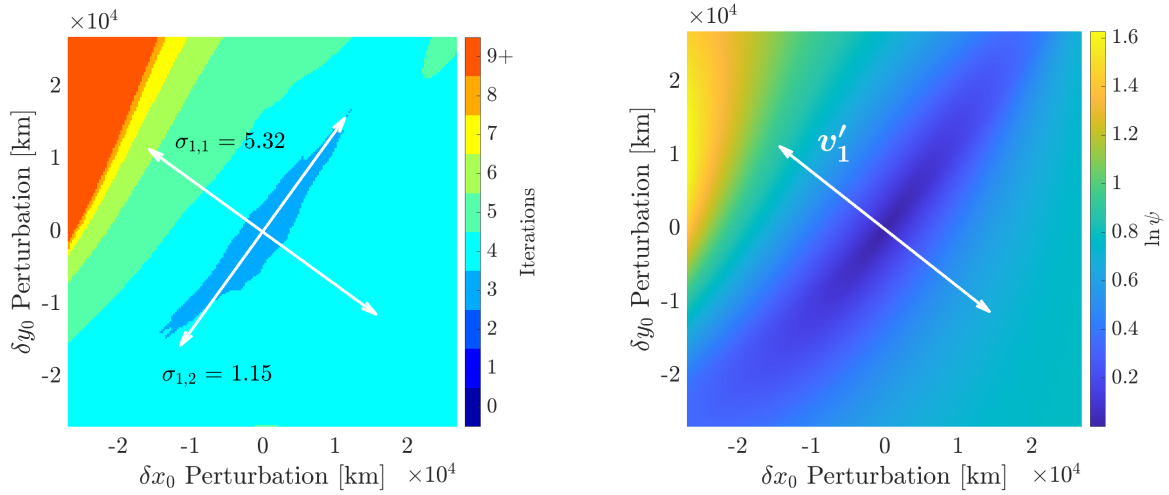

(a) Iterations to Converge

(b) Evaluated Scalar ψ

Figure 5.24. The Position Perturbation Space $\boldsymbol{\mathcal{Y}}_1$ for Two-Maneuver DRO Targeting ($t_1 \approx 0.54T$)

responding singular values, and the form of the basin for small iteration counts is structured along these directions. Additionally, the evolution of the design Jacobian correlates with the structure that limits the main basin at high iteration limits, as shown via the plot of ψ values at each point in Figure 5.24a, which also includes the direction of the maximum local normalized change in the design Jacobian due to perturbations in initial position, $\boldsymbol{v}_1'$. Over-

all, the information gained by the perturbation Jacobian matrix and the normalized change in the design Jacobian matrix from the reference provides insight into the basin structure.

The perturbation subspace associated with change in the initial velocity possesses a more complex structure of the local main basin. Plotted in Figure 5.25a, the convergence basin emanates from the origin with greater uniformity for small iteration counts, a characteristic that is predicted by the relative magnitudes of the singular values $\sigma_{2,1}$ and $\sigma_{2,2}$. For regions

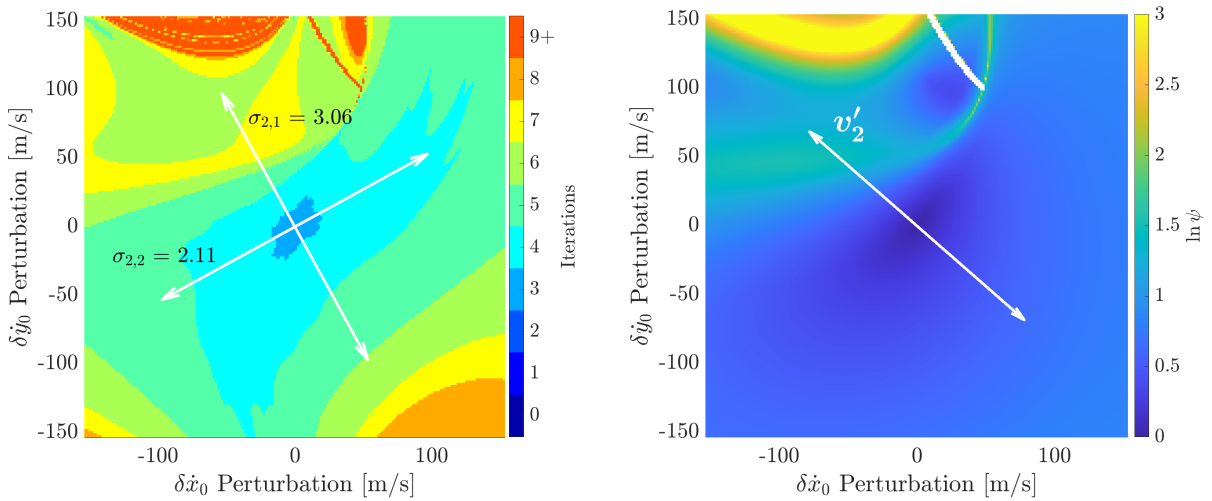

(a) Iterations to Converge

(b) Evaluated Scalar ψ

Figure 5.25. The Velocity Perturbation Space $\boldsymbol{\mathcal{Y}}_2$ for Two-Maneuver DRO Targeting ($t_1 \approx 0.54T$)

where the iteration count exceeds 6 in this velocity perturbation subspace, nonlinear effects begin to dominate, and the structure of the basin develops less predictably. The values of ψ in the subspace are plotted in Figure 5.25b, and regions with elevated values of ψ appear to correlate with the locations of iteration contours in the top left portions of the figures. The directions $\boldsymbol{v_{2,1}}$ and $\boldsymbol{v_2'}$ continue to correlate closely with the direction that results in the steepest iteration gradient in the monotonic region. Therefore, even in convergence basins with more ambiguous, uniform local development and significant contributions from nonlinear terms, the directions computed from the partial derivatives evaluated at the reference solution provide useful information about the local structure.

The scenario with a maneuver event at $t_1 \approx 0.54T$ is selected due to conditions that violate the co-planar assumption of the principal plane strategy; therefore, a difference is expected between the tradespaces generated via the 4-dimensional discretization via expanding shells and the principal plane analysis. The position-velocity tradespace associated with the fuller expanding shell method is plotted in Figure 5.26a, and the tradespace resulting from the linear searches along the parameterized vectors $\boldsymbol{\eta}(s)$, defined in Equation (4.18), that comprise the principal plane are shown in Figure 5.26b. For iteration limits of 6 and

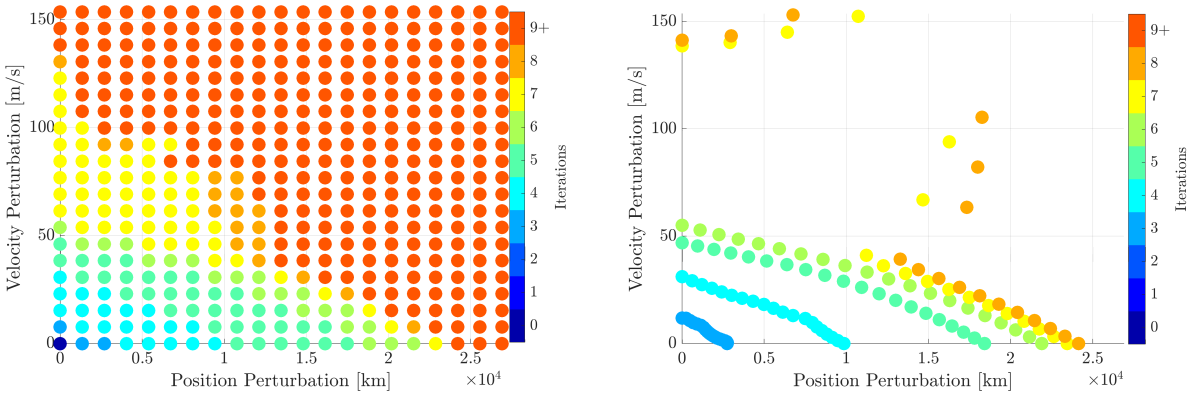

(a) Expanding Shell Discretization

(b) Principal Plane Approximation

Figure 5.26. Position-Velocity Tradespace for Two-Maneuver DRO Targeting ($t_1 \approx 0.54T$)

fewer, the contours derived from the principal plane analysis mirror those of the more complete discretization of the perturbation space. In fact, the low iteration count region is represented in a plot of ψ in the joint perturbation space in Figure 5.27 by the blue-colored region, associated with small changes in the design Jacobian matrix. As the iteration limit increases, however, the tradespace approximation in the principal plane overestimates the allowable combinations of position and velocity magnitude for which the targeting problem always converges within a given number of iterations. As apparent in the depiction of the independent velocity subspace in Figure 5.25a, the tradespace develops less predictably for these higher iteration limits, especially in regions of the principal plane that possess a larger component in the velocity subspace. This complexity is observed in the depiction of ψ in the same velocity-dominated region of the tradespace. Though not a perfect characterization

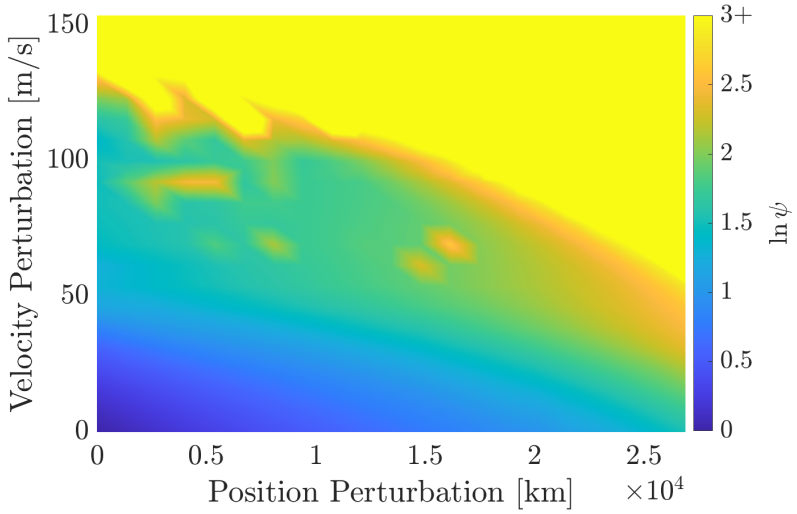

Figure 5.27. Evaluated Scalar ψ in the Position-Velocity Tradespace for Two-Maneuver DRO Targeting ($t_0 \approx 0.54T$)

of the tradespace, the principal plane analysis provides a reasonable approximation for the upper limit of convergence performance in the full perturbation space, and the knowledge obtained from the co-planar criteria provides an apt warning that the approximation may struggle to approximate the critical features.

6. APPLICATION TO EARTH-MOON L2 SOUTHERN HALO ORBITS

As potential destination orbits for spacecraft conducting scientific activities in the vicinity of the Moon, the family of L_2 halo orbits are a focus of ongoing research. In particular, the Near Rectilinear Halo Orbits (NRHOs), a subset of this periodic orbit family, garner significant attention as the destination orbit for NASA's Gateway mission, consisting of a crewed outpost in the lunar vicinity [65]–[67]. The periodic orbit family is obtained through analysis of the CRTBP and results from a bifurcation from planar motion about the L_2 point, i.e., a particular member of the L_2 Lyapunov family of periodic orbits. Each member of the L_2 halo orbit family has a counterpart with motion that is reflected across the $\hat{\boldsymbol{x}}$-$\hat{\boldsymbol{y}}$ plane, and the "southern" subset of the family corresponds to trajectories with an apolune in the $-\hat{\boldsymbol{z}}$ direction. A sampling of periodic orbits in the Earth-Moon L_2 southern halo family are depicted in Figure 6.1a, beginning with the bifurcating planar orbit and ending with the NRHO with a perilune distance equal to the lunar radius. This family consists of periodic

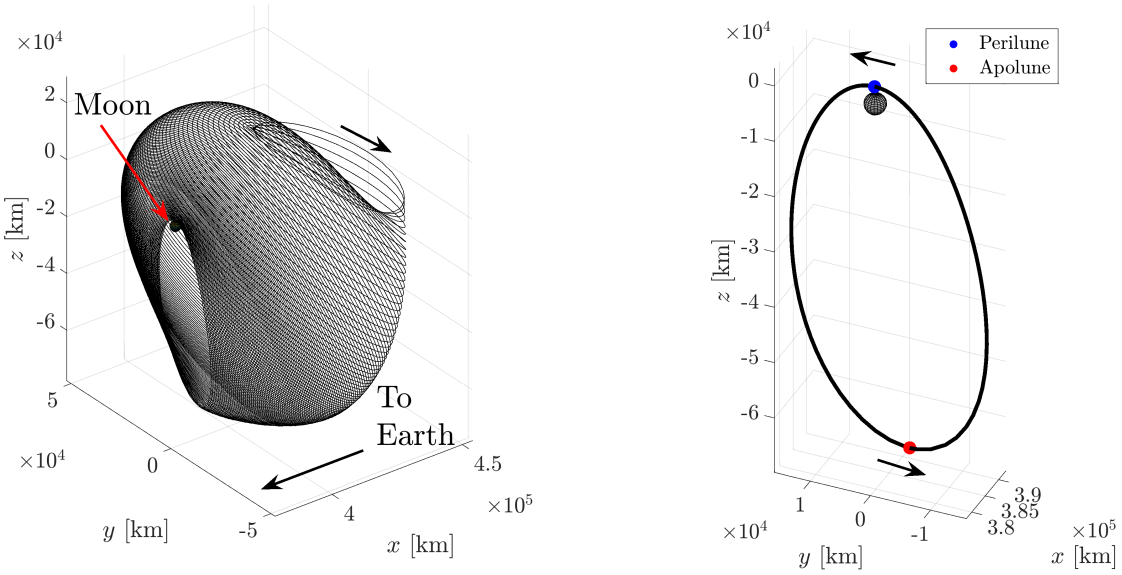

(a) L_2 Southern Halo Family (b) 9:2 NRHO

Figure 6.1. L_2 Southern Halo Family in the Earth-Moon Rotating Frame

orbits that exist in three spatial dimensions, vary greatly in their proximity to the primary gravitational bodies, and possess differing stability properties; thus, investigation of the L_2 southern halo orbit family is a useful application for the characterization of convergence behavior. The particular NRHO, possessing 9:2 lunar synodic resonance, is plotted in Figure 6.1b and serves as a representation of the reference motion for the Gateway mission in the CRTBP. The nearly-stable 9:2 NRHO is characterized by a large apolune distance, oriented out-of-plane relative to the Earth-Moon orbital plane, and a relatively close perilune passage near the Moon, both denoted in Figure 6.1b, providing dynamically-interesting reference motion for the study of convergence in perturbed targeting problems.

6.1 Convergence Behavior Across the L_2 Southern Halo Family

A scenario is considered where a trajectory designer seeks to identify potential periodic orbits for a mission from the L_2 southern halo orbit family. Supposing the engineer seeks to maintain the geometry and period of the reference orbit, a preliminary station-keeping concept is considered that involves the execution of a maneuver at apolune to target back to the reference apolune position at a fixed time-of-flight downstream that is an integer multiple of the orbital period. To investigate the permissible error in the spacecraft state at the time of the targeting and maneuver execution, a perturbed targeting problem is formulated and represented as

$$\boldsymbol{\mathcal{F}} = \boldsymbol{\rho}(t_1) - \boldsymbol{\rho_d} \ , \ \boldsymbol{\mathcal{X}} = \dot{\boldsymbol{\rho}}(t_0) \ , \ \boldsymbol{\mathcal{Y}} = \begin{bmatrix} \boldsymbol{\mathcal{Y}}_1 \\ \boldsymbol{\mathcal{Y}}_2 \end{bmatrix} = \begin{bmatrix} \boldsymbol{\rho}(t_0) \\ \dot{\boldsymbol{\rho}}(t_0) \end{bmatrix} \tag{6.1}$$

where the set of perturbation variables is decomposed into $\boldsymbol{\mathcal{Y}}_1$ and $\boldsymbol{\mathcal{Y}}_2$, representing the initial position and velocity vectors, respectively. The desired final position, $\boldsymbol{\rho_d}$, is defined as the position of the apolune point for the reference periodic orbit, and the propagation time, t_1, is fixed within the targeting problem.

The convergence behavior of the perturbed targeting problem is investigated across a sampling of L_2 southern halo orbits for fixed times-of-flight, and the case where t_1 is equal to 1 period of the underlying periodic orbit is examined first. Measurements of the independent $\boldsymbol{\mathcal{Y}}_1$ and $\boldsymbol{\mathcal{Y}}_2$ perturbations subspaces via PDA provide insight into the trends in convergence

behavior across family of reference orbits. For each subspace $\boldsymbol{\mathcal{Y}}_i$, the principal directions of discretization are comprised of the vectors $\boldsymbol{v_{i,j}}$ for $j = 1 \dots p_i$, i.e., the right singular vectors of $\frac{\partial \boldsymbol{\mathcal{F}}}{\partial \boldsymbol{\mathcal{Y}}_i}\Big|_{(\boldsymbol{\mathcal{X}}^*, \boldsymbol{\mathcal{Y}}^*)}$, and the vector $\boldsymbol{v_i'}$, i.e., the mode-3 singular vector associated with the largest singular value of $\frac{\partial \boldsymbol{\mathcal{F}}}{\partial \boldsymbol{\mathcal{X}}}\Big|^{-1}_{(\boldsymbol{\mathcal{X}}^*, \boldsymbol{\mathcal{Y}}^*)} \frac{\partial^2 \boldsymbol{\mathcal{F}}}{\partial \boldsymbol{\mathcal{X}} \partial \boldsymbol{\mathcal{Y}}_i}\Big|_{(\boldsymbol{\mathcal{X}}^*, \boldsymbol{\mathcal{Y}}^*)}$. For the independent position and velocity perturbation subspaces, the basin width magnitudes in each principal direction are plotted in Figure 6.2a and 6.2b, respectively, with a limit of 3 targeting iterations for each sampled trajectory in the L_2 southern halo orbit family, uniquely defined by its perilune radius. In

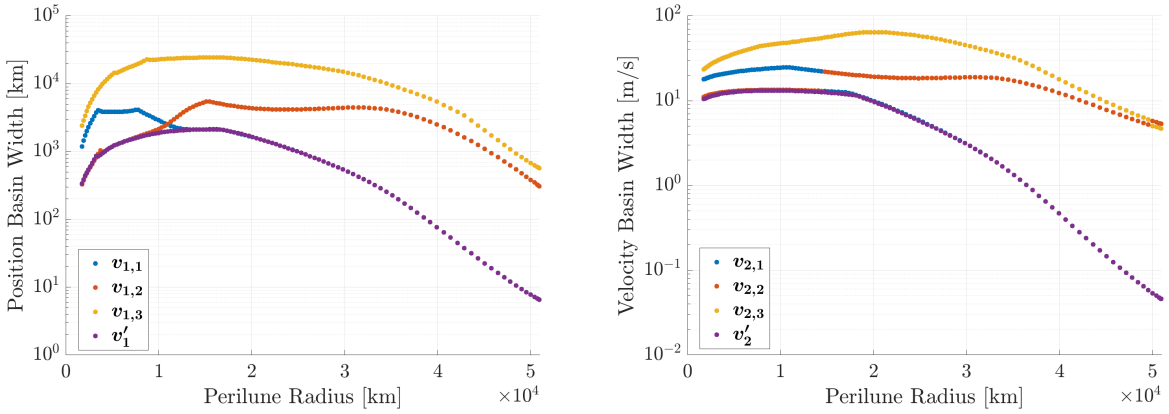

(a) Position Perturbation Subspace

(b) Velocity Perturbation Subspace

Figure 6.2. Individual Principal Direction Measurements 1-Period Halo Targeting with a 3-Iteration Limit

Figure 6.2a, the minimum basin width value across the set of directions is associated with the vector $\boldsymbol{v_1'}$, corresponding to the direction with the largest local normalized change in the design Jacobian due to 2nd-order influences. Though these measurements are roughly equivalent to information gained from the vectors associated with the perturbation Jacobian, the limiting behavior switches between $\boldsymbol{v_{1,2}}$ and $\boldsymbol{v_{1,1}}$ at the trajectory with a reference perilune radius of approximately 11,000 km. Thus, discretization solely along the dominant direction in the $\boldsymbol{\mathcal{Y}}_1$ subspace driving growth in the constraints, reflected in the vector $\boldsymbol{v_{1,1}}$, does not provide sufficient information to approximate the basin width across the family of orbits. A similar phenomenon is observed in Figure 6.2b, where the limiting feature of the convergence basin for the selected iteration limit switches between $\boldsymbol{v_{2,2}}$ and $\boldsymbol{v_{2,1}}$ but is consistently aligned with the vector $\boldsymbol{v_2'}$, reflecting the dominant direction of relative

nonlinearity to 2nd order. These results indicate that the local relative nonlinearity across the perturbation space characterizes the basin width in these targeting scenarios rather than the local linear rate of growth in the constraint vector.

The convergence basins associated with these targeting problems are further characterized by taking the minimum basin width value obtained via the PDA measurement technique for a range of iteration limits. For a 1-period time-of-flight, the basin width measurements for perturbations in the initial position across the family are colored in Figure 6.3a for limits of 4 through 8 iterations. For most of the reference trajectories, the trend is consistent across the

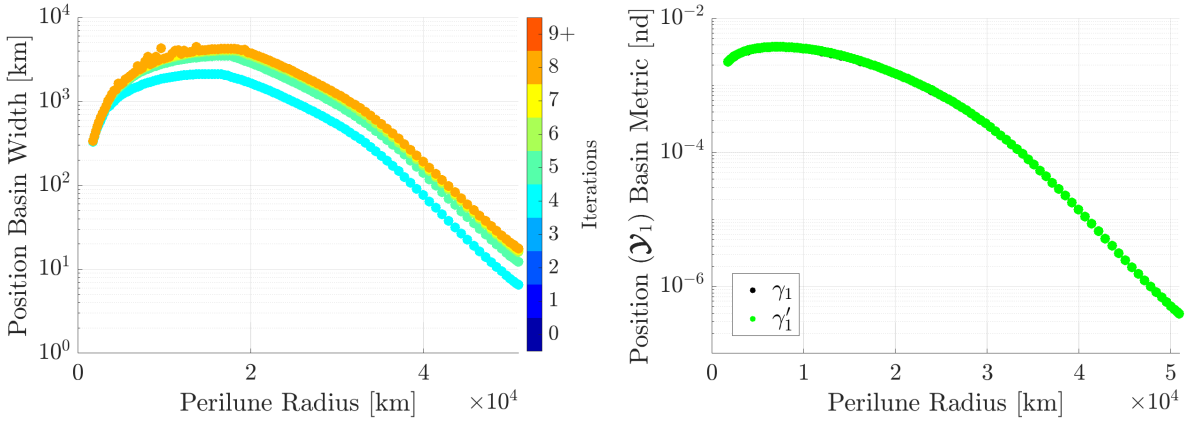

(a) Position Basin Width via PDA

(b) Position Basin Metric

(c) Velocity Basin Width via PDA

(d) Velocity Basin Metric

Figure 6.3. 1-Period Halo Targeting PDA Basin Width Measurements and Evaluated Basin Metrics

range of iteration limits; however, scattered behavior is visible at limits of 7 and 8 iterations for reference trajectories with perilune radii less than 20,000 km. This non-smooth behavior

is indicative of traversal into the chaotic region between main basins in perturbation space and suggests that limits above 6 iterations fail to guarantee predictable convergence to the main basins of the reference solutions in this perilune range. The basin metrics γ_1 and γ_1', computed via Equations (4.35) and (4.44), respectively, in the $\boldsymbol{\mathcal{Y}}_1$ subspace measure the local normalized rate of change in the design Jacobian for each targeting problem and are plotted in Figure 6.3b. Across the range of reference orbits, the basin metric essentially captures the (relatively simple) features of the trends in measured convergence basin width for targeting scenarios with 1-period times-of-flight. Additionally, the value of basin metric is observed to be insensitive to the method of computation. In other words, the matrix-norm approximation in Equation (4.35) produces similar results to the more costly higher-order singular value computation in Equation (4.44). Similar analysis of the $\boldsymbol{\mathcal{Y}}_2$ velocity subspace indicates that the trends in the PDA-measured basin width across the set of reference trajectories, shown in Figure 6.3c, are also reflected in the plots of the basin metrics γ_2 and γ_2', shown in Figure 6.3d. Defined by Equation (4.15), the values of the FTLE-inspired metrics $\lambda_{\boldsymbol{\mathcal{Y}}_1}$ and $\lambda_{\boldsymbol{\mathcal{Y}}_2}$, which utilize 1$^{\text{st}}$-order information about local growth rate in constraints, are plotted in Figure 6.4 and do not accurately predict the relative convergence behavior for reference trajectories with perilune radii of less than 10,000 km. This result suggest that the relative nonlinearity in

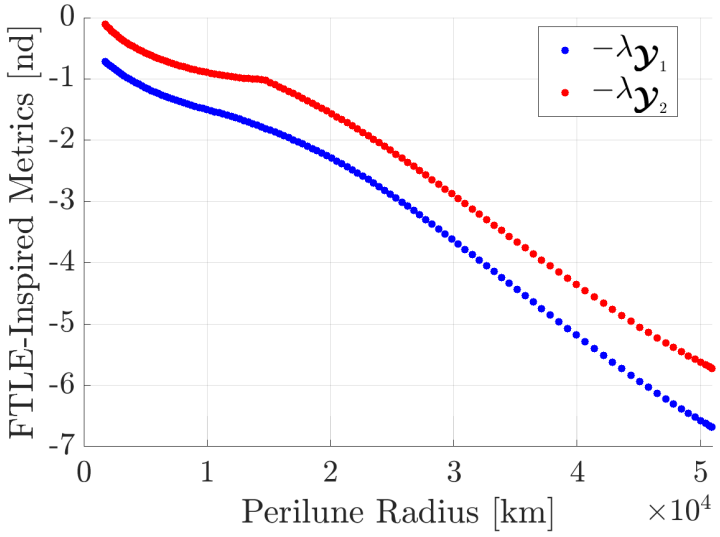

Figure 6.4. FTLE-Inspired Quantities for 1-Period Halo Targeting

each $\boldsymbol{\mathcal{Y}}_i$ perturbation subspace, measured via γ_i or γ_i', is the dominant factor in convergence behavior for the 1-period perturbed targeting problem across the set of reference orbits.

More complex trends in convergence behavior are observed by increasing the time-of-flight in these perturbed targeting problems to 2 periods of the underlying reference orbits. The PDA-measured basin widths in Figure 6.5a for iteration limits from 4 through 8 characterize the trends in convergence behavior in the $\boldsymbol{\mathcal{Y}}_1$ position perturbation subspace for these 2-period fixed-time targeting problems. As the reference trajectories evolve in perilune radius,

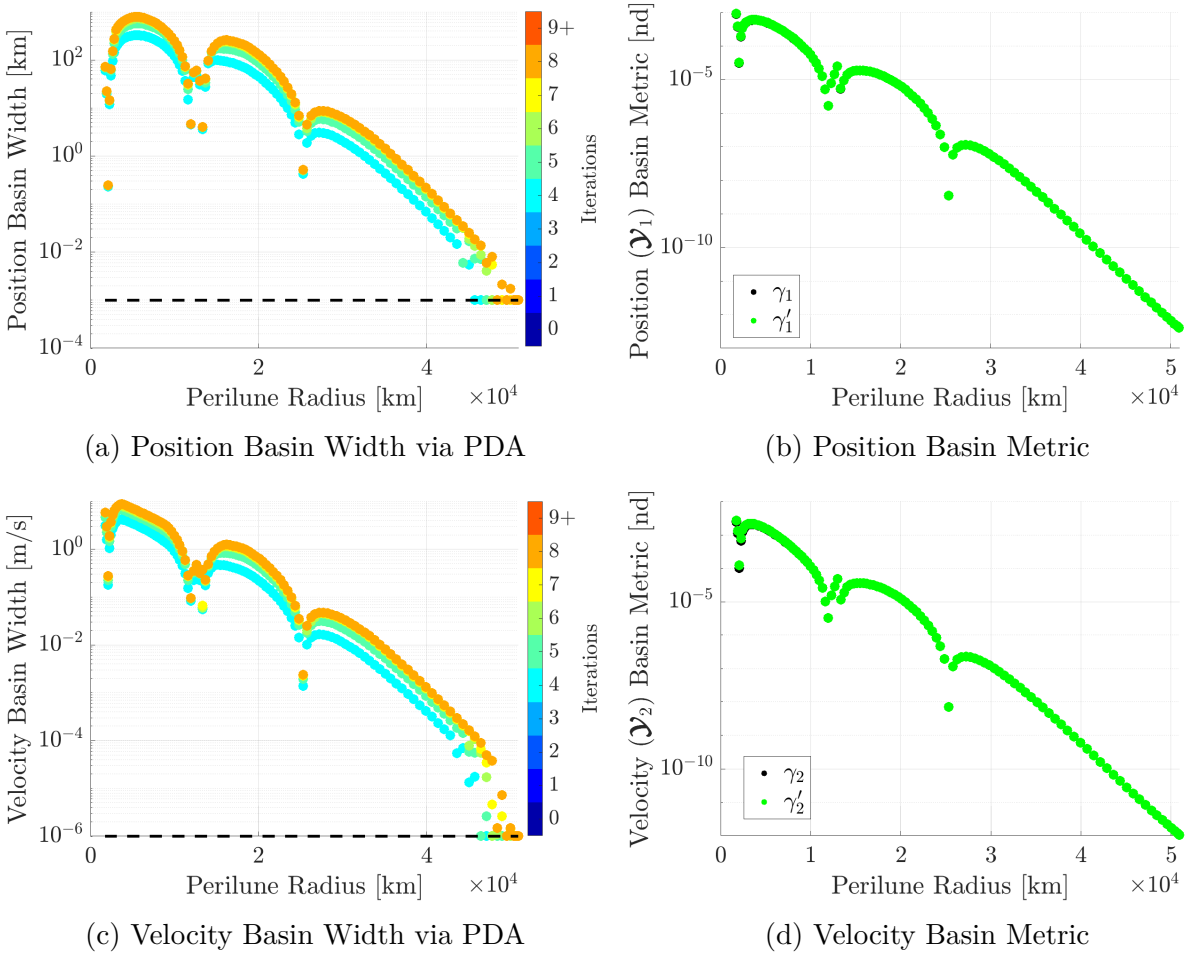

(a) Position Basin Width via PDA

(b) Position Basin Metric

(c) Velocity Basin Width via PDA

(d) Velocity Basin Metric

Figure 6.5. 2-Period Halo Targeting PDA Basin Width Measurements and Evaluated Basin Metrics

contractions in the convergence basin are indicated by rapid decreases in the measured basin width values. The measurements are truncated at a lower limit of 1 m, illustrated with a dashed line, reflecting the point beyond which the convergence basin is impractically small

and dominated by numerical tolerances in the problem. While the basin width measurements in Figure 6.5a are computed via numerous targeting simulations, basin metrics γ_1 and γ_1', plotted in Figure 6.5b, are evaluated at the reference solutions. Comparison of Figures 6.3a and 6.5b results in the observation that basin width contractions, or local minima, correlate with local minima in the basin metrics for the same reference trajectories. Additionally—though the magnitudes differ—the qualitative form of the trends in basin metric matches that of the measured basin width values. Figures 6.5c and 6.5d represent the PDA-measured basin width, truncated at 1 μm/s, and evaluated basin metric values, respectively, in the $\boldsymbol{\mathcal{Y}}_2$ velocity perturbation subspace, and the same predicative capability is observed. In contrast, the FTLE-inspired metrics $\lambda_{\boldsymbol{\mathcal{Y}}_1}$ and $\lambda_{\boldsymbol{\mathcal{Y}}_2}$ in Figure 6.6 fail to correlate with the measured local minima in convergence behavior across the family of reference orbits. However, the FTLE-

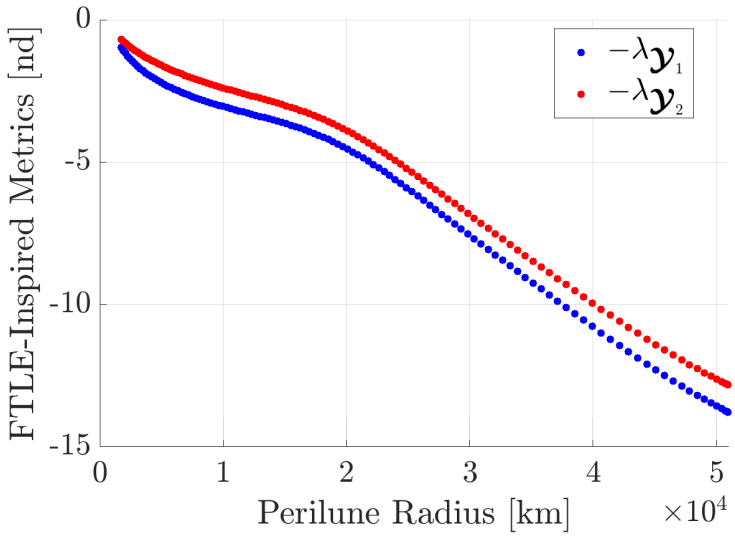

Figure 6.6. FTLE-Inspired Quantities for 2-Period Halo Targeting

inspired metrics appear to roughly reflect the trend in convergence behavior in the absence of these contracting regions, producing an incomplete but situationally-useful characterization.

Extending the analysis to a reference trajectory with a 3-period time-of-flight from apolune to apolune provides supporting evidence that the evaluated basin metric values constitute a useful measure of relative basin width across the family of reference orbits. The width of the convergence basin in the $\boldsymbol{\mathcal{Y}}_1$ position subspace is plotted in Figure 6.7a for different iteration

limits to produce a physical characterization of the main basin for each reference trajectory. In Figure 6.7b, the basin metric values, γ_1 and γ_1', in the $\boldsymbol{\mathcal{Y}}_1$ subspace are evaluated along

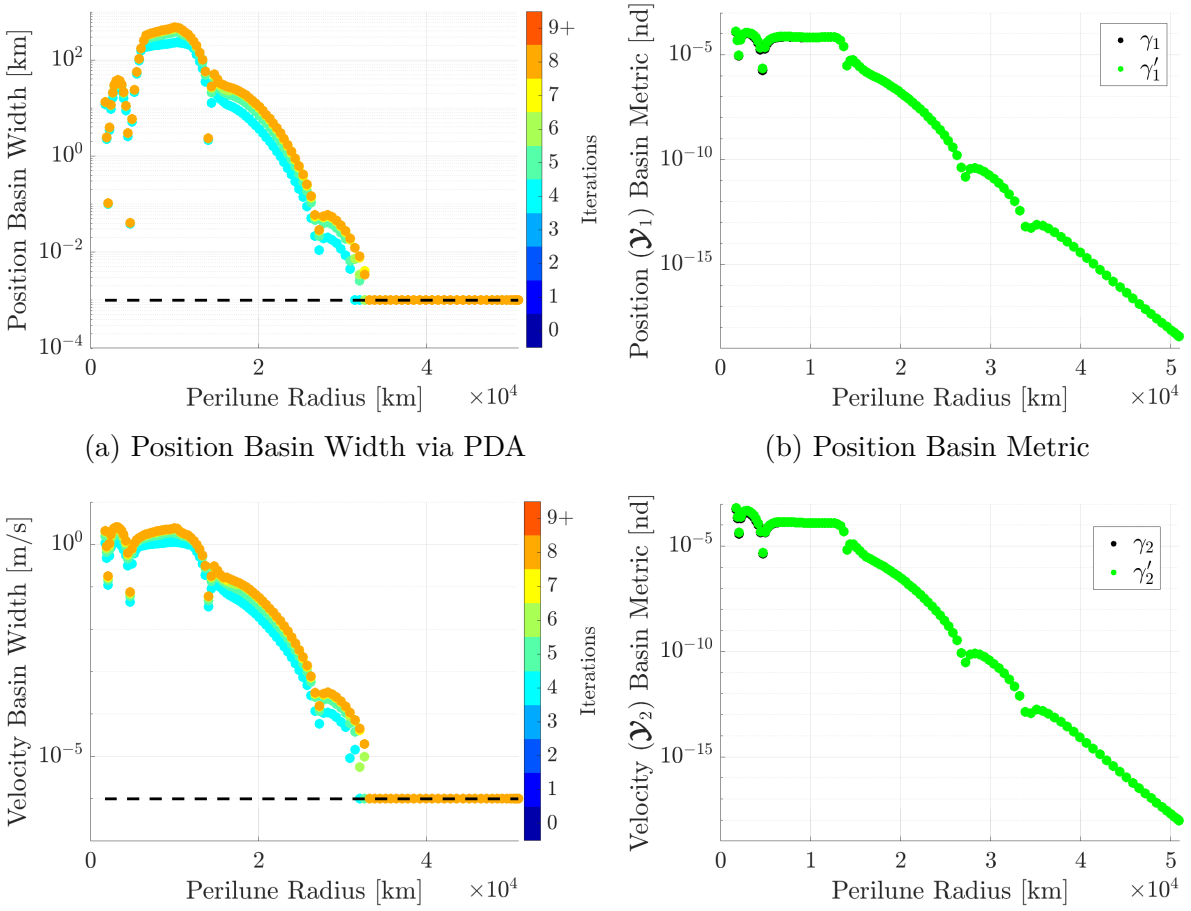

(a) Position Basin Width via PDA

(b) Position Basin Metric

(c) Velocity Basin Width via PDA

(d) Velocity Basin Metric

Figure 6.7. 3-Period Halo Targeting PDA Basin Width Measurements and Evaluated Basin Metrics

each reference solution, indexed by the perilune distance. Consistent with the 1-period and 2-period targeting scenarios, the basin metrics—both roughly equivalent despite their differing computation methods—follow the form of the PDA-measured basin width values across the family of solutions. Additionally, the trend in basin metric values, plotted in Figure 6.7d, serve to predict the relative trend in basin width measurements in the $\boldsymbol{\mathcal{Y}}_2$ velocity subspace in Figure 6.7c. While the FTLE-inspired values, defined in Equation (4.15), for each perturbation subspace match the general change in convergence behavior as the reference orbit increases in perilune radius, the evolution of the FTLE-inspired quantities does

not predict the local minima in the basin width measurements that occur across the family. The additional computational burden in producing the 2nd-order partial derivatives for the

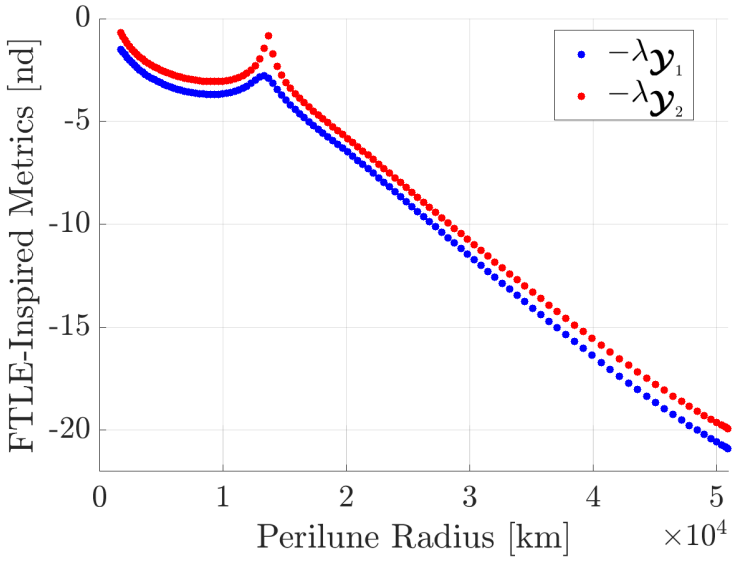

Figure 6.8. FTLE-Inspired Quantities for 3-Period Halo Targeting

evaluation of the γ_i basin metric values is justified by their strong correlation with the PDA-measured basin width values and the weaker correlation with the 1st-order FTLE-inspired quantities. Overall, the information gained from the local normalized rate of change in the design Jacobian, measuring nonlinearity in the perturbed targeting problem at the reference solution, yields a relative performance metric that allows for the prediction and comparison of convergence behavior across a set of reference trajectories in the L_2 southern halo orbit family without the need for numerous simulations of the iterative targeting problem.

6.2 Convergence Behavior for Targeting Problems in the 9:2 NRHO

The representation of particular events in a mission, e.g., the application of constraints or the execution of maneuvers, at discrete points are not the only use for nodes, or patch points, along a trajectory. Frequently, nodes are employed in multiple-shooting problems to alter the problem in a way that improves the convergence behavior without changing the functional design of the mission [20]–[22]. To accommodate these "support" patch points, full state

continuity constraints are added to the targeting problem, ensuring equality between the incoming and outgoing states at the associated times. Due to its utilization as the reference motion for NASA's Gateway mission [65]–[67], the L_2 southern NRHO that possesses a 9:2 synodic resonance with the period of the Earth-Moon orbital motion is chosen to investigate the impact of a support patch point on convergence behavior.

6.2.1 Targeting on the 9:2 NRHO with a Support Patch Point

With the inclusion of a support patch point, a study of potential locations along the reference trajectory and a comparison to an equivalent "unsupported" single-shooting problem are naturally of interest. The perturbed targeting problem in Equation (6.1), previously applied across the family of L_2 southern halo orbits, serves as an appropriate single-shooting problem for comparative analysis. On the reference solution, the spacecraft is located at the apolune point along the 9:2 NRHO at both the initial and final times. After the inclusion of initial state perturbations, impulsive changes in velocity are employed to target back to the reference apolune position after a fixed time-of-flight. The addition of a support patch point requires the extension from a single-shooting to a multiple-shooting problem. While the position at the final time, t_2, is still constrained to the desired position vector, $\boldsymbol{\rho_d}$, the constraint vector is augmented to produce full state continuity at time t_1, associated with the support patch point. To allow movement of this patch point in the full 6-dimensional phase space, the outgoing position and velocity vectors at t_1 are appended to the set of design variables. The perturbed targeting problem is consequently expressed as

$$\boldsymbol{\mathcal{F}} = \begin{bmatrix} \boldsymbol{\rho}(t_1)^- - \boldsymbol{\rho}(t_1)^+ \\ \dot{\boldsymbol{\rho}}(t_1)^- - \dot{\boldsymbol{\rho}}(t_1)^+ \\ \boldsymbol{\rho}(t_2)^- - \boldsymbol{\rho_d} \end{bmatrix} \ , \boldsymbol{\mathcal{X}} = \begin{bmatrix} \dot{\boldsymbol{\rho}}(t_0)^+ \\ \boldsymbol{\rho}(t_1)^+ \\ \dot{\boldsymbol{\rho}}(t_1)^+ \end{bmatrix} \ , \boldsymbol{\mathcal{Y}} = \begin{bmatrix} \boldsymbol{\mathcal{Y}}_1 \\ \boldsymbol{\mathcal{Y}}_2 \end{bmatrix} = \begin{bmatrix} \boldsymbol{\rho}(t_0)^+ \\ \dot{\boldsymbol{\rho}}(t_0)^+ \end{bmatrix} \tag{6.2}$$

By varying t_1 as a parameter on the reference solution, the effect of the placement of the support patch point on the convergence behavior is studied. An example configuration, propagated in the CRTBP, is illustrated in Figure 6.9. The parameterized value of t_1 is

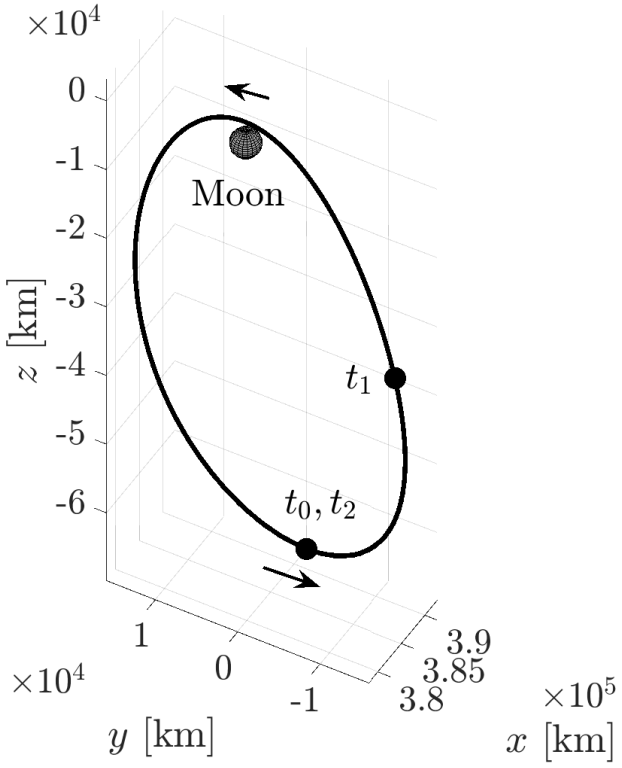

Figure 6.9. Reference Solution for 9:2 NRHO Targeting with Support Patch Point

varied from $t_0 = 0$ to $t_2 = 2T$, where T is the period of the underlying 9:2 NRHO, allowing the impact of the support patch point's placement to be predicted and measured.

Characterization of the convergence behavior for the set of targeting problems parameterized by t_1 is first accomplished by measuring the basin width through the PDA method. Plotted in Figure 6.10a, the width of the 3-iteration convergence basin in the $\boldsymbol{\mathcal{Y}}_1$ position perturbation subspace is measured along 4 directions, $\boldsymbol{v}_{\mathbf{1},j}$ for $j = 1, 2, 3$ and $\boldsymbol{v}'_{\mathbf{1}}$, associated with the perturbation Jacobian defined (Equation (4.17)) and the normalized rate of change in the design Jacobian (Equation (4.45)), respectively. The partial derivatives in the problem are computed via numerical integration of the state transition tensors according to the equations of motion that govern the CRTBP. By choosing a sufficiently small iteration limit, the convergence behavior in the monotonic region in the vicinity of the reference solution is measured. The measured basin width along the dominant right singular vector of $\frac{\partial \boldsymbol{\mathcal{F}}}{\partial \boldsymbol{\mathcal{Y}}_1}\Big|_{(\boldsymbol{\mathcal{X}}^*, \boldsymbol{\mathcal{Y}}^*)}$,

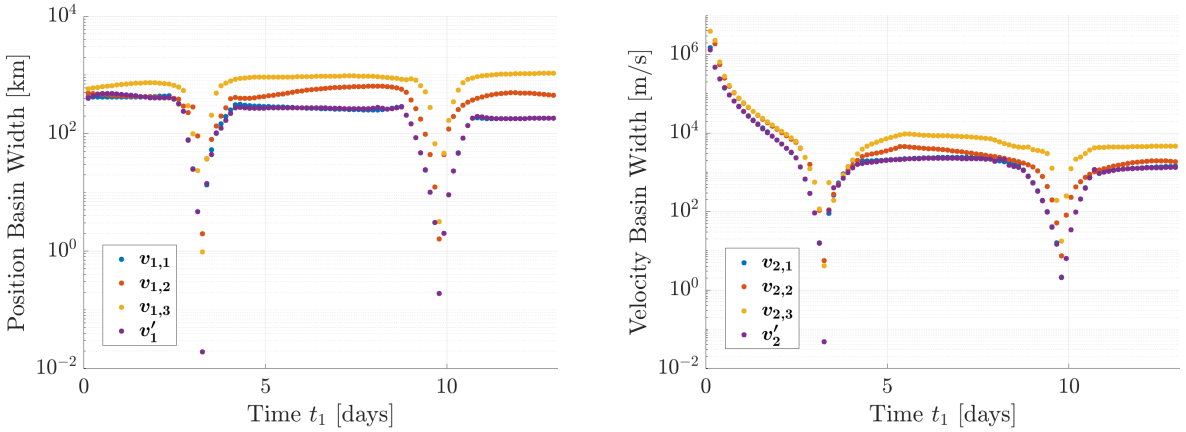

(a) Position Perturbation Subspace

(b) Velocity Perturbation Subspace

Figure 6.10. Individual Principal Direction Measurements for 9:2 NRHO Targeting with Support Patch Point for a 3-Iteration Limit

denoted $\boldsymbol{v_{1,1}}$, and the dominant mode-3 singular vector of $\frac{\partial \mathcal{F}}{\partial \boldsymbol{\mathcal{X}}}\Big|^{-1}_{(\boldsymbol{\mathcal{X}}^*,\boldsymbol{\mathcal{Y}}^*)} \frac{\partial^2 \mathcal{F}}{\partial \boldsymbol{\mathcal{X}} \partial \boldsymbol{\mathcal{Y}}_1}\Big|_{(\boldsymbol{\mathcal{X}}^*,\boldsymbol{\mathcal{Y}}^*)}$, denoted $\boldsymbol{v'_1}$, are approximately equal across the domain of t_1, signifying that the largest directions of absolute change in the constraint vector and relative change in the design Jacobian are nearly aligned at the reference solution. In this particular problem, therefore, the vectors $\boldsymbol{v_{1,1}}$ and $\boldsymbol{v'_1}$ are interchangeable as discretization directions for developing a preliminary description of the convergence behavior. Analogous measurements in the 4 directions in the $\boldsymbol{\mathcal{Y}}_2$ velocity perturbation subspace in Figure 6.10b yield similar results, indicating that critical features of the local main basin lie along the directions associated with the nearly-interchangeable vector directions $\boldsymbol{v_{2,1}}$ and $\boldsymbol{v'_2}$ for this particular perturbed targeting problem.

By only recording the minimum value measured in each direction of PDA strategy, the convergence behavior of the multiple-shooting problem with a support patch point at t_1 is compared to that of the analogous single-shooting problem for limits of 4 through 8 iterations. The PDA-measured basin width values in the $\boldsymbol{\mathcal{Y}}_1$ subspace are plotted in Figure 6.11a for each value of t_1 and colored according to the corresponding iteration limit. For a given value of t_1, the basin width intuitively grows larger as the iteration count increases, and the values fall closer together for higher iteration counts, signifying the steep gradient associated a boundary of the main basin. Plotted as dashed lines for comparison, the basin widths at each iteration limit for the single-shooting problem lack a support patch point

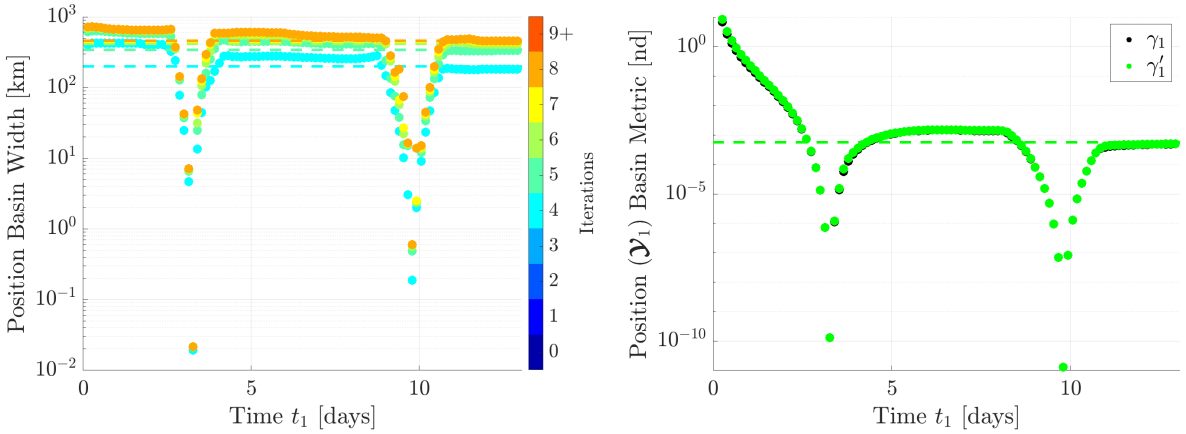

(a) Position Basin Width via PDA

(b) Position Basin Metric

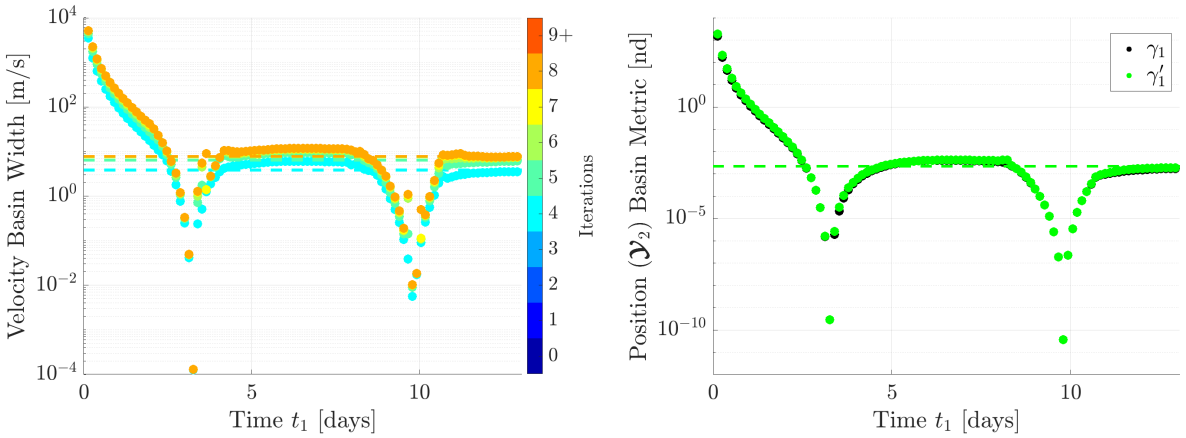

(c) Velocity Basin Width via PDA

(d) Velocity Basin Metric

Figure 6.11. 9:2 NRHO Targeting PDA Basin Width Measurements and Evaluated Basin Metrics with Support Patch Point

and, therefore, do not depend on t_1. Figure 6.11a demonstrates that the inclusion of a support patch point improves the convergence behavior for some values of t_1 and worsens the convergence behavior for others. The rapid contractions in the convergence basin width are associated with placement of the support patch point near the two perilune passes of the reference solution, a region of significant dynamical sensitivity due the proximity to the Moon. The plots of γ_1 (Equation (4.35)) and γ_1' (Equation (4.44)) in Figure 6.11b also display steep decreases in the basin metric values near these perilune passes, predicting the measured behavior. The method of computation of the basin metric—whether through the simpler matrix-norm or the optimization to yield the higher-order singular value–does

not have a significant impact on the prediction in this particular scenario. The baseline value of γ_1' in the single-shooting problem is plotted as a dashed line in Figure 6.11b. By comparing to the constant single-shooting value, the basin metric values at each t_1 correlate with whether the inclusion of the support patch point will improve or worsen the measured convergence basin width in Figure 6.11a, providing an locally-evaluated predicative measure of the convergence behavior relative to both other potential times of t_1 and to the simpler single-shooting formulation. Though the trends in the basin metric values closely follow those of the PDA measurements, an exception occurs for the segment between the initial apolune and the first perilune where the basin metrics γ_1 and γ_1' overestimate the relative basin sizes. However, an improvement in convergence behavior is still both predicted and measured. Subsequent analysis of the convergence behavior in the $\boldsymbol{\mathcal{Y}}_2$ velocity subspace yields comparable findings. The PDA measurements in Figure 6.11c reflect reductions in the basin width when the support patch point is placed near perilune on the reference orbit, and changes in the convergence behavior relative to the dashed single-shooting basin width are correlated with the relative changes in γ_2 and γ_2' in Figure 6.11d. Avoiding the numerous targeting simulations required to compute the PDA measurements, the locally-evaluated basin metrics, γ_1 and γ_2, predict the relative convergence performance in comparison to other values of the parameter t_1 as well as the absence of a support patch point.

Though the local minima in basin width are located at the perilune locations on the reference orbit, the basin contracts to for a duration of time before and after this point of closest approach of the Moon. The 2^{nd}-order basin metric values for both the position and velocity subspaces are plotted together in Figure 6.12a, where the time of the first perilune, $t_1 = 0.5T$, is marked with a dashed red line. By visual inspection, times of entering and exiting the contracted duration are approximated as $t_1 = 0.42T$ and $t_1 = 0.64T$, respectively. In Figure 6.12b, the locations of these approximate boundaries in the convergence contraction are plotted on the reference orbit. It is apparent that the basin contraction is not restricted to the immediate vicinity of the perilune point but is instead distributed across a significant portion of the reference trajectory.

As alternative predictors of convergence behavior, the FTLE-inspired quantities are computed for the various possible placements of the support patch point. The quantities $\lambda_{\boldsymbol{\mathcal{Y}}_i}$

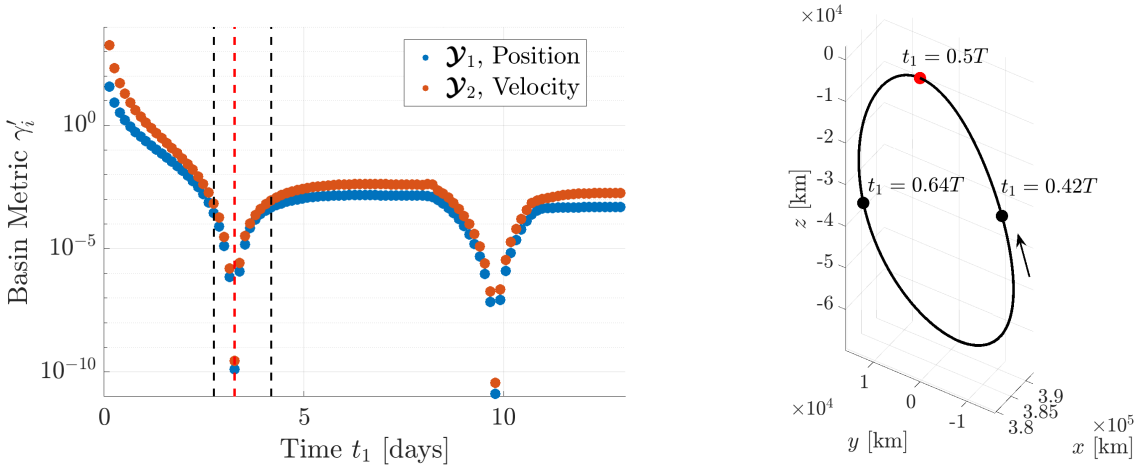

(a) Basin Metric Values

(b) Locations on Reference

Figure 6.12. First Perilune Basin Contraction for 9:2 NRHO Follow-On Targeting

for $i = 1, 2$, defined in Equation (4.15), and $\lambda_{\boldsymbol{\mathcal{X}}}$, defined in Equation (4.14), are plotted in Figure 6.13 with a multiplication by -1 across the domain of the parameter t_1 from 0 to $2T$. Consistent with the plots of the basin width measurements in Figure 6.11a and 6.11c,

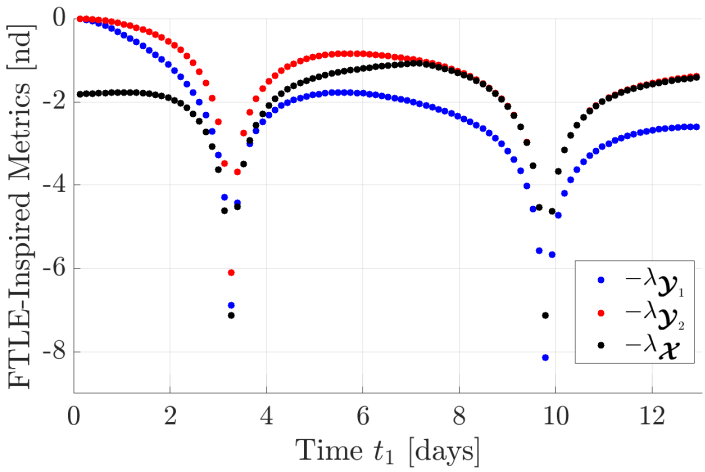

Figure 6.13. FTLE-Inspired Quantities for 9:2 NRHO Targeting with Support Patch Point

there is a large degree of growth in the constraint vector due to changes in perturbation and design variables at the perilune passes. Qualitatively, the FTLE-inspired quantities $\lambda_{\mathcal{Y}_i}$ and $\lambda_{\boldsymbol{\mathcal{X}}}$ mirror the trends in the basin width measurements over much of the domain of t_1. These

results suggest the measures of absolute growth in the constraint vector and the relative change in the design Jacobian due to perturbations are positively correlated in this particular scenario. In other words, support patch point placements with larger local sensitivity in the constraints also have larger local sensitivity in the design Jacobian. However, the basin metric values remain a more consistent indicator of the relative convergence properties of the parameterized perturbed targeting problems.

In the independent subspaces consisting solely of position or velocity, a comparison of basin metric values across a set of solutions provides mission designers with insight into potentially problematic trajectories, and the basin width measurements allow engineers to disqualify reference trajectories with convergence basins that cannot accommodate expected position or velocity trajectory dispersions derived from guidance and navigation performance. However, an accurate description of the position-velocity tradespace allows for the determination of unsuitable solutions in the really-existing presence of combined perturbations in position and velocity. To begin this analysis, two times of interest are selected for the placement of support patch point at t_1 by examining features in the evolution of the basin metric in the independent subspaces. The basin metric values γ_1' and γ_2', reproduced in Figure 6.14, significantly reduce in magnitude at the two perilune passes and plateau at relatively consistent value between them. For a support patch point placed at $t_1 = 6.80$ days, there

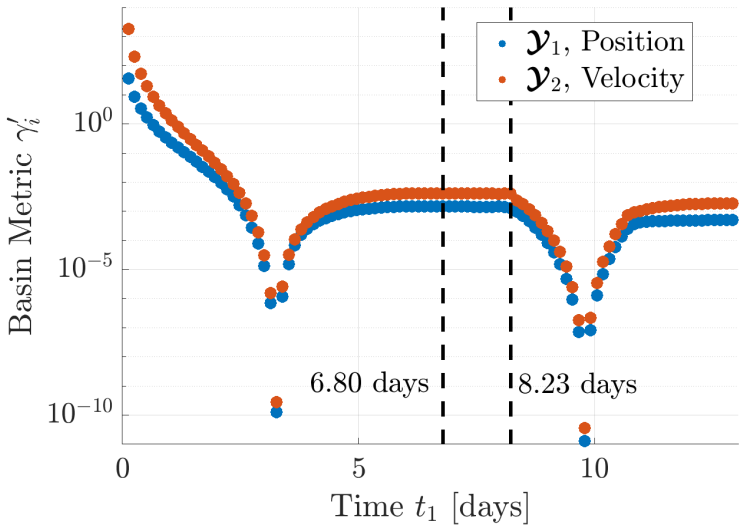

Figure 6.14. Basin Metric Values for 9:2 NRHO Targeting with Support Patch Point

is relatively little change in the predicted convergence behavior for neighboring values of t_1, and the PDA-measured basin width values, shown in Figures 6.11a and 6.11c, level off, confirming this prediction. Relative to the changing parameter t_1, a support patch point at $t_1 = 6.80$ days sits in the "stable" center of the plateau. A support patch point placed at $t_1 = 8.23$ days along the reference trajectory has similar convergence behavior according to the basin metric and PDA measurements; however, the support node is positioned at an "unstable" edge edge of the plateau, or the beginning of a rapid change in the size of the convergence basin as the parameter t_1 evolves. Because the support patch points at $t_1 = 6.80$ days and $t_1 = 8.23$ days yield similar results for independent analyses of the position and velocity subspaces but are differently situated with respect to evolution of the convergence behavior in t_1, these times are selected for tradespace analysis.

To characterize the position-velocity tradespace, the results of a 6-dimensional expanding shell discretization and the reduced principal plane discretization are compared. The principal plane discretization strategy assumes that the critical limiting features of the tradespace exist in a plane constructed by the the dominant right singular vectors of the perturbation Jacobian matrices in the independent position and velocity perturbation subspaces, i.e., $\boldsymbol{v_{1,1}}$ and $\boldsymbol{v_{2,1}}$. The principal plane heuristic approximation is assumed to be most applicable when these direction are co-planar with the dominant right singular vector of the combined perturbation Jacobian matrix, $\boldsymbol{v_1}$, and the Equations (4.24), (4.25), and (4.20) outline the criteria to assess this applicability. First, the angles between the dominant left singular vectors in the individual subspaces, defined in Equation (4.24) and shown in Figure 6.15a, are computed. When the vectors $\boldsymbol{u_{1,1}}$ and $\boldsymbol{u_{2,1}}$ are aligned, the co-planar assumption that supports the principal plane approximation is upheld, and small angular deviations suggest that the assumption is reasonable. For $t_1 = 6.80$ days and $t_1 = 8.23$ days, the angular deviations are approximately 26 deg and 15.5 deg, respectively. Though the vectors are not nearly orthogonal, intuition does not necessarily provide guidance on if these deviations are "sufficiently" small, so the other criteria are consulted to assess the expected validity of a principal plane approximation. From the criteria in Equation (4.25), the relative levels of dominance of the singular vectors are computed as the ratios of the largest to second-largest singular values in the independent subspaces and plotted across the domain of t_1 in Figure

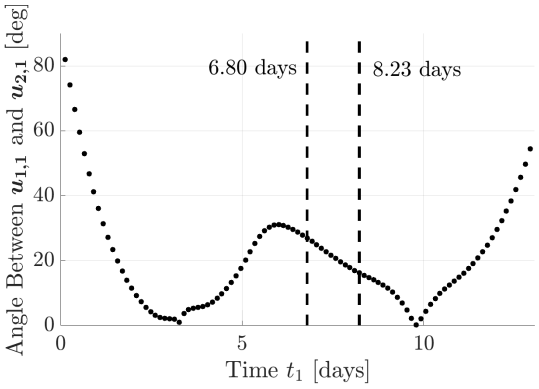

(a) Constraint Principal Direction Angle

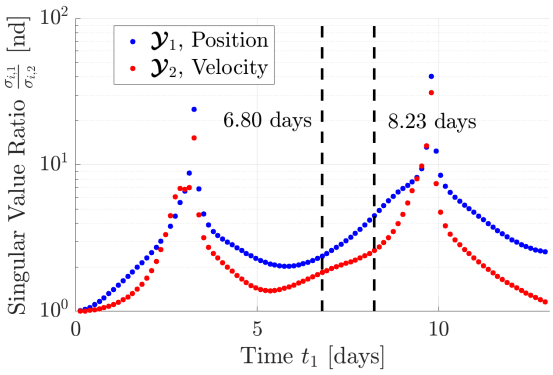

(b) Singular Value Ratio

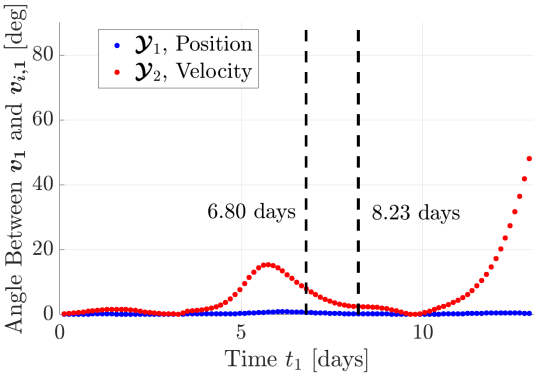

(c) Principal Direction Projection Angles

Figure 6.15. Principal Plane Conditions for 9:2 NRHO Targeting with Support Patch Point

6.15b. In both the $\mathcal{Y}_1$ and $\mathcal{Y}_2$ subspaces, the singular value ratios fall between 1 and 10 for the times of interest. Large magnitudes of the ratios are preferred to support the principal plane heuristic approximation, so a direct measurement of the co-planar nature of the vectors $\boldsymbol{v_{1,1}}$, $\boldsymbol{v_{2,1}}$, and $\boldsymbol{v_1}$ is required. Reflecting the co-planar criteria in Equation (4.20), Figure 6.15c depicts the angle between the subspace directions $\boldsymbol{v_{i,1}}$ and the projection of the vector $\boldsymbol{v_1}$ in that subspace. The small angular deviations from the principal plane show that the three vectors are nearly co-planar in the full 6-dimensional space, and this property supports the validity of the principal plane discretization strategy as a potentially useful approximation of the tradespace.

The position-velocity perturbation tradespace is characterized via two methods: the naïve expanding shell discretization and the principal plane approximation. To determine

the tradespace via expanding shells, position perturbation vectors are computed from 30 longitudinal angles and 15 latitudinal angles that are evenly spaced on sphere with a constant radius, i.e., constant position perturbation magnitude. Position perturbation vectors are then computed via the same process for spheres of increasing radii. The process is repeated in the velocity subspace to generate velocity perturbation vectors from similarly expanding spherical shells. For each pair of pre-generated position and velocity perturbation vectors, a full iterative targeting problem is simulated. For the scenario with a support patch point placed at $t_1 = 6.80$ days, the resulting tradespace is depicted in Figure 6.16a, where each point corresponds to the maximum number of iterations required to converge to a new solution for the associated pair of position and velocity perturbation magnitudes. As

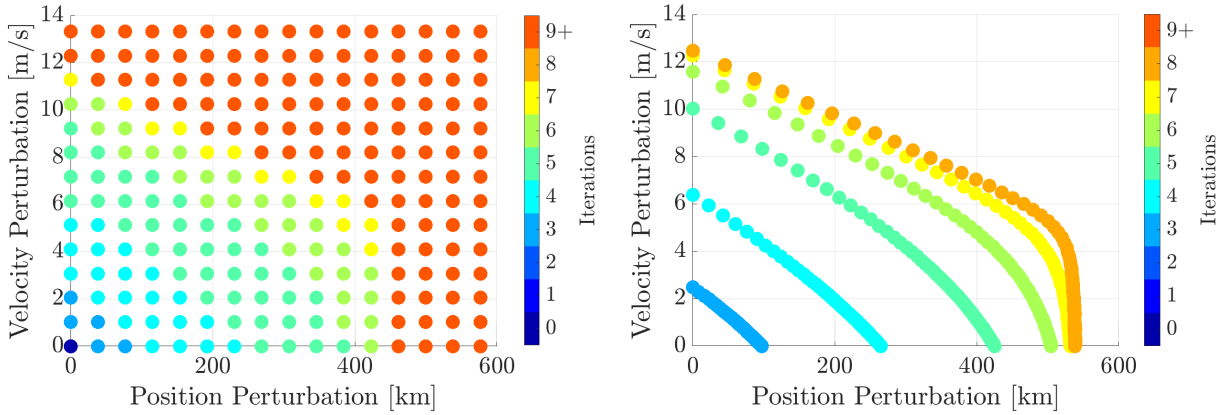

(a) Expanding Shell Discretization

(b) Principal Plane Approximation

Figure 6.16. Position-Velocity Tradespace for 9:2 NRHO Targeting with Support Patch Point ($t_1 = 6.80$ days)

a more computationally-efficient alternative, the principal plane approximation restricts the discretization to points along the parameterized vector $\boldsymbol{\eta}(s)$, defined in Equation (4.18), and results in the tradespace approximation in Figure 6.16b. Comparing the results obtained from the two methods, the principal plane approximation provides an accurate characterization of the position-velocity tradespace for 5 or fewer iterations and a slightly over-generous but useful prediction for greater iteration counts. When the analysis is repeated with a support patch point placed at $t_1 = 8.23$ days, the expanding shell discretization produces the tradespace depicted in Figure 6.17a. For comparison, the principal plane discretization

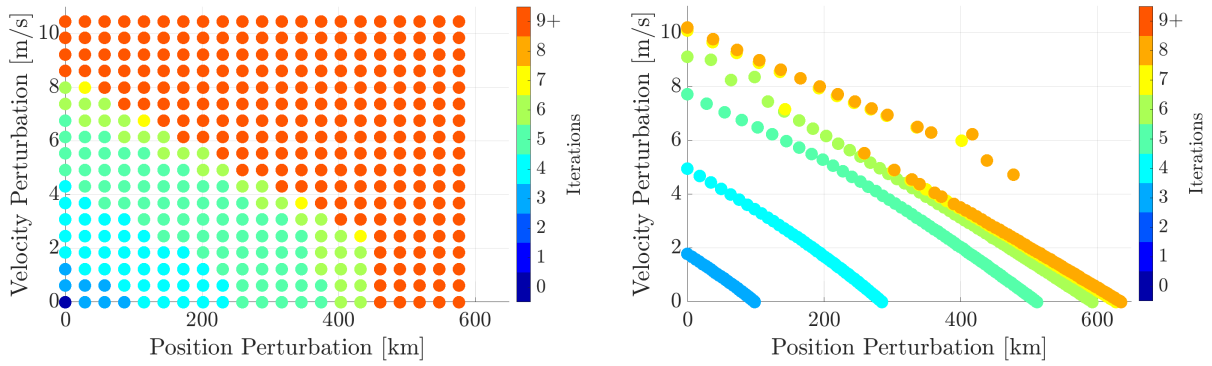

(a) Expanding Shell Discretization

(b) Principal Plane Approximation

Figure 6.17. Position-Velocity Tradespace for 9:2 NRHO Targeting with Support Patch Point ($t_1 = 8.23$ days)

technique produces the tradespace in Figure 6.17b. As before, the principal plane analysis renders a useful and more efficient approximation of the position-velocity tradespace for a preliminary assessment. Though the method slightly overestimates the allowable pairs of position and velocity magnitude for a given iteration limit, the results are reasonable, suggesting that the critical features that define the tradespace exist in the vicinity of the principal plane. The independent PDA analyses and combined principal plane approximation provide insight into the convergence basin widths and position-velocity perturbation tradespaces for both possible support patch point times.

6.2.2 Follow-On Single-Shooting Corrections on the 9:2 NRHO

To further examine the convergence behavior of perturbed targeting problems along the 9:2 NRHO, a follow-on single-shooting problem is introduced. Suppose that the support patch point is repurposed to provide an additional correction maneuver to clean up any error after the targeting and execution of the first correction maneuver. The correction maneuver at time t_1 leverages a change in impulsive velocity change to mitigate the effect of a simultaneous state perturbation on the targeting of a desired final position at the reference apolune point at the final time t_2, illustrated in Figure 6.18. This perturbed targeting

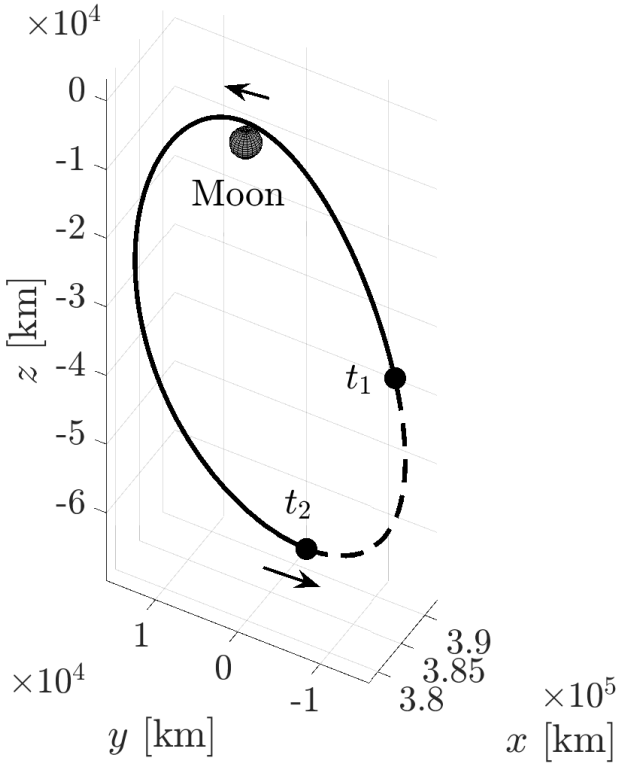

Figure 6.18. 9:2 NRHO Follow-On Reference Solution

problem formulation is expressed mathematically as

$$\boldsymbol{\mathcal{F}} = \boldsymbol{\rho}(t_2)^- - \boldsymbol{\rho_d} \ , \ \boldsymbol{\mathcal{X}} = \dot{\boldsymbol{\rho}}(t_1)^+ \ , \ \boldsymbol{\mathcal{Y}} = \begin{bmatrix} \boldsymbol{\mathcal{Y}}_1 \\ \boldsymbol{\mathcal{Y}}_2 \end{bmatrix} = \begin{bmatrix} \boldsymbol{\rho}(t_1)^+ \\ \dot{\boldsymbol{\rho}}(t_1)^+ \end{bmatrix} \tag{6.3}$$

where $\boldsymbol{\rho_d}$ is the position vector associated with the apolune point on the 9:2 NRHO reference orbit. In keeping with the previous scenario, the convergence behavior of the perturbed targeting problem is investigated as t_1, the time of the perturbation and maneuver, is varied across two periods of the underlying orbit.

To characterize the form of the local convergence basin, the convergence basin width is measured in the 4 principal directions with a limit of 3 iterations in the targeting process. As defined in Equations (4.17) and (4.45), the first 3 principal directions correspond to the right singular vectors of the local perturbation Jacobian matrix, i.e., $\boldsymbol{v_{i,j}}$ with $j = 1, 2, 3$ in the

$\boldsymbol{\mathcal{Y}}_i$ subspace, and the final principal direction is the dominant mode-3 singular vector of the normalized rate of change in the design Jacobian. Figures 6.19a and 6.19b show the width of the convergence basin in each direction for the $\boldsymbol{\mathcal{Y}}_1$ position perturbation subspace and $\boldsymbol{\mathcal{Y}}_2$ velocity perturbation subspace, respectively. In both subspaces, the vector $\boldsymbol{v}_i'$, associated

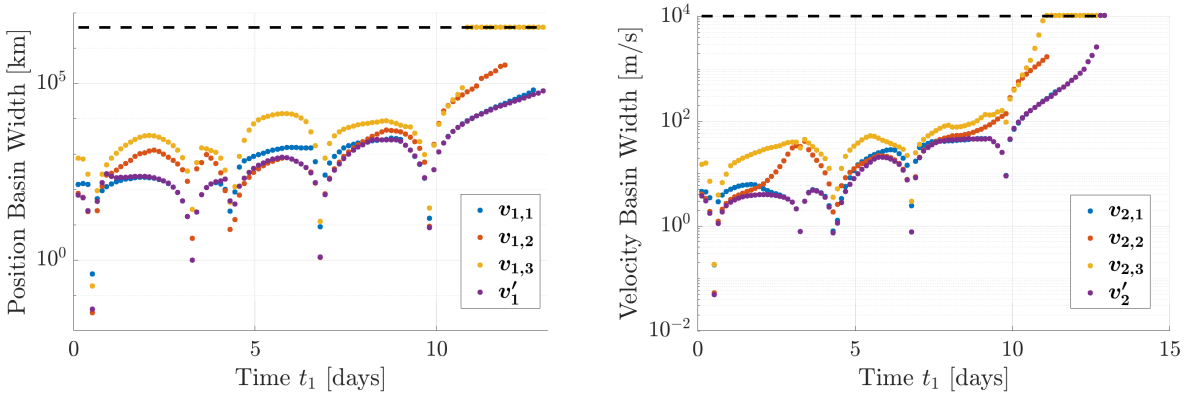

(a) Position Perturbation Subspace

(b) Velocity Perturbation Subspace

Figure 6.19. Individual Principal Direction Measurements for 9:2 NRHO Follow-On Targeting for a 3-Iteration Limit

with nonlinearity in the design Jacobian $\frac{\partial \boldsymbol{\mathcal{F}}}{\partial \boldsymbol{\mathcal{X}}}\Big|_{(\boldsymbol{\mathcal{X}}^*, \boldsymbol{\mathcal{Y}}^*)}$ at the solution, consistently produces the minimum width measurement, meaning the worst-case performance is aligned with the direction that possesses the largest relative measure of nonlinearity. For various intervals along the evolution of the parameter t_1, the measurements in the $\boldsymbol{v}_{i,\mathbf{1}}$ and $\boldsymbol{v}_{i,\mathbf{2}}$ directions exhibit a switching behavior, alternating in which direction most closely approximates the minimum value. For rapid analysis, the vectors $\boldsymbol{v}_i'$ produce a useful upper bound for the convergence basin width at a given iteration limit.

The convergence behavior of the perturbed targeting problem is characterized by the minimum measured value from the PDA method as the parameter t_1 varies across two periods of the underlying periodic orbit. For limits from 3 to 8 iterations, the PDA-measured basin width is plotted in Figure 6.20a for perturbations in the $\boldsymbol{\mathcal{Y}}_1$ subspace, i.e., initial position. Across the possible values of t_1, there exist local minima that provide evidence for 5 rapid contractions in the main convergence basin; these local minima also appear in plots of the basin metrics γ_1 and γ_1', measures of nonlinearity defined in Equations (4.35) and (4.44),

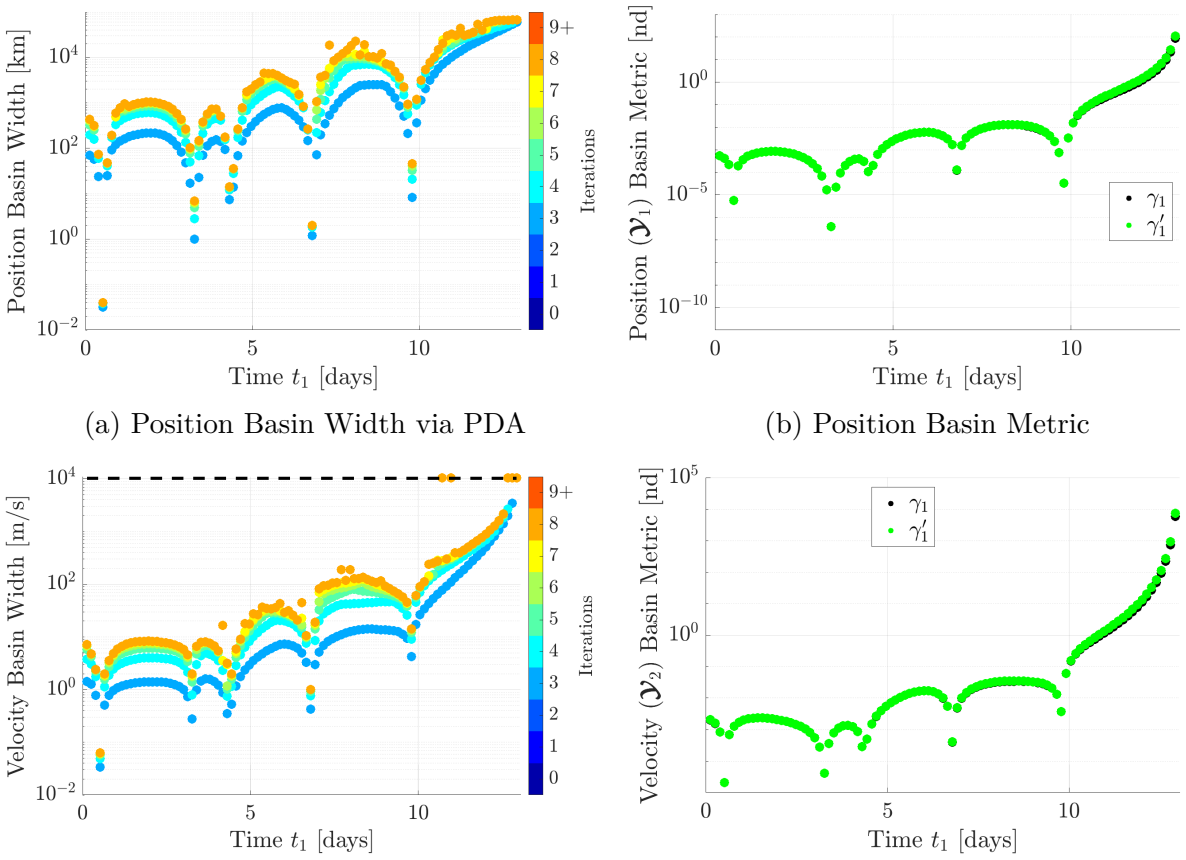

(a) Position Basin Width via PDA

(b) Position Basin Metric

(c) Velocity Basin Width via PDA

(d) Velocity Basin Metric

Figure 6.20. 9:2 NRHO Targeting PDA Basin Width Measurements and Evaluated Basin Metrics with Support Patch Point

respectively, shown in Figure 6.20b. The overall forms of the plots of basin width and basin metrics are also consistent, indicating that changes in the convergence basin are driven and predicted by the local nonlinearity. The PDA-measured basin widths for perturbations in the $\mathcal{Y}_2$ subspace, i.e., initial velocity, are plotted in Figure 6.20c. The dashed lines represent a chosen upper limit of 10 non-dimensional units that prevent the computation of preposterously large measurements. Similarly, the values of t_1 with the smallest convergence basin widths also have local minima in the basin metric quantities shown in Figure 6.20d. The efficacy of the basin metric values is explainable by noting that the vectors $\boldsymbol{v}_i'$ and values γ_i' are related through the higher-order singular vectors and values of $\frac{\partial \mathcal{F}}{\partial \mathcal{X}}\Big|^{-1}_{(\mathcal{X}^*,\mathcal{Y}^*)} \frac{\partial^2 \mathcal{F}}{\partial \mathcal{X} \partial \mathcal{Y}_i}\Big|_{(\mathcal{X}^*,\mathcal{Y}^*)}$. The vectors $\boldsymbol{v}_i'$ are shown to correspond to the directions of the worst-case basin features in

Figures 6.19a and 6.19b, and the basin metrics γ_i' evaluated at the reference solution serve as a relative indicator of convergence behavior as measured via iterative targeting simulations.

For comparison, the FTLE-inspired quantities derived from the perturbation and design Jacobian matrices are investigated as a relative predictor of convergence behavior. The velocity vector at the time t_1 comprises both $\boldsymbol{\mathcal{X}}$ and $\boldsymbol{\mathcal{Y}}_2$ in this problem, so the values of $\lambda_{\boldsymbol{\mathcal{Y}}_2}$ and $\lambda_{\boldsymbol{\mathcal{X}}}$, defined in Equations (4.15) and (4.14), respectively, are equivalent. Plotted with a multiplication by -1 in Figure 6.21 to reflect the expected inverse nature of the relationship between the convergence basin width and dynamical stretching, the values of $\lambda_{\boldsymbol{\mathcal{Y}}_1}$ and $\lambda_{\boldsymbol{\mathcal{Y}}_2}$ across the evolution of the parameter t_1 exhibit very little correlation with the PDA-measured basin width values in Figures 6.20a and 6.20c. The only features hinted at by the FTLE-

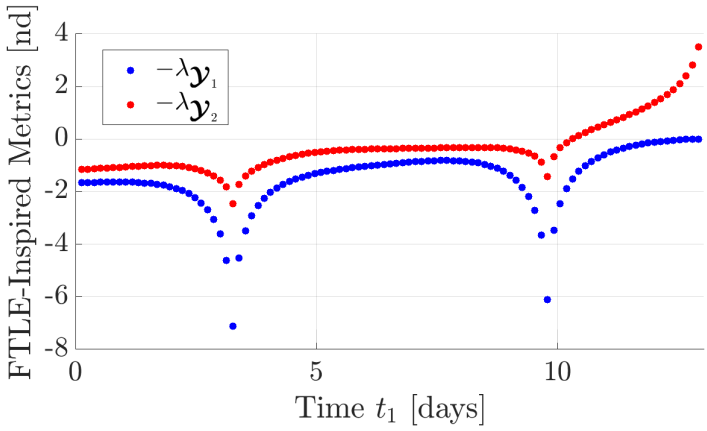

Figure 6.21. FTLE-Inspired Quantities for 9:2 NRHO Follow-On Targeting

inspired quantities reflect the narrowing of the convergence basin at the close perilune passes. Therefore, these results suggest that the evolution of the convergence behavior depends more on the measures of nonlinearity, i.e., γ_1' and γ_2', than on the magnitude of growth in the constraint vector across the perturbation and design variable spaces represented by the FTLE-inspired quantities.

While descriptions and predictions of the convergence behavior for independent perturbations in position or velocity are useful, a characterization of the position-velocity tradespace requires additional analysis. Because a characterization of the position-velocity perturbation tradespace via naïve discretization techniques across the entire sampling of the parameter t_1 bears a prohibitive computational burden, two particular times for t_1 are selected to study

the efficacy of the principal plane approximation in representing the tradespace. The two times of interest are chosen by examining the key features in the plots of the subspace basin metrics γ_1' and γ_2' over the parameter patch point time parameter depicted in Figure 6.22. At

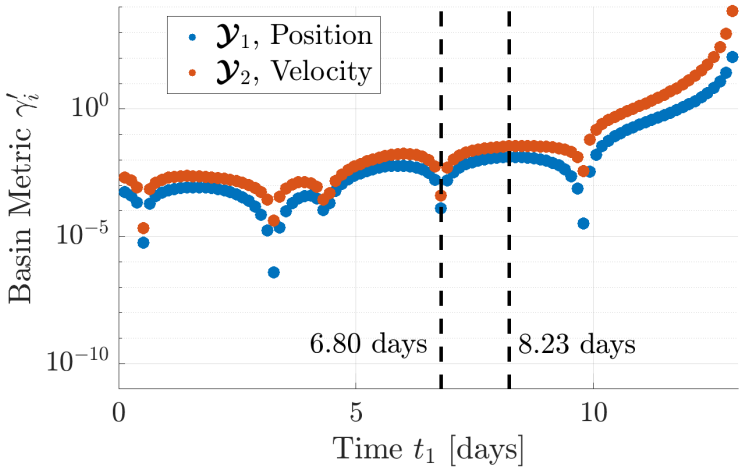

Figure 6.22. Basin Metric Values for 9:2 NRHO Follow-On Targeting

$t_1 = 6.80$ days, the both convergence basin width and the basin metric values experience a substantial reduction, indicating a rapid narrowing of the convergence basin for a perturbation and maneuver at that time. However, near $t_1 = 8.23$ days, the width of the convergence basin experiences relatively little change, sitting in an region of relatively consistent convergence behavior. Interestingly, the previous multiple-shooting problem exhibits the opposite behavior where the convergence behavior changes slowly near $t_1 = 6.80$ days and rapidly near $t_1 = 8.23$ days. This feature demonstrates the need to couple both the dynamics on the trajectory and the particular problem formulation when characterizing convergence behavior. In the hypothetical mission scenario with a multiple-shooting problem and follow-on single-shooting problem, the value of t_1 should be chosen to create favorable convergence behavior in both targeting problems.

Because the principal plane approximation relies on the idea that the critical features of the tradespace exist in a single plane within the higher-dimensional perturbation space, it is necessary to assess indications of this behavior through the co-planar criteria outlined in Equations (4.24), (4.25), and (4.20). Indicating the directions with the largest degree

of 1st-order stretching, the right singular vectors $\boldsymbol{v_{1,1}}$ and $\boldsymbol{v_{2,1}}$ are co-planar with $\boldsymbol{v_1}$ when their complementary vectors $\boldsymbol{u_{1,1}}$ and $\boldsymbol{u_{2,1}}$ are parallel. The angle between these constraint place vectors is plotted in Figure 6.23a across the domain of t_1, and the angular difference is not negligible. By observing the singular value ratios in Figure 6.23b, it is evident that the

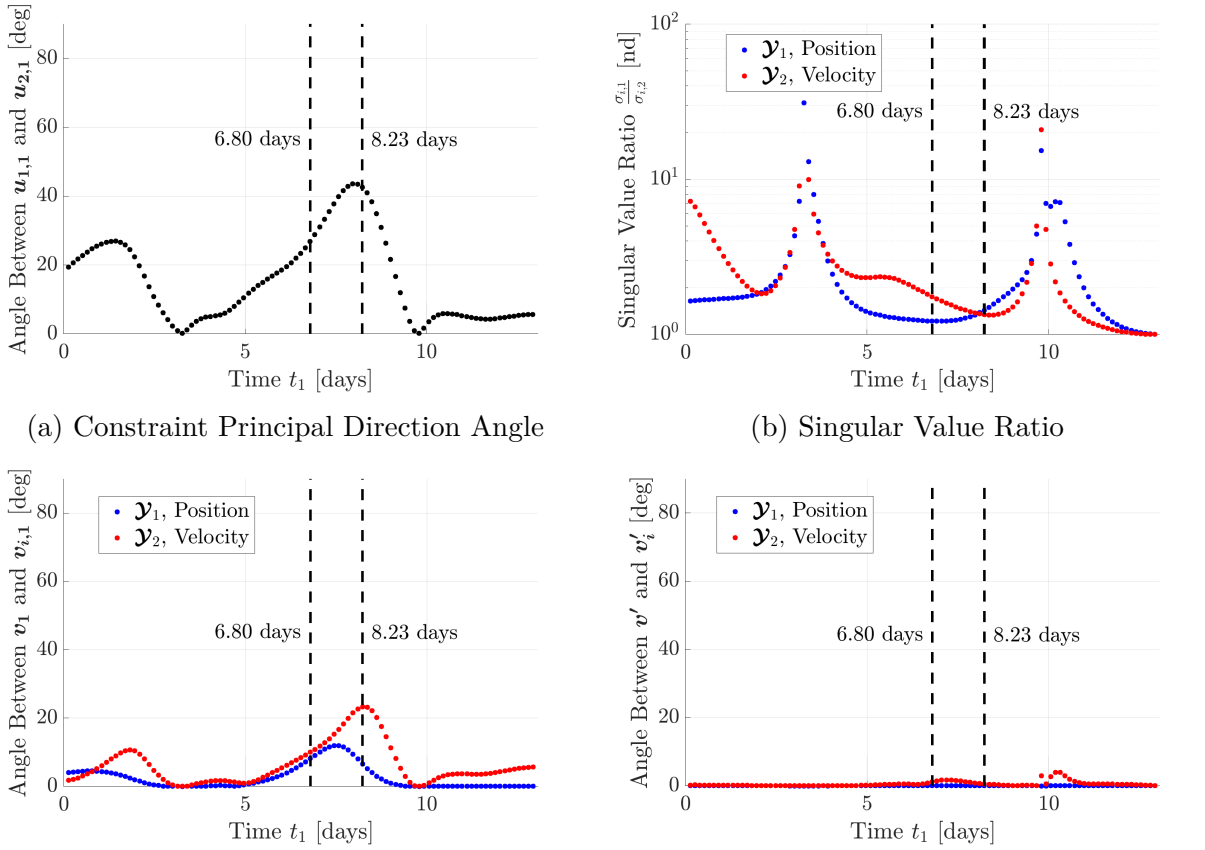

(a) Constraint Principal Direction Angle

(b) Singular Value Ratio

(c) Principal Direction Projection Angles

(d) Mode-3 Singular Vector Projection Angles

Figure 6.23. Principal Plane Conditions for 9:2 NRHO Follow-On Targeting

independent position and velocity subspaces do not have clearly-dominant singular values. Taken together, the large angular difference and lack of dominating singular values indicates that singular vectors $\boldsymbol{v_{1,1}}$, $\boldsymbol{v_{2,1}}$, and $\boldsymbol{v_1}$ are not likely to be co-planar, and this prediction is confirmed through direction computation of non-negligible projected angular differences in Figure 6.23c. Therefore, there is little evidence to support the claim that the tradespace is well-approximated within a plane defined by $\boldsymbol{v_{1,1}}$ and $\boldsymbol{v_{2,1}}$. This result is not surprising when viewed within the context of the switching behavior observed in Figures 6.19a and

6.19b where the vectors $\boldsymbol{v_{1,1}}$ and $\boldsymbol{v_{2,1}}$ are not consistently useful in measuring the basin widths of the independent subspaces. However, the vectors associated with the largest normalized changes in the design Jacobian matrix, $\boldsymbol{v_1'}$ and $\boldsymbol{v_2'}$, are demonstrated to indicate the direction associated with the minimum basin width, and an analogous angular measure expressed as $\angle\left(\text{proj}_{\boldsymbol{\mathcal{Y}}_i}\boldsymbol{v}', \boldsymbol{v_i'}\right)$ is plotted in Figure 6.23d. The negligible angular difference indicates that the three vectors are nearly co-planar and supports the use of a discretization across a principal plane comprised of $\boldsymbol{v_1'}$ and $\boldsymbol{v_2'}$ to approximate the tradespace.

The ability of the principal plane approximation to capture the key features of the position-velocity perturbation tradespace is assessed through comparison to more complete expanding shell discretizations. For a patch point placed at $t_1 = 6.80$ days where the convergence behavior is rapidly changing, the tradespace generated from the naïve discretization scheme is plotted in Figure 6.24a. Each point is colored according to the maximum number

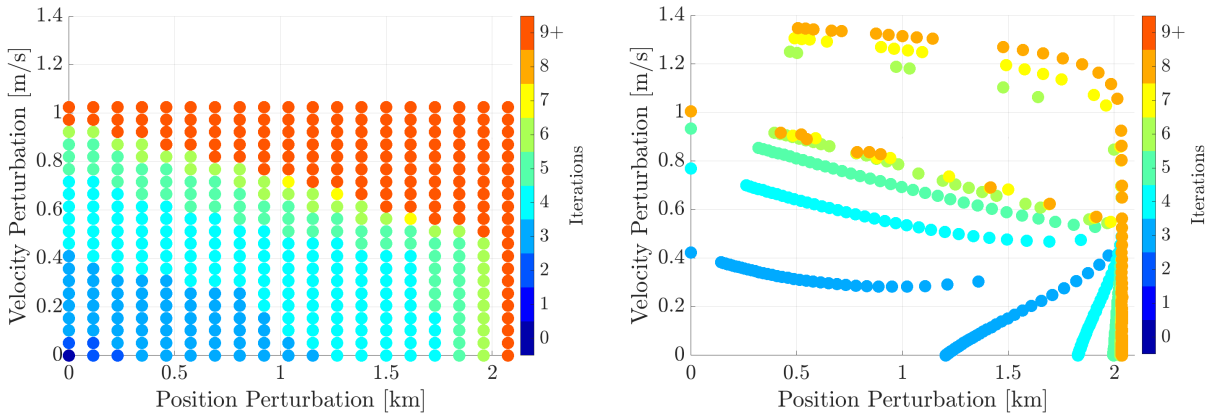

(a) Expanding Shell Discretization

(b) Principal Plane Approximation

Figure 6.24. Position-Velocity Tradespace for 9:2 NRHO Follow-On Targeting ($t_1 = 6.80$ days)

of iterations required to achieve convergence over a given pair of spheres in the position and velocity subspaces, each discretized by 30 longitudinal and 15 latitudinal angles. The iteration counts increase sharply as the colors transition from green through yellow to red, indicating a boundary in the main basin. Reducing the number of targeting simulations to points along the parameterized vector $\boldsymbol{\eta}(s)$, altered slightly from its formulation in Equation (4.18) to be a linear combination of the vectors $\boldsymbol{v_1'}$ and $\boldsymbol{v_2'}$, the principal plane approximation

of the tradespace is depicted in Figure 6.24b. The nearly-vertical boundary for perturbations with a roughly 2 km component in position is apparent in both the full discretization as well as the principal plane approximation, and the iteration contours are consistent between the two methods for limits between 4 and 6 iterations with few exceptions. At high iteration counts, the allowable velocity component is occasionally over-predicted in the principal plane approximation, indicating a departure into chaos for these iteration limits in the reduced analysis; however, the true boundary is still evident from visual inspection. A similar comparison is conducted between the expanding shell discretization, shown in Figure 6.25a, and the principal plane approximation, shown in Figure 6.25b, for a node placed at $t_1 = 8.23$ days from the reference apolune point. Near this value of t_1, the convergence

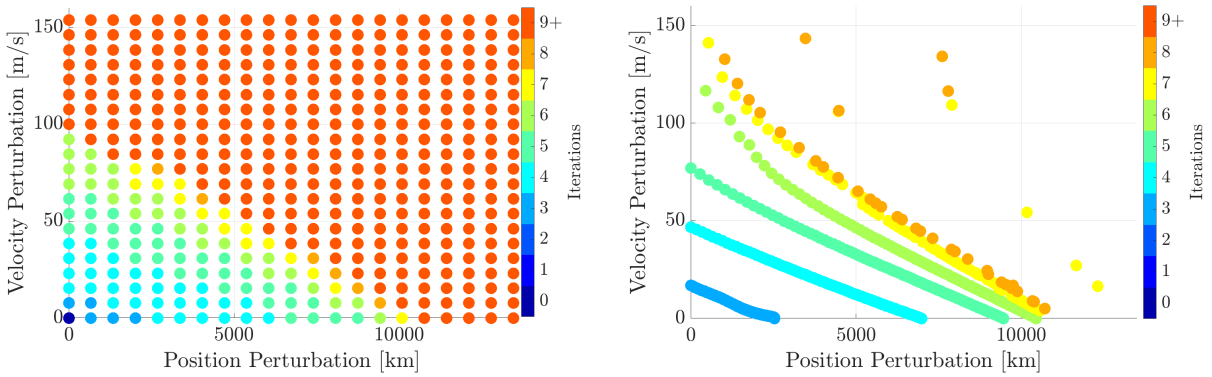

(a) Expanding Shell Discretization

(b) Principal Plane Approximation

Figure 6.25. Position-Velocity Tradespace for 9:2 NRHO Follow-On Targeting ($t_1 = 8.23$ days)

behavior within the position and velocity subspaces is relatively constant, and the principal plane analysis that incorporates the directions with the largest local 2^{nd}-order nonlinearity provides a representative approximation of the tradespace. In both scenarios, the principal plane approximation provides useful insight into the position-velocity tradespace while reducing the discretization and, therefore, the targeting simulation requirement from a 6-dimensional space to a 2-dimensional plane.

A natural question in the characterization of the convergence behavior for a targeting problem with a trajectory governed by the CRTBP is to inquire about the ability to extrapolate results to a higher-fidelity ephemeris force model. To investigate this question, a

reference solution based on the Earth-Moon 9:2 NRHO is produced in an ephemeris force model, defined in Equation (2.36), with gravitational influence from the Earth, Moon, and Sun. In an inertial reference frame with the Earth as the central body, an initial condition at time t_1 is given in dimensional units by

$$\tilde{\boldsymbol{r}}(t_0) = \begin{bmatrix} -122,269.633 \\ -298,632.161 \\ -229,602.973 \end{bmatrix} \text{ km}, \qquad {}^{I}\frac{\mathrm{d}\tilde{\boldsymbol{r}}}{\mathrm{d}\tilde{t}}(t_0) = \begin{bmatrix} -325.445 \\ -794.869 \\ -611.134 \end{bmatrix} \text{ m/s} \tag{6.4}$$

where the notation in Equation (2.36) is abbreviated such that $\boldsymbol{r}$ denotes the position vector from the Earth to the spacecraft. The trajectory, depicted in the Earth-Moon rotating frame in Figure 6.26, is propagated for a time-of-flight equivalent to 2 periods of the underlying 9:2 NRHO in the CRTBP. An analogous targeting problem is formulated such that a per-

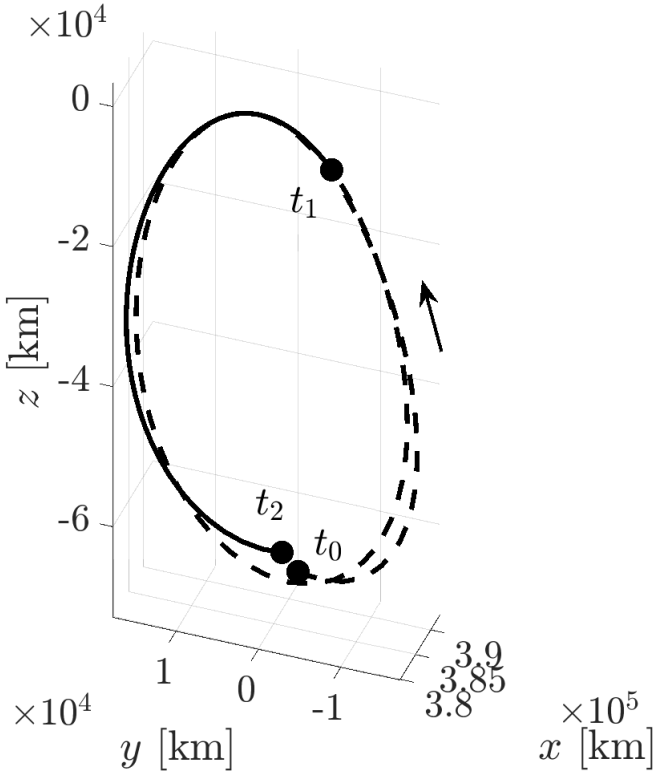

Figure 6.26. 9:2 NRHO Follow-On Ephemeris Reference Solution

turbation from the reference solution is applied at the maneuver time t_1, a parameter for study, to target back to the reference position at the final time t_2. The perturbed targeting problem is expressed as

$$\boldsymbol{\mathcal{F}} = \boldsymbol{r}(t_2)^- - \boldsymbol{r_d} \ , \ \boldsymbol{\mathcal{X}} = \frac{{}^I\mathrm{d}\boldsymbol{r}}{\mathrm{d}t}(t_1)^+ \ , \ \boldsymbol{\mathcal{Y}} = \begin{bmatrix} \boldsymbol{\mathcal{Y}}_1 \\ \boldsymbol{\mathcal{Y}}_2 \end{bmatrix} = \begin{bmatrix} \boldsymbol{r}(t_1)^+ \\ \frac{{}^I\mathrm{d}\boldsymbol{r}}{\mathrm{d}t}(t_1)^+ \end{bmatrix} \tag{6.5}$$

where the desired final position vector is given by

$$\tilde{\boldsymbol{r}}_{\boldsymbol{d}} = \begin{bmatrix} 92,019.878 \\ 383,356.665 \\ 117,470.635 \end{bmatrix} \ \mathrm{km} \tag{6.6}$$

In this scenario, the perturbation, propagation, and targeting is conducted in the Earth-centered J2000 inertial frame.

For the analogous scenario in the CRTBP, the basin width measurement appears to be governed by the vectors associated with the largest normalized change in the design Jacobian due to perturbations, so these vectors, $\boldsymbol{v_i'}$, for the $\boldsymbol{\mathcal{Y}}_i$ subspaces are employed to characterize the convergence basin width in the higher-fidelity scenario. In the ephemeris force model, the tensor quantity $\frac{\partial \boldsymbol{\mathcal{F}}}{\partial \boldsymbol{\mathcal{X}}}\Big|^{-1}_{(\boldsymbol{\mathcal{X}}^*,\boldsymbol{\mathcal{Y}}^*)} \frac{\partial^2 \boldsymbol{\mathcal{F}}}{\partial \boldsymbol{\mathcal{X}} \partial \boldsymbol{\mathcal{Y}}_i}\Big|_{(\boldsymbol{\mathcal{X}}^*,\boldsymbol{\mathcal{Y}}^*)}$ is computed via central differencing on the reference solution for a range of values of t_1 to produce the mode-3 singular vectors $\boldsymbol{v_i'}$ and basin metric values γ_i'. In the $\boldsymbol{\mathcal{Y}}_1$ position perturbation subspace, the convergence basin width with limit of 4 iterations, chosen sufficiently small to produce information about the local main basin, is measured in the $\boldsymbol{v_1'}$ direction and plotted in black in Figure 6.27a. For comparison, the position subspace basin width values from the CRTBP-governed scenario across the same values of t_1 are reproduced in Figure 6.27a in red. The same basin contractions, or local minima, are apparent in both data sets though slightly offset in time to reflect the difference in reference trajectories and force models. In addition the overall qualitative trends are consistent between the two force models, and the magnitudes of the allowable perturbations are similar. The values of γ_1', measuring the largest 2^{nd}-order nonlinearity at the reference solutions, are plotted in black and red in Figure 6.27b for the problems in the ephemeris and

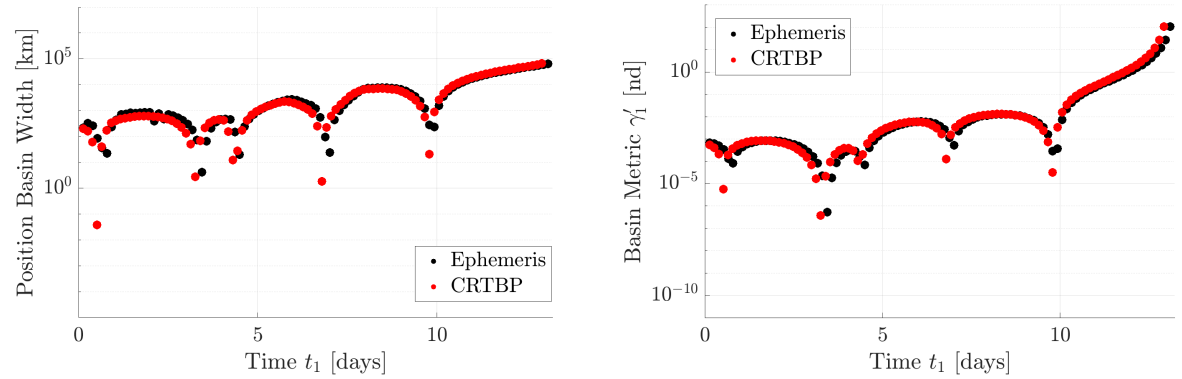

(a) 4-Iteration Position Basin Width

(b) Position Basin Metric

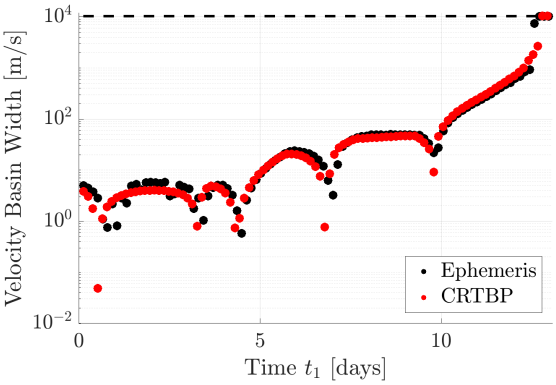

(c) 4-Iteration Velocity Basin Width

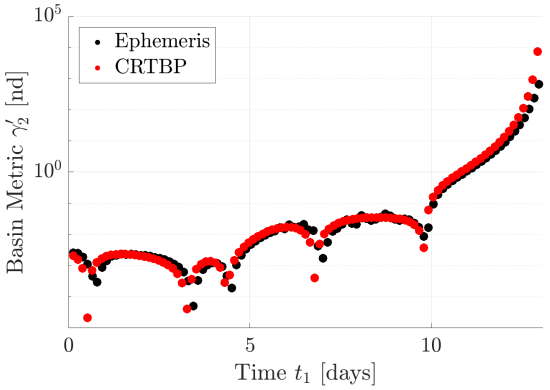

(d) Velocity Basin Metric

Figure 6.27. CRTBP and Higher-Fidelity Ephemeris Model 9:2 NRHO Follow-On Targeting

CRTBP models, respectively. Again, the results are consistent between the two scenarios, and the evaluated values of γ_1' in both the CRTBP and higher-fidelity models are useful in predicting the simulation-measured basin width results. The basin width measurements for a 4-iteration limit and the basin metric values in the $\boldsymbol{\mathcal{Y}}_2$ velocity perturbation subspaces are plotted in Figure 6.27c and 6.27d, respectively, with the higher-fidelity results in black and the CRTBP results in red. In general, the convergence characteristics over the parameter t_1 within the CRTBP are preserved as the trajectory and problem are transitioned to satisfy the higher-fidelity equations of motion, so the lower-fidelity model offers valuable insight into higher-fidelity analog.

As the maneuver time parameter is varied across the time-of-flight, five contractions in the convergence basin, where the allowable perturbation magnitudes for a given iteration

limit are smaller, are evident in both models. The locations of these contractions along the reference periodic orbit in the CRTBP are plotted in red in Figure 6.28a. In this model,

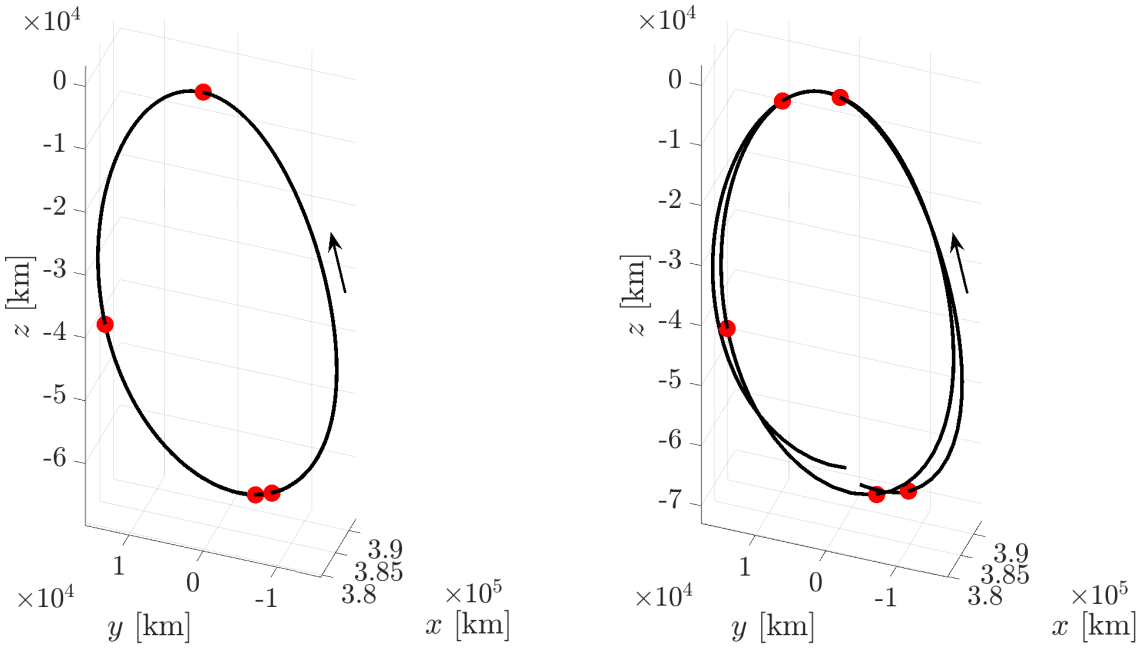

(a) CRTBP Model (b) Ephemeris Earth-Moon-Sun Model

Figure 6.28. 9:2 Follow-On Targeting Basin Contraction Locations

two points, overlapping in the figure, correspond to the perilune point, and two points are situated just after the apolune point on each revolution. The fifth basin contraction occurs within the first revolution at a mean anomaly of approximately 118 deg from perilune. In the Earth-Moon-Sun ephemeris force model, the predicted and measured basin contractions, depicted in Figure 6.28b, are plotted against the reference solution. The similarity in the placement of these sensitive regions around the trajectory is evident. The information gained from analysis in the CRTBP provides insight into the regions in the higher-fidelity model that cannot accommodate large state perturbations in the targeting process.

7. APPLICATION TO TRANSFER TRAJECTORIES IN AN EPHEMERIS FORCE MODEL

Though the CRTBP and the periodic orbits that it governs are frequently of interest in trajectory and targeter design problems, transfer trajectories in a higher-fidelity ephemeris force model allow for an exploration of the proposed convergence behavior prediction and measurement strategies in dynamically-interesting regions of space. To examine these techniques in complex dynamical regimes, hypothetical targeting scenarios and reference solutions based on previously-flown spaceflight missions are produced. By varying a parameter in the design of these targeting problems and solutions, the relative convergence properties with respect to design alternatives are studied.

7.1 Sun-Earth L_1-to-L_2 Transit Trajectory

To explore the correlation of the predictive evaluated quantities and the numerically-produced basin width measurements in a complex dynamical environment, a transfer trajectory that leverages structures in the Sun-Earth system is constructed to represent motion similar to the Genesis mission. The Genesis mission trajectory, reproduced in Figure 7.1 from NASA's mission website [68], entered into an L_1 halo orbit to collect solar wind samples before leveraging dynamics near the L_2 point to return to Earth [69]. A trajectory, shown

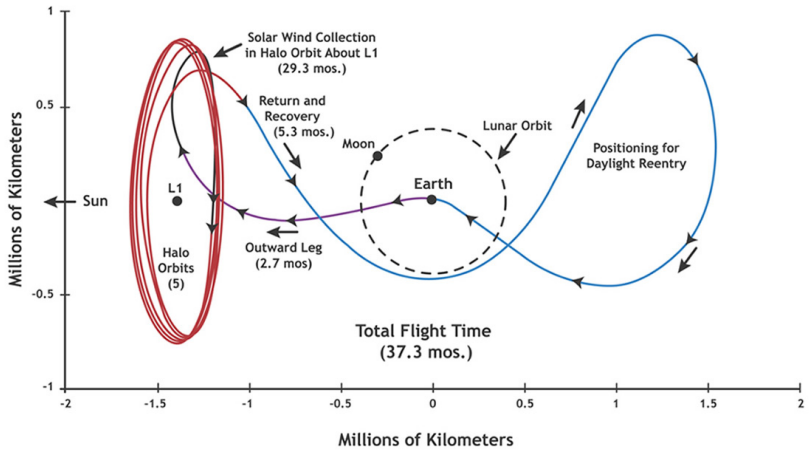

Figure 7.1. Genesis Mission Trajectory (Reproduced from NASA.gov [68])

in Figure 7.2, is generated based on work in support of the Genesis mission [70], [71] and corrected to be continuous in position and velocity in an ephemeris force model, consisting of the Sun, Earth, and Moon. In Figure 7.2, the entire trajectory, as viewed in the Sun-Earth

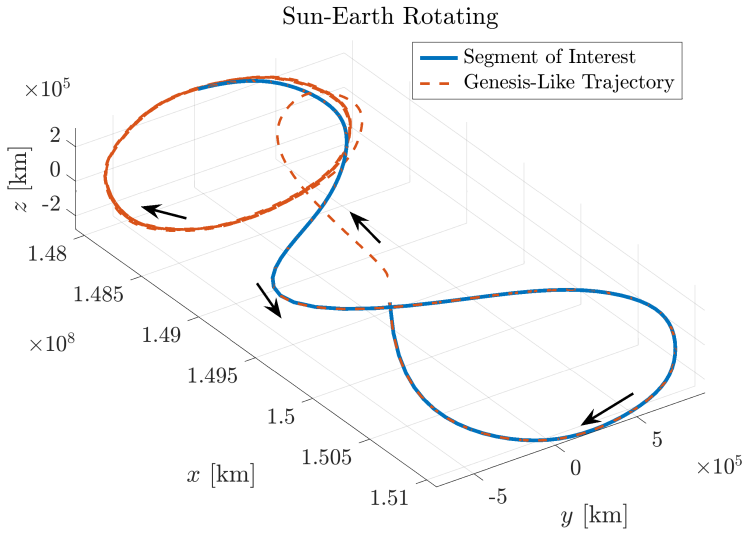

Figure 7.2. Genesis-Like Trajectory with L_1-to-L_2 Transit of Interest

rotating reference frame, is represented as a dashed orange line, and the blue portion denotes the portion that consists of a departure from the L_1 halo orbit, transit to the L_2 vicinity, and return to the Earth vicinity. This final segment, traversing the L_1 and L_2 vicinities with a relatively close pass of the Earth-Moon system, provides a dynamically-interesting reference trajectory that serves as the baseline solution to a proposed targeting problem and the focus of convergence analysis. Two characterizations of the convergence basin are assessed: (*i*) as the spacecraft moves downstream along the reference trajectory and (*ii*) as the arrival epoch is offset over the course of 28 days. These applications reflect typical analyses that may be of interest to mission designers.

7.1.1 Convergence Basin Analysis Along the Baseline Trajectory

Knowledge of the convergence behavior along a baseline trajectory allows mission designers to determine times when re-targeting to correct for accumulated errors is more or less likely to converge upon a new feasible solution. Therefore, a perturbed targeting problem

is formulated to characterize the convergence behavior across a set of reference solutions parameterized by the time t_1 that moves downstream along the full reference. Starting from an initial time, t_0, the spacecraft travels along the reference path; however, a state perturbation is introduced and a differential corrections process is executed at the targeting epoch t_1. The corrections process leverages a change in the inertial velocity at t_1 to target back to the reference position vector, $\boldsymbol{r_d}$, at the fixed final epoch t_2. Mathematically, the perturbed targeting problem is formulated as

$$\boldsymbol{\mathcal{F}} = \boldsymbol{r}(t_2)^- - \boldsymbol{r_d} \ , \ \boldsymbol{\mathcal{X}} = \frac{{}^I\mathrm{d}\boldsymbol{r}}{\mathrm{d}t}(t_1)^+ \ , \ \boldsymbol{\mathcal{Y}} = \begin{bmatrix} \boldsymbol{\mathcal{Y}}_1 \\ \boldsymbol{\mathcal{Y}}_2 \end{bmatrix} = \begin{bmatrix} \boldsymbol{r}(t_1)^+ \\ \frac{{}^I\mathrm{d}\boldsymbol{r}}{\mathrm{d}t}(t_1)^+ \end{bmatrix} \tag{7.1}$$

where $\boldsymbol{r}$ represents the inertial position vector from the Earth to the spacecraft in the J2000 inertial frame. The trajectory and the nodes associated with t_0, t_2, and a candidate for t_1 are depicted in Figure 7.3 in the Sun-Earth rotating frame with the origin at the Sun-Earth barycenter. Because the reference frame does not pulsate to incorporate the changing

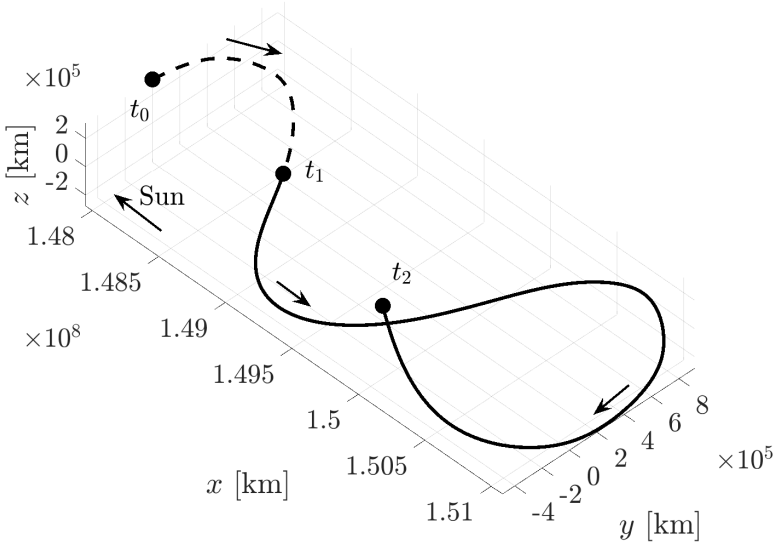

Figure 7.3. Reference Solution for Targeting Along the L_1-to-L_2 Transit

distance between the bodies, the positions of the Sun and Earth along the $\hat{\boldsymbol{x}}$-axis evolve in time in this reference frame.

The convergence behavior is measured and predictive quantities are evaluated on reference solutions defined by t_1 as it moves between the initial and final epochs, t_0 and t_2. Across the set of baseline solutions, the basin width, defined for the iteration limit of 5 iterations, for perturbations in the position at t_1 is numerically measured via the PDA method and plotted in Figure 7.4a. In this plot, the time along the trajectory is measured as the difference

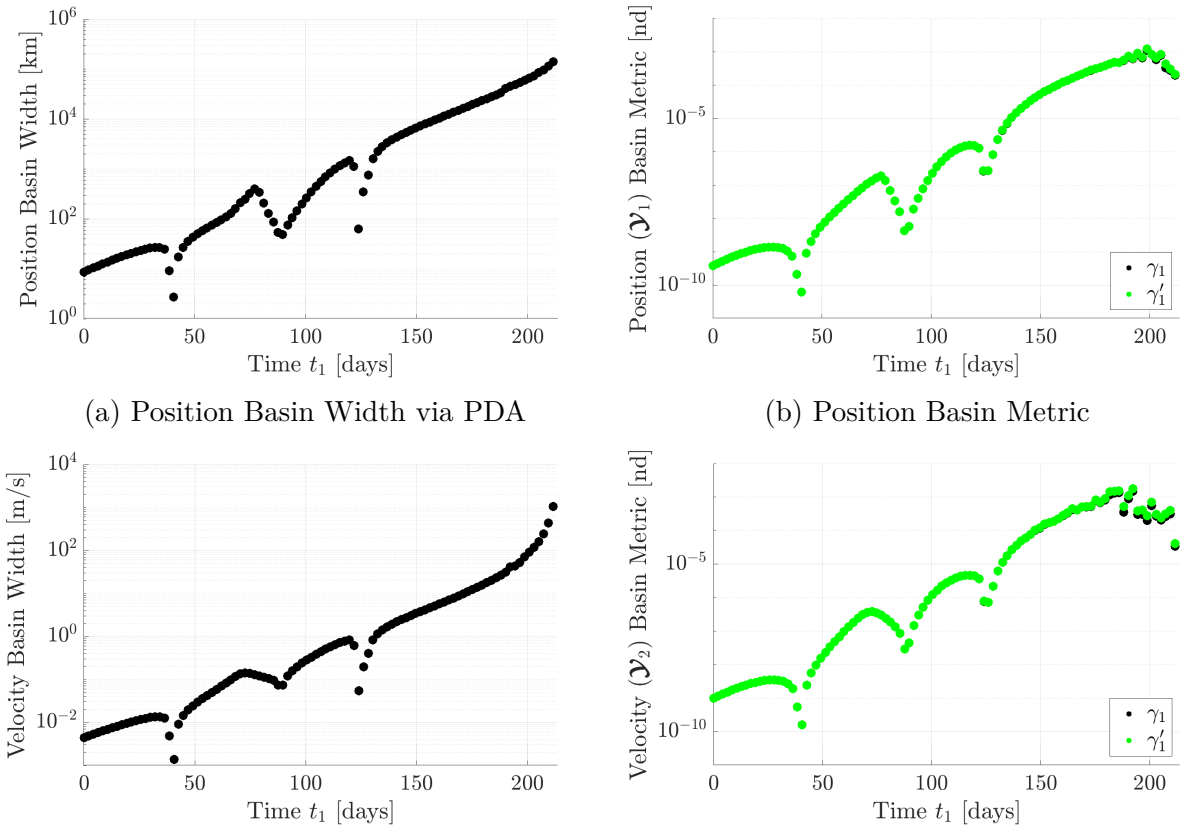

(a) Position Basin Width via PDA

(b) Position Basin Metric

(c) Velocity Basin Width via PDA

(d) Velocity Basin Metric

Figure 7.4. PDA Basin Width Measurements and Evaluated Basin Metrics for Targeting Along the L_1-to-L_2 Transit

between the parameter t_1 and the fixed t_0, reflecting the elapsed time since the last perilune along the L_1 halo orbit. In general, as the targeting epoch is brought closer to the final time, the basin width increases, indicating an expansion of the main basin. However, the generally positive trend is punctuated by local minima and maxima, representing intervals of time for which convergence is easier and more difficult, respectively. Figure 7.4b shows the evaluated basin metrics γ_1 and γ_1', which both reflect the local normalized rate of change

in the design Jacobian due to perturbations in position at t_1. However, these quantities differ in their method of calculation. While γ_1, defined in Equation (4.35), approximates the quantity with the l_2 matrix norm of a flattened 3-dimensional tensor, the basin metric γ_1', defined in Equation (4.44), is a function of the largest higher-order singular value of the tensor, computed via an optimization problem. In this scenario, both methods produce similar results, as apparent by their overlapping nature in Figure 7.4b, and the basin metric values correlate strongly with the trends in the measured basin width in Figure 7.4a. For perturbations in the velocity subspace, the basin width measurements, defined for a limit of 5 iterations and plotted in Figure 7.4c, also have a strong correlation with the relative behavior of their associated basin metric values in Figure 7.4d as t_1 progresses downstream.

The valleys in convergence basin width and metric signify regions along the trajectory for which the differential corrections process is particularly sensitive to state perturbations and may fail to reliable converge to a reference solution on the same constraint manifold. To represent the convergence properties along the reference trajectory, the basin widths in the position perturbation subspace are reproduced in Figure 7.5a. The local minima in basin

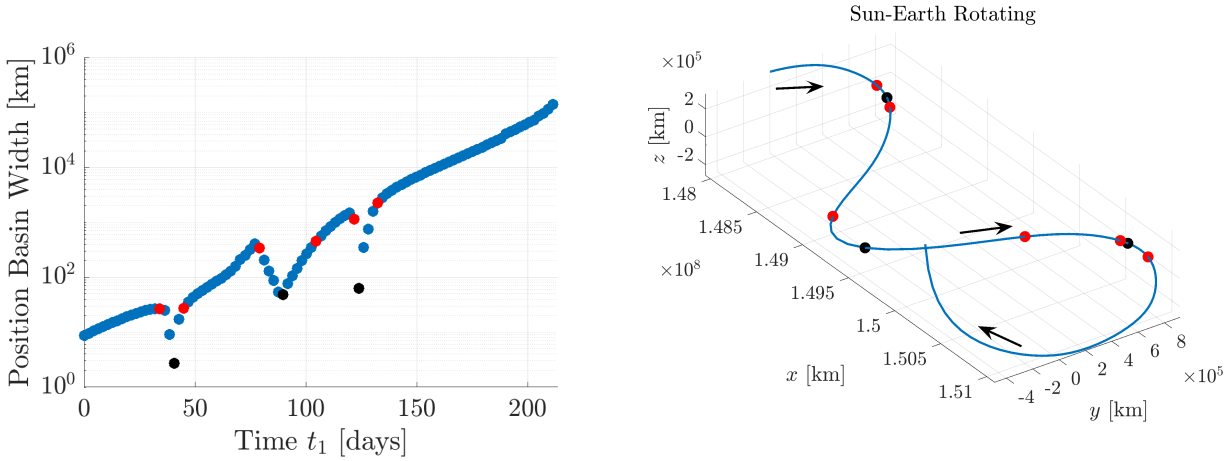

(a) Position Basin Width

(b) L_1-to-L_2 Transit

Figure 7.5. Locations Along the Baseline Trajectory with Constricted Convergence Basins for Targeting Along the L_1-to-L_2 Transit

width, marked in black, occur at three locations along the trajectory and accompany regions of basin constriction, marked in red on either side. The corresponding locations along the

reference trajectory are marked in Figure 7.5b in black and red, as appropriate. The second local minimum occurs at the closest pass to the Earth-Moon vicinity, a region commonly identified as dynamically sensitive. However, the first and third local minima may not fit within the intuition of a mission designer. The ability to predict these minima with the evaluated basin metric and efficiently confirm their existence with the PDA discretization strategy is valuable, because it provides key insights into a particular combination of a targeting formulation and trajectory design options without requiring large batches of targeting simulations.

The PDA discretization strategy generates points along a reduced set of vectors in the perturbation space, and the minimum result across these directions is recorded as the approximate basin width for a given combination of targeting problem and reference solution. The $\boldsymbol{\mathcal{Y}}_1$ and $\boldsymbol{\mathcal{Y}}_2$ subspaces, each possess three dimensions, and the first three directions are taken as the right singular vectors $\boldsymbol{v_{i,j}}$ for $j = 1, 2, 3$ of $\frac{\partial \boldsymbol{\mathcal{F}}}{\partial \boldsymbol{\mathcal{Y}}_i}\Big|_{(\boldsymbol{\mathcal{X}}^*, \boldsymbol{\mathcal{Y}}^*)}$, indicating the principal directions of change in the constraint vector due to perturbations in $\boldsymbol{\mathcal{Y}}_i$ at the solution. The final direction in the PDA corresponds to the dominant mode-3 singular vector of the normalized rate of change in the design Jacobian, i.e., $\frac{\partial \boldsymbol{\mathcal{F}}}{\partial \boldsymbol{\mathcal{Y}}_i}\Big|^{-1}_{(\boldsymbol{\mathcal{X}}^*, \boldsymbol{\mathcal{Y}}^*)} \frac{\partial^2 \boldsymbol{\mathcal{F}}}{\partial \boldsymbol{\mathcal{X}} \partial \boldsymbol{\mathcal{Y}}_i}\Big|_{(\boldsymbol{\mathcal{X}}^*, \boldsymbol{\mathcal{Y}}^*)}$. This vector, $\boldsymbol{v_i'}$, indicates the direction of the largest relative change in the partial derivatives used for targeting. The measurement results in each of these four directions for the position and velocity perturbation subspaces are captured in Figures 7.6a and 7.6b, respectively. Diving into the results

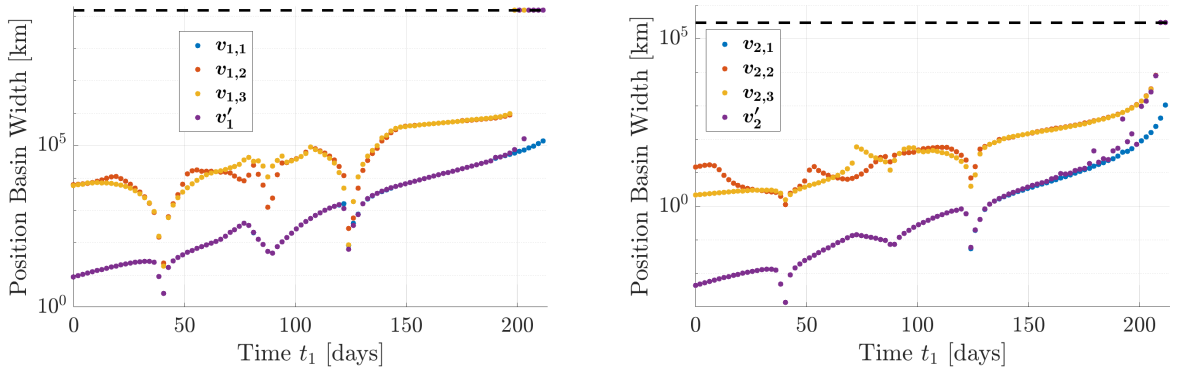

(a) Position Perturbation Subspace

(b) Velocity Perturbation Subspace

Figure 7.6. Individual Principal Direction Measurements for Targeting Along the L_1-to-L_2 Transit for a 5-Iteration Limit

of the individual measurement directions of the PDA method gives insight into the link between the basin width and the basin metric. As the targeting epoch is moved downstream, the measurements in the $\boldsymbol{v}_{i,\mathbf{1}}$ and $\boldsymbol{v}_i'$ directions consistently represent the minimum value, indicating that the basin is smallest in directions with larger growth in the constraint vector and larger relative change in the design Jacobian matrix. Because the PDA strategy does not interrogate the entire perturbation space, it is possible that even smaller measurements are available in unexplored directions; however, the PDA-measurement provides an upper bound for the basin width along the trajectory and is able to positively identify unfavorable targeting conditions.

The correlation between the PDA-measured basin width and evaluated basin metric values is further explored by examining the FTLE-based quantities, defined in Equations (4.15) and (4.14). For this targeting scenario, $\boldsymbol{\mathcal{Y}}_2$ and $\boldsymbol{\mathcal{X}}$ both consist of the outgoing velocity at the time t_1, so $\lambda_{\boldsymbol{\mathcal{X}}}$ is equivalent to $\lambda_{\boldsymbol{\mathcal{Y}}_2}$. As the targeting time moves in downstream along the reference trajectory, the values of $-\lambda_{\boldsymbol{\mathcal{Y}}_1}$ and $-\lambda_{\boldsymbol{\mathcal{Y}}_2}$ are plotted in Figure 7.7. These

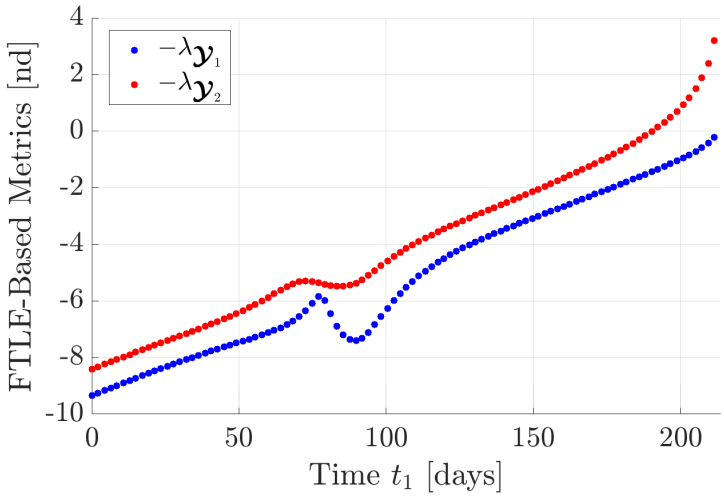

Figure 7.7. FTLE-Based Quantities for Targeting Along the L_1-to-L_2 Transit

quantities are multiplied by -1 to reflect the expected inverse relationship between stretching in the constraint vector and the size of the convergence basin. In Figure 7.7, a small dip is visible where t_1 is approximately 90 days downstream from the initial time. This dip appears to correspond with the increased sensitivity as the spacecraft passes the Earth-Moon vicinity;

however, the other basin width minima are not represented in the FTLE-based quantities. While the basin metrics γ_i' are related to the vectors $\boldsymbol{v_i'}$ through the higher-order singular value and singular vector computation, $\lambda_{\boldsymbol{\mathcal{Y}}_i}$ are functions of the singular values corresponding to the vectors $\boldsymbol{v_{i,1}}$. Though $\boldsymbol{v_{i,1}}$ and $\boldsymbol{v_i'}$ produce similar basin width measurements in Figures 7.6a and 7.6b, the lack of correlation of the basin widths and the values of $\lambda_{\boldsymbol{\mathcal{Y}}_i}$ suggests that the strategies associated with the tensor $\frac{\partial \boldsymbol{\mathcal{F}}}{\partial \boldsymbol{\mathcal{Y}}_i}\Big|^{-1}_{(\boldsymbol{\mathcal{X}}^*,\boldsymbol{\mathcal{Y}}^*)} \frac{\partial^2 \boldsymbol{\mathcal{F}}}{\partial \boldsymbol{\mathcal{X}} \partial \boldsymbol{\mathcal{Y}}_i}\Big|_{(\boldsymbol{\mathcal{X}}^*,\boldsymbol{\mathcal{Y}}^*)}$, i.e., $\boldsymbol{v_i'}$ and γ_i', possess more predictive power.

7.1.2 Convergence Basin Analysis with Varying Arrival Epochs

Another possible mission design task is assessing changes in the targeting feasibility for new reference trajectories generated by varying the epoch of key events. To simulate this task, new baseline trajectories are produced by shifting the arrival epoch for the original baseline trajectory, plotted in Figure 7.2, in single day increments over the course of 28 days, capturing the effects of lunar phasing by spanning approximately one period of the Moon's orbit around Earth. The original baseline trajectory, plotted in Figure 7.2, is conceived as possessing a +0 day epoch offset. To preserve the basic geometry of the transfer, this original reference trajectory is discretized into a series of patch points which are transitioned to the Sun-Earth rotating frame via the ATD software package to maintain the relevant dynamical structures from the Sun-Earth CRTBP. At each new epoch, the transit segment and approximately 4.5 periods of the L_1 halo orbit structure are transitioned back into the Earth-Centered J2000 inertial frame and re-targeted to achieve state continuity and fix the arrival epoch at the offset value by employing a multiple-shooting targeter within the ATD software package. This transition and re-targeting process results in 28 new baseline trajectories, plotted in Figure 7.8 against the entire original dashed trajectory, that begin at the final crossing of the $\hat{\boldsymbol{x}}$-$\hat{\boldsymbol{z}}$ plane along the L_1 halo orbit. These new reference solutions all possess a similar geometry but reflect changes in the positioning and orientation of the gravitational bodies, providing a set of design alternatives for convergence basin analysis.

A perturbed targeting problem is formulated to target back to the position at the arrival epoch t_1 of each epoch-shifted reference solution by imposing a change to in the velocity at t_0,

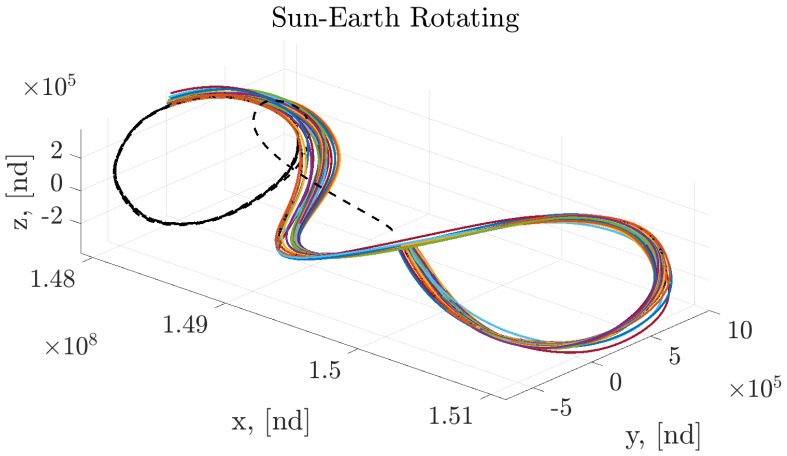

Figure 7.8. Reference Solution for Targeting for Epoch-Shifted L_1-to-L_2 Transits

corresponding to the final crossing of the $\hat{\boldsymbol{x}}$-$\hat{\boldsymbol{z}}$ plane along the L_1 halo orbit. Mathematically, this problem is expressed in the inertial frame as

$$\boldsymbol{\mathcal{F}} = \boldsymbol{r}(t_1)^- - \boldsymbol{r_d} \ , \ \boldsymbol{\mathcal{X}} = \frac{{}^I\mathrm{d}\boldsymbol{r}}{\mathrm{d}t}(t_0)^+ \ , \ \boldsymbol{\mathcal{Y}} = \begin{bmatrix} \boldsymbol{\mathcal{Y}}_1 \\ \boldsymbol{\mathcal{Y}}_2 \end{bmatrix} = \begin{bmatrix} \boldsymbol{r}(t_0)^+ \\ \frac{{}^I\mathrm{d}\boldsymbol{r}}{\mathrm{d}t}(t_0)^+ \end{bmatrix} \tag{7.2}$$

and the partial derivatives are computed via a central differencing scheme. For each baseline trajectory across the 28 days survey, the basin width in the position perturbation subspace, measured via numerous targeting simulations leveraging the PDA strategy, for a limit of 5 targeting iterations is plotted in Figure 7.9a. The basin width has local minima associated with epoch shifts of +14 and +25 days, and the convergence basin expands to allow larger perturbations for arrival epoch offsets of +7 and +18 days. Defined in Equation (4.44), the basin metric, computed via state transition tensors for each baseline trajectory, is plotted in Figure 7.9b for the position perturbation subspace. As observed previously, the relative features present in the basin metric for each epoch-shifted trajectory mirror the features seen in the measured basin width. As the arrival epoch is varied, all the expansions and contractions of the local convergence basin are represented in the purely-evaluated basin metric quantity, γ_1'. The basin width and basin metric values in the velocity subspace for each epoch-shifted solution are plotted in Figures 7.9c and 7.9d, respectively. Again, the local

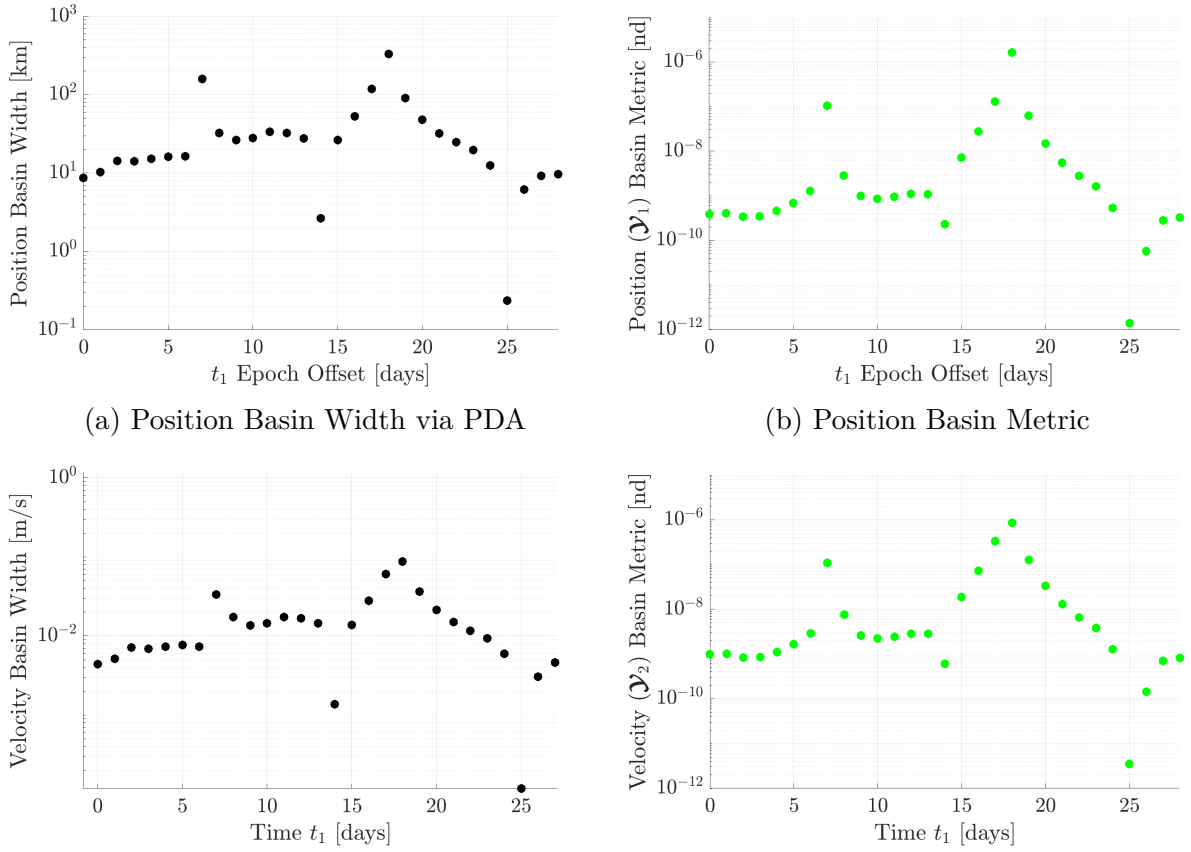

(a) Position Basin Width via PDA

(b) Position Basin Metric

(c) Velocity Basin Width via PDA

(d) Velocity Basin Metric

Figure 7.9. PDA Basin Width Measurements and Evaluated Basin Metrics for Targeting for Epoch-Shifted L_1-to-L_2 Transits

minima and maxima are visible in both sets of data, indicating that a relative comparison of basin metric values is a useful predictor of changes in the convergence behavior within the set of reference solutions.

Intuitively, the rate of growth in the constraint vector is a factor in the convergence behavior of a given perturbed targeting problem, so the FTLE-based quantities, $\lambda_{\mathcal{Y}_1}$ and $\lambda_{\mathcal{Y}_2}$, are investigated for any correlation with the basin width. The FTLE-based quantities, defined in Equation 4.15, are multiplied by -1 for each epoch-shifted solution and plotted in Figure 7.10. Local maxima in the plotted values occur at +7 and +18 indicate lower sensitivity in the constraints and correspond to the basin width local maxima in Figures 7.9a and 7.9c. Lower values in Figure 7.10 at the +25 day epoch-shifted solution have some correlation to the measured local minimum in basin width; however, the basin contraction

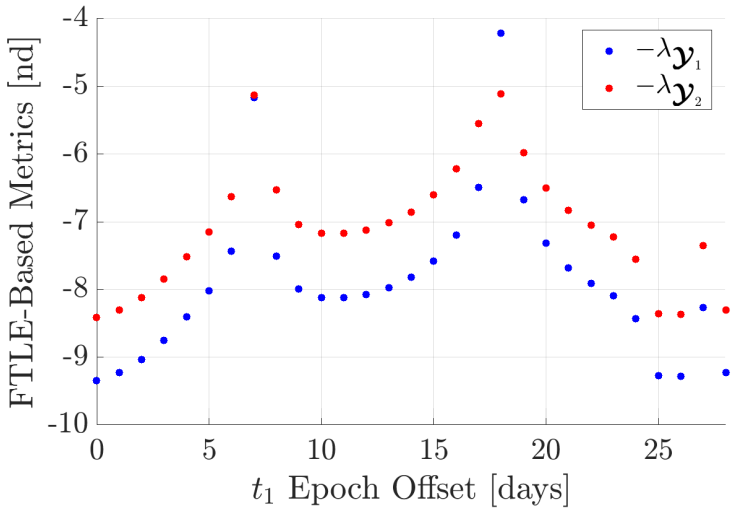

Figure 7.10. FTLE-Based Quantities for Targeting for Epoch-Shifted L_1-to-L_2 Transits

at the +14 day shifted solution is not predicted by the values of $\lambda_{\mathcal{Y}_1}$ and $\lambda_{\mathcal{Y}_2}$. Overall, the basin metric, measuring the relative rate of change in the partial derivatives of the targeting problem, appears to predict the relative convergence behavior better than the FTLE-based quantities that measure the rate of change in the constraints.

7.2 Trans-Lunar Return Transfer Trajectory

To investigate convergence behavior along a trans-lunar return trajectory, a segment of the Artemis I mission is selected to generate a transfer under an ephemeris force model with gravitational influence from the Earth, Moon, and Sun. In the Artemis I mission, the Orion spacecraft travels along a DRO in the Earth-Moon system with a reference distance of 70,000 km from the Moon and execute a series of maneuvers to return to the Earth [62]–[64]. To represent this motion, a 70,000 km reference DRO is transitioned to satisfy the equations of motion in the ephemeris force model, shown in dashed gray in Figure 7.11, and a trans-lunar return leg, shown in solid black, consists of two maneuvers, i.e., the DRO Departure (DRD) and Return Powered Fly-By (RPF) maneuvers, and the Entry Interface (EI) point, associated with the atmospheric entry conditions of the spacecraft. This reference motion is based on a representation of the Artemis I trajectory in the CRTBP employed by Spreen

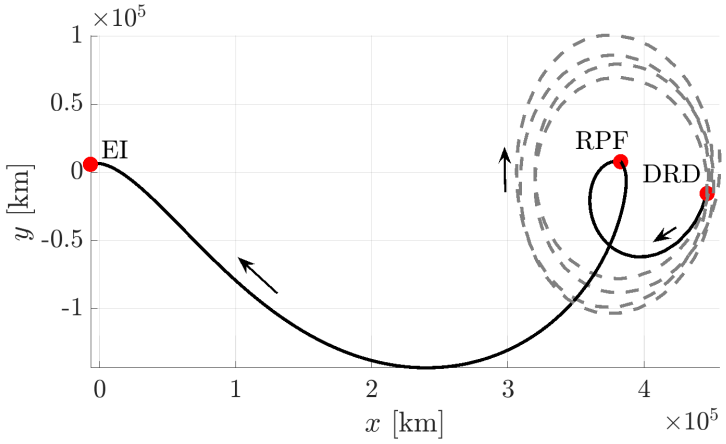

Figure 7.11. Artemis I-Like Lunar Return Reference Trajectory in the Earth-Moon Rotating Frame

[21]. Though the motion possesses components in three dimensions, the projection of the reference trajectory into the $\hat{\boldsymbol{x}}$-$\hat{\boldsymbol{y}}$ plane in the Earth-Moon rotating frame is sufficient for visualization and, therefore, displayed in Figure 7.11.

Because atmospheric entry carries significant risks to the mission and spacecraft, constraints are imposed on the EI point to control the entry conditions. Two constraints are formulated in terms of angles with respect to an Earth-centered, body-fixed reference frame that follows the rotation of the Earth. This rotating reference frame is defined in terms of the vector $\hat{\boldsymbol{i}}$, aligned with the prime meridian in the equatorial plane, the vector $\hat{\boldsymbol{k}}$, pointed toward the North pole, and the vector $\hat{\boldsymbol{j}}$, completing the triad as $\hat{\boldsymbol{k}} \times \hat{\boldsymbol{i}}$ in the equatorial plane. In this investigation, the orientation of the Earth relative to the J2000 inertial frame is computed via the SPICE toolkit. The longitude, θ_{lon}, and the latitude, θ_{lat}, are expressed mathematically as

$$\theta_{\text{lon}} = \tan^{-1}\left(\frac{\boldsymbol{r} \cdot \hat{\boldsymbol{j}}}{\boldsymbol{r} \cdot \hat{\boldsymbol{i}}}\right) \tag{7.3}$$

$$\theta_{\text{lat}} = \sin^{-1}\left(\frac{\boldsymbol{r} \cdot \hat{\boldsymbol{k}}}{\|\boldsymbol{r}\|}\right) \tag{7.4}$$

where the proper quadrant of θ_{lon} is computed from the component signs. Another common constraint on entry conditions is the inertial flight path angle of the spacecraft relative to the Earth. The sine of the flight path angle, θ_{fpa}, is constrained and computed as

$$\sin(\theta_{\text{fpa}}) = \frac{\boldsymbol{r} \cdot \frac{{}^{I}\mathrm{d}\boldsymbol{r}}{\mathrm{d}t}}{\|\boldsymbol{r}\| \, \|\frac{{}^{I}\mathrm{d}\boldsymbol{r}}{\mathrm{d}t}\|} \tag{7.5}$$

Finally, the altitude of the spacecraft from the Earth's surface, h_{alt}, is frequently used to define the interface point and is, therefore, a natural constraint on the entry conditions. Assuming a spherical Earth with a constant radius $R_E = 6378.137$ km, the altitude is computed via

$$h_{\text{alt}} = \|\boldsymbol{r}\| - R_E \tag{7.6}$$

While alternative quantities of interest exist, these four scalar quantities serve to constrain the body-fixed position and the flight path angle of the spacecraft, requiring at least four design variables to produce a fully- or under-constrained targeting problem.

A perturbed targeting problem is devised with four design variables that act to produce a new solution under the influence of state perturbations, and the reference trajectory in Figure 7.11 is the baseline solution to this targeting problem. Suppose the epoch time at EI, denoted t_2, is 17:19:00 UTC on 11 December 2022. Working backward along the trajectory, a node at the epoch t_1 represents the time of of targeting and execution of the final maneuver in the mission. At this targeting epoch, a perturbation is applied, modeling an error in the state of the spacecraft, and differential corrections are employed to compute a change in the velocity at t_1 as well as a variable time-of-flight to target a set of EI constraints. At the EI epoch, the longitude and latitude are constrained to 120 deg W and 20 deg S, respectively. The flight path angle is constrained to -5.8 deg at an altitude of 121.92 km. This set of

design variables, perturbation variables, and constraints results in a perturbed targeting problem formulated as

$$\boldsymbol{\mathcal{F}} = \begin{bmatrix} \theta_{\text{lon}}(t_2) - (-120\,\text{deg}) \\ \theta_{\text{lat}}(t_2) - (-20\,\text{deg}) \\ \sin(\theta_{\text{fpa}}(t_2)) - \sin(-5.8\,\text{deg}) \\ h_{\text{alt}}(t_2) - 121.92\ \text{km} \end{bmatrix}, \boldsymbol{\mathcal{X}} = \begin{bmatrix} {}^{I}\frac{\mathrm{d}\boldsymbol{r}}{\mathrm{d}t}(t_1) \\ t_2 \end{bmatrix}, \boldsymbol{\mathcal{Y}} = \begin{bmatrix} \boldsymbol{\mathcal{Y}}_1 \\ \boldsymbol{\mathcal{Y}}_2 \end{bmatrix} = \begin{bmatrix} \boldsymbol{r}(t_1) \\ {}^{I}\frac{\mathrm{d}\boldsymbol{r}}{\mathrm{d}t}(t_1) \end{bmatrix} \tag{7.7}$$

As t_1 is moved backward from EI, the impact of the placement of this targeting epoch on the convergence behavior is studied.

The basin metric is compared to the PDA-measured basin width to assess its ability to predict changes in the convergence behavior as the targeting epoch is moved from 1 hour to 12 hours before EI in 30 minute increments. For limits of 1 to 8 iterations in the targeting process, Figure 7.12a the PDA-measured basin width in the $\boldsymbol{\mathcal{Y}}_1$ position subspace as t_1 is varied. As the iteration count increases, the basin width measurements grow closer together, indicating the approach of a bounding structure of the main basin. As t_1 moves backward in time from 1 hour to 12 hours before EI, the basin width measurements generally decrease gradually; however, a pronounced decrease in the convergence basin width occurs when t_1 is placed 3.5 hours before EI. For this maneuver placement, the basin width drops from approximately 900 km to only about 5 km with an 8-iteration limit. Plotted in Figure 7.12b, the basin metric in the position subspace, γ_1', defined in Equation (4.44), is a measure of the relative rate of change in the partial derivatives used for targeting as the solution is perturbed. As t_1 varies, the trends in γ_1' mirror the trends seen in the measured basin width, and the local minima at 3.5 hours before EI is predicted. The velocity basin width, depicted in Figure 7.12c, also decreases rapidly at this targeting epoch, dropping from roughly 50 m/s to 5 m/s, and the plot of γ_2' in Figure 7.12d predicts this basin contraction. The FTLE-based quantities, measuring the maximum degree of local stretching in the constraints, are plotted in Figure 7.13, and, in contrast to the basin metric, the values of $\lambda_{\boldsymbol{\mathcal{Y}}_i}$ and $\lambda_{\boldsymbol{\mathcal{X}}}$ do not predict the observed decrease in the size of the basin. Of the available quantities, the basin

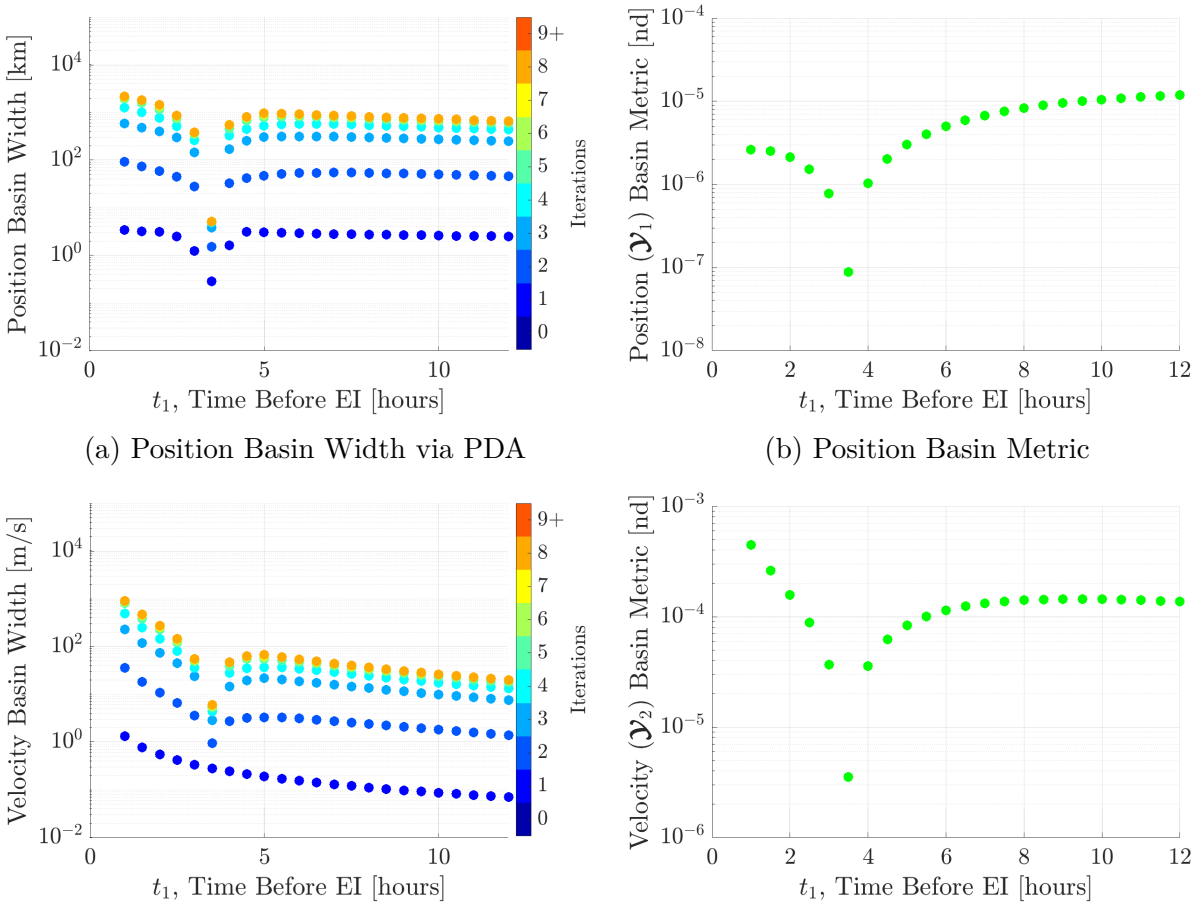

(a) Position Basin Width via PDA

(b) Position Basin Metric

(c) Velocity Basin Width via PDA

(d) Velocity Basin Metric

Figure 7.12. PDA Basin Width Measurements and Evaluated Basin Metrics for Trans-Lunar Return

metric, measuring the local nonlinearity in the targeting problem, is the best predictor of the measured convergence behavior in this scenario.

The predictive capability of the convergence basin metric provides valuable information where a visual inspection of the trajectory for known sources of sensitivity may fail to produce insight. The location of the targeting node when t_1 is placed 3.5 hours prior to EI is depicted on the reference trajectory in the Earth-Moon rotating frame in Figure 7.14. From viewing the trajectory in the Earth-Moon rotating frame, there are no obvious indications, e.g., close proximity to a primary body, that convergence basin rapidly decreases in the vicinity of the point associated with $t_1 = 3.5$ hours. A close-up view of the trajectory in the Earth-Centered J2000 inertial frame, shown in Figure 7.15, also does not bear any intuitive hallmarks of

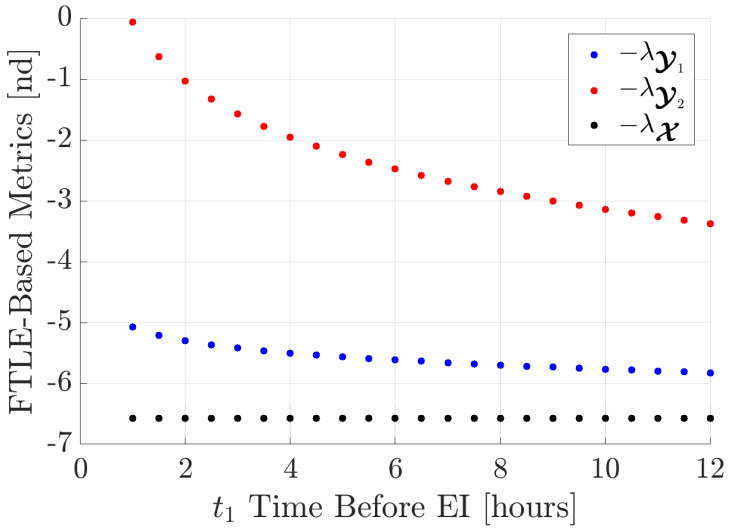

Figure 7.13. FTLE-Based Quantities in Trans-Lunar Return Targeting

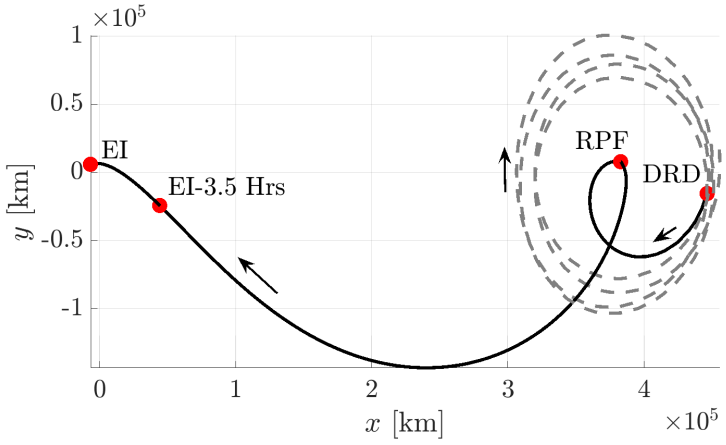

Figure 7.14. Trans-Lunar Return Reference Trajectory in the Earth-Moon Rotating Frame with Location of Basin Contraction

dynamical sensitivity. Nonetheless, a constriction in the convergence basin is measured at this point, and the basin metric provides a method for predicting the existence of this narrowing without the need for running numerous costly targeting simulations.

Though the computation of the position-velocity perturbation tradespace via a full 6-dimensional expanding shell discretization is impractical for this investigation, the interaction

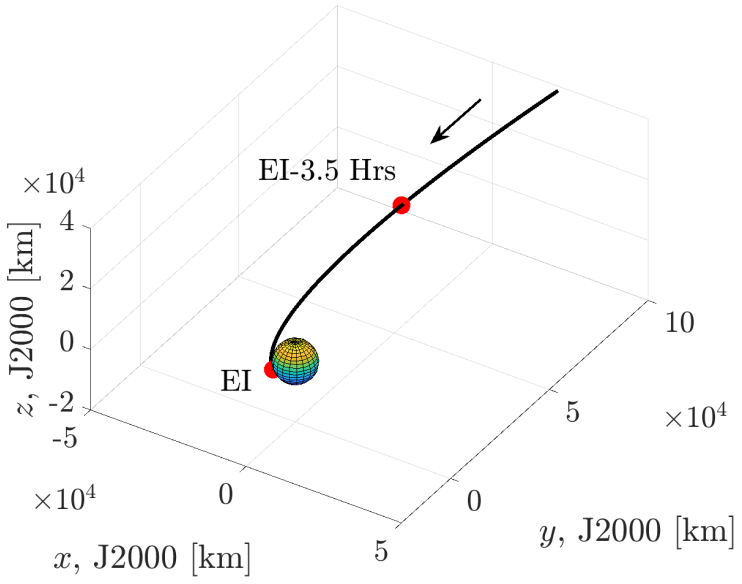

Figure 7.15. Trans-Lunar Return Reference Trajectory in the Earth-Centered J2000 Frame with Location of Basin Contraction

of position and velocity perturbations for a targeting epoch 3.5 hours before EI is estimated via the more efficient principal plane approximation. In this scenario, the principal direction associated with the smallest basin measurement in the position PDA is given along the $\boldsymbol{v_{1,3}}$ direction, or the right singular value corresponding to the smallest singular value of the perturbation Jacobian matrix $\frac{\partial \mathcal{F}}{\partial \mathcal{Y}_1}\Big|_{(\mathcal{X}^*,\mathcal{Y}^*)}$. However, all directions in the analysis, including $\boldsymbol{v_{1,1}}$ and $\boldsymbol{v_1'}$ that correspond to largest growth in the constraints and largest normalized change in the design Jacobian, respectively, exhibit the steep decrease in measurements at this epoch. This result suggests that more significant higher order effects beyond 2$^{\text{nd}}$ order may happen to align most closely with the vector $\boldsymbol{v_{1,3}}$ at this contraction point. In the $\mathcal{Y}_2$ velocity perturbation subspace, however, the minimum measurement corresponds with $\boldsymbol{v_2'}$, the direction of largest normalized change in the design Jacobian matrix. From these analyses of the independent subspaces, the vectors $\boldsymbol{v_{1,3}}$ and $\boldsymbol{v_2'}$ are selected to define the principal plane, and the results of the measurements in this plane are shown in Figure 7.16. From this tradespace, a mission designer is able to determine if a given pair of position and velocity perturbation magnitudes are likely to converge reliably to new solution on the constraint

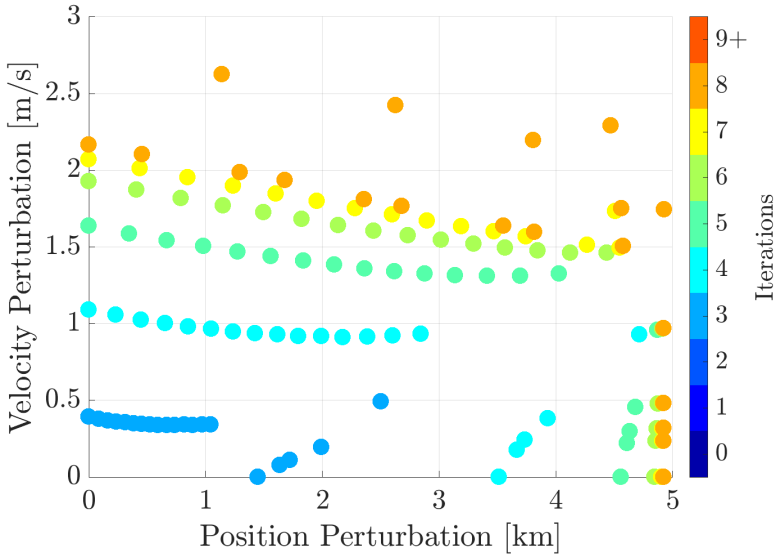

Figure 7.16. Principal Plane Approximation for $t_1 = 3.5$ Hours Prior to EI in Trans-Lunar Return Targeting

manifold of the baseline solution. For example, while perturbations of 4 km and 1.75 m/s are independently accommodated, the combination of the two perturbations, if oriented in the wrong direction, falls in a region with high iteration counts that appears to traverse the chaotic boundary of the main convergence basin. In this mission scenario, however, the mission designer would do well to shift the targeting epoch out of the contracted region and into a region where the allowable perturbations are orders of magnitude larger.

8. CONCLUDING REMARKS

As space flight missions are developed to leverage structures within complex multi-body dynamical environments, the ability to design trajectories and targeting schemes in a concurrent manner, taking into account the convergence behavior in determining new feasible solutions that incorporate inevitable perturbations, is essential to mission success. Traditionally, mission designers rely on techniques such as Monte Carlo simulations that require substantial computational and human resources within the verification and validation stage of a mission. Additionally, the capability to compute information *a priori* about favorable and unfavorable targeting and maneuver times along a reference trajectory would provide valuable on-board flexibility. The methodologies presented in this investigation seek to address these items by leveraging information about the rates of change in both the constrained quantities and targeting-employed partial derivatives of those constraints with respect to perturbations from the reference trajectory. The insight gained from these local analyses yield methods to reduce the computational effort in approximating the worst-case convergence performance with a series of perturbed targeting simulations and predictive metrics that closely correlate with worst-case performance in targeting problems. The results of the present investigation is are summarized below.

8.1 Discretization Techniques for the Measurement of Convergence Behavior

In pursuit of an empirical description of convergence behavior, the definition of a perturbed targeting problem is formalized in terms of a set of constraints, design variables, and perturbation variables. The space consisting of variations in the perturbation variables around a particular solution is characterized in terms of a local main basin with typically-monotonic convergence behavior and surrounding regions of chaotic convergence behavior. The number of iterations required to converge to a solution on the same constraint manifold is employed as a useful characterization of the space to identify the main basin and the boundary. For a given maximum iteration count, the basin width is defined as the largest hyper-sphere for which all perturbations converge to a solution onto the same constraint manifold, providing a theoretical measure of worst-case performance. In the absence of an

analytic description, numerical discretization techniques are necessary to approximate the measurement.

As an alternative to brute force discretization techniques, the simulation of perturbed targeting problems along principal directions informed by partial derivatives at the reference solution is presented. A first method is proposed that employs the SVD of the perturbation Jacobian matrix, or the derivative of the constraints with respect to the perturbation variables. This method produces an orthogonal set of right singular vectors in the perturbation space that correspond to principal directions of scaling in the constraints. The use of the dominant singular vector is justified by positing that large magnitudes of growth in the constraints correlate to challenges in the corrections process, and the remaining vectors provide an orthogonal set to verify the results. This PDA method reduces the discretization from a problem that grows exponentially as the number of perturbation elements increases to a problem that grows linearly with the perturbation variables. A second method is formulated by observing that the bounding structures of the basin correlate to large relative changes in the design Jacobian matrix, i.e., the partial derivatives employed in the differential corrections process. Higher-order singular vectors are computed to determine the direction with the largest degree of relative local nonlinearity. Both methods are employed in the principal direction analysis to produce a more-efficient approximation of the worst-case convergence performance.

For applications in a variety of regions of space and in both the CRTBP and ephemeris force models, the basin width measurements in each principal direction are recorded to gain insight into the factors driving the structures of convergence basins. In general, the worst-case convergence performance is found to occur along the direction associated with the largest normalized change in the design Jacobian matrix. Frequently, measurements in this direction are determined to align with the measurements in the direction of largest growth in the constraints; however, this property is not guaranteed and is partially dependent on the relative scaling of the constraints. Though the nonlinearity-associated higher-order singular vector requires the additional computation of 2^{nd}-order partial derivatives and the solution to a constrained optimization problem, its value as a discretization direction for producing an efficient upper bound for the worst-case convergence behavior is notable.

For perturbations of mixed dimensional quantities, such as perturbations in position and velocity, a strategy for producing a tradespace is presented. A heuristic method is developed with the assumption that the critical features of the tradespace lie in a plane within the higher-dimensional combined perturbation space. Criteria are outlined to test if the assumption is justifiable in a given case, and the principal plane approximation method is defined in terms of discretization along a series of parameterized vectors, based on the worst-case principal directions in the two individual subspaces. The results of the principal plane approximation are compared to the tradespace produced by a brute force discretization scheme, and the approximation is found to provide significant value in efficiently characterizing the coupled effect of position and velocity perturbations.

8.2 Predictive Metrics for Preliminary Convergence Analysis

Even improved discretization schemes require the simulation of iterative targeting problems, so an effective characterization of worst-case convergence behavior is sought that solely employs information from the reference solution itself. This work investigates scalar values that are functions of the local partial derivatives in the perturbed targeting problem as predictors of the relative worst-case convergence behavior amongst a set of reference solutions. First, quantities based on the FTLE are defined to quantify the maximum rate of growth in the constraints relative to changes in the perturbation variables based on the linearized system. The FTLE-inspired quantities are related to the principal directions of growth in the constraint vector through the SVD of the perturbation Jacobian. Second, the basin metric is introduced as a measure of the largest local normalized change in the design Jacobian matrix and is connected to the previously-defined nonlinearity-associated principal direction.

The relative convergence behavior of sets of solutions to perturbed targeting problems is studied and compared to evaluated quantities. The changes in convergence behavior are characterized as a perturbation and maneuver time is moved downstream along various reference trajectories based on segments of past and planned missions, including planar and spatial periodic orbits, a Sun-Earth L_1-to-L_2 point transit trajectory, and a trans-lunar return trajectory, and in the CRTBP and ephemeris force models. Additionally, the characterization

of convergence behavior is applied to a changing arrival epoch for a Sun-Earth L_1-to-L_2 point transit trajectory. While the FTLE-based quantities are found to correlate somewhat with the general trends in basin width, the basin metric, quantifying local nonlinearity, consistently mirrors the evolving basin width across the set of solutions. Without running any iterative targeting simulations, the computation of the locally-evaluated basin metric allows for the identification of solutions with unfavorable convergence behavior.

8.3 Recommendations for Future Work

Areas for future work that could enhance and continue this investigation are summarized as follows:

1. *Investigate the combined problem of the evolution of perturbations and the evolution of the convergence basin as a node is moved downstream along a reference trajectory.*

   In this investigation, the evolution of the worst-case convergence behavior as a patch point node is moved downstream along a reference trajectory is explored. At the node, the perturbations are modeled as instantaneous changes in the state, applied at the same time as the targeting process and execution of the maneuver. This procedure gives insight into the size of the perturbation that the targeting process is able to accommodate; however, the investigation could be furthered by applying the perturbation upstream at a reference time and comparing its evolution to the basin width as the targeting and maneuver are delayed.

2. *Investigate the ability to predict the effect of the incremental implementation of constraints in the targeting process.*

   For difficult-to-converge targeting problems, a known strategy to assist in convergence is to incrementally impose constraints until a satisfactory trajectory is determined. Frequently, this process is conducted through trial-and-error, relying on the intuition of a specialist. The characterization and prediction strategies developed in this investigation could provide insight into the development of a formal methodology for identifying which constraints to apply and in which order.

3. *Investigate the use of these strategies in measuring and predicting the effect of changes in the targeting scheme on convergence behavior.*

   Numerous alterations to the Newton-Raphson corrections scheme are expected to change the convergence behavior in the vicinity of a particular solution. Possible changes to the targeting scheme include the use of design variable weighting in the minimum-norm update, the implementation of an attenuation factor or line search algorithm, and the incorporation of higher-order derivatives into the update equation. The strategies and methods outlined in this investigation are possible tools to study the effects of these enhancements on convergence and to potentially provide a process for selecting changes to the targeting scheme with the greatest impact.

REFERENCES

[1] G. Deleuze and F. Guattari, *Mille plateaux* (Collection "Critique"). Paris: Éditions de minuit, 1980, 645 pp., ISBN: 978-2-7073-0307-3.

[2] M. G. Epitropakis and M. N. Vrahatis, "Studying the basin of convergence of methods for computing periodic orbits," *International Journal of Bifurcation and Chaos*, vol. 21, no. 8, pp. 2079–2106, Aug. 2011, ISSN: 0218-1274, 1793-6551. DOI: 10.1142/S0218127411029653. [Online]. Available: https://www.worldscientific.com/doi/abs/10.1142/S0218127411029653.

[3] S. Amat and S. Busquier, Eds., *Advances in Iterative Methods for Nonlinear Equations*, vol. 10, SEMA SIMAI Springer Series, Cham: Springer International Publishing, 2016, ISBN: 978-3-319-39227-1 978-3-319-39228-8. DOI: 10.1007/978-3-319-39228-8. [Online]. Available: http://link.springer.com/10.1007/978-3-319-39228-8.

[4] M. Hintermuller, "Semismooth newton methods and applications," Oberwolfach-Seminar on "Mathematics of PDE-Constrained Optimization" at Mathematisches Forschungsinstitut, Oberwolfach, Germany, Nov. 2010.

[5] L. B. Rall, "Convergence of the Newton process to multiple solutions," *Numerische Mathematik*, vol. 9, no. 1, pp. 23–37, Nov. 1966, ISSN: 0029-599X, 0945-3245. DOI: 10.1007/BF02165226. [Online]. Available: http://link.springer.com/10.1007/BF02165226.

[6] L. B. Rall, "A note on the convergence of Newton's method," *SIAM Journal on Numerical Analysis*, vol. 11, no. 1, pp. 34–36, Mar. 1974, ISSN: 0036-1429, 1095-7170. DOI: 10.1137/0711004. [Online]. Available: http://epubs.siam.org/doi/10.1137/0711004.

[7] J. Chen, "The convergence analysis of inexact Gauss–Newton methods for nonlinear problems," *Computational Optimization and Applications*, vol. 40, no. 1, pp. 97–118, May 2008, ISSN: 0926-6003, 1573-2894. DOI: 10.1007/s10589-007-9071-7. [Online]. Available: http://link.springer.com/10.1007/s10589-007-9071-7.

[8] I. K. Argyros, "On a class of newton-like methods for solving nonlinear equations," *Journal of Computational and Applied Mathematics*, vol. 228, no. 1, pp. 115–122, Jun. 2009, ISSN: 03770427. DOI: 10.1016/j.cam.2008.08.042. [Online]. Available: https://linkinghub.elsevier.com/retrieve/pii/S0377042708004433.

[9] I. K. Argyros and S. Hilout, "On the convergence of Newton-type methods using recurrent functions," *International Journal of Computer Mathematics*, vol. 87, no. 14, pp. 3273–3296, Nov. 2010, ISSN: 0020-7160, 1029-0265. DOI: 10.1080/00207160903023557. [Online]. Available: https://www.tandfonline.com/doi/full/10.1080/00207160903023557.

[10] J. F. Epperson, *An introduction to numerical methods and analysis*, Rev. ed. Hoboken, N.J: Wiley-Interscience, 2007, 572 pp., OCLC: ocm85851582, ISBN: 978-0-470-04963-1.

[11] T. Sun and M. Xin, "Hypersonic entry vehicle state estimation using nonlinearity-based adaptive cubature Kalman filters," *Acta Astronautica*, vol. 134, pp. 221–230, May 2017, ISSN: 00945765. DOI: 10.1016/j.actaastro.2017.01.036. [Online]. Available: https://linkinghub.elsevier.com/retrieve/pii/S0094576516308529.

[12] S. K. Biswas, L. Qiao, and A. G. Dempster, "A quantified approach of predicting suitability of using the unscented kalman filter in a non-linear application," *Automatica*, vol. 122, p. 109 241, Dec. 2020, ISSN: 00051098. DOI: 10.1016/j.automatica.2020.109241. [Online]. Available: https://linkinghub.elsevier.com/retrieve/pii/S0005109820304398.

[13] R. S. Park and D. J. Scheeres, "Nonlinear semi-analytic methods for trajectory estimation," *Journal of Guidance, Control, and Dynamics*, vol. 30, no. 6, pp. 1668–1676, Nov. 2007, ISSN: 0731-5090, 1533-3884. DOI: 10.2514/1.29106. [Online]. Available: https://arc.aiaa.org/doi/10.2514/1.29106.

[14] J. Junkins, M. Akella, and K. Alfriend, "Non-Gaussian error propagation in orbital mechanics," *The Journal of the astronautical sciences*, vol. 44, no. 4, pp. 541–563, 1996, Place: SPRINGFIELD Publisher: Amer Astronautical Soc, ISSN: 0021-9142.

[15] J. L. Junkins and P. Singla, "How nonlinear is it? a tutorial on nonlinearity of orbit and attitude dynamics," *The Journal of the Astronautical Sciences*, vol. 52, no. 1, pp. 7–60, Mar. 2004, ISSN: 0021-9142, 2195-0571. DOI: 10.1007/BF03546420. [Online]. Available: https://link.springer.com/10.1007/BF03546420.

[16] R. S. Park and D. J. Scheeres, "Nonlinear mapping of gaussian statistics: Theory and applications to spacecraft trajectory design," *Journal of Guidance, Control, and Dynamics*, vol. 29, no. 6, pp. 1367–1375, Nov. 2006, ISSN: 0731-5090, 1533-3884. DOI: 10.2514/1.20177. [Online]. Available: https://arc.aiaa.org/doi/10.2514/1.20177.

[17] E. L. Jenson and D. J. Scheeres, "Semianalytical measures of nonlinearity based on tensor eigenpairs," presented at the AAS/AIAA Astrodynamics Specialist Conference, Aug. 9, 2021, p. 16.

[18] K. Oguri, K. Oshima, S. Campagnola, *et al.*, "EQUULEUS trajectory design," *The Journal of the Astronautical Sciences*, vol. 67, no. 3, pp. 950–976, Sep. 2020, ISSN: 0021-9142, 2195-0571. DOI: 10.1007/s40295-019-00206-y. [Online]. Available: http://link.springer.com/10.1007/s40295-019-00206-y.

[19] E. S. Gawlik, J. E. Marsden, P. C. Du Toit, and S. Campagnola, "Lagrangian coherent structures in the planar elliptic restricted three-body problem," *Celestial Mechanics and Dynamical Astronomy*, vol. 103, no. 3, pp. 227–249, Mar. 2009, ISSN: 0923-2958, 1572-9478. DOI: 10.1007/s10569-008-9180-3. [Online]. Available: http://link.springer.com/10.1007/s10569-008-9180-3.

[20] G. Harden, A. Haapala, K. C. Howell, and B. Marchand, "Automated patch point placement for spacecraft trajectory targeting," presented at the AAS/AIAA Space Flight Mechanics Meeting, Santa Fe, New Mexico, Jan. 26, 2014, p. 18.

[21] C. M. Spreen, "Automated patch point placement capability for hybrid trajectory targeting," Ph.D. dissertation, Purdue University, West Lafayette, Indiana, Dec. 2017.

[22] C. Spreen, K. Howell, and B. Marchand, "Node placement capability for spacecraft trajectory targeting in an ephemeris model," presented at the AAS/AIAA Astrodynamics Specialist Conference, Vail, Colorado, Aug. 9, 2015, p. 20.

[23] C. York and K. C. Howell, "A two-level differential corrections algorithm for low-thrust spacecraft trajectory targeting," presented at the 29th AAS/AIAA Space Flight Mechanics Meeting, Ka'anapali, Maui, Hawaii, Jan. 13, 2019.

[24] V. Muralidharan and K. C. Howell, "Leveraging stretching directions for stationkeeping in Earth-Moon halo orbits," *Advances in Space Research*, vol. 69, no. 1, pp. 620–646, Jan. 2022, ISSN: 02731177. DOI: 10.1016/j.asr.2021.10.028. [Online]. Available: https://linkinghub.elsevier.com/retrieve/pii/S0273117721007882.

[25] V. Muralidharan and K. C. Howell, "Stretching directions in cislunar space: Applications for departures and transfer design," *Astrodynamics*, Sep. 29, 2022, ISSN: 2522-008X, 2522-0098. DOI: 10.1007/s42064-022-0147-z. [Online]. Available: https://link.springer.com/10.1007/s42064-022-0147-z.

[26] C. K. McCord, K. R. Meyer, and Q. Wang, *The integral manifolds of the three body problem* (Memoirs of the American Mathematical Society no. 628). Providence, R.I: American Mathematical Society, 1998, 91 pp., ISBN: 978-0-8218-0692-0.

[27] D. Guzzetti, N. Bosanac, and K. C. Howell, "A framework for efficient trajectory comparisons in the Earth-Moon design space," in *AIAA/AAS Astrodynamics Specialist Conference*, San Diego, CA: American Institute of Aeronautics and Astronautics, Aug. 4, 2014, ISBN: 978-1-62410-308-7. DOI: 10.2514/6.2014-4110. [Online]. Available: https://arc.aiaa.org/doi/10.2514/6.2014-4110.

[28] C. H. Acton, "Ancillary data services of NASA's navigation and ancillary information facility," *Planetary and Space Science*, vol. 44, no. 1, pp. 65–70, Jan. 1996, ISSN: 00320633. DOI: 10.1016/0032-0633(95)00107-7. [Online]. Available: https://linkinghub.elsevier.com/retrieve/pii/0032063395001077.

[29] C. H. Acton, *Ancillary data services of NASA's navigation and ancillary information facility*, Jan. 1996. [Online]. Available: https://naif.jpl.nasa.gov/naif/.

[30] C. Acton, N. Bachman, B. Semenov, and E. Wright, "A look towards the future in the handling of space science mission geometry," *Planetary and Space Science*, vol. 150, pp. 9–12, Jan. 2018, ISSN: 00320633. DOI: 10.1016/j.pss.2017.02.013. [Online]. Available: https://linkinghub.elsevier.com/retrieve/pii/S0032063316303129.

[31] S. M. Roberts and J. S. Shipman, *Two-point boundary value problems: shooting methods* (Modern analytic and computational methods in science and mathematics no. 31). New York: American Elsevier Pub. Co, 1972, 269 pp., ISBN: 978-0-444-00102-3.

[32] H. B. Keller, *Numerical Solution of Two Point Boundary Value Problems*. Society for Industrial and Applied Mathematics, 1976. [Online]. Available: https://epubs.siam.org/doi/abs/10.1137/1.9781611970449.

[33] T. J. Ypma, "Historical development of the Newton–Raphson method," *SIAM Review*, vol. 37, no. 4, pp. 531–551, Dec. 1995, ISSN: 0036-1445, 1095-7200. DOI: 10.1137/1037125. [Online]. Available: http://epubs.siam.org/doi/10.1137/1037125.

[34] N. Kollerstrom, "Thomas Simpson and 'Newton's method of approximation': An enduring myth," *The British Journal for the History of Science*, vol. 25, no. 3, pp. 347–354, Sep. 1992, ISSN: 0007-0874, 1474-001X. DOI: 10.1017/S0007087400029150. [Online]. Available: https://www.cambridge.org/core/product/identifier/S0007087400029150/type/journal_article.

[35] I. Newton, *De methodis fluxionum et serierum infinitorum*, D. T. Whiteside, Ed., trans. by J. Colson. London, 1736.

[36] J. Raphson, *Analysis Aequationum UNIVERSALIS, SEU Ad AEQUATIONES ALGEBRAICAS Resolvendas METHODUS Generalis, et Expedita, Ex nova Infinitarum serierum Doctrina, DEDUCTA AC DEMONSTRATA*. London, 1690.

[37] T. Simpson, *Essays on Several Curious and Useful Subjects in Speculative and Mix'd Mathematicks*. London: Printed by H. Woodfall, jun. for J. Nourse, at the Lamb without Temple-Bar, 1740.

[38] D. Grebow, "Trajectory design in the Earth-Moon system and lunar south pole coverage," Ph.D. dissertation, Purdue University, West Lafayette, Indiana, May 2010.

[39] T. Pavlak, "Trajectory design and orbit maintenance strategies in multi-body dynamical regimes," Ph.D. dissertation, Purdue University, West Lafayette, Indiana, May 2013.

[40] P. Deuflhard, *Newton Methods for Nonlinear Problems: Affine Invariance and Adaptive Algorithms* (Springer Series in Computational Mathematics). Berlin, Heidelberg: Springer Berlin Heidelberg, 2011, vol. 35, ISBN: 978-3-642-23898-7 978-3-642-23899-4. DOI: 10.1007/978-3-642-23899-4. [Online]. Available: https://link.springer.com/10.1007/978-3-642-23899-4.

[41] M. Gockenbach and C. Liu, "Local convergence of Newton's method in the classical calculus of variations," *Optimization*, vol. 64, no. 4, pp. 957–980, Apr. 3, 2015, ISSN: 0233-1934, 1029-4945. DOI: 10.1080/02331934.2013.811664. [Online]. Available: http://www.tandfonline.com/doi/abs/10.1080/02331934.2013.811664.

[42] H. B. Keller, "Numerical solutions of bifurcations and nonlinear eigenvalue problems," in *Applications of Bifurcation Theory*, P. Rabinowitz, Ed., Academic Press, 1977, pp. 359–384.

[43] E. Doedel and V. Romanov, "Elemental periodic orbits associated with the libration points in the circular restricted 3-body problem," *International Journal of Bifurcation and Chaos*, vol. 17, no. 8, pp. 2625–2677, 2007.

[44] K. C. Howell and H. J. Pernicka, "Numerical determination of lissajous trajectories in the restricted three-body problem," *Celestial Mechanics*, vol. 41, no. 1, pp. 107–124, 1988.

[45] R. S. Wilson and K. C. Howell, "Trajectory design in the Sun-Earth-Moon system using lunar gravity assists," *Journal of Spacecraft and Rockets*, vol. 35, no. 2, pp. 191–198, Mar. 1998, ISSN: 0022-4650, 1533-6794. DOI: 10.2514/2.3309. [Online]. Available: https://arc.aiaa.org/doi/10.2514/2.3309.

[46] B. G. Marchand, K. C. Howell, and R. S. Wilson, "An improved corrections process for constrained trajectory design in the n-body problem," *Journal of Spacecraft and Rockets*, vol. 54, no. 1, pp. 884–897, Aug. 2007.

[47] S. Scarritt, B. Marchand, and M. Weeks, "An autonomous onboard targeting algorithm using finite thrust maneuvers," in *AIAA Guidance, Navigation, and Control Conference*, Chicago, Illinois: American Institute of Aeronautics and Astronautics, Aug. 10, 2009, ISBN: 978-1-60086-978-5. DOI: 10.2514/6.2009-6104. [Online]. Available: https://arc.aiaa.org/doi/10.2514/6.2009-6104.

[48] B. G. Marchand, M. W. Weeks, C. W. Smith, and S. Scarritt, "Onboard autonomous targeting for the trans-Earth phase of Orion," *Journal of Guidance, Control, and Dynamics*, vol. 33, no. 3, pp. 943–956, May 2010, ISSN: 0731-5090, 1533-3884. DOI: 10.2514/1.42384. [Online]. Available: https://arc.aiaa.org/doi/10.2514/1.42384.

[49] A. Daza, A. Wagemakers, B. Georgeot, D. Guéry-Odelin, and M. A. F. Sanjuán, "Basin entropy: A new tool to analyze uncertainty in dynamical systems," *Scientific Reports*, vol. 6, no. 1, p. 31 416, Nov. 2016, ISSN: 2045-2322. DOI: 10.1038/srep31416. [Online]. Available: http://www.nature.com/articles/srep31416.

[50] E. E. Zotos, "Investigating the Newton–Raphson basins of attraction in the restricted three-body problem with modified Newtonian gravity," *Journal of Applied Mathematics and Computing*, vol. 56, no. 1, pp. 53–71, Feb. 2018, ISSN: 1598-5865, 1865-2085. DOI: 10.1007/s12190-016-1061-4. [Online]. Available: http://link.springer.com/10.1007/s12190-016-1061-4.

[51] J. Pollock, *Convergence*, 1952. [Online]. Available: https://buffaloakg.org/artworks/k19567-convergence.

[52] C. D. Martin and M. A. Porter, "The extraordinary SVD," *The American Mathematical Monthly*, vol. 119, no. 10, p. 838, 2012, ISSN: 00029890. DOI: 10.4169/amer.math.monthly.119.10.838. [Online]. Available: https://www.tandfonline.com/doi/full/10.4169/amer.math.monthly.119.10.838.

[53] G. W. Stewart, "On the early history of the singular value decomposition," *SIAM Review*, vol. 35, no. 4, pp. 551–566, Dec. 1993, ISSN: 0036-1445, 1095-7200. DOI: 10.1137/1035134. [Online]. Available: http://epubs.siam.org/doi/10.1137/1035134.

[54] W. Greiner, "Lyapunov exponents and chaos," in *Classical Mechanics*. Berlin, Heidelberg: Springer Berlin Heidelberg, 2010, pp. 503–516, ISBN: 978-3-642-03433-6 978-3-642-03434-3. DOI: 10.1007/978-3-642-03434-3_26. [Online]. Available: https://link.springer.com/10.1007/978-3-642-03434-3_26.

[55] J. L. Junkins, "Von Karman lecture: Adventures on the interface of dynamics and control," *Journal of Guidance, Control, and Dynamics*, vol. 20, no. 6, pp. 1058–1071, Nov. 1997, ISSN: 0731-5090, 1533-3884. DOI: 10.2514/2.4176. [Online]. Available: https://arc.aiaa.org/doi/10.2514/2.4176.

[56] J. Hahn and T. F. Edgar, "A Gramian based approach to nonlinearity quantification and model classification," *Industrial & Engineering Chemistry Research*, vol. 40, no. 24, pp. 5724–5731, Nov. 1, 2001, ISSN: 0888-5885, 1520-5045. DOI: 10.1021/ie010155v. [Online]. Available: https://pubs.acs.org/doi/10.1021/ie010155v.

[57] M. Majji, J. L. Junkins, and J. D. Turner, "A high order method for estimation of dynamic systems," *The Journal of the Astronautical Sciences*, vol. 56, no. 3, pp. 401–440, Sep. 2008, ISSN: 0021-9142. DOI: 10.1007/BF03256560. [Online]. Available: http://link.springer.com/10.1007/BF03256560.

[58] J. L. Junkins, M. Majji, and J. D. Turner, "High order Keplerian state transition tensors," presented at the F. Landis Markley Astronautics Symposium, Cambridge, Maryland, 2008, pp. 169–186.

[59] T. G. Kolda and B. W. Bader, "Tensor decompositions and applications," *SIAM Review*, vol. 51, no. 3, pp. 455–500, Aug. 6, 2009, ISSN: 0036-1445, 1095-7200. DOI: 10.1137/07070111X . [Online]. Available: http://epubs.siam.org/doi/10.1137/07070111X.

[60] S. Rabanser, O. Shchur, and S. Günnemann, *Introduction to tensor decompositions and their applications in machine learning*, Nov. 29, 2017. arXiv: 1711.10781[cs,stat]. [Online]. Available: http://arxiv.org/abs/1711.10781.

[61] L.-H. Lim, "Singular values and eigenvalues of tensors: A variational approach," in *1st IEEE International Workshop on Computational Advances in Multi-Sensor Adaptive Processing, 2005.*, Puerto Vallarta, Mexico: IEEE, 2005, pp. 129–132, ISBN: 978-0-7803-9322-6. DOI: 10.1109/CAMAP.2005.1574201. [Online]. Available: http://ieeexplore.ieee.org/document/1574201/.

[62] J. P. Gutkowski, T. F. Dawn, and R. M. Jedrey, "Evolution of Orion mission design for Exploration Mission 1 and 2," presented at the AAS Guidance, Navigation, and Control Conference, Breckenridge, Colorado, Feb. 5, 2016.

[63] T. Dawn, J. P. Gutkowski, A. L. Batcha, and S. M. Pedrotty, "Trajectory design considerations for Exploration Mission 1," presented at the AAS/AIAA Space Flight Mechanics Meeting, Kissimee, Florida, Jan. 2018.

[64] A. L. Batcha, J. Williams, T. F. Dawn, *et al.*, "Artemis I trajectory design and optimization," presented at the AAS/AIAA Astrodynamics Specialist Conference, Virtual, Aug. 9, 2020.

[65] E. M. Zimovan, K. C. Howell, and D. C. Davis, "NEAR RECTILINEAR HALO ORBITS AND THEIR APPLICATION IN CIS-LUNAR SPACE," presented at the 3rd International Academy of Astronautics Conference on Dynamics and Control of Space Systems, Moscow, Russia, 2017.

[66] D. Davis, S. Bhatt, K. Howell, *et al.*, "Orbit maintenance and navigation of human spacecraft at cislunar near rectilinear halo orbits," presented at the 27th AAS/AIAA Space Flight Mechanics Meeting, San Antonio, Texas, Feb. 5, 2017, p. 20.

[67] J. C. Crusan, R. M. Smith, D. A. Craig, *et al.*, "Deep Space Gateway concept: Extending human presence into cislunar space," in *2018 IEEE Aerospace Conference*, Big Sky, Montana: IEEE, Mar. 2018, pp. 1–10. DOI: 10.1109/AERO41646.2018.

[68] NASA. "Genesis mission trajectory and flight plan." (Nov. 2009), [Online]. Available: https://solarsystem.nasa.gov/genesismission/gm2/images/gallery/artist_renderings/%20artist_renderings9.htm.

[69] M. W. Lo, B. G. Williams, W. E. Bollman, *et al.*, "Genesis mission design," *The Journal of the Astronautical Sciences*, vol. 49, no. 1, pp. 169–184, Mar. 2001, ISSN: 0021-9142, 2195-0571. DOI: 10.1007/BF03546342. [Online]. Available: https://link.springer.com/10.1007/BF03546342.

[70] B. Barden, R. S. Wilson, K. C. Howell, and B. Marchand, "Summer launch options for the Genesis mission," presented at the AAS/AIAA Astrodynamics Specialists Conference, Quebec City, Canada, Jul. 30, 2001.

[71] B. Marchand, *Genesis trajectory data*, 2019.

VITA

Collin Eugene York was born in Holland, Michigan and raised in the city of Hudson, Ohio, where he graduated from Hudson High School. He attended Purdue University in West Lafayette, Indiana, majoring in Aeronautical and Astronautical Engineering and minoring in Political Science in May 2013. For three years, Collin worked as a product engineer, designing and releasing turbocharger technologies for diesel engines at Cummins Inc. in Columbus, Indiana. With the support of his wife, Caroline, he returned to the academy to study astrodynamics and space applications in the Multi-Body Dynamics Research Group with Professor Kathleen Howell at Purdue University in August 2016. As part of his graduate studies, Collin investigated low-thrust trajectory design and the development of a two-level differential corrections scheme for low-thrust applications, writing his thesis on the topic and earning an MS degree. For his Ph.D., he continued his studies at Purdue University by researching methods for the measurement and prediction of convergence behavior in space flight trajectory targeting problems. During his graduate studies, Collin completed five internships at NASA Johnson Space Center and was hired as a Pathways Intern, working in the Autonomous Guidance, Navigation and Control Branch and the Flight Mechanics and Trajectory Design Branch within Engineering and the Flight Dynamics Branch within Flight Operations. During his tenure at NASA JSC, he contributed to the Artemis I and II missions as well as the Boeing Starliner Commercial Crew Program. Collin will continue his career at NASA JSC as an aerospace engineer for the Artemis program.